Development of $Mg_2(Si, Sn)$-based thermoelectric generators: investigating contacting solutions, fabrication process, evaluating measurement reliability and optimization paths via modelling

Von der Fakultät für Ingenieurwissenschaften

Abteilung Elektrotechnik und Informationstechnik

der Universität Duisburg-Essen

zur Erlangung des akademischen Grades

Doktor der Ingenieurwissenschaften (Dr. Ing.)

genehmigte Dissertation

von

Julia Camut
aus
Frankreich

Gutachter: Prof. Dr. Johannes de Boor
Gutachter: Prof. Dr. Gabi Schierning
Tag der mündlichen Prüfung: 24.03.2023

Printed and/or published with the support of the German Academic Exchange Service.

This cumulative thesis contains the following publications:

1. **Chapter 3 (Paper 1):** J. Camut, N.H. Pham, D.Y. Nhi Truong, G. Castillo-Hernandez, N. Farahi, M. Yasseri, E. Mueller, J. de Boor, *Aluminum as promising electrode for Mg2(Si,Sn)-based thermoelectric devices*, Materials Today Energy, 2021, Volume 21, p. 100718, https://doi.org/10.1016/j.mtener.2021.100718.

2. **Chapter 4 (Paper 2):** J. Camut, S. Ayachi, S.; G. Castillo-Hernández, S. Park, B. Ryu, S. Park, A. Frank, C. Stiewe, E. Müller, J. de Boor, *Overcoming Asymmetric Contact Resistances in Al-Contacted Mg2(Si,Sn) Thermoelectric Legs*, Materials, 2021, 14, 6774, https://doi.org/10.3390/ma14226774

3. **Chapter 5 (Paper 3):** J. Camut, P. Ziolkowski, P. Ponnusamy, C. Stiewe, E. Mueller, J. de Boor, *Efficiency Measurement and Modeling of a High-Performance Mg2(Si,Sn)-Based Thermoelectric Generator,* Adv. Eng. Mater., 2022, 2200776. https://doi.org/10.1002/adem.202200776

These papers are implemented as Chapters 3, 4 and 5, preceded by an introduction and overview of the thesis (Chapters 1 and 2) and succeeded by discussion (Chapter 6), conclusion and outlook (Chapter 7) and references for Chapters 1, 2, 6 and 7. Each chapter containing a published paper includes a brief summary on the contents at the beginning.

Each paper is added to the thesis as the final revised submitted version, including its own references and Supplementary Material if any.

Declaration of Independence

(Versicherung & Selbständigkeitserklärung)

I hereby affirm that I have prepared the submitted thesis independently and without unauthorized outside support. All provided help and supervision are specified in the thesis and/or the acknowledgement, and all data taken from published work is marked as it is. Utilized methods, instruments and experimental setups are also all indicated in the corresponding chapter. Results and data resulting from collaborative work are specified as such, and were utilized with full agreement of the collaborators.

The three papers included in this cumulative thesis as Chapters 3, 4 and 5 were added after knowledge and agreement of all co-authors. An exhaustive list of all co-authors, as well as task distribution, is provided at the end of this manuscript.

Julia Camut

Date: 05/12/2022

Signature: 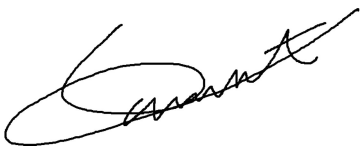

Short Abstract

Thermoelectric (TE) technology has the ability to convert heat into electricity and is therefore attractive in the context of the search for new green energy sources. The aim of this thesis is to successfully build, characterize and model eco-friendly TE generators (TEG) made of p- and n-type $Mg_2(Si,Sn)$ TE materials.

The TE materials are already well-researched but a compatible electrode, electrically interconnecting the TE elements, is missing on the road towards a TEG. Moderately satisfying electrodes were reported in literature, but lacked chemical or mechanical stability. In this work, we find Al to be a promising electrode for $Mg_2(Si,Sn)$: we report no cracking nor delamination, a stable interface through annealing and contact resistivities below 10 $\mu\Omega cm^2$ and stable TE materials directly after joining. This is an essential milestone towards the TEG.

We then successfully build and characterize a full $Mg_2(Si,Sn)$-based TEG. The first efficiency measurement of such a module is reported and we measure a high power density of 0.9 W/cm^2. We combine the TEG characterization with an analysis based on constant property model (CPM) to identify loss mechanisms. An increase of the inner resistance of the TEG, attributed to cracking due to high thermal stress, is observed. It is predicted that both efficiency and power output could be realistically increased by 30% solely by preventing this cracking.

Finally, we test the hypothesis that the TEG mechanical failure is due to the ceramic plate by using an open module design with bare Cu bridges. Additional voltage probes are soldered to monitor the resistance of each leg during the measurement. This innovative approach consistently shows that the resistance of the n-type legs systematically increases even at low temperatures. It is found that increasing the cross-section of the legs solves the issue when the hot side temperature remains below 300 °C; suggestions for even further improvement are given.

Overall, we identify the first truly promising electrode for $Mg_2(Si,Sn)$ and use it to successfully build one of the first eco-friendly $Mg_2(Si,Sn)$-based TEGs. We report the first efficiency measurement for such a module and implement a different design to improve the performance. Strategies for further improvement are identified and tested with innovative measurement and modelling techniques.

Kurze Zusammenfassung

Thermoelektrische (TE) Technologie kann Wärme in Elektrizität umwandeln und ist daher im Zusammenhang mit der Suche nach neuen grünen Energiequellen attraktiv. Ziel dieser Arbeit ist es, die Herstellungsroute eines umweltfreundlichen TE-Generator (TEG) aus p- und n-Typ

$Mg_2(Si,Sn)$ zu etablieren und so die praktische Anwendbarkeit von TE Technologie zu verbessern. Währen p- und n-Typ $Mg_2(Si,Sn)$ als thermoelektrische Materialien erforscht und zu Teilen optimiert sind, fehlt eine funktionierende Anschluss- und Verbindungstechnik sowie der Nachweis eines funktionierenden Demonstrators. Die Arbeit umfasst daher die Suche und Identifikation einer geeigneten Elektrode (als mechanisches und elektrisches Bindeglied zwischen TE Material und Kupferbrücken), die Herstellung von TEG Prototypen sowie deren experimentelle Charakterisierung und Modellierung. In der Literatur wurde über einige, nicht zufriedenstellende Elektroden für $Mg_2(Si,Sn)$ berichtet, denen es an chemischer oder mechanischer Stabilität mangelt. In dieser Arbeit wird mit Al eine vielversprechende Alternative aufgezeigt. Mittels mikrostruktureller und elektrischer Untersuchungen konnte gezeigt werden, dass bei geeigneten Prozessparametern mechanisch stabile Grenzfläche ohne Rissbildung und mit elektrischen Kontaktwiderständen < 10 $\mu\Omega cm^2$ hergestellt werden können; weiterhin ist das TE-Material direkt nach dem Fügen unverändert.

Anschließend wurde eine Herstellungsroutine etabliert und ein TEG vollständig auf $Mg_2(Si,Sn)$-Basis demonstriert und charakterisiert. . Es wird über die erste Effizienzmessung eines solchen Moduls berichtet, und wir messen eine hohe Leistungsdichte von 0,9 W/cm^2. Ein Modell auf Basis konstanter (gemittelter) Materialeigenschaften wird verwendet, um die Messergebnisse zu analysieren und die Zuverlässigkeit der Messung zu bewerten. Es wird ein Anstieg des Innenwiderstands des TEGs beobachtet, welcher mittels einer *post mortem* Analyse auf Rissbildung aufgrund hoher thermischer Belastung zurückgeführt werden kann. Weiterhin kann gezeigt werden, dass sowohl der Wirkungsgrad als auch die nutzbare elektrische Leistung realistischerweise um 30 % gesteigert werden können, wenn die Rissbildung verhindert wird.

Schließlich testen wir die Hypothese, dass das mechanische Versagen des TEG auf die üblicherweise verwendeten, einhausenden Keramikplatte zurückzuführen ist, indem wir ein offenes Moduldesign mit blanken Cu-Brücken verwenden. Zur Überwachung des Widerstands der einzelnen Schenkel während der Messung werden zusätzliche Spannungssonden angelötet. Dabei wird durchweg beobachtet, dass der Widerstand der n-Typ-Schenkel auch bei niedrigen Temperaturen systematisch über das erwartete Maß hinaus zunimmt. Es wird festgestellt, dass eine Vergrößerung des Querschnitts der Beine das Problem löst, wenn die Temperatur der heißen Seite unter 300 °C bleibt. Die Grenzen der derzeitigen Methodik in Bezug auf die Risslokalisierung werden aufgezeigt und Verbesserungsvorschläge unterbreitet.

Insgesamt gelingt es uns eine geeignete Elektrode für $Mg_2(Si,Sn)$ zu identifizieren, einen umweltfreundlichen TEG-Demonstrator auf $Mg_2(Si,Sn)$-Basis herzustellen und diesen zu charakterisieren. Verbesserungsmöglichkeiten werden mit Hilfe von innovativen Mess- und Modellierungsansätzen identifiziert.

Acknowledgements

I would like to thank my supervisors Jun.-Prof. Johannes de Boor and Prof. Eckhard Müller for allowing me to pursue my research in their group as a PhD candidate after welcoming me as a Master student. I would like to thank them for supporting me in DLR and in Germany, for their patience, advice and knowledge.

Jun.-Prof. Johannes de Boor was my direct supervisor during my PhD study. We had a pleasant atmosphere in the group which made research fun and enjoyable, in large part thanks to his presence and investment (and for once, the "thanks to" really does apply!). He always encouraged me to be more positive and see my results in a brighter light, which is a state of mind I will always try to bring further with me in my career.

I would like to thank Christian Stiewe for his tips and tricks around the lab and his guidance in my journey towards TEG building, Przemyslaw Blaschkewitz for his long-lasting support with the TEGMA and thermoelectric measurements (since the Masters time!) and Pawel Ziolkowski for his patient help and many advices for the PSM and TEGMA measurements. Thanks to the three of you for your smile and good mood!

Much love and many wishes to my several office mates over the years: Antoine, Mohammad, Nacho, Laura, Léo, Harshita and Amandine. Thank you for the entertaining debates (related to TE… or not!), laughter and the numerous tea/coffee breaks we shared. While I'm at it, I also want to thank Nacho, Laura, Léo and Amandine for being all motivated, excited, curious and thorough students (and lovely friends). I had a wonderful time guiding you through the lab and assisting you in each of your Masters research; thank you for introducing me to supervision in such a fun and friendly way! Arthur, we have met only for a short time but I am sure those words apply to you too and I wish you the best.

I would also like to thank my amazing colleagues Prasanna, Sahar, Gustavo, Mila, Aryan, Nader, Nhi, Radhika, Kunal, Silvana, Gregor, Karsten, Severin, Jhonatan, Sanyukta, Kalpna, Matthias, Lennart, Vidushi, Adina, Frederic, Didem and Louis for their support, and for the enjoyable working environment. Thank you for all the yummy food and hilarious Werewolf games we shared over the years. I would like to particularly thank Gustavo for being my "administration dad": thank you for your invaluable assistance when I struggled with German.

I would like to thank our collaborators Byungki Ryu, Sungjin Park and Sudong Park as well as everyone else in their team in the Korea Electrotechnology Research Institute (KERI) in

Changwon, South Korea. Thank you for providing us with all the hybrid-DFT calculations that allowed me to deepen our understanding of important results.

Last but not least, I would like to thank my family: my parents Pierre and Mireille, by sister Alexandra, my brother Vincent and my partner Louis. Alex, Vinc, thank you for being such an inspiration growing up, for teaching me courage and perseverance. Papa, Maman, thank you for believing in me and always supporting me, even when I move far away and I forget to call. You are the reason I am me. Louis, thank you for your patience, for sticking up with me through all of this and for being you. I would have never made it without your continuous support.

Abstract

In the context of global warming and the will to reduce the use of fossil fuels, new environment-friendly energy sources are actively researched. Thermoelectric (TE) technology has the attractive ability to convert heat into electricity and can therefore be used to exploit and recycle the heat lost in many processes, including power generation, heavy industries and transport.

The aim of this thesis is to successfully build, characterize and understand a TE generator (TEG) made of p- and n-type $Mg_2(Si,Sn)$ TE materials, which are well-investigated and performant TE materials in the range between room temperature and 450 °C. The development of a TEG requires many steps, including the search of a compatible metallic electrode, which is used to electrically connect the TE elements of a generator in series, the manufacturing process of the TEG itself and its characterization.

Moderately satisfying electrodes were reported for $Mg_2(Si,Sn)$ in literature: their drawback was that they altered the properties of the n-type material [1, 2], or the samples showed cracking or delamination [2, 3]. In this work, we find Al to be a promising electrode for $Mg_2(Si,Sn)$ [4]. We report no cracking nor delamination contrarily to previously reported electrodes, a stable interface through annealing and contact resistivities below 10 $\mu\Omega cm^2$, while no change in the TE materials are observed directly after joining.

It is further observed that the main drawback of using Al is the lack of reproducibility of the samples, with varying and asymmetric contact resistances [5]. We identify the origin of the asymmetry to be during the dicing step. Ion etching of the Al foils before sputtering an oxidation barrier is tested and found to be an effective strategy to maintain symmetrically low contact resistivities below 10 $\mu\Omega cm^2$ after the dicing step. The Zn used as oxidation barrier induces a slight carrier concentration gradient in the n-type material; the process is nevertheless kept to build a TEG.

Finally, in [6], we build and characterize a full $Mg_2(Si,Sn)$-based TEG. The first efficiency measurement of such a module is reported and we measure a high power density of 0.9 W/cm^2. A constant property model (CPM) is used, assuming homogeneous n-type material, to evaluate the reliability of the measurement. A further analysis combining carrier concentration profiling of the n-type material and the single parabolic band (SPB) model is made in this thesis, bringing more nuance to the conclusions drawn in [6]. The CPM allows to identify the origin of the

degradation of the TEG prototype, by the increase of its inner resistance, attributed to cracking due to high thermal stress. It is predicted that both efficiency and power output could be realistically increased by 30% by preventing cracking.

In this thesis, we test the hypothesis that the TEG mechanical failure is due to the Al_2O_3 plate by using an open module design with only Cu bridges. Additional voltage probes are soldered to monitor the resistance of each leg during the measurement. It is consistently observed that the resistance of the n-type legs systematically increases even at low temperatures. It is found that increasing the cross-section of the legs solves the issue when the hot side temperature remains below 300 °C. It is also pointed that the current methodology has its limits in terms of crack localization.

Overall, we find a suitable electrode for $Mg_2(Si,Sn)$ and successfully build and characterize an eco-friendly $Mg_2(Si,Sn)$-based TEG building. Paths for improvement are identified and tested with an innovative measurement technique which allows to isolate each leg of the TEG.

Table of Contents

List of Symbols

Thermoelectric properties

Symbol	Description	Unit
α	Seebeck coefficient	[V K^{-1}]
κ	Thermal conductivity	[W K^{-1} m^{-1}]
σ	Electrical conductivity	[S m^{-1}]
ρ	Electrical resistivity, $\rho = \frac{1}{\sigma}$	[Ωm]

Generic parameters

Symbol	Description	Unit
T	Temperature	[K]
T_h	Temperature at hot side	[K]
T_c	Temperature at cold side	[K]
U, V	Voltage	[V]
τ	Thomson coefficient	[V K^{-1}]
Π	Peltier coefficient	[V]
z	Material figure of merit	[K^{-1}]
Z	Device figure of merit	[K^{-1}]
PF	Power Factor	[W m^{-1} K^{-2}]
P	Electrical power	[W]
η	Efficiency	-
K	Thermal conductance	[W m^{-1}]
W	Thermal resistance	[m W^{-1}]

R	Inner electrical resistance	[Ω]
R_{L}	Load resistance	[Ω]
x	Position along the length of the TE leg	[m]
I	Electric current	[A]
j	Electrical current density	[A/m^2]
$\dot{Q}$, Q	Heat flow	[W]
Q_{in}	Heat flow in at the hot side	[W]
Q_{out}	Heat flow out at the cold side	[W]
Q_{Π}	Peltier heat flow	[W]

Constant property model parameters

Symbol	**Description**	**Unit**
U_0	Seebeck Voltage	[V]
$T_{\mathrm{h,m},I}$, $T_{\mathrm{c,m},I}$	Temperature at the hot, cold block in TEG measurement at current I	[K]
$T_{\mathrm{h,TE},I}$, $T_{\mathrm{c,TE},I}$	Temperature at the hot, cold side of the TE legs at current I	[K]
$\Delta T_{\mathrm{par},I}$	Parasitic temperature loss at current I	[K]
Q_I	Heat flow at the hot side (Q_{in}) at current I	[W]
K_{TE}	Thermal conductance of the TE legs	[W/K]
R_{TE}	Electrical resistance of the TE legs	[Ω]
R_{c}	Electrical contact resistance	[Ω]
r_{c}	Electrical contact resistivity	[Ω]
N	Number of leg pairs	-

L	Length of TE element	[m]
A	Cross-sectional area of TE element	[m^2]
I_{opt}, $I_{opt,p}$	Current at maximum power	[A]
$I_{opt,\eta}$	Current at maximum efficiency	[A]
P_{max}	Maximum power output	[W]
η_{max}	Maximum efficiency	-

Single parabolic band model parameters

Symbol	Description	Unit
y	Atomic composition in Sn ($Mg_2Si_{1-y}Sn_y$)	-
μ	Electron mobility	[$m^2 V^{-1}s^{-1}$]
κ_{lat}	Lattice thermal conductivity	[W K^{-1} m^{-1}]
κ_e	Electronic thermal conductivity	[W K^{-1} m^{-1}]
n	Electron concentration	[m^{-3}]
m_s^*	Single valley effective mass	[kg]
m_D^*	Density of states effective mass	[kg]
$\hbar$	Reduced Planck's constant	[J s]
η_c	Reduced chemical potential	[eV]
L	Lorentz number	[$V^2 K^{-2}$]
k	Electron wave vector	[m^{-1}]
E_g	Band gap	[eV]
E	Energy	[eV]
E_F	Fermi energy	[eV]

$F_i(\eta_c)$	Fermi integral of order i	-
ρ_d	Mass density	[kg m^{-3}]
N_V	Valley degeneracy	-
λ	Scattering parameter	-
E_{Def}	Deformation potential constant	[eV]
E_{AS}	Alloy scattering parameter	[eV]
v_l	Longitudinal velocity of sound	[m s^{-1}]

Other

Symbol	Description	Unit
Φ	Work function	[eV]
E	Young‘s Modulus	[GPa]
σ_S	Mechanical stress	[GPa]
a	Coefficient of thermal expansion	[K^{-1}]
ν	Poisson ratio	-
c_p	Specific heat	[J kg^{-1} K^{-1}]
D	thermal diffusivity	[m^2 s^{-1}]
C_V^{DP}	Dulong-Petit limit	[J kg^{-1} K^{-1}]
β_T	Coefficient of compressibility	[m s^2 kg^{-1}]

Fundamental Constants

Symbol	Quantity	Value
e	Electronic charge	1.6×10^{-19} C

h	Planck´s constant	6.62×10^{-34} m^2 kg s^{-1}
m_0	Electron rest mass	9.1×10^{-31} kg
k_B	Boltzmann's constant	8.61×10^{-5} eV K^{-1}

List of Acronyms

General

Short form	Expansion
1D	One-dimensional
2D	Two-dimensional
3D	Three-dimensional
RTG	Radioisotope Thermoelectric Generator
DLR	German Aerospace Center (“Deutsches Zentrum für Luft- und Raumfahrt“)
TE	Thermoelectric
TEG	Thermoelectric Generator (equivalently used for Thermoelectric Module)
CB	Conduction Band
VB	Valence Band
CBM	Conduction Band Minimum
VBM	Valence Band Maximum
TAv	Temperature average
CTE	Coefficient of Thermal Expansion
HMS	Higher Manganese Silicide

Experimental, characterization

Short form	Expansion
DSP	Direct Sinter Press
ECAS	Electric Current-Assisted Sintering
PVD	Physical Vapor Deposition

PSM	Potential & Seebeck Microprobe (inhouse device)
EDX	Energy-Dispersed X-Ray Spectroscopy
DBC	Direct Bonded Copper
SEM	Scanning Electron Microscope/Microscopy
BS	Backscattered Electrons
SE	Secondary Electrons
HT-*S*-σ	High Temperature Seebeck Sigma (inhouse device)
LFA/XFA	Laser/Xenon Flash Analysis
TEGMA	Thermoelectric Generator Measurement Apparatus
HFM	heat flow meter
DC	Direct Current
RSS	Rapid Steady State
GHP	Guarded Heater Plate
APM	Additional Probes Measurement
RM	Regular Measurement

Modelling

Short form	**Expansion**
FEM	Finite Element Method
CPM	Constant Properties Model
SPB	Single Parabolic Band
DFT	Density Functional Theory
AP	Acoustic Phonon
AS	Alloy Scattering

List of Figures

1. Chapter 1: Introduction

Since the 1950th, global energy consumption has increased by a factor of six, and it has doubled since 1980 [7]. The fossil fuel resources, meanwhile, are diminishing and their detrimental impact on the environment is becoming more and more relevant on the political stage, and more and more tangible in the daily life in European regions. As a consequence, renewable energy sources like solar and wind have been studied for a long time, to eventually stop relying on fossil fuels. However, these technologies still cannot be used independently as they highly depend on weather conditions and as their storage and production capacity are limited. Therefore, new environment-friendly energy sources are actively researched.

Among these alternatives, thermoelectricity has proved itself to be an efficient useful alternative to increase the efficiency in existing processes [8]. Thermoelectric technology has the ability to convert heat into electricity and can therefore be used to exploit and recycle the heat lost in many processes, including power generation, heavy industries and transport. Historically, thermoelectric generators (TEG) were designed and used for space applications such as the Voyager 1 and 2 probes and the Curiosity and Perseverance rovers on Mars, which cannot be fed by solar cells due to the lack of sunlight in several encountered environments. Those generators use the heat released by the natural decay of radioactive materials as heat source, which is why they are known as Radioisotope Thermoelectric Generators (RTG) [9]. TEG are highly reliable, have a long lifespan and require low maintenance due to their lack of moving parts, which makes them very attractive for space applications.

Nowadays, research focuses on implementing thermoelectric energy sources on a wider scope, not only in space, but also for terrestrial applications. Recycling the heat released in the engines of cars and airplanes [2], in the steel industry [10] or in power plants [11] is an attractive strategy for energy generation. Thermoelectricity is also considered for small scale applications such as wearable devices and electronics [9].

The aim of this work at the German Aerospace Center (DLR) is to develop high-performance TEGs based on light-weight and high-performance thermoelectric silicide materials. On the road leading to such generators, a first step is the synthesis and optimization of the thermoelectric materials, as well as the selection and development of adapted contacting solutions. In this work, we test a new electrode for a specific and performant TE material and optimize the contacting process to identify the best electrode, in order to pave the way towards

industrial production of viable TEG technology. A full TEG building routine is then implemented and prototypes are obtained and successfully characterized. The measurements are compared to theoretical predictions which reveals a path for further improvement of the built TEGs.

1.1. Thermoelectric effects

The phenomenon of thermoelectricity can be described by three different effects.

The first effect is the Seebeck effect. It was first observed in 1821 by Thomas J. Seebeck [12]. It corresponds to the generation of an electrical potential difference due to a difference of temperature in a material, as represented in Figure 1.

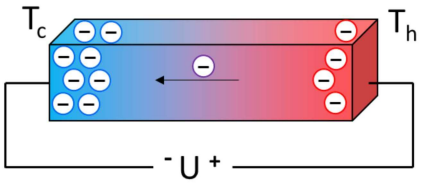

Figure 1 - Schematics of the Seebeck effect: when a temperature difference is applied to a material, the charge carriers (here electrons) move faster on the hot side, which leads to an accumulation of charges on the cold side. This creates a thermovoltage in the material.

The application of a temperature difference between both sides of a material will lead to the thermodiffusion of the charge carriers inside this material. Assuming that only one type of carrier exists in the material, an equivalent electron gas model can be considered [12]. In the Drude model, the mean kinetic energy of the charge carriers is related to temperature. Particles coming from a warmer place have a higher velocity and momentum than those coming from a colder place, therefore when those particles collide, the vectoral sum of the momentum (which is conserved during the scatter event) statistically has a nonzero net value. As a result, a net thermodiffusion current of moving particles from warm to cold takes place. The voltage obtained due to the Seebeck effect is proportional to the temperature difference and therefore can be described by the following equation:

$$U_0 = -\alpha \Delta T \tag{1}$$

where U_0 is the Seebeck voltage, α is the Seebeck coefficient of the material and $\Delta T = T_\mathrm{h} - T_\mathrm{c}$ is the temperature difference applied to the material (T_h and T_c being the hot and cold side

temperatures respectively). It can be noted that the sign of α depends on the majority charge carriers in the materials. In case of electrons, α will be negative, as a positive potential is created at the hot side, while a negative potential is created in case of holes.

The second effect is the Peltier effect. It was first observed by Jean Charles Athanase Peltier in 1834 [12]. Contrarily to the Seebeck effect which generates a voltage due to a temperature difference, the Peltier effect corresponds to the release or absorption of heat at a junction between two materials when a current is flowing through it [13]. With finite thermal coupling, this generates a temperature difference within each material, as a consequence the Peltier effect is often referred to as a reverse Seebeck effect although it is not strictly correct. The Peltier effect is more easily understood considering infinite coupling (i.e. the temperatures at both contact points of a junction are kept constant), when formation of a thermal gradient is suppressed and only the junction is absorbs/releases heat. The Peltier effect at a metal-semiconductor junction, like it is found in a thermoelectric device, is represented in Figure 2.

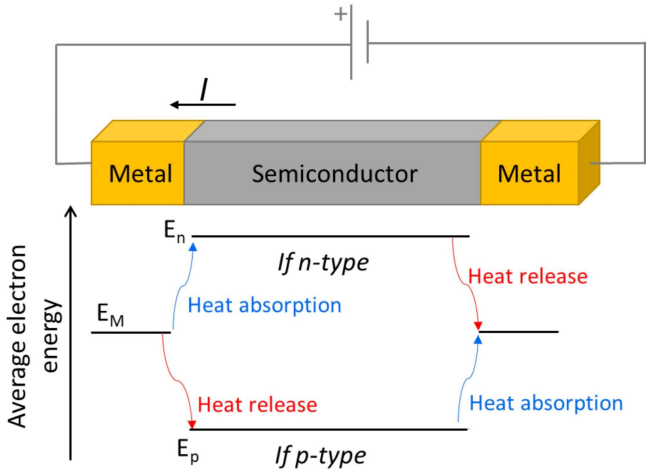

Figure 2 - Schematics of the Peltier effect between metal-semiconductor junctions under isothermal conditions. Both metallic portions are made of the same material. When an electrical current is applied, the electrons move from one material to the other, and the difference between the mean energy of the carriers in the different materials (E_M, E_n, E_p) leads to either heat absorption or release. Note that these energies are not the same as the respective chemical potentials. A vertical energy axis is shown on the left for reference.

A potential difference causes the electrons to move along the different materials of the circuit. The metal and TE materials have different Seebeck coefficients as their carriers move at different average energy levels. Heat is absorbed when electrons have to jump from a material with lower average energy level to a material with higher average energy level (metal to n-type, p-type to metal) and heat is released in the opposite case, as electrons release energy by passing from one material to the other. In reality, there would also be a decrease in the average energy

level along the semiconductor material, and between both metallic electrodes due to Ohm's law, but this is not represented in Figure 2.

It can be understood from Figure 2 that the heat emission or absorption at each junction depends on the direction of the electrical current and on the majority carrier type of the semiconductor. This is why in a TE cooling device, p- and n-type elements should be assembled such as represented in Figure 3. This ensures that the hot and cold junctions between TE material and metal are on the same side for all elements.

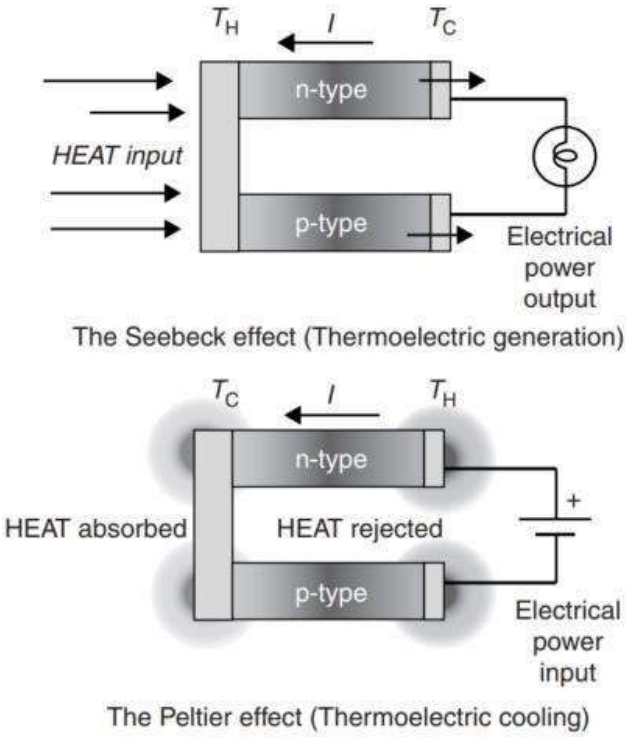

Figure 3 – Basic schematics of the use of the Seebeck effect in a thermoelectric generator (upper) and of the Peltier effect in a thermoelectric refrigerator (lower). Here the technical current direction is employed. Taken from [14].

The emitted/absorbed Peltier heat per time unit at a junction between two material M1 and M2 can be described as follows:

$$Q_{\Pi} = I(\Pi_{\mathrm{M1}} - \Pi_{\mathrm{M2}}) \tag{2}$$

where I is the electrical current and Π is the Peltier coefficient. Usually the symbol $\dot{Q}$ is rather used for heat flows, but since only heat flows and no heat are used in this thesis the symbol Q is preferred for simplicity and consistency with [6]. The Peltier effect and the Seebeck effects are related by the first Thomson (Kelvin) relation [12, 14], such as:

$$\Pi = \alpha T \ . \tag{3}$$

Thermoelectric technology takes advantage of the Seebeck effect for power generation from heat sources, and of the Peltier effect for cooling applications, as represented in Figure 3.

The third effect is the Thomson effect, discovered by Lord Kelvin in 1855 [12]. For real materials, the Seebeck coefficient is a temperature-dependent property. When a temperature difference is applied to a material, a temperature gradient forms along this material, which means that it can be considered as a continuum of junctions between materials with different Seebeck coefficients. This induces a continuous Peltier effect, resulting in heat emission or absorption along the material. This is the Thomson heat, which can be expressed such as:

$$dQ = \tau \cdot I \cdot \frac{\partial T}{\partial x} dx \tag{4}$$

where $\tau = T \frac{d\alpha}{dT}$ is the Thomson coefficient, given by the second Thomson (Kelvin) relation [12, 14]. As will be discussed below, the Thomson effect is not of primary importance in most thermoelectric devices, however in some cases it should not be neglected in detailed calculations [14].

1.2. Modelling of TEG performance

A TEG is typically composed of p- and n-type TE legs, which are connected to metal-bonded ceramic plates electrically in series and thermally in parallel [15, 16]. The legs are usually functionalized: they are contacted with an intermediate metallic layer that will be then soldered to the metallic bridges which interconnect the legs in an electrical circuit. (The metallization will be discussed in Section 1.6.) This simple design is shown in Figure 4.

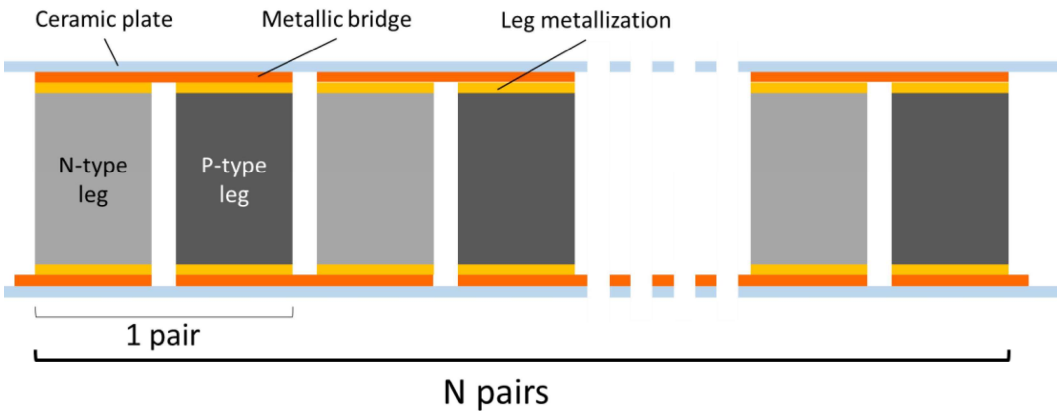

Figure 4 - Schematics of a basic TEG design, with p- and n-type legs, metallic bridges and ceramic substrates

In this section, a single TEG leg is considered. The equations for a real TEG made of several pairs of different n- and p-type materials will be given in section 2.

1.2.1. Performance of a TEG

The two main performance parameters of a TEG are its power output and its conversion efficiency. The power output of a TEG in a close circuit is given by

$$P = U \cdot I \tag{5}$$

where

$$U = U_0 - RI \tag{6}$$

where

$$R = R_{\mathrm{TE}} + 2R_{\mathrm{c}} = \frac{\rho L}{A} + \frac{2r_{\mathrm{c}}}{A} \tag{7}$$

U is the output voltage at the TEG terminals, $U_0 = \alpha\Delta T$ is the Seebeck voltage generated at open loop, introduced in Section 1.1. R is the inner electrical resistance of the TEG, RI is the voltage drop due to the electrical internal resistance of the TEG. R is composed of R_{TE}, the electrical resistance of the TE legs of the TEG, and the contact resistance of one TE/metal interface R_{c}. r_{c} is the contact resistivity of one TE/metal interface (or specific contact resistance) and it is geometry independent. L is the length of the TE leg (between hot and cold sides), A its cross section, and ρ its electrical resistivity. The metallization bulk resistance is neglected.

The efficiency of a TEG η is given by:

$$\eta = \frac{P}{Q_{\mathrm{in}}} \tag{8}$$

Where Q_{in} is the heat flow entering the TEG. Figure 5 shows the heat flow mechanisms in a single TE leg maintained between constant hot and cold sides temperatures. There are three mechanisms contributing to the heat flow:

- Fourier heat conduction from the hot side towards the cold side
- Peltier heat flowing from the hot side towards the cold side and
- Half of the heat from resistive Joule heating flowing towards the hot side and the second flowing towards the cold side.

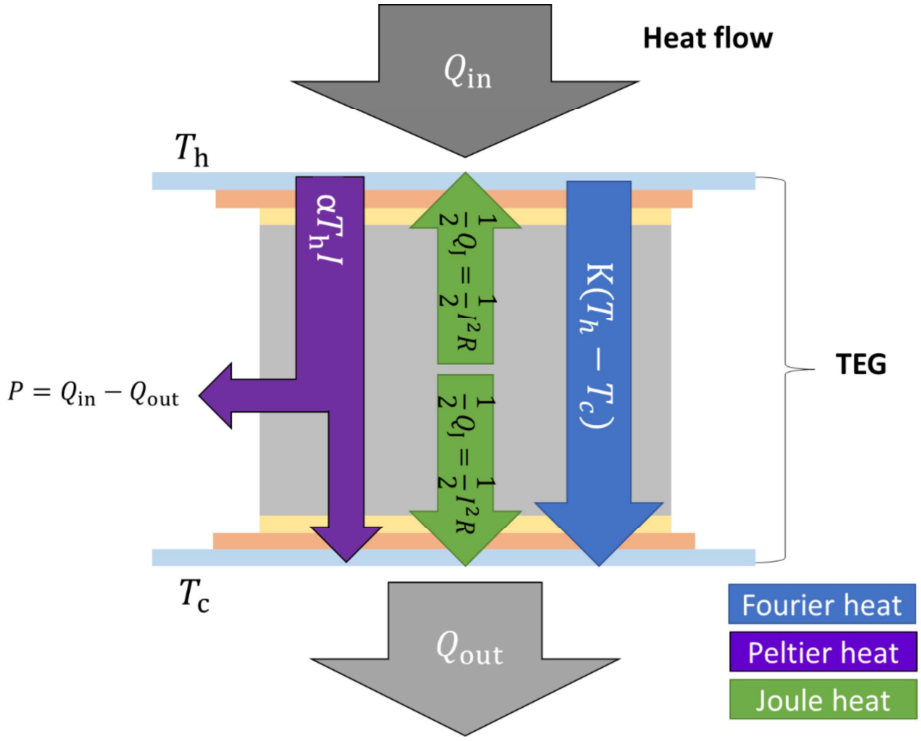

Figure 5 - Schematic representation of heat transfer and electrical power production in a single leg TEG assuming temperature-independent properties. K is the thermal conductance of the TE leg and will be described below. Reproduced and adapted from [12].

The incident heat flow is given by the Fourier's law, considering additional Peltier heat at the hot metal/TE interface:

$$Q_{\text{in}} = -\kappa_{\text{h}} A \frac{dT}{dx_{\text{h}}} + I\alpha_{\text{h}} T_{\text{h}} \tag{9}$$

The term $-\kappa_{\text{h}} A \frac{dT}{dx_{\text{h}}}$ is the Fourier heat flow and the term $I\alpha_{\text{h}} T_{\text{h}}$ is the absorbed Peltier heat flow at the hot side, κ is the thermal conductivity of the TE material. Here, $\kappa_{\text{h}} = \kappa(T_{\text{h}})$ and $\alpha_{\text{h}} =$

$\alpha(T_{\mathrm{h}})$. To obtain $\frac{dT}{dx}$ in the Fourier term, the thermoelectric heat balance equation (in 1D) given below has to be solved for $T(x)$ [17]:

$$\kappa(T)\frac{\partial^2 T}{\partial x^2}+\frac{d\kappa}{dT}\left(\frac{\partial T}{\partial x}\right)^2-\frac{I}{A}T\frac{d\alpha}{dT}\frac{\partial T}{\partial x}=-\rho(T)\left(\frac{I}{A}\right)^2 \qquad (10)$$

This equation is obtained considering an isotropic material. It is obtained starting from the energy conservation such as $\nabla Q = p_v$ where p_v is the electrical power produced per volume, and using the equality between the divergence of flowing Fourier heat and the sum of the source terms (Joule heat and Thomson heat) [18].

$\kappa(T)\frac{\partial^2 T}{\partial x^2}+\frac{d\kappa}{dT}\left(\frac{\partial T}{\partial x}\right)^2$ corresponds to the local change of the Fourier heat, $\frac{I}{A}T\frac{d\alpha}{dT}\frac{\partial T}{\partial x}$ to the Thomson heat and $\rho(T)\left(\frac{I}{A}\right)^2$ to the Joule heat. The Joule heat is generated by the self-heating of a material due to the flow of electrical current. Unlike the Peltier heat which is reversible with current direction, the Joule heat is irreversible.

When considering temperature dependent properties $\alpha(T)$, $\kappa(T)$ and $\rho(T)$, equation (10) is a second order non-linear partial differential equation, which can be solved using numerical methods like Finite Element Methods (FEM) [12, 19] and similar numerical tools [20-24]. However, such numerical methods are costly and time consuming, which is partly why the Constant Property Model (CPM) was used in this work.

Along a working TE leg, the temperature profile is slightly bent, as shown in Figure 6a. This is due to the contribution of Joule and Thomson heat for $I \neq 0$ and to the temperature dependence of κ, which makes it more or less accentuated depending on the material type. Figure 6b shows calculations of the relative bending of the temperature profile compared to linearity normalized for ΔT, using $(T(x)-T_{\mathrm{linear}})/\Delta T$, for several materials (x being the position along the TE leg, on the axis going from the hot side to the cold side). It shows that for Mg_2X materials the temperature profile does not differ a lot from linearity (<2.5%) contrarily to the Bi_2Te_3 or SnSe material classes. Typically, the bowing in case of power generation is weak due to relatively lower current in efficient operation, compared to cooling applications [12].

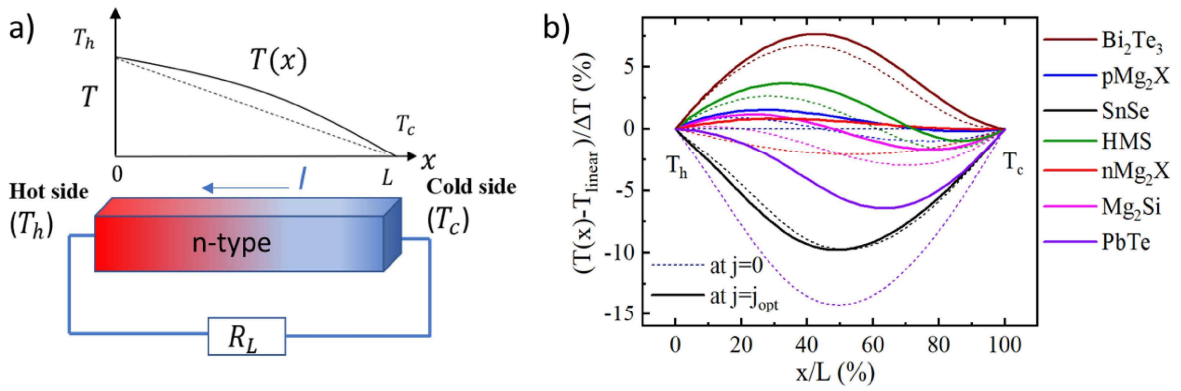

Figure 6 - a) Temperature profile (solid curve) along a n-type TE leg, considering the Thomson, Fourier and Joule effects with temperature-dependent material properties. The TE leg of length L is represented underneath. It is connected to an external load with an electrical resistance R_L. The linear profile (dotted line) is shown for comparison. Modified from [25]. b) Relative deviation of temperature profiles compared to linearity for various materials (temperature dependent properties) at current densities $j = 0$ (dotted lines) and $j = j_{opt}$ (solid lines), normalized. Taken from [26].

It is worth mentioning that those calculations were made considering fixed hot and cold side temperatures. In real life applications, the temperature difference at the TE legs can significantly change for $I \neq 0$ conditions, as the Peltier and Joule heat can be emitted or absorbed by neighboring materials (electrodes, parts acting as heat transmitters, etc.), as represented in Figure 5. The extent of this phenomenon again depends on the TE material class and the application temperatures of each TEG, but also the properties of the neighboring materials. Such behaviors can be observed and accounted for during a TEG measurement as will be discussed in section 6.

1.2.2. Constant Property Model

In this work, calculations are compared to measurements in order to check for the reliability of the latter, and identify room for improvement in the TEG building process. Advanced module modeling requires many resources and significant physical insight can be more easily gained from simple models, the well-known simplified 1D Constant Properties Modeling is often used to calculate TEG performance [27].

The CPM method neglects the temperature dependence of TE properties and assumes that the whole TE leg has homogeneous, averaged properties for a certain temperature difference. It can be seen that such assumption simplifies equation (10) into $\kappa \frac{d^2T}{dx^2} = -\rho \left(\frac{I}{A}\right)^2$, which shows that the CPM approach neglects Thomson heat.

The energy balance at the hot and cold junctions can respectively be expressed such as:

$$Q_{\text{in}} = K\Delta T + I\alpha T_{\text{h}} - \frac{1}{2}I^2R \tag{11}$$

$$Q_{\text{out}} = K\Delta T + I\alpha T_{\text{c}} + \frac{1}{2}I^2R \tag{12}$$

Where Q_{out} is the heat flowing out of the TEG and $K = \frac{\kappa L}{A}$ is the thermal conductance. In this thesis, thermal contact resistances are not considered, but in reality K is composed of the conductance of the TE legs, of the substrates and the inverse of the thermal contact resistances. This will be further discussed in section 2.

As the heat flows through the TEG, a portion of the heat is converted into electrical power. Therefore, considering the global heat balance of the system:

$$Q_{\text{in}} - Q_{\text{out}} = P = I(U_{\text{o}} - IR) \tag{13}$$

The maximum power P_{max} is obtained by finding the current value for which $\frac{dP}{dI} = 0$, noted $I_{\text{opt,p}}$. This results in:

$$P_{\text{max}} = \frac{{U_0}^2}{4R} \tag{14}$$

$$I_{\text{opt,p}} = \frac{U_0}{2R} \tag{15}$$

In power generation applications, the TEG is connected to an external load R_{L}, represented in Figure 6. This plays an important role in the TEG optimization, as it influences the performance conditions of the TEG. The voltage at the external load can be written such as:

$$R_{\text{L}}I = U_{\text{o}} - RI\ . \tag{16}$$

It follows:

$$I = \frac{U_0}{R + R_{\text{L}}} = \frac{U_0}{R(1+m)} \tag{17}$$

with $m = R_{\text{L}}/R$. Therefore, combining equations (13) and (17):

$$P = \frac{{U_0}^2}{R}\frac{m}{(m+1)^2} \tag{18}$$

and $\frac{dP}{dI} = 0$ occurs for $m = 1$ which links back to the optimum current value obtained in equation (15).

Combining equations (8), (11), (17) and (18), the efficiency η is obtained such as [12]:

$$\eta = \frac{P}{Q_{\text{in}}} = \frac{\Delta T}{T_{\text{h}}}\frac{m}{m+1+\frac{(m+1)^2}{ZT_{\text{h}}} - 0.5\frac{\Delta T}{T_{\text{h}}}} \tag{19}$$

Where $ZT = \frac{\alpha^2}{KR}T$ is called the device figure of merit. The maximum efficiency η_{max} is obtained for $m = \sqrt{1+ZT_{\text{m}}}$ [12] where T_{m} is the average of T_{h} and T_{c} . This results in:

$$\eta_{\text{max}} = \frac{\Delta T}{T_{\text{h}}}\frac{\sqrt{1+ZT_{\text{m}}}-1}{\sqrt{1+ZT_{\text{m}}}+\frac{T_{\text{c}}}{T_{\text{h}}}} \tag{20}$$

where T_{m} is the average value of T_{c} and T_{h}.

The corresponding current value for those conditions is noted as $I_{\text{opt},\eta}$. It can be obtained using equation (17), which gives:

$$I_{\text{opt},\eta} = \frac{U_0}{R\left(1+\sqrt{1+ZT_{\text{m}}}\right)} \tag{21}$$

It can be seen that always $I_{\text{opt,p}} > I_{\text{opt},\eta}$. In practical cases, both conditions are quite close to each other such as the output power will decrease only slightly when switching from $I_{\text{opt,p}}$ to $I_{\text{opt},\eta}$, and vice versa for efficiency [12].

Although the CPM is widely used in the scientific community for simple estimations of the power output and efficiency of TEGs, its basic assumption of constant properties can make it incompatible in some cases. As it dismisses the contributions of Thomson heat and the asymmetry of Joule heat, CPM is not well suited for materials for which these effects are non-negligible (e.g. overestimation of efficiency by 6% for PbTe materials [26]). Furthermore, the averaging method used for the calculation of the constant properties is not straightforward, as

its error compared to FEM calculations highly depends on application temperatures and temperature-dependence of the material's properties. Nevertheless, for the Mg_2X materials which are the only materials practically used in this work, it was shown above that the deviation from linearity of its temperature profile is quite small. It was also shown by Ponnusamy *et al.* that temperature averaging (TAv) is a satisfyingly reliable method for constant property calculations in terms of efficiency prediction for this material class (error < 2% between CPM and FEM, which is much smaller than a measurement error) [28]. This method determines the averaged property $\bar{X}$ of $X(T)$ between T_h and T_c such as $\bar{X} = \frac{1}{\Delta T}\int_{T_\mathrm{c}}^{T_\mathrm{h}} X(T)\mathrm{d}T$. Therefore, the CPM can be reliably used for our purpose of measurement analysis in section 5.

The CPM also does not account for 2D and 3D effects, such as current constriction, which effectively changes the local current density in a TE leg, or the occurrence of parasitic heat bypasses by means of radiation. While the former can only be accounted for in more complex models such as FEM, the relevance of the latter effect will be discussed in section 5.

1.3. Influence of different parameters on TEG performance

One thing that can be seen from the equations presented in Section 1.2.2 is that, in order to maximize the performance of a TEG, different parameters can be adjusted: the properties of the TE materials, the electrical contact resistance, the geometry of the legs and the applied temperatures. Strategies to optimize each of those different parameters for performance enhancement are explored below.

1.3.1. Thermoelectric material properties

The dependence of efficiency on theoretical ZT values is shown in Figure 7. Realistically, $ZT \geq 3$ are unlikely to be achieved, which is partly why thermoelectric technologies cannot reach very high efficiencies compared to other power generation technologies such as solar cells.

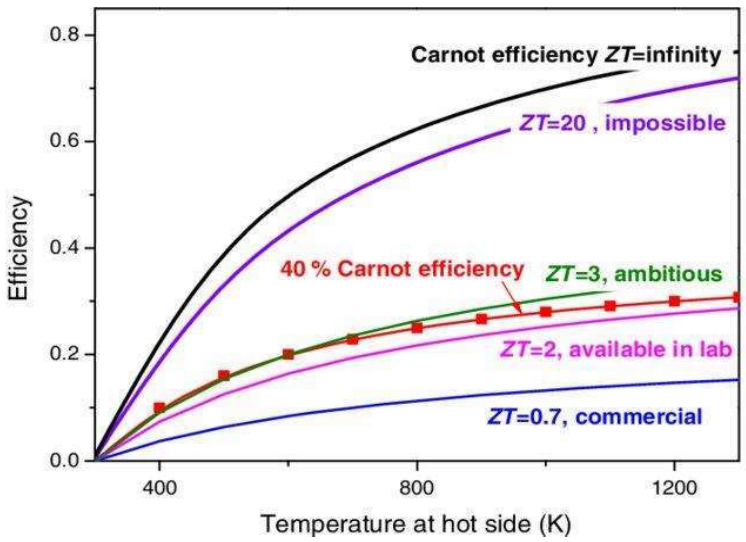

Figure 7 - Efficiency with respect to device figure of merit ZT. Taken from [29]

For low enough electrical contact resistances, the device figure of merit is close to the materials' figure of merit zT, defined such as:

$$z = \frac{\alpha^2}{\rho\kappa} \tag{22}$$

In the field of TE properties optimization, a TE material is considered of high performance for $zT \geq 1$ [30].

Neglecting electrical contact resistances, equations (14) and (20) can be written such as:

$$P_{\max} = \frac{A(\alpha\Delta T)^2}{4\rho L} \tag{23}$$

$$\eta_{\max} = \frac{\Delta T}{T_h} \frac{\sqrt{1+zT_m}-1}{\sqrt{1+zT_m}+\frac{T_c}{T_h}} \tag{24}$$

Equations (23) and (24) show that, respectively, the power factor $PF = \frac{\alpha^2}{\rho}$ and the material figure of merit zT need to be maximized to increase the efficiency of a TEG. For this aim, the Seebeck coefficient of a TE material has to be increased, while its thermal conductivity and electrical resistivity have to be decreased.

a) Semiconductors, band theory and Single Parabolic Band model

In solid state physics, band theory is used to describe the electronic structure of compounds. Electrons can only take defined levels of energy, these levels forming continuums of states which form "allowed" bands. These continuums can be separated or not by an energy gap; below this gap lies the valence band (VB) and above lies the conduction band (CB). Electronic bands are represented by allowed energy states in function of the wave vector k.

Electrical conduction generally happens when electrons reach the CB states (and/or when holes are in the VB states), usually by thermal excitation. In insulators, the energetic width of the band gap, E_g, is significantly large (> 3 eV at 0 K) which prevents electrical conduction; in semiconductors it has a smaller value while there is no gap in metals. This is represented in Figure 8a. The electrochemical potential, or Fermi level E_F, is the state with a 50% probability of occupancy at a given temperature [31].

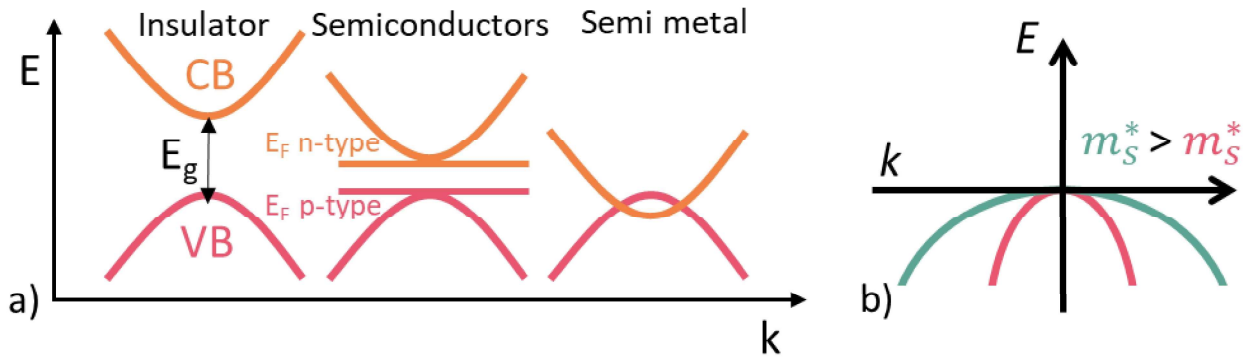

Figure 8 – Schematics of: a) The band gap energy difference in insulator, semiconductor and metal with valence band (pink) and conduction band (orange), b) Comparison of the effective masses m_s^* of a wider and a narrower band: the effective mass decreases with increasing curvature of the band.

In doped semiconductor materials, two kinds of electrical behavior can be distinguished: extrinsic, at low temperatures, and intrinsic, at very low and high temperatures. Extrinsic conduction is ensured by the charge carriers which are brought by doping (donor defects for n-type, acceptor defects for p-type); it is represented in Figure 9. In n-type doping, the dopant atoms bring electrons typically at a level of energy close to the conduction band (often below, sometimes within): low thermal excitation is needed for them to jump into the conduction band. In p-type doping, the dopant atom brings a level of energy close to the valence band. The electrons of the valence band require very low thermal excitation to jump on this level, creating holes for conduction in the valence band. N-type doping shifts the Fermi level up while p-doping shifts it down. In the extrinsic regime, one carrier type dominates the conduction.

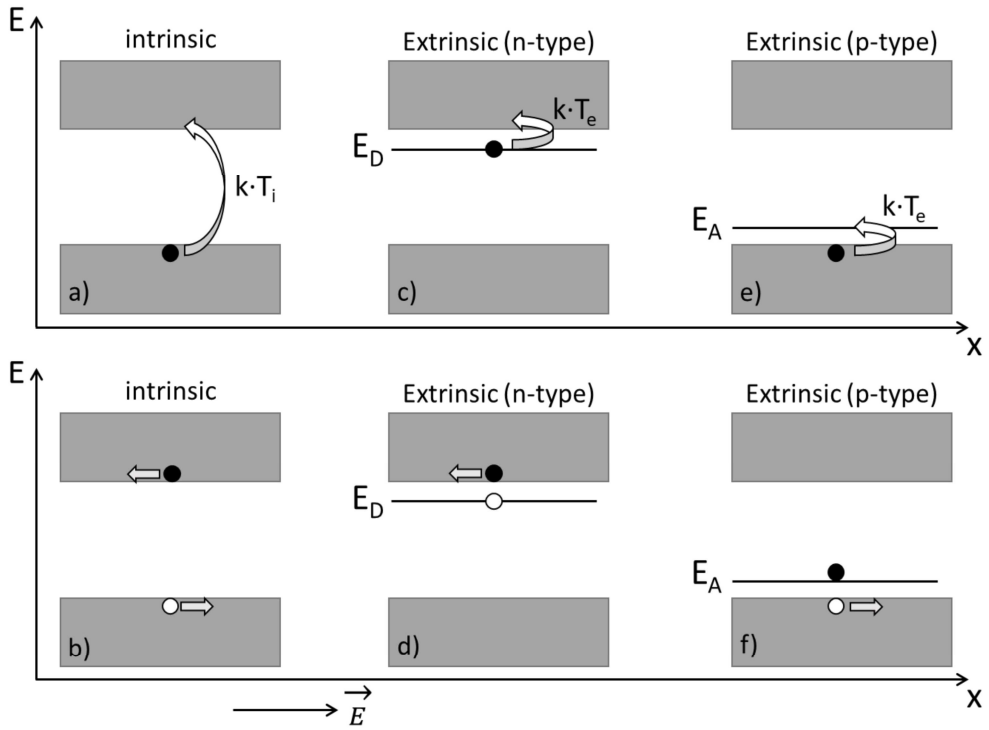

Figure 9 – Intrinsic conduction (a and b), extrinsic conduction with n-type doping (c and d) and p-type doping (e and f): a) the electron is in the VB, thermal excitation brings the electrons from the VB to the CB, b) electrical conduction by the electron in the CB and resulting hole in the VB, c) the dopant atom (donor) brings a new energy E_D level below the CB, thermal excitation brings the electrons on E_D to the CB, d) electrical conduction by the electrons in the CB, e) the dopant atom (acceptor) brings a new energy E_A level above the VB. Thermal excitation brings the electrons from the VB to on E_A, creating a hole in the valence band, f) electrical conduction by the hole in the VB. T_i is the temperature from which intrinsic conduction happens, T_e is the temperature from which extrinsic conduction happens (depends on the dopant); $T_i > T_e$.

When a certain temperature is reached, a significant number of electrons in the valence band have enough energy to jump in the conduction band and both carrier types significantly contribute to the conduction: this is the intrinsic regime. For undoped semiconductors, the conduction behavior is only intrinsic on the whole temperature range and the Fermi level is approximately in the middle of the band gap.

The band structure influences the TE properties through several parameters, such as the effective mass and the carrier concentration. In many cases, for simplicity, the band structure is assumed to be a single parabola with a defined effective mass m_s^* such as:

$$m_s^* = \hbar^2 \left(\frac{d^2E}{dk^2}\right)^{-1} . \qquad (25)$$

The effective mass is a quantity used to account for the effects of the electronic band structure on the electrical transport by modelling the behavior of charge carriers as free particles. It represents the (quasi) particle mass under an influence of external fields (applied electric field or temperature) which differentiates it from the free electron mass, which is a fundamental

constant. As can be seen in equation (25), the effective mass is related to the curvature of the band (conduction band for electrons, valence band for holes): the stronger curved the band, the smaller the effective mass. This is illustrated in Figure 8b.

TE properties are largely affected by the carrier concentration and the carrier mobility. Carrier concentration, or carrier density, is the number of carriers per volume unit, and it is defined by:

$$n = \int_0^\infty N(E) f_0(E) dE \tag{26}$$

where $N(E)$ is the density of electronic states per energy unit and volume and $f_0(E)$ is the Fermi function, which describes the probability that a state of energy E in a band is occupied by an electron. It depends on the Fermi level and temperature.

The carrier mobility μ is inversely proportional to the effective mass. It depends on the relaxation time of the carriers, τ_r, which is given by the Matthiessen rule such as:

$$\frac{1}{\tau_r} = \sum_{s=1}^{s} \frac{1}{\tau_s} \tag{27}$$

where τ_s is the scattering time of the types of scattering s simultaneously occurring in a material. This will be further described in section 6, but for $Mg_2(Si,Sn)$, which is the material used in this work, the main scattering mechanisms for electrons are acoustic phonons scattering, alloy scattering and grain boundary scattering.

The single parabolic band (SPB) model, like its name suggests, is a model which assumes that the conduction in a material is governed only by a single band with a parabolic shape (and therefore one carrier type and extrinsic behavior). One of its main assumptions is that the effective mass does not depend on carrier concentration. Its main advantage is its simplicity, as the parameters can be calculated from easily obtained experimental data. It is applicable for many highly doped semiconductors but it has limitations at higher temperatures, where the influence of minority carriers is relevant, and for materials with temperature-dependent band structures [32]. It is also valid only near the band edge, as the effective mass may change deeper in the band. It will be further discussed in section 6.

b) Thermoelectric properties described with a Single Parabolic Band model

For the limiting case of metals or very highly doped semiconductors, the Seebeck coefficient can be described with the SPB model and assuming energy-independent scattering, with the following equation [15]:

$$\alpha = \frac{8\pi^2 k_B^2}{3eh^2} m_s^* T \left(\frac{\pi}{3n}\right)^{\frac{2}{3}} \tag{28}$$

where k_B and h are respectively the Boltzmann constant and the Planck constant. This formula is cited here as it easily highlights the interdependence of carrier concentration and Seebeck coefficient, which will be further discussed in this thesis. However, for the actual calculations presented in this work, more correct equations will be used with regard to our TE materials.

The electrical conductivity σ is given by the following equation [15]:

$$\sigma = \frac{1}{\rho} = ne\mu \tag{29}$$

where n is the concentration in electrons and μ is the electron mobility, for an n-type material. For a p-type material the concentration in holes, p, and the holes mobility, μ_h, would be used. Comparing the equations (28) and (29), it can be noticed that the carrier concentration has an opposite relation to the Seebeck coefficient and to the electrical conductivity. Both properties can therefore not be maximized in parallel. A compromise between the two can however be found to maximize zT, as can be seen in Figure 10. For most TE materials, this ideal range of carrier concentration is between 10^{19} and 10^{21} cm^{-3} (range of highly doped semiconductors).

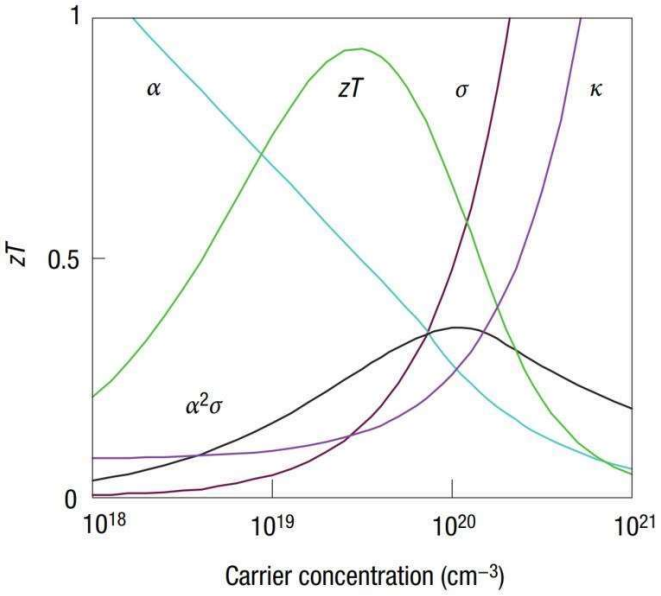

Figure 10 - Influence of carrier concentration on transport and thermoelectric properties for Bi_2Te_3, based on empirical data. However, most interesting thermoelectric materials are highly doped semiconductors (carrier concentration in the range of 10^{19} to 10^{21} carriers per cm^3) for which those trends are also applicable. Taken from [15]

In semiconductors and insulators, heat is mainly carried by phonons, unlike in metals where it is rather related to charge carriers which are much higher concentrated there. A phonon is a quasiparticle, which is an excitation state in a periodic and elastic arrangement of atoms in condensed matter. More concretely, it can represent the "wave" created by neighboring atoms' vibration in a lattice.

The thermal conductivity of a thermoelectric material can be split in different contributions from different effects, giving the following equation [33]:

$$\kappa = \kappa_{\mathrm{e}} + \kappa_{\mathrm{lat}} + \kappa_{\mathrm{bi}} \tag{30}$$

where $\kappa_{\mathrm{e}} = L\sigma T$ (Wiedermann-Franz law) is the electronic contribution of charge carriers, which increases with the electrical conductivity, κ_{lat} is the contribution of the phonons in the lattice and κ_{bi} is the bipolar thermal conductivity, which is negligible for the lower temperature range but increases with temperature. It can be seen that electrical and thermal conductivity increase simultaneously (also represented in Figure 10), whereas it is desired to increase the first while decreasing the latter.

Different strategies can be applied to increase zT. Good TE materials usually have an "electron crystal, phonon glass" structure, which means that their structure is favorable to electron conduction, while favorable to phonon scattering to reduce the κ_{lat} contribution to thermal

conductivity [15]. Phonon scattering can be enhanced by creating disorder in the unit cell (vacancies, atom substitution, interstitial atoms) which can be obtained by tuning the stoichiometry of the material. Nanostructuring is also a strategy to increase phonon scattering, although it can also lead to more electron scattering which is not desired [34]. The Seebeck coefficient and the electrical conductivity can usually be optimized through doping, which can modify the carrier concentration in a favorable way. This will be discussed in Section 1.5.2.

1.3.2. Electrical contact resistance

The electrical contact resistance, previously referred to as R_c, designates the resistance due to a drop of the electrical potential at the interface between two physically connected materials. In this thesis, the electrical contact resistivity or specific electrical contact resistance r_c (in Ωcm²) is also frequently used due to its advantage of being geometry-independent.

Figure 11 shows the exemplary dependence of maximum power output and efficiency with respect to the electrical contact resistivity in the case of a Zn_4Sb_3 leg. For a contact between metal and semiconductor, the range of 1-100 μΩcm² can reasonably be experimentally achieved [2, 4, 35-38].

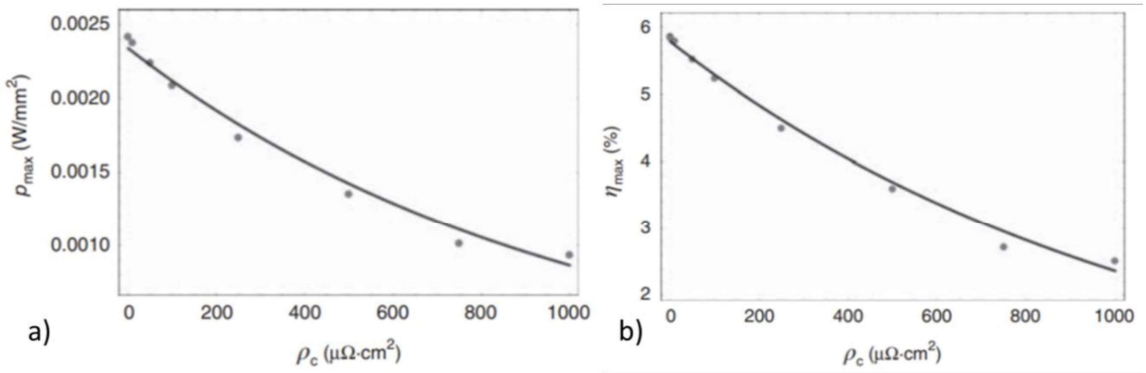

Figure 11 - a) maximum power output, b) maximum efficiency, for different electrical contact resistivities r_c (ρ_c in the figure) computed for Zn_4Sb_3 material. The points are calculated maximum values, and the solid lines represent polynomial fits, which serve as an eye guide. Taken from [12], where the material properties are given in Table 2.8 and the geometry parameters are given in Figure 2.16 (p. 130). The calculated resistance of the TE material is 124 mΩ.

It has also been shown that to limit the efficiency loss to 20%, the electrical contact resistance should not represent more than 30% of the total leg resistance, neglecting the thermal contact resistance [39]. Figure 12 shows practically achievable maximum efficiency with respect to r_c for a $Mg_2(Si,Sn)$ legs pair similar to those used in this work. It can be seen that maximum efficiency can be preserved for $r_c \leq 10$ μΩcm². This threshold is therefore set as the aim for our functionalized legs.

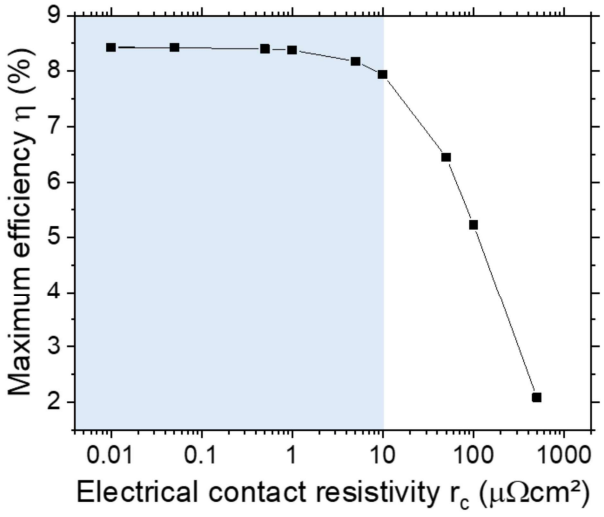

Figure 12 - Maximum efficiency with respect to electrical contact resistivity calculated for one leg of n-type $Mg_2(Si,Sn)$ (experimental properties used in this thesis, see section 5), with leg length L = 0.4 cm, cross-section A = 0.12 cm², T_c = 50 °C and T_h = 375 °C.

The establishment of an electrical contact between a metal and a semiconductor looking at their energy band diagram is shown in Figure 13. The mechanism mainly depends on the relative work functions of the materials of the metal Φ_M and of the semiconductor Φ_S [40]. The work function of a material is defined as the difference in energy between the material's Fermi level and the vacuum level. The vacuum level is defined by the energy level of an electron positioned at rest within a "few nanometers" outside the sample, i.e. with zero kinetic energy with respect to the sample surface.

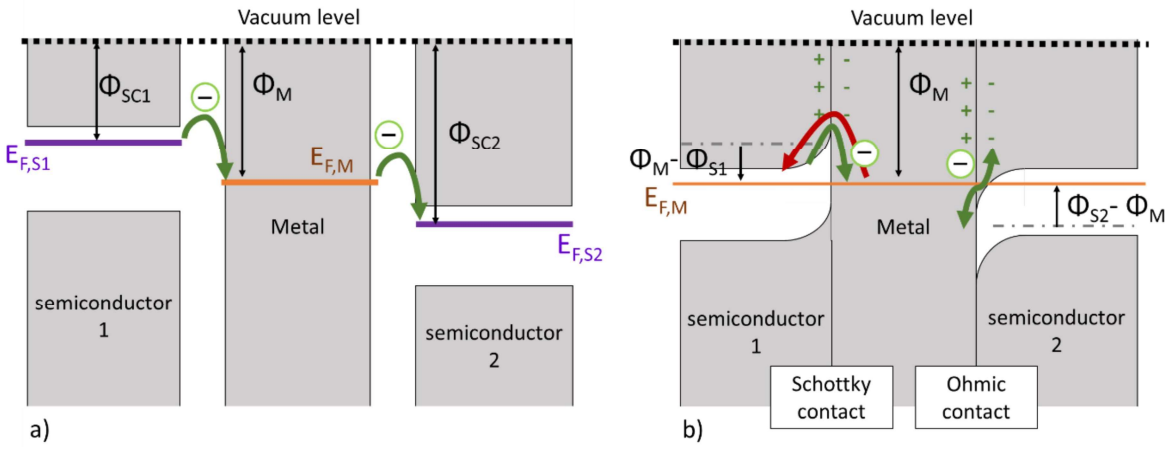

Figure 13 - Schematics of ohmic and Schottky contacts between metal and different semiconductors (SC). a) Before intimate contact, the electrons can flow in one direction (green arrow), b) The unidirectional electron flow in a) caused local electron accumulation/depletion zones on each side of the junction (represented by green + and – charges). As intimate contact is established, the Fermi levels of the semiconductors close to the junction align with the metal's, and the band bending resulting

from the accumulation/depletion zones either creates a Schottky barrier preventing the electrons flow (red arrow, between SC1 and metal), or an easy energy state transition through an ohmic contact (green arrow, between SC2 and metal).

Without intimate contact (Figure 13a), the difference in Fermi levels between the metal and the semiconductor creates an energy barrier which prevents the charge carriers to move freely from one material to the other. The electrons could jump from a higher Fermi level to a lower Fermi level, but the opposite is prevented by the large difference in Fermi levels. After intimate contacting (Figure 13b), the Fermi levels of the semiconductors equilibrate with the metal's by equalization of their work functions close to the interface. The band edges of the semiconductor will therefore be changed by $\Phi_S - \Phi_M = E_{F,S} - E_{F,M}$.

The Fermi level equalization leads to a bending in the valence and conduction bands of the semiconductors at the interface, due to the formation of electron accumulation or depletion layers before intimate contact and Fermi levels alignment (green arrows in Figure 13a) [41]. The bands bend up towards negative charges accumulation. The height of the bending forms the Schottky barrier and it is related to the relative Fermi levels and the carrier concentrations of the materials forming the junction. In case of a contact between a metal and a highly doped semiconductor with $\Phi_M < \Phi_S$, there is no barrier to be overcome by electrons in both current directions (metal to semiconductor 2 in Figure 13b): it is an ohmic contact. The generated contact resistance is supposed to be negligible enough so that the I-U behavior of the junction is linear [42]. Unlike for ohmic contacts, in Schottky contacts the potential barrier is higher in one current direction [43], which blocks the electrical current flow in this direction (metal to semiconductor 1 in Figure 13b).

In Figure 13, junctions between metal and n-type semiconductors are presented. In the case of p-type semiconductors, the Fermi level is closer to their valence band and inversely to n-type, an ohmic contact is formed for $\Phi_M > \Phi_S$ and a Schottky contact for $\Phi_M < \Phi_S$, although the mechanisms leading to the establishment of the electrical contact remain similar. This is due to the fact that holes are the majority carrier type in p-type materials: the band bending resulting from the Fermi levels equilibrium is inversely favorable to hole conduction and to electron conduction.

The work functions of the TE materials used in this thesis (p- and n-type $Mg_2(Si,Sn)$) were not theoretically nor experimentally determined to date to the best of our knowledge. Moreover, in the case of Al that is used as metallization, the work function highly depends on the surface quality (e.g. presence of absence of oxide layer [44]). Therefore, it is unknown whether in our

case $\Phi_M > \Phi_S$ or $\Phi_M < \Phi_S$ holds. However, like will be shown in sections 3 and 4, low contact resistances can be obtained for both TE materials, which would indicate that our contacts are either ohmic, or Schottky contacts with a low energetic barrier which would be due to the high doping concentration of our TE materials.

In more practical terms, the contact resistance can depend on different factors such as the nature of the materials forming the interface, the geometry of the interface, the total or partial presence of an oxide layer or impurities, the surfaces roughness and the pressure applied on the interface. In this thesis, the contacting between the semiconductor (TE) material and the metal is established either through direct bonding, meaning that the components remain in a solid state, or using a Zn layer (~ 8 µm) as a liquid solder between the SC and the metal. Preparation steps will be discussed in section 2.1.2, however our preparation process cannot ensure a nanometer scale flatness of the interface between the SC and the metal. Secondary phases could also grow during the contacting process, which could alter the flatness of the surfaces; an extreme example is shown in Figure 14a. Therefore, the intimate contact between the materials is not continuous and uniform, which leads to locally higher or lower current density. It is represented in Figure 14b, where the current lines deviate and concentrate around local contact spots to flow from one material to the other. This electrical behavior is called current constriction, and it contributes to the contact resistance of a junction, additionally to the resistance due to transition at the contact point between the two materials.

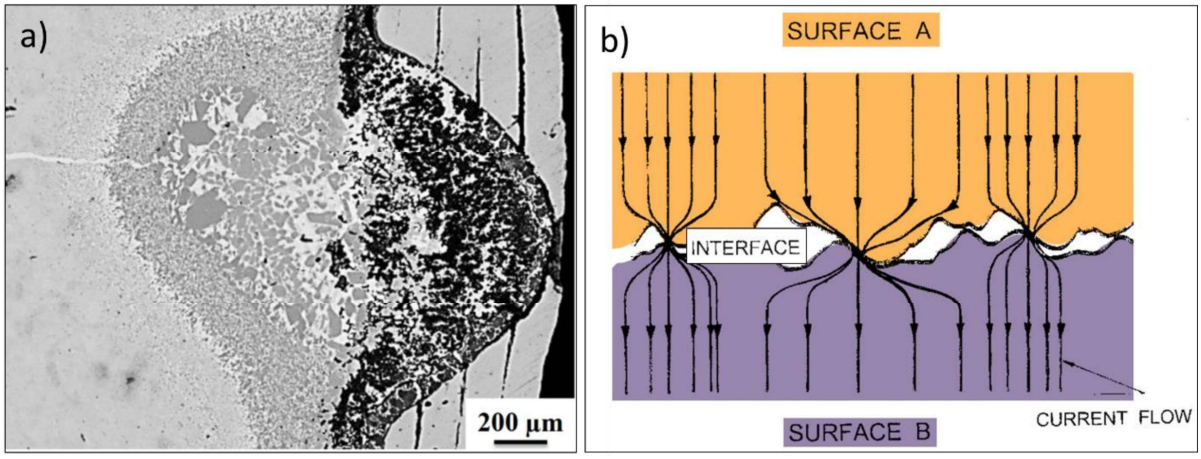

Figure 14 – a) Picture of a reacted area between n-type $Mg_2(Si,Sn)$ and a Cu electrode. The growth of a secondary phase led to the delamination of the Cu foils, taken from [35]. b) Schematics of the interface between two material surfaces A and B. Even with precise surface preparation, on the nanometer scale, continuous contact between the materials cannot be guaranteed. This leads to current constriction, meaning that the current density is locally changing at the interface, as the electrical current in the whole materials can only be transmitted through limited local contact points. Adapted from [45].

Additionally, as contacting experiments are done under high temperature, diffusion and reaction between the involved materials is expected. This can result in the formation of reaction layers which can potentially contain new phases that are less conductive, which inevitably adds resistance and hinders the current flow. Those new phases could also be more brittle and have a different thermal behavior, which could cause cracking and therefore also increase the electrical resistance at the interface due to the created void. The possible secondary phases should be identified as part of the electrode selection criteria, which are discussed in Section 1.6.1. Another possibility is the formation of voids at the interface due to diffusion mechanisms, known as the Kirkendall effect.

1.3.3. TEG design

After optimizing the TE properties of the materials used for the legs and the contact resistance, which have the largest influence, the performance of a TEG can be finely tuned using design and geometrical parameters.

Power output increases with the number of leg pairs, and equation (23) shows that it increases with their cross-section and that it decreases with increasing leg length. From this equation, it can seem like the power output increases infinitely for a leg of infinitesimally small length. However, there is actually a peak in achievable power output due to the dominance of electrical contact resistance for shorter legs. Oppositely, efficiency increases with leg length for non-negligible contact resistances [16], therefore the optimum design of a given thermoelectric module is likely to be a compromise between high power output and high efficiency.

The filling factor corresponds to the ratio between the cross-section occupied by the TE legs and the surface of the TEG (ceramic plates). It can be modified by changing the legs cross-section and the spacing of the legs. While spacing shows little effect on the absolute power output (considering constant number of legs), it can however have an effect on efficiency since with a wider spacing a larger part of the heat flow can be lost as radiation between the top and the bottom plates of the TEG [46]. Practically, the size of the TEG is restricted by its application and then the filling factor and the power density rather than the absolute power must be considered. Heat loss could also occur along the TE legs with increasing leg length, due to convection, which would be detrimental for the TEG performance. Losses due to convection can usually be prevented by the use of vacuum conditions while filling the gaps between the legs with a non-conductive wool can help avoiding thermal bypass between the hot and cold sides of the TEG.

The performance can also be optimized by tuning the cross-section ratio of the p- and n-type elements in order to reach optimum current for power and efficiency for different legs. It follows from equations (15) and (21) that in case of asymmetric p- and n-type properties in a TEG (which is usually the case), the current density $j = I/A$ at which the highest power or efficiency is reached is different for both leg types. Therefore, varying their respective cross-section ensures that both types of leg reach their optimum performance at similar temperatures. The optimum area ratios and their corresponding simplification of the material figure of merit and power output is given in Table 1 [12].

Table 1 – Optimum $\frac{A_p}{A_n}$ ratios and their corresponding expressions of the material figure of merit and maximum power output [12]

	Area ratio $\frac{A_\mathrm{p}}{A_\mathrm{n}}$	**Corresponding optimum performance parameter**
Maximum z and η	$\sqrt{\frac{\kappa_\mathrm{n}\sigma_\mathrm{n}}{\kappa_\mathrm{p}\sigma_\mathrm{p}}}$	$z_{\mathrm{opt}\_\eta} = \left(\frac{\alpha_\mathrm{p} - \alpha_\mathrm{n}}{\sqrt{\frac{\kappa_\mathrm{n}}{\sigma_\mathrm{n}}} + \sqrt{\frac{\kappa_\mathrm{p}}{\sigma_\mathrm{p}}}}\right)^2$
Maximum P	$\sqrt{\frac{\sigma_\mathrm{n}}{\sigma_\mathrm{p}}} = \sqrt{\frac{\rho_\mathrm{p}}{\rho_\mathrm{n}}}$	$P_{\max} = \left[\frac{\alpha_\mathrm{p} - \alpha_\mathrm{n}}{\sqrt{\rho_\mathrm{p}} + \sqrt{\rho_\mathrm{n}}}\right]^2 \frac{(\Delta T)^2}{4L} A_\mathrm{n}\left(1 + \sqrt{\frac{\rho_\mathrm{p}}{\rho_\mathrm{n}}}\right)$

Conversion efficiency will always be limited by the Carnot factor $\frac{\Delta T}{T_\mathrm{h}}$, however it can be increased by increasing the temperature difference applied to the TEG. Overall, thermoelectric technology can be used over a wide range of temperatures, as the performance of the different material classes is widely spread, as shown in Figure 15.

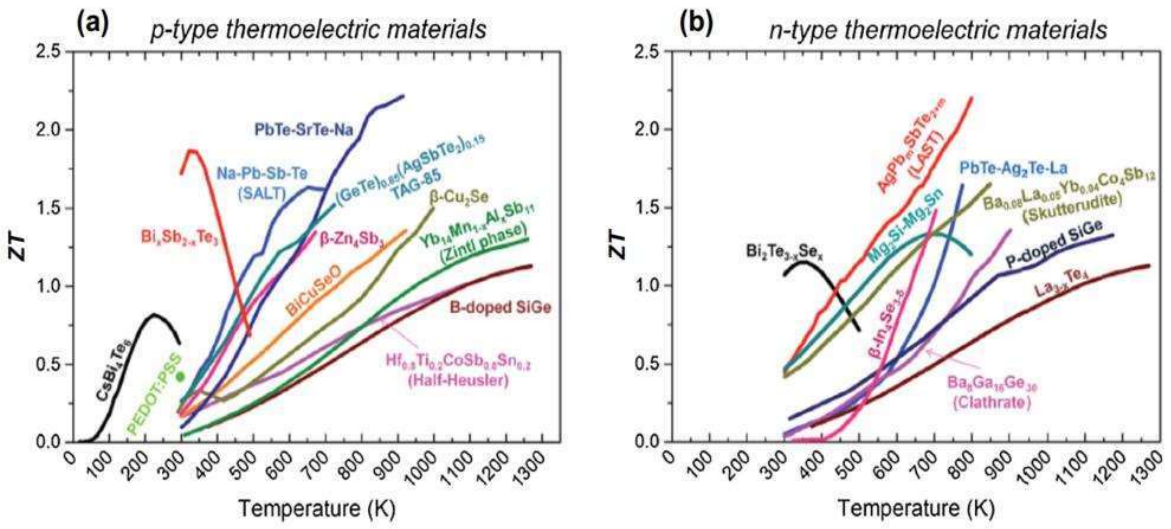

Figure 15 – Figure of merit of different thermoelectric materials depending on their application temperature a) p-type materials, b) n-type materials. Taken from [34].

T_h and T_c are obviously limited by the temperature dependence of the properties of the chosen materials, which restricts their temperature range for optimal performance and therefore the tuning of ΔT. However, some design strategies exist to widen the application temperature range or the performance of a TEG, such as building multi-stage modules by cascading and segmenting. Cascading consists in stacking two TEG modules made of different materials, such that one lies on the colder side and the other on the hotter side. Segmenting (also referred to as stacking) consists in joining different TE materials within each TE leg. Both techniques rely on using different types of TE materials which have high performance in adjacent temperature ranges, and place them accordingly on the cold or hot side of the TEG in order to increase the overall performance. Apart from being more difficult to manufacture, the main disadvantage of cascaded and segmented TEGs are their lower mechanical stability under thermal stresses, due to the higher number of components with differing mechanical properties, as well as the additional contributions to electrical and thermal contact resistance due to an increased number of interfaces [47].

Various other design adaptations can be made to optimize the TEG performance: variation of the leg geometry, flexible or foldable substrates to reduce failure due to thermal stress [48], etc. The design can also be adapted to the target application: i.e. cylindrical TEGs to set around pipes, flexible substrates for wearable TEG devices, layered TEG for parallel electrical current and heat flow, micro- or nanofilm TE materials for cooling of electronics [36], etc.

1.4. Applications

Thermoelectrics have a low efficiency compared to other electrical energy sources, as represented in Figure 16. Therefore, they are not used as a primary source of energy for most applications.

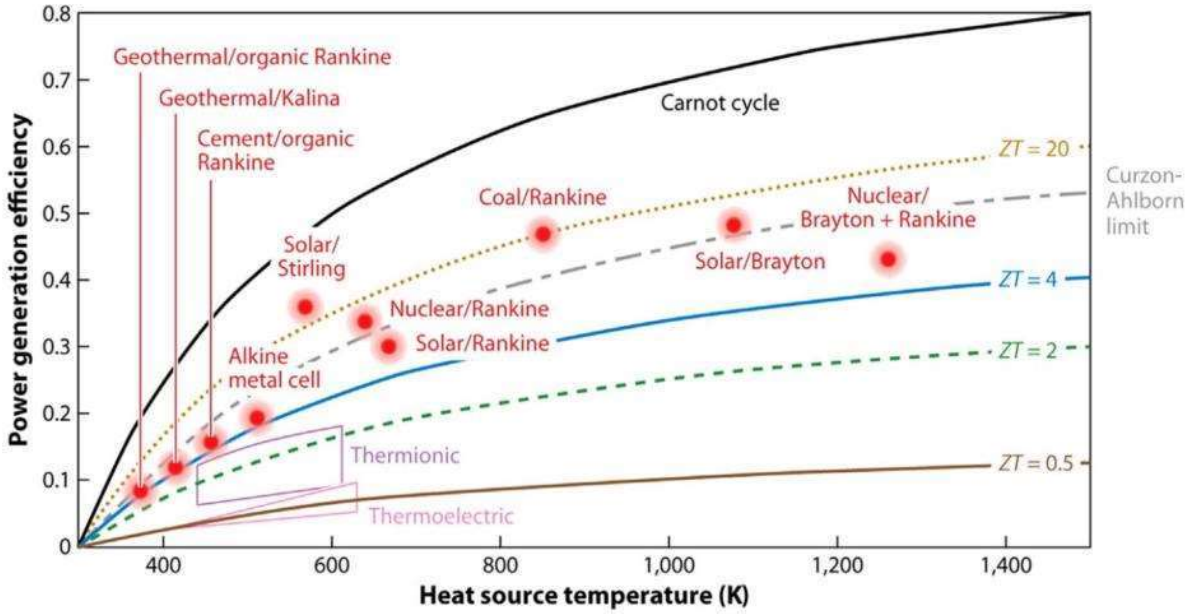

Figure 16 - Power generation efficiency for various energy conversion technologies on a large temperature range. Taken from [49].

However, as waste heat is generated in most fields, thermoelectrics can be widely used as an energy-recuperation method wide range of applications, as shown in Figure 17.

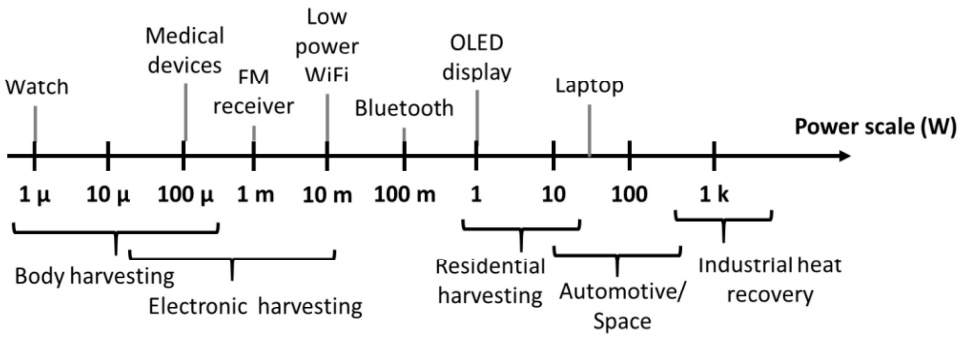

Figure 17 - Power scales of TEG. For comparison, the typical supply needs for common electronic devices are reported for reference. Currently, most promising applications are below 100 W. Reproduced from [50].

TEG were initially developed for high-power generation application in the aerospace industry, as they showed the advantages of having a long lifetime, high reliability and low maintenance

needs due to no moving parts [51]. The heat source is typically a radioactive material providing a hot side temperature up to 1000 °C, while the cold side, due to radiation, is at 300-400 °C.

Intermediate applications are usually targeting the automotive industry, with the idea to integrate a TEG on the exhausts line of a car [52, 53]. Integrating TEGs in vehicles could increase the system efficiency while saving fuel; these advantages would especially be applicable to larger vehicles such as trucks, for which the additional weight represented by the TEGs is negligible. This however might become obsolete due to the recent focus of the society on electric cars.

Low-power generation is a growing area of interest, as general electronics demand increases and their components needs in power scale match a TEG power output. The biggest obstacle in this field is the limited volume available for the TEG. Those applications usually provide narrower ΔT due to the limited volume and heat dissipation at the cold side, which is the key development in this field. An interesting and popular application in this power range is the human-body heat harvesting (e.g. smart watches or medical sensors), for which the performance is still low due to a limited ΔT, but which offers a constant, available and cost-free heat source [54].

1.5. $Mg_2(Si,Sn)$ materials

The TE materials used in this work are $Mg_2(Si,Sn)$ solid solutions, also referred to as Mg_2X materials (with X = Si, Sn). They have the advantages of being light-weight, abundant, non-toxic and cheap, comparatively to other TE materials that operate in similar temperature ranges and contain toxic and expensive compounds such as Te. Their application temperature range lies between 200 and 500 °C, which corresponds to mid- to high-temperature range, and they have high TE performance with $zT > 1$, especially the n-type material.

1.5.1. Crystalline and electronic structure

Mg_2X has a cubic anti-flourite $Fm\bar{3}m$ crystal structure with the Mg atoms occupying the eight tetrahedral positions (Wyckoff positions 8c) and the X atoms (Si, Sn) at the corners and face centers (Wyckoff positions 4a) [55]. It is shown in Figure 18. The combination of those elements lead to a low density (2 g/cm^3 for Mg_2Si and 3.6 g/cm^3 for Mg_2Sn) compared to other high-performance thermoelectric materials such as tellurides, Skutterudites [56, 57] and half-Heusler compounds [58, 59].

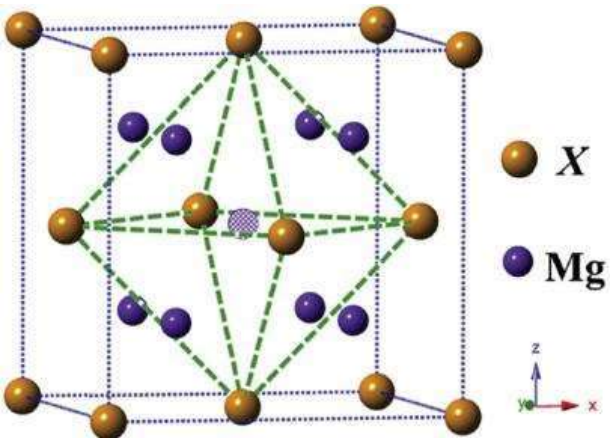

Figure 18 - Schematic of the crystal structure of Mg_2X materials (X = Si, Sn, Ge). The center site can be occupied by interstitial atoms. Taken from [55]

All Mg_2X compounds have a similar electronic band structure, shown in Figure 19a. They have an indirect band gap, which means that the valence band maximum (VBM) and conduction band minimum (CBM) are not aligned in the k-space. The energetic width of the band gap (difference between the CBM and the VBM) is approximately 0.78 eV for Mg_2Si and 0.35 eV for Mg_2Sn [60-62]. For $Mg_2Si_{1-y}Sn_y$ solid solutions, the approximate position of the bands is represented in Figure 19, where it can be seen that a band convergence occurs in the conduction band for $y = 0.6 - 0.7$ [63]. This increases the effective density-of-states mass and therefore leads to a higher n-type Seebeck coefficient (following Equation (28)). These compositions give the highest zT for the n-type material.

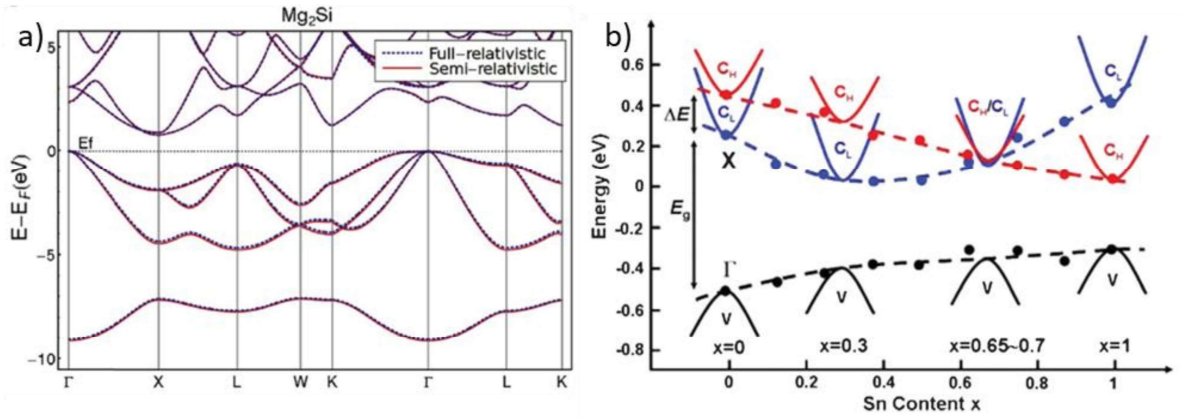

Figure 19 – a) Diagram of the electronic band structure of Mg_2X obtained by density functional theory (DFT) calculations for undoped Mg_2Si, taken from [60]. b) Schematics of the relative position of the heavy conduction (C_H) band (red) and the light conduction (C_L) band (blue) depending on the Sn content in $Mg_2Si_{1-y}Sn_y$ (y=x in the figure) based on DFT calculation. The band convergence occurs for y = 0.65–0.7. Taken from [63].

1.5.2. Thermoelectric properties

As discussed in Section 1.3.1, the optimization of TE properties is crucial for the performance of a TEG. Many material classes currently reach $zT > 1$ [56-59, 64-69] including n-type $Mg_2(Si,Sn)$ [63, 70, 71]. P-type $Mg_2(Si,Sn)$ has a lower performance, strategies to enhance its TE properties are still investigated [72-74]. State-of-the-art properties of both materials are shown in Figure 20a.

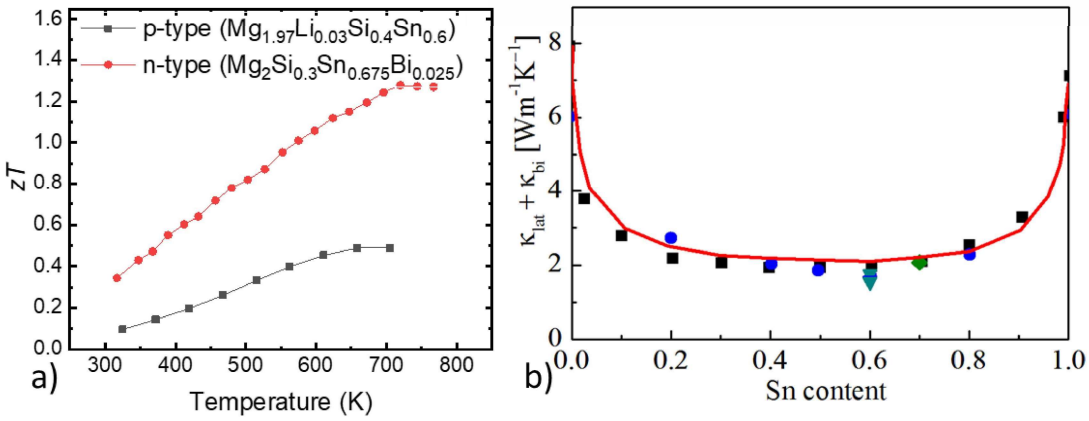

Figure 20 - a) Figure of merit of optimally doped p- and n-type $Mg_2(Si,Sn)$, data was taken from [75] and [76], respectively. b) Variation of lattice thermal conductivity with the Sn content of $Mg_2Si_{1-y}Sn_y$ at room temperature. Taken from [77] ;the calculated data (red line) is taken from [78], experimental data (points) are from [74, 79, 80].

The high performance of the $Mg_2(Si,Sn)$ solid solutions partly comes from an alloying-induced lowered lattice thermal conductivity, compared to the binaries Mg_2Si and Mg_2Sn. The change of $\kappa - \kappa_e = \kappa_{lat} + \kappa_{bi}$ (from Equation (30)) with composition is shown in Figure 20, although as said above the bipolar effect contribution κ_{bi} is negligible at room temperature.

However, for both n- and p-type, another key aspect for the optimization of the TE properties lies in finding a suitable dopant. Doping consists in substituting a small fraction of an element in the composition, by an alioelectronic element, which has a different number of valence electrons (i.e. synthesizing $Mg_2Si_{0.3}Sn_{0.7-x}Bi_x$ instead of $Mg_2Si_{0.3}Sn_{0.7}$). The impurity element atoms will substitute lacking atoms in the crystal structure, and therefore modify the carrier concentration depending on their valence number. In theory, thermodynamics indicate whether a substitution is energetically favorable or not. In practice, this is not so trivial as solubility limits have to be considered, and in the course of the synthesis problems might occur that lead a change in the assumed system: loss of the impurity element, oxidation or formation of other

more stable compounds than the substitution in the target compound, evaporation, preferential sticking to or reaction with vessels and tools, etc.

For n-type $Mg_2(Si,Sn)$, Sb and Bi have both been shown to be stable and efficient dopants [76, 81]. For p-type, Li provides the highest carrier concentration, which makes it the best dopant so far [74, 79, 80, 82].

1.5.3. Mechanical properties

Mechanical properties of TE materials have not been widely studied compared to their TE properties, although they are essential to understand how to reach mechanical stability in a TEG during thermal cycling. Indeed, cracking due to mechanical stresses is a typical cause of device failure [36, 83-85].

The Vickers hardness and the Young modulus of Mg_2X and other TE materials are reported in Table 2. They respectively correspond to the material's resistance to indentation (localized plastic deformation) and the resistance to elongation when under elastic deformation.

Table 2 - Mechanical properties of Mg_2X and other TE materials with similar application temperature ranges

Material	**Hardness [GPa]**	**Young modulus *E* [GPa]**	**References**
$Mg_2Si_{0.4}Sn_{0.6}$	3.06-3.57	83-88	[86, 87]
$Mg_2Si_{0.6}Sn_{0.4}$	4.5	90	[88]
Mg_2Si	5	85-145 (various measurement types)	[89-95]
Mg_2Sn	1.7	82	[86, 96, 97]
PbTe	0.3-0.5	56	[98, 99]
Skutterudites	2-5.6 (median = 5)	100-148	[100, 101]
High-Manganese Silicides (HMS)	11.9-16	160-281	[87, 88]

It can be seen from Table 2 that the Mg_2X materials have higher values of mechanical properties for Si-rich compositions. Literature reports indicate that this is due to the more covalent nature of the Si-Mg bond compared to Mg-Sn, which makes the materials stronger [102]. This nature of bond is also favorable to thermal stability.

It can also be observed that, compared to other materials with a similar application temperature range, Mg_2X materials are generally softer. This can be an advantage, as harder materials tend to also be more brittle/sensitive to crack propagation, although this is more defined by the fracture toughness. However, the materials other than Mg_2X have a higher mass density, which is detrimental for many applications.

The linear Coefficient of Thermal Expansion (CTE) defines how the length of a material changes with temperature. It is also a very important material property, as it plays a major role in the thermally induced mechanical stresses developing in a TEG during thermal cycling. Indeed, thermal mechanical stress is defined such as $\sigma_S = \frac{Ea\Delta T}{1-\nu}$ with a the CTE and ν the Poisson ratio [103]. The CTE of Mg_2X materials, other TE materials and typical components of a TEG are shown in Table 3. The CTE is also used as a selection criterion for the material used for the leg metallization, as will be explained in Section 1.6.1.

Note that the product Ea is the driving force for thermally induced stress, thus materials with different mechanical properties will undergo different stress under the same temperature difference. In this regard, Mg_2X materials show a very similar potential to develop stress compared to its competitors in the same temperature range (Skutterudites), albeit with a definite advantage in density and toxicity [103].

Table 3 - CTE of Mg_2X, other TE materials with similar application temperature ranges and usual components of a TEG

Material	**CTE a ($\times 10^{-6}$ K^{-1})**	**References**
$Mg_2(Si,Sn)$	16-18	[86-88]
Skutterudites	10-13	[104]
PbTe	20.9	[105]
BiTe	16.4	[106]
HMS	9-13	[84, 88]
Cu (Cu-DHP, 99.9% Cu)	17	[107] (Appendix 1)
Al	25	[107] (Appendix 1)
Al_2O_3	5.9-7.4	[107] (Appendix 1)

1.6. Material selection for leg metallization

Leg metallization refers to the metallic layer which is located between the TE leg and the metallic bridge. It is usually pre-contacted to the TE leg before being soldered to the bridge.

There are two main reasons for using this metallization layer. First, it can act as a diffusion barrier to protect the TE material, as metallic bridges are typically made of fast diffusing elements such as Cu or Ag, which could therefore lead to unwanted reactions. Secondly, contacting the metallic bridges directly to the TE materials can be challenging. Typical solders are composed of multiple elements, which increases the risk of unwanted interaction with the TE material. The wetting behavior of solders directly on TE materials is also not always favorable to the establishment of a good contact. Moreover, TE materials typically have a low compressive strength, which means that a high pressure cannot always be applied to directly bond the TE legs to the metallic bridges, although pressure is usually necessary for a good bonding to fill voids at the interface and cracking the oxides which could reside on the surfaces [37]. Therefore, having an intermediate metallic layer attached to the TE leg makes the soldering to the bridge easier. In this work, metallization onto the leg's contact faces will equally be referred to as electrode.

1.6.1. Usual pre-selection criteria

The many existing metallic materials cannot realistically be tested all as electrode candidates when developing a TEG. Obvious criteria are a high electrical and thermal conductivity, to ensure good electrical conduction and limit thermal losses in the TEG; however most metallic materials meet those expectations. Beyond, other selection criteria can be applied to reduce the number of potential candidates for an electrode material, before doing any modelling or experimental tests. The main criteria are the following:

- Coefficient of thermal expansion: the electrode's CTE should be as close as reasonably possible to that of the TE material. This criterion has some flexibility as some metals are very ductile, which means they can easily accommodate the mechanical stress resulting from CTE mismatch.
- Melting point: it is usually considered that the maximum joining temperature should be between 50 and 80% of the electrode melting temperature [37]. The maximum joining temperature is restricted by the TE material's thermal stability (i.e. maximum application temperature of 500 °C for $Mg_2(Si,Sn)$), which therefore restricts the maximum melting point and the number of candidates.

Looking at the phase diagram of the considered electrode and the components of the TE material, if available, can help anticipating detrimental reactions at the interface. If no secondary phase is formed at/below the joining temperature, it could indicate that adhesion

between the two materials will be more difficult. On the other hand, if the TE material's elements have a high solubility in the electrode material or vice-versa, it is possible that those will diffuse and locally change the TE material's composition (leading to uncontrolled doping or counter-doping). This is however hardly predictable, as phase diagrams give the phases' stability at thermodynamic equilibrium, which is not necessarily achieved after contacting, and in the real situation the materials brought into contact are alloys and not pure elemental Mg, Si, Sn. Most of the time, the phase diagrams involving three of more components are also not readily available, and need to be calculated based on available databases using CalPhaD methods [108, 109].

Of course, depending on the application and economical context, other criteria can be additionally considered such as material toxicity, price, etc.

1.6.2. DFT calculations of point defects formation energies for electrode selection

Another interesting pre-experimental electrode selection tool was recently investigated by Ayachi *et al.* [1]. It deals with the possible interaction between the electrode and the TE material, in terms of change in carrier concentration.

As explained in Section 1.3.1, the Seebeck coefficient depends on the carrier concentration in the TE material. This concentration itself depends on the amount and nature of defects in the structure. The term "defects" is used in this work to designate crystallographic point defects, which are punctual disturbances to a perfect arrangement of the atoms in the lattice structure of a material. The different types of point defects are atom vacancies, substitutional atoms and interstitial atoms (either atoms from the intrinsic structure or impurity atoms). In undoped Mg_2X materials, Mg vacancies and Mg interstitials are found to be the dominant defects and their competition directly determines the variable native conduction in Mg_2X (n- or p-type, respectively) [55].

With DFT calculations, the nature and stability of defects induced by diffusion of electrode atoms into the TE material can be predicted. If those defects are not charged or significantly less stable than the intrinsic defects of the TE material, a change of Seebeck coefficient is not expected. However, if those new defects are charged, stable enough, and reach a significantly high concentration depending on the considered temperature, a change in Seebeck coefficient can be expected. This change will depend on the charge of the new defects, i.e. if the new

defects add or remove electrons or holes, depending on the dominant carrier type of the original material.

This method can be useful to narrow down the candidate number of electrode materials before starting experimental work, which is more demanding in terms of time and resources.

1.6.3. Electrode selection through experimental work

The criteria which qualify an electrode with respect to an experimental evaluation are the following:

- Good mechanical adhesion between the electrode and the TE leg, directly after joining and through thermal cycling. This is where a CTE mismatch can show itself critical or bearable by the materials.
- Controlled reaction and diffusion between the bonding partners, directly after joining and through thermal cycling. A thin reaction layer is usually desired, as it may enable an intimate contact between the materials. Once formed, it can also have the advantage of acting as a diffusion barrier between the electrode and the TE material. The reaction should however not dramatically progress upon thermal cycling/annealing to not consume the electrode and TE materials, and phenomena such as pore formation (Kirkendall effect) should be avoided to not fragilize the contact.
- Low specific electrical contact resistance r_c at the TE/electrode interface, as described in Section 1.3.2. The value of the specific contact resistance should not increase through thermal cycling/annealing. This could occur in the case of growing cracks resulting from a CTE mismatch, or in the case of formation of poor-conductive secondary phases at the interface.

In this work, contacting is made via direct bonding of an electrode foil to a TE material. Several process parameters such as contacting temperature, pressure and time can be varied to optimize the bonding between the two materials. The contacting step can be made either simultaneously to the TE material sintering [38, 110], or posteriorly [4, 35]. The first case allows for a contacting at higher temperature and pressure, but reduces the control over the final sample dimensions and could enhance the diffusion of the electrode material along grain boundaries into the TE material. Other process adjustments can be made, such as the removal of an oxidation or contamination layer from the surface of a reactive material by sputter-etching, immediately before the metallization step [5] (this will be discussed in section 4), or inserting

a layer of powder made of a mix of the TE and the electrode materials between the two bonding partners, to create an intermediate layer which facilitates the bonding, both chemically and mechanically [110]. Contacting technology will be discussed in more detail in the section 2.

Although not discussed in this work, other contacting methods exist which do not involve direct bonding. Often, metallization layers are directly sputtered or coated on the TE materials using various methods [83, 84, 111-113], before being brazed or soldered to the metallic bridges. The main advantage of this method is the better control over the atmospheric conditions (inert gas, vacuum) and therefore a better layer purity.

1.6.4. Electrode selection for the $Mg_2(Si,Sn)$ material system

Numerous electrodes were tested on the $Mg_2(Si,Sn)$ material system. Ni was identified as a good matching electrode for binary Mg_2Si [38, 114, 115], therefore it was also tested on the solid solution material [2]. Although the resulting electrical contact resistance was satisfying (25-50 μΩcm²), cracks at the interface were reported, which were attributed to the mismatch in CTE. In the same study, Ag was also tested as an electrode for the solid solution [2]. It gave a lower r_c value (9-15 μΩcm²) but seemed to alter the transport properties of the n-type material by modifying the carrier concentration. This effect was later studied using defect formation energy DFT calculations of Ag defects in Mg_2Si and Mg_2Sn [1], such as presented in section 1.6.2.

Another study reported the use of Cu and constantan ($Ni_{45}Cu_{55}$) as new potential electrodes for $Mg_2(Si,Sn)$ [35]. They both show quite low specific contact resistance (<10 and <50 μΩcm², respectively). However, some cracks formed in the sample with the constantan electrode, this being attributed to CTE mismatch. As for copper, it massively reacted with the TE material, which could occasionally cause local delamination of the electrode. Cu seemed to alter the carrier concentration of the n-type material as well, however it is not clear if the change was rather due to TE material stability itself. Goyal et al. used a layer mixing Cu powder and Mg_2X powder as a diffusion barrier between the Cu foil and the Mg_2X material [110]. This method showed good stability and little impact on the Seebeck coefficient of the materials [110], although the annealing temperature was lower than in reference [35] in which the annealing temperature was closer to the material's degradation temperature [116], therefore the comparability of those results is limited.

The use of other electrodes was reported in works dealing directly with TEG prototypes manufacturing and testing, where the contact resistivity, Seebeck changes and contact stability were not the main interest. Skomedal et al. used Ni and Pb layers as solders which led to the formation of reacted areas with the $Mg_2(Si,Sn)$ material [84]; De Padoue, Shikiya et al. sputtered an Au layer on the TE legs and soldered to Ag bridges using Ag paste [112]; The Au layers seemed to improve contact adhesion on the hot side; Kim et al. directly used commercial solder alloys (Ag-Cu-Sn-Zn) on the legs [113].

Finally, Al was tested as an electrode in this thesis, with promising results. This will be discussed in section 3.

1.7. Building and life cycle of a TEG

1.7.1. Module manufacturing

Unlike the metallization step, a thorough study of the process optimization of TEG building was not accurately reported in literature, as it heavily depends on the TE material selection and the target application itself. Usually, once the metallization on the TE legs has been optimized, the legs are then easily soldered to metallic bridges which are typically made of Cu. Therefore, commercial solders or Ag pastes tend to be used for the joining [84, 111-113, 117, 118]. Like for the metallization step, the joining temperature and pressure should be chosen accordingly to the TE materials thermal stability and the application conditions of the TEG.

Tarantik *et al.* investigated brazing conditions for a HMS/$Mg_2(Si,Sn)$ TEG module, using a 1 µm layer of Ni as a diffusion barrier with various solders at different brazing time/temperatures [111]. Most tests were unsuccessful, as several legs got cracked, some joints were not stable or in some cases the inner electrical resistance remained high despite a satisfying soldering. This work shows that module assembly is not necessarily more trivial than the metallization step, and that bridge and brazing materials, as well as soldering time and temperatures can have a considerable impact on the module quality. This is even more relevant in case of thin sputtered metallization layers which will have a more limited diffusion barrier and mechanical buffer function [118] between TE and bridge materials.

1.7.2. Cycling and typical failures causes

Depending on their applications, TEG modules can be damaged due to several causes as high load, atmospheric attack, exposure to corrosive media, etc. However, what is common to all

applications is that they all consist in applying a temperature difference to the device, which leads to thermal and mechanical stresses, especially on the hot side.

The consequences are multiple. As mentioned in Section 1.5.3, the thermally induced stress can lead to the formation of cracks close to the TE/metallization interface due to a mismatch in CTE [36, 119]. This increases the inner resistance of the TEG and decreases its performance. Furthermore, thermally induced stresses are asymmetric between hot and cold side, as the expansion of the hot side with a pinned cold side causes a bending of the TE legs, which can also be a cause of failure in the assembly [83].

The hot side temperature enhances diffusion, which may lead to further reaction and degradation of the interface between the metallization and the TE material [120], as was described in sections 1.3.2 and 1.6. Depending on the diffusion-engendered defects stability, the carrier concentration in the TE legs could also be impacted by the diffusion of metallic elements into their structure, which could also deteriorate the TEG performance.

Finally, depending on the application conditions, the TE materials themselves could deteriorate [119]. Electrical transport and microstructure in $Mg_2(Si,Sn)$ materials are found to be sensitive to Mg content, especially at high temperatures. Consequences of Mg loss are twofold: decrease of carrier concentration (due to Mg vacancies forming in the lattice) and later thermodynamic unmixing of Mg_2Si and Mg_2Sn.

Recently, Sankhla *et al.* (in SI of [116]) showed a rapid functional degradation of the n-type material when held at 425 °C for only 40 hours under vacuum (decrease of ~12% of the electrical conductivity), while there was almost no change for similar durations at temperatures of 375 °C and 350 °C. Similar decrease of carrier concentration in n-type samples have already been experimentally observed [121, 122]. This is due to Mg vacancies, which are very stable acceptor defects [1, 123], and whose concentration increases at high temperature due to Mg evaporation.

For the p-type material, multiple cycling to 530 °C was reported without a change in the TE properties [80], and no change was either observed in p-type contacted samples after 1 and 2 weeks of annealing at 450 °C [4, 35]. Studies for longer durations or higher temperatures are however lacking. Performance degradation of a $Mg_2(Si,Sn)$-based TEG due to change of carrier concentration will be discussed in section 6.2.

Mg loss also leads, on the longer term, to phase separation of the solid solution to the boundary compositions of the miscibility gap in the quasibinary Mg_2Si-Mg_2Sn system upon annealing [85, 124].

1.7.3. State of the art of silicide-based TEGs

Although silicides have been extensively studied in the field of TE properties optimization, work focusing on using them as TEG components is recent. A summary of the performance of some silicide-based TEG development reported in literature is shown in Table 4.

Table 4 - Summary of the maximum power output density and efficiency (with corresponding temperature difference) of silicide-based TEGs reported in literature

Leg materials (n-type / p-type)	**Maximum power density (TE area) [W/cm²]**	**Temperature difference [K]**	**Number of leg pairs**	**Efficiency [%] (*italic if predicted*)**	**Reference**
Mg_2Si / -	0.2	500	12	-	[125]
Mg_2Si / Si-Ge	1	620	2	-	[126]
$Mg_2(Si,Sn)$ / HMS	0.3	480	14	-	[111]
$Mg_2(Si,Sn)$ / HMS	3	710	6	*5.3*	[84]
$Mg_2(Si,Sn)$ / HMS	0.9 (cascaded with n/p- Te-based alloys)	520	16 (total)	8 (Si-based half), 12 (cascaded)	[83]
Mg_2Si / HMS segmented with n/p-Bi_2Te_3-based	0.8	500	2	4.6	[113]
$Mg_2(Si,Sn)$ / $Mg_2(Si,Sn)$	0.5	330	2	-	[127]
$Mg_2(Si,Sn)$ / $Mg_2(Si,Sn)$	0.52	331	2	*5*	[128]

HMS has slightly higher performance than p-type $Mg_2(Si,Sn)$ in the same temperature range, which is why it was usually chosen so far for power generation. However, its main disadvantage is that it has different mechanical properties to the n-type that it is associated to, which could result in poor mechanical stability of the TEGs. Skomedal *et al*. used spring loading under the TE legs in order to minimize the impact of differential thermal dilatation between the n- and p-type materials, this however makes the design of the module much more complicated [84]. The mechanical compatibility is a strong argument in favor of the combination of n- and p-type $Mg_2(Si,Sn)$ in a TE module. As can be seen in Table 4, only two fully $Mg_2(Si,Sn)$-based TEG were reported yet [127, 128] (it is worth noting that at the start of this PhD work only one of the two, the PhD thesis by Gao, was published). Our work will also present power density measurements of such a module and the first efficiency measurement of a $Mg_2(Si,Sn)$-only TEG module will be discussed in section 5.

1.8. Aim and overview of the thesis

The aim of this thesis is to successfully build, characterize and understand a TEG made of p- and n-type $Mg_2(Si,Sn)$ TE materials.

At the beginning of this work, $Mg_2(Si,Sn)$ already was a well-investigated TE material class in terms of properties optimization and understanding [63, 72, 81, 116, 121-123, 129]. However, research on the next steps in the development of a TEG made of these materials, such as contacting and TEG building, was scarce. Moderately satisfying electrodes were reported in literature, such as Ag which showed low contact resistances but altered the properties of the n-type material [1, 2], while Ni, Cu and constantan led to cracking or delamination [2, 3]. Additionally, at this stage, no fully $Mg_2(Si,Sn)$-based TEG was reported in literature, which means that knowledge was lacking on their manufacturing, mechanical behavior, performance characterization nor performance modelling.

In section 3 ([4]), we find Al to be a promising electrode for $Mg_2(Si,Sn)$. We report no cracking nor delamination contrarily to previously reported electrodes and measured contact resistivities below the set threshold of 10 $\mu\Omega cm^2$, while no change in the TE materials are observed.

It is later observed section 4 ([5]) that the main drawback of using Al as electrode for $Mg_2(Si,Sn)$ is the lack of reproducibility of the samples, with varying and asymmetric contact resistances. We identify the origin of the asymmetry to be during the dicing step, which is unavoidable in the current leg fabrication process (direct bonding of metallic foil). Ion etching

of the Al foils before sputtering a Zn layer as oxidation barrier is tested and found to be an effective strategy to maintain symmetrically low contact resistivities after the dicing step.

In section 5 ([6]), a full $Mg_2(Si,Sn)$-based TEG is build and characterized. The first efficiency measurement of such a module is reported and we measure a high power density, which scales with comparable TEG recently reported in literature [84, 128]. CPM is used for theoretical calculations meant to evaluate the reliability of the measurement. It also allows to identify the degradation of the TEG prototype, by the increase of its inner resistance, very likely due to thermally induced stress which led to cracking. It is predicted that both efficiency and power output could be realistically increased by 30% by improving the mechanical stability of the module. This failure due to high thermal stress is imputed to the Al_2O_3 plate of the Direct Bonded Copper (DBC) substrates used in the TEG design.

This CPM analysis in [6] is done assuming a homogeneous n-type material, neglecting the Seebeck coefficient gradient in the n-type legs which is induced by the Zn barrier diffusion. A further analysis combining carrier concentration profiling and the SPB model is made in section 6.1, bringing more nuance to the conclusions previously drawn.

In section 6.2, we test the hypothesis that the TEG mechanical failure is due to the Al_2O_3 plate by using an open module design with only Cu bridges. Additional voltage probes are soldered to monitor the resistance of each leg during the measurement. It is observed, on several TEGs, that the resistance of the n-type legs systematically increases even if keeping the hot side temperature below 200 °C, while the p-type legs match their predicted values. It is found that increasing the cross-section of the legs partially solves the issue, as no degradation is observed in a third module when the hot side temperature remains below 300 °C.

Overall, our work on TEG building and characterization pointed out very good chemical and mechanical stability of the p-type legs in the first few measurement cycles, and our early research develops a successful TEG making process, at least for lower hot side temperatures.

2. Chapter 2: Methods

This section presents the experimental procedures used in this work. The synthesis route of the thermoelectric powders and the process leading from those powders to metallized legs and to a generator are described. The methods used for legs and TEG characterization are also detailed. Finally, detailed equations of the CPM calculations to evaluate the TEG performance are provided.

2.1. Experimental Procedure: from powder to generator

2.1.1. Powder synthesis: Induction melting and high-energy ball-milling

N-type and p-type powders used in this work were obtained following a procedure reported by Farahi et al. [76]. This method has the advantage of producing larger quantities (25-50 g per batch) than ball-milling only synthesis methods (typically 10-15 g per batch) for equivalent qualities and operating time. The powders were synthesized by two colleagues: Gustavo Castillo-Hernandez and Radhika Ravindra Deshpande.

The melting is done in a direct-current sintering press chamber (Dr. Fritsch GmbH, DSP 510 SE) under partial Ar gas atmosphere. The initial pressure at room temperature was 0.35 - 0.5 bar depending on the highest temperature of the process, during which the pressure is aimed to be as close to atmospheric pressure as possible to limit Mg evaporation (considering that the DSP cannot work at overpressure).

The process consists of three melting cycles, each cycle being divided into three steps of temperature increase and hold, with a progressive increase of the final temperature for each cycle to increasing stoichiometric homogeneity. Those steps are described in Table 5 below. The first temperature is chosen above Sn melting point (232 °C) to start dissolving Mg particles. The second temperature (600°C) is chosen to further enhance Mg dissolution by reaching the Mg-rich Mg-Sn liquidus [130] and partially form Mg_2Sn. The third temperature of the first cycle is set ~25 °C above the melting temperature of Mg_2Sn (778 °C), while the 3rd cycle ends ~25°C above the melting temperature of the intended final composition $Mg_2Si_{0.3}Sn_{0.7}$ (875.2 °C). Si (T_m = 1410 °C) will progressively be dissolved by the melt to form the final composition. The final temperature of each cycle should not be higher to avoid too large amounts of Mg evaporating. The second temperature step is different for n- and p-type due to the difference in Mg excess content, which is not added in the p-type composition contrarily to the n-type composition: therefore, the melting of p-type is maintained at a slightly lower temperature to avoid larger Mg loss, which can lead to a change in the TE properties. This

process is more detailed in: [131]. The impact of Mg loss on the TE properties will be further discussed in sections 3 and 6.2.

The duration of each heating step is 10 min and each holding step lasts 20 min, beyond the first temperature step of each cycle (at 300 °C) that is only held for 10 min.

Table 5 – Cycles of the melting process and their respective temperature steps for $Mg_{2.06}Si_{0.3}Sn_{0.665}Bi_{0.035}$ (3% Mg excess, n-type) and $Mg_{1.97}Li_{0.03}Si_{0.3}Sn_{0.7}$ (p-type).

	Temperature step 1	Temperature step 2 (n-type / p-type)	Temperature step 3
Melting cycle 1	300 °C for 10 min	600 / 575 °C for 20 min	800 °C for 20 min
Melting cycle 2			850 °C for 20 min
Melting cycle 3			900 °C for 20 min

The melting is done inside a BN-coated graphite crucible shown in Figure 21a. All precursors are weighed correspondingly to the aimed compositions: $Mg_{2.06}Si_{0.3}Sn_{0.665}Bi_{0.035}$ (3% Mg excess, 3.5% Bi doping) and $Mg_{1.97}Li_{0.03}Si_{0.3}Sn_{0.7}$ (1.5% Li doping). The used precursors were Mg turnings (Merck), Si (< 6 mm, ChemPur), Sn (< 71 µm, Merck) along with the dopants which are Bi granules (99.999%, Goodfellow, ~ 7 mm) for n-type, and Li granules (> 99.5%) for p-type. The n-type composition contains 3 at% excess Mg to compensate for the Mg loss that occurs during the higher and longer temperature step of the material preparation compared to the p-type [76, 81, 132].

The BN-coated crucible is maintained closed inside the DSP chamber using a plunger as represented in Figure 21c. The heat is produced via a direct electric current running through the graphite crucible. The BN coating serves to prevent the current to flow through the melted ingot, therefore the heat transfer from the crucible to the elements inside it occurs through heat conduction, radiation and convection. The temperature close to the inner wall of the crucible is monitored with a type K-type thermocouple.

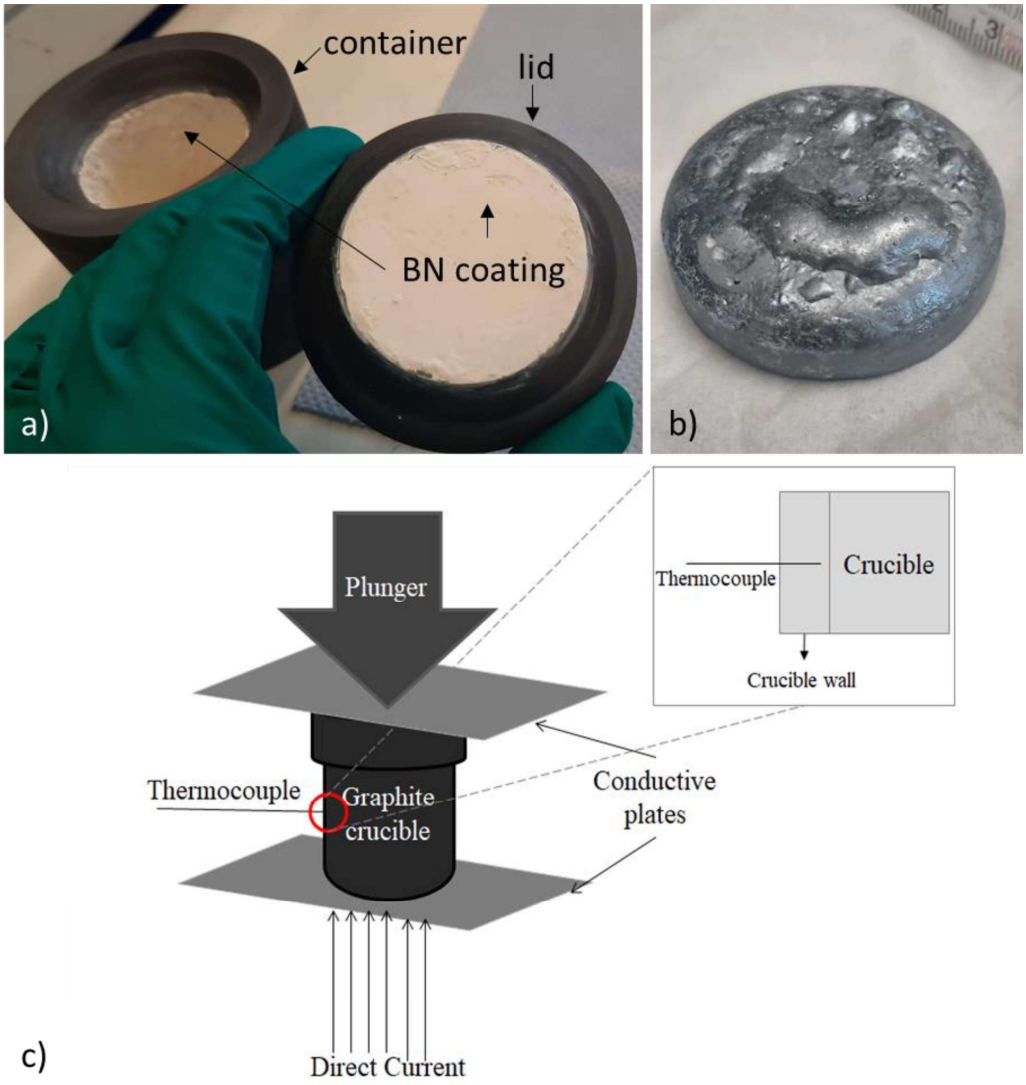

Figure 21 -a) picture of the opened BN-coated graphite crucible, b) picture of the ingot after three melting cycles and after ethanol cleaning, c) Schematics of the graphite crucible fixed inside the DSP chamber, taken from [3]. The zoomed-in section shows the thermocouple that is inserted inside the wall of the crucible, close to the inner edge.

The obtained ingot (shown in Figure 21b) is broken into smaller pieces with a chisel. Those pieces are then ball-milled for one hour with stainless-steel balls (with balls in a ratio of 1 ball per 10 g of material) in a high energy ball mill (SPEX 8000D Shaker Mill). A fine homogeneous powder with an average particle size ranging between 7 and 10 µm ready for sintering is obtained.

2.1.2. Pellet sintering and metallization

In this work, the powder as obtained after high energy ball milling is sintered using a current-assisted direct sinter press (DSP). Current-assisted sintering and hot pressing are the two processes used in this work with the DSP and are very commonly used processes for powder compaction, especially in the TE field. In addition to compacting the powder, this high-

temperature step also completes the material synthesis. The powder is held inside the die using a graphite foil (200 µm thick) wrapped around the inner wall of the die. Graphite foil disks are used between the powder and the graphite plungers to avoid powder loss and unwanted reaction.

Hot-pressing involves uniaxial pressure and high temperature to sinter powder into a high-density condensed pellet. A plunger is transferring a force to the punches that are pressing the powder inside a die, as represented in Figure 22a. The temperatures applied in hot pressing are such as the powder material is in the plastic deformation regime [133]. This plastic yielding leads to an increase of the contact surface area which favors interparticle diffusion mechanisms and bonding of the grains.

Electric current-assisted sintering (ECAS) is a type of hot pressing where heat is provided by an electric field to enhance interparticle bonding and densification. An electrical current runs through the die and sample system, similarly to the setting shown in Figure 21 (replacing the graphite crucible on the figure by a graphite die). With EACS, the powder is mainly heated through Joule heating, while hot-pressing mainly relies on heating by radiation and eventually convection and/or conduction. The resistive heat manifests in the bulk of the particles but also in particular, due to the electric interface resistance between the particles, at particle interfaces. This serves to bond particles with each other, and also promotes plastic deformation upon sintering within the bulk [134].

The plungers and die are usually made of graphite, due to its mechanical strength, electrical conductivity, low thermal expansion coefficient, ease of machining and low cost [135]. The sintering is also usually kept in a non-oxidizing atmosphere (vacuum or inert gas) due to the high temperatures and possibly highly reactive materials involved.

All sintering experiments were done in the same direct sinter press DSP used for the induction melting step, under an axial pressure of 66 MPa, with a heating rate of 1 K/s. All experiments were conducted under vacuum condition (~10^{-5} bar). N-type samples were pressed at T = 700 °C for t = 1200 s, while p-type samples were pressed at T = 650 °C for t = 600 s. These selected pressing conditions give high-density materials with state-of-the-art properties. The system is allowed to cool down to room temperature passively, as the uniaxial pressure is released at the beginning of this step.

The same process can be used for the metallization (contacting) step, in which the compacted pellet and metallic foils are pressed together.

Before contacting, the compacted pellets are wet ground using ethanol and SiC paper down to a P2500 grit to remove the remainders of graphite foil and obtain pellets with parallel base faces. The parallelism of the surfaces was checked using a digital caliper by measuring the sample height at different parts of the sample, allowing for a precision of ± 10 µm.

In this work, the pellets were contacted with aluminum electrodes. The joining temperature will be first discussed in section 3 and set in consequence to 475 °C for the following chapters. In all cases, the heating rates were 1 K/s, the axial pressure and the holding time were maintained at 28 MPa and 10 min, respectively. The electrode material softens when the target temperature is reached and adheres to the rough surface (surface roughness ~2 µm) of the TE pellet. Diffusion and reaction can also occur between the electrodes and the pellet. This will be discussed in sections 3 and 4.

In some cases (sections 4, 5 and 6), the Al foils were etched to remove their native oxide layer and coated with an oxidation barrier, using an AixPLORER 4375 S3E1 PVD machine. Those processes were either done by the colleagues M. Sc. Adina Frank, Dr. Christian Stiewe or by the author of this work. An ion etching process was performed at the Al foil surface prior to the Zn coating in order to remove the native oxide layer. Zn was selected as an oxidation barrier and was sputtered at room temperature on a substrate rotating at 10 min^{-1} in a starting vacuum of $5 \cdot 10^{-6}$ mbar using ionized Ar. The duration of the sputtering was 90 min with a growth rate of 1.3 nm/s. The Zn target used for this process was provided by EvoChem (purity 99.99%). The choice of Zn as protective coating will be discussed in section 4.

Due to the limited spatial resolution the Potential & Seebeck Microprobe (PSM) facility (Section 2.2.3), thick electrodes were applied (minimum thickness of 200 µm before contacting). In case of availability of thin foils only, several layers of the same material were piled up to provide the necessary thickness of the electrode.

A layer of Al_2O_3 powder of a thickness of ~2-3 mm is laid into the graphite die on both sides of the TE/electrode assembly. This loose powder layer helps evenly distributing the pressure across the pellet and lowers the risk of cracking in the TE material. This presumably also prevents the flow of electrical current through the sample, as Al_2O_3 is electrically insulating. As a consequence, this process is closer to simple hot-pressing as heating of the sample would occur through radial heating by Joule heating of the die.

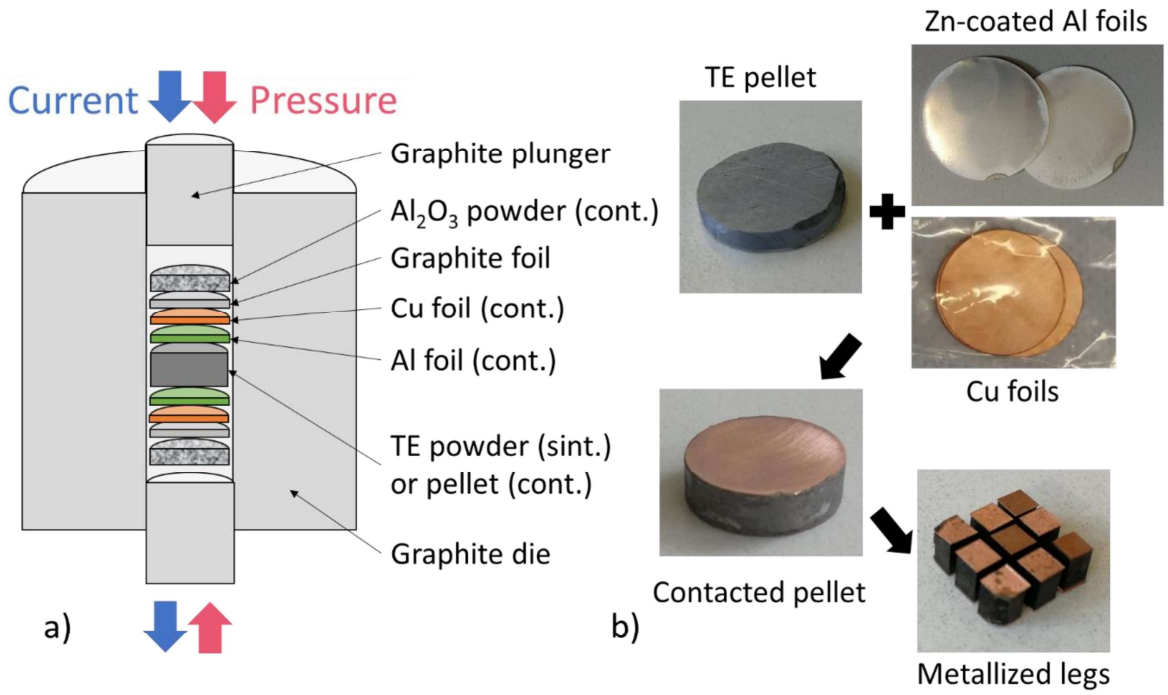

Figure 22 - a) Schematics of a sintering die and the layers used in the sintering ("sint.") and contacting ("cont.") processes. In case of pellet contacting, Al_2O_3 powder layers are added in the die on top of and below the electrode-pellet. b) Road from TE pellet to metallized legs. The TE pellet is compacted by sintering the powder obtained as described above. After grinding, the pellet is sinter-bonded with metallic foils (here Zn-coated Al foils and Cu foils) to obtained a metallized pellet. This pellet can then be cut into metallized legs.

2.1.3. Legs dicing and grinding

After joining, the metallized pellet needs to be diced into functionalized TE legs, as shown in Figure 22b. The dicing device is an automatic dicing disco saw (DISCO, DAD 3231) with an translational speed of 0.3 mm/s and disk rotation speed of 30,000 rpm. The sample is set on a large sticky polymer foil which is held in place by a sucking pump on the cutting table. The dicing is made in a stream of water to prevent the elements from overheating.

After cutting, often, smearing of the electrode material over the cut surface is observed due to the travel of the blade through the sample. The legs were therefore be slightly ground on the outer part of their electrodes to avoid this smearing and have a flat surface for correct length measurement.

Furthermore, it often happens that, during the grinding of the base faces of the TE pellet prior to contacting, the pellet is thinner on its outer edges, due to the rotation of the grinding plate which consumes more material the farther it is from the center of rotation. Therefore, after cutting and suppressing the electrode smearing, the length of the metallized legs should be checked and adjusted by continued grinding if necessary, such as all legs composing an

assembled generator have to have an equal length (here again, the required precision is ± 10 µm).

After dicing, the external surface of the TE material is oxidized due to the cutting water, as can be seen in Figure 22b. For legs that are meant to be assembled in a TEG, grinding this oxidation layer is not necessary as it might rather act as a diffusion/Mg evaporation barrier which might be beneficial. However, for characterization such as measurement in the PSM (see section 2.2.3) or Energy-Dispersed X-Ray Spectroscopy (EDX) (section 2.2.1), the oxidation layer needs to be removed on the characterized side of the leg.

2.1.4. Module assembly and cable soldering

After preparing the metallized legs, they can be assembled into a module. The procedure is shown in Figure 23. It should be mentioned that in this thesis, "module" and "TEG" are used interchangeably, while strictly a TEG (generator) is made of the TE module and of the electronics implemented for its designed application.

The top and bottom substrates are standard commercial DBC plates obtained from HHI Industrievertretungen. DBC are Al_2O_3 ceramic plates bonded with layers of Cu which form the pattern of bridges forming an electrical circuit once the TE elements are placed between both DBC. They are a standard component of TE modules.

Each leg is soldered to the DBC at both sides using Sn foil (12.5 µm thick) and flux paste (Stannol Lötfett soldering grease) at each interface. Non-conductive foam masks can be used to maintain the legs and the top DBC in place relatively to each other during manipulation. This is however not necessary for small modules containing few elements, e.g. for 2-pair modules. The assembly is made inside a graphite die such as shown in Figure 24a.

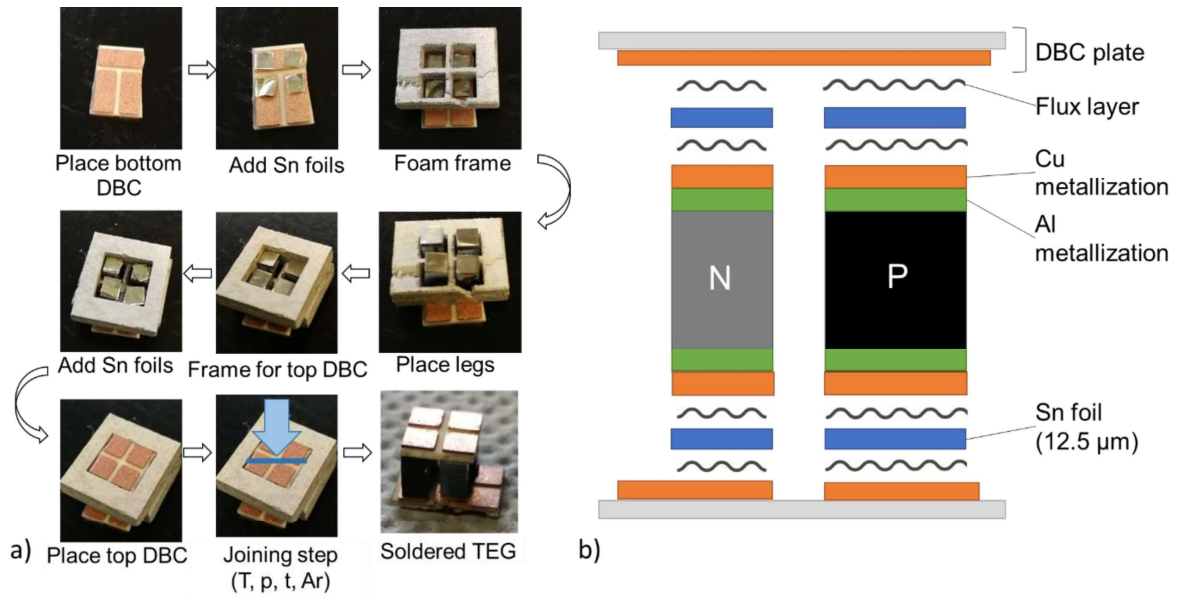

Figure 23 - a) step-by-step building procedure of a module, b) side-view schematics of the several layers used in the building procedure.

Soldering of the legs to the DBCs is done in an induction furnace, shown in Figure 24b. The bonding parameters are 280 °C for 30 min with a heating rate of 25 °C/min and a load of 4 kg (0.6 MPa) under partial Ar atmosphere, unless specified otherwise in following chapters. The module assembly is set inside a graphite die which is placed at the center of the copper induction coil, through which an alternative current flows. This generates a rapidly reversing magnetic field that induces eddy (electrical) currents inside the graphite, which gets heated up due to the Joule effect. A thermocouple is inserted in the wall of the die to monitor the temperature close to the inner wall, similarly to what was represented in Figure 21.

After the module assembly, cables are soldered to the terminals of the electrical path for TEG module characterization, using Stannol Lötfett soldering grease and Stannol S-Sn60Pb39Cu1 soldering alloy. It is possible that the surface of the Cu bridges contacted by soldering gets contaminated; in this case the surface is gently ground with SiC paper and ethanol before soldering. Two cables are soldered at each terminal in order to conduct a four-point measurement, which allows to disregard the electrical resistance added by the cables. This will be more thoroughly discussed in the section 2.2.4. A TEG module ready for measurement is shown in Figure 24c.

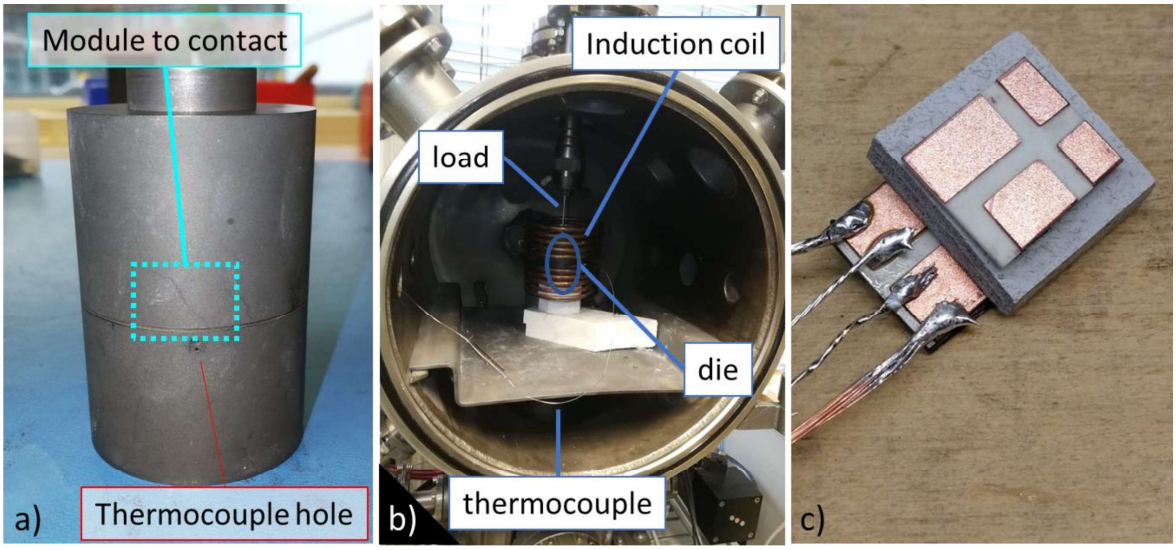

Figure 24 – a) graphite die used for module joining, b) chamber of the induction furnace in which the module is joined, c) assembled 2-pairs TEG module with soldered cables, taken from [6].

2.1.5. Annealing experiments of metallized samples

To study the thermal stability of the tested contacts in section 3, annealing experiments were conducted on some metallized legs. The samples were coated with a thick solution of boron nitride (BN) and ethanol to minimize Mg evaporation from the TE material. They were then placed in quartz ampoules containing Argon atmosphere with a pressure of 560 Torr which were sealed at room temperature. The quartz ampoules were then kept in an annealing furnace for 7 or 14 days, at a temperature of 450 °C. The heating rate was 1 K/s, and the samples were cooled down through radiative free cooling.

2.2. Characterization

2.2.1. Scanning Electron Microscopy (SEM) and Energy dispersive X-ray Spectroscopy (EDX)

a) Sample preparation

Most samples are embedded in a cold embedding resin (Demotec 70). After embedding, the sample is wet ground with a grinding machine (ATM Metallography, SAPHIR 250 M2) using ethanol and SiC grinding papers (800, 1200, 2500 and 4000 µm size) to obtain a mirror-like surface. Some samples were also polished using an automatic grinding and polishing machine (ATM Metallography, SAPHIR 550) with alcohol-based diamond solutions (Schmitz Diamond suspensions) with particle sizes 3 µm, 1 µm and 0.25 µm. Each polishing step is done under a pressure of 15 N for 5 min with a separate disk. A final cleaning step is done using a cloth disk under constant stream of ethanol for 10 mins, and under a pressing force of 10 N.

Two different SEM devices were used in this work: the Zeiss Ultra 55 SEM and the Hitachi SU3900 SEM, both equipped with an EDX detector. For analysis in the Zeiss Ultra 55 SEM, the samples need to be electrically conductive. Therefore, a copper tape is applied such as it electrically links the sample to the bottom of the embedding pellet (which lies in contact with the SEM sample holder).

b) Description of the characterization technique

SEM is used to observe sample surfaces and microstructure, while EDX allows to measure the chemical composition of local areas or points in the samples. A focused beam of high-energy electrons is projected onto the surface of the sample and different information can be obtained from the different resulting electron-sample interactions. The ones used in this work are:

- Backscattered electrons (BS): from the surface to deeper into the material, primary electrons can be reflected by atoms, as their trajectory is deflected when approaching an atom. Heavier elements tend to stronger backscatter primary electrons; they therefore appear lighter. Backscattered electrons have higher energies than secondary electrons (> 50 eV) [136, 137]. They are used to distinguish different phases present in the material, their domain shape and their distribution by showing the contrast between their respective shade of grey which gives a first indication on their composition.

- Secondary electrons (SE): they are electrons ejected from the conduction band of material's atoms due to the transfer of energy from the primary electrons (from the beam). Secondary electrons usually have low energy (< 3-5 eV) and are emitted from areas close to the surface (information depth of a few nm) [137]. The texture of the sample has an influence on the number of secondary electrons which are detected, which is why they are usually used to observe the surface topography (pores, voids, uneven surfaces, etc.).

- X-ray: in the inner electronic shells of the sample's atoms, the same phenomenon as for secondary electrons can happen: a primary electron ionizes an atom's electron by energy transfer, which creates a hole in the shell. This hole can then be filled by an electron from outer shells; this transition emits a characteristic X-ray line. The characteristic X-rays can, using EDX, allow identifying an element in a micrometer range of depth.

In this work, SE and BS imaging, EDX elemental mappings, line scans and compositional point analysis are combined to study the interfaces between the TE material, the metallization layers and the Cu bridges of a TEG.

X-ray spatial resolution depends on the sample density and acceleration voltage. The following equation has been shown to give a good practical estimate of X-ray interaction with actual samples [138]:

$$\delta = \frac{0{,}064\left(E_0^{1{,}68} - E_c^{1{,}68}\right)}{\rho_d} \tag{31}$$

with δ the spatial resolution (arbitrary symbol), E_0 the acceleration voltage, E_C the critical excitation energy (of the heaviest element in the system) and ρ_d the mean sample density. The heaviest element of $Mg_2(Si,Sn)$ is tin, its highest detected energy is 3.443 keV, the accelerating voltage used for SEM observations is between 10 and 15 keV and the density of the $Mg_2(Si,Sn)$ samples used in this work is about 3.1 g/cm³. This gives a theoretical spatial resolution between 0.8 and 1.8 µm. The limitation to the application of this formula is that, if a large secondary phase domain (size > R) or an interface with a different material (metallization) is investigated, then the local values of E_C and ρ_d are different from the values applying to the matrix of the TE material, therefore, the calculated resolution is not accurate.

Lastly, the EDX Oxford software used in this work has a quantitative detection limit of ~ 2 at% and an accuracy of 5-10%. It is thus not reliable in the case of element diffusion at the interface, where low atomic percentages are involved. The detected concentrations could also vary depending on the angle at which the sample is set, and this can lead to some uncertainties.

2.2.2. Measurement of thermoelectric properties

For the CPM calculations (see sections 1.2.2 and 2.3), the temperature-dependent TE properties of the legs' materials are required as an input. Therefore, TE pellets are sintered using the powder from each batch and prepared for measurement of their electrical conductivity, Seebeck coefficient and thermal conductivity between room temperature and 450 °C.

a) HT-*S*-σ

The HT-*S*-σ is an inhouse device developed by the Department of Thermoelectrics at DLR. It can measure the temperature dependent Seebeck coefficient and electrical conductivity of thermoelectric samples, using electrically heated gradient heaters, thermocouples and voltage sensors as shown in Figure 25. The thermocouples are Inconel-sheathed type N (Nicrosil (Ni + 14.2 at.% Cr + 1.4 at.% Si) and Nisil (Ni + 4.4 at.% Si + 0.1 at.% Mg)), individually separated by ceramic filling. The voltage sensors are made of tungsten carbide.

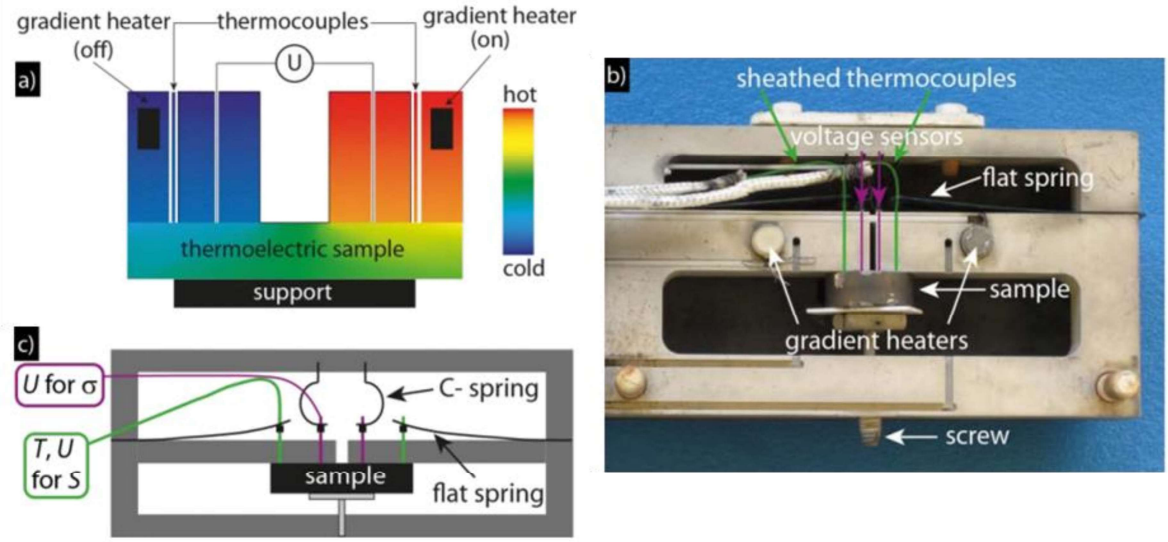

Figure 25 - Schematics and picture of HTSσ device. a) was taken from [6]

It is important to first set a stable temperature in the furnace. The gradient heaters generate a gradient of temperature on the sample. The thermocouples measure the temperature on both sides of the sample, T_1 and T_2, as well as the voltage generated by this gradient due to the Seebeck effect, U. The Seebeck coefficient can be calculated from the ratio between voltage and temperature difference, using the following equation:

$$\alpha = -\frac{U}{T_2 - T_1} + \alpha_{\mathrm{w}} \tag{32}$$

where α_{w} the Seebeck coefficient of the material the wires are made of. U, T_1 and T_2 are measured during a relaxation period that occurs after switching off the heater after a short heating time (60 s). For the measurement result, all available data for U is fitted [139].

To measure the electrical conductivity, an alternating current I is led via the thermocouples and the resulting voltage U is measured between the inner probes. The electrical conductivity is then obtained with the following formula [140]:

$$\sigma = \frac{I}{2\pi d U C} \tag{33}$$

$d = 3$ mm being the distance between the tips (probes) and C a geometrical factor that can be found in literature for standard geometries (bars, cylinders) (references are given in [140]). The measurement uncertainty for both α and σ is estimated to be around 5%.

The $Mg_2(Si,Sn)$ samples typically need to undergo two temperature cycles in the HT-*S*-σ to reach stable properties. During the first cycle, some changes occur in the sintered pellet such that the heating curve and the cooling curve do not match. Therefore, a second cycle is added

to ensure that stability has been reached whereas the first cycle serves as an annealing step. A representative 2-cycles measurement is shown in Figure 26a. For TE legs (which are made from a different pellet than the pellet used for this kind of measurement, but using the same powder batches), this annealing-like step is undertaken during the metallization and module assembly steps, performed at 475 °C for 10 min and 280 °C for durations from 15 to 30 min, respectively.

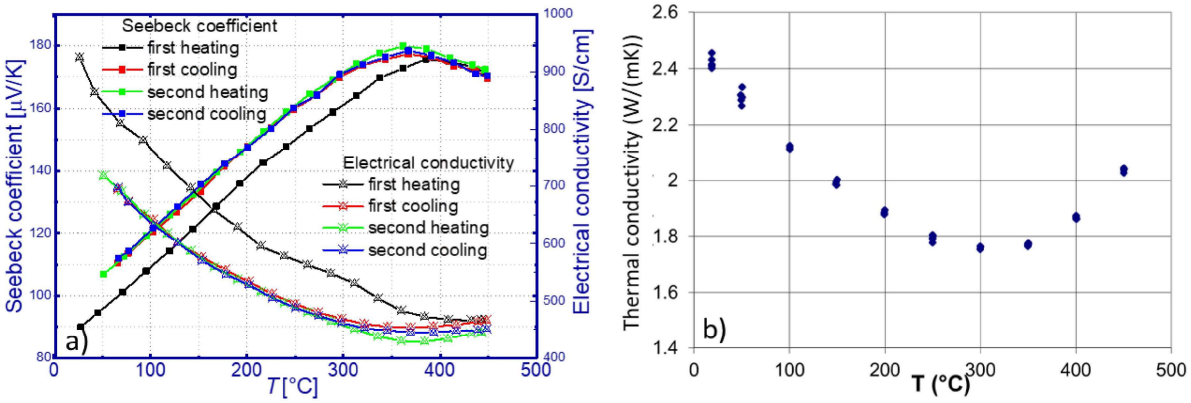

Figure 26 – For a $Mg_{1.97}Li_{0.03}Si_{0.3}Sn_{0.7}$ pellet: a) 2-cycles HT-S-σ measurement of the Seebeck coefficient and the electrical conductivity, b) thermal conductivity measurement

b) Laser Flash Analysis and Xenon Flash Analysis

Two machines were used to obtain thermal conductivity, NETZSCH LFA 427 and LFA 467HT Hyperflash (XFA). Both machines measure the thermal diffusivity D, which is then used to calculate the thermal conductivity κ by the following equation:

$$\kappa = \rho_{\mathrm{d}} * c_p * D \tag{34}$$

where c_p is the specific heat and ρ_{d} the mass density. The thermal diffusivity is obtained similarly with both machines: a short laser (for LFA) or Xenon flash lamp (for XFA) pulse is irradiating one side of the sample. The resulting temperature rise on the backside is measured by a high-speed infrared detector. The measurement uncertainty of the thermal conductivity is 8%.

For most materials c_p varies at low temperatures before reaching a plateau, following the Dulong-Petit law $c_p = c_v^{\mathrm{DP}} + \frac{9a^2T}{\beta_T \rho}$ where C_V^{DP} is the Dulong Petit limit, a the coefficient of thermal expansion and β_T the coefficient of isothermal compressibility [141]. The values for $Mg_2Si_{0.3}Sn_{0.7}$ are $2 \cdot 10^{-5}$ K^{-1} and $2.07 \cdot 10^{-11}$ Pa^{-1}, respectively [142]. The corresponding temperature dependence of c_p is shown in Figure 27.

Accidentally, the p-type data used in sections 5 and 6.1 was obtained considering a constant c_p value of 0.536 J/g/K. This leads to an underestimation of the p-type average thermal conductivity of 4-6%, which lies within the measurement uncertainty. Therefore, the impact on the results analysis should be negligible.

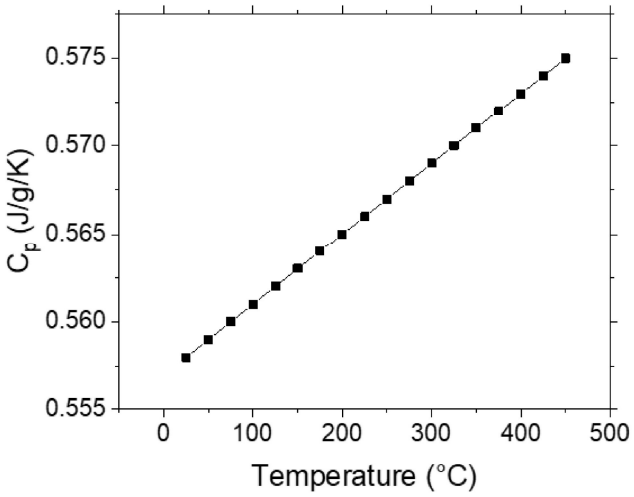

Figure 27 - Temperature dependence of c_p for $Mg_2Si_{0.3}Sn_{0.7}$

2.2.3. Potential & Seebeck Microprobe (PSM)

a) Device operation

The electrical contact resistance can be obtained using an in-house built device called the Potential & Seebeck Microprobe (PSM) [143, 144]. This device locally measures the Seebeck coefficient and the voltage along a conductive sample, which in the case of a TE leg allows to calculate the electrical contact resistance. All measurements are done at room temperature. Schematics of the Seebeck coefficient and the voltage measurements are shown in Figure 28.

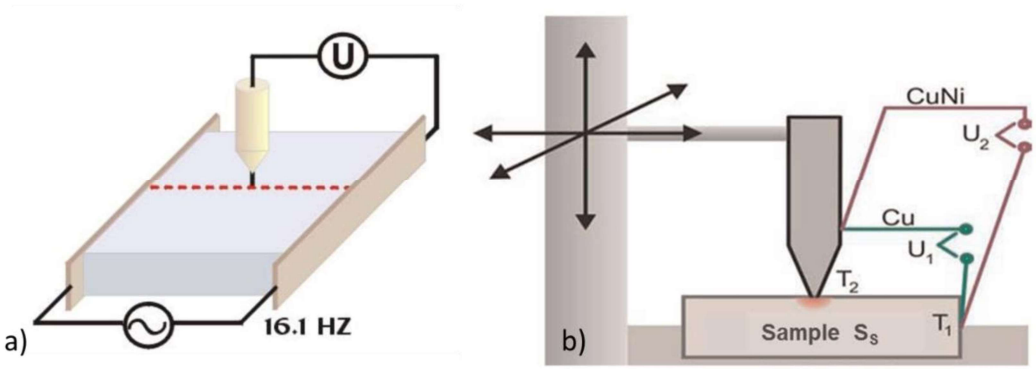

Figure 28 - Schematic of a) the potential drop measurement in the PSM facility (taken from [144]), b) the Seebeck coefficient microprobe measurement, taken from [143].

The PSM device allows to map local Seebeck coefficient and voltage values, using a tip travelling across the sample fixed between two Cu blocks. The voltage is measured in a three-point scheme, between the measuring tip and the Cu blocks, which act as a low- and high potential electrodes as represented in Figure 28a. The measurement is done using a lock-in amplifier (LIA-BV-150-L, FEMTO Messtechnik GmbH). An electrical alternative current (AC) is applied to the sample, and as the microprobe scans at different positions, a reading of the local electric potential is measured by the tip which is traveling across the sample. In the case of a TE material contacted to a metallic electrode, the tip can point at the TE material and also at the electrodes, locally, which allows to measure the voltage drop across the interface between the two materials. This will be explained further below.

The tip is a heated microprobe, which is connected to a type T (Cu–CuNi) thermocouple. The tip is used to heat a small volume of the sample around it, as represented in Figure 28b. This induces a temperature gradient and therefore a thermovoltage is generated, which is how the local Seebeck coefficient can be measured. As represented in Figure 28b, two voltages U_1 and U_2 can be measured and expressed such as:

$$U_1 = -(\alpha_S - \alpha_{Cu})(T_2 - T_1) \quad (35)$$

$$U_2 = -(\alpha_S - \alpha_{CuNi})(T_2 - T_1) \quad (36)$$

where T_1 is the temperature measured at the junction between the heat sink (Cu block) and the sample, T_2 is the temperature of the tip and α_{Cu} and α_{CuNi} are respectively the known Seebeck coefficients of Cu and CuNi [144]. The sample Seebeck coefficient α_S can be obtained combining equations (35) and (36) such as:

$$\alpha_s = -\frac{U_1}{U_2 - U_1}(\alpha_{CuNi} - \alpha_{Cu}) + \alpha_{Cu} \quad (37)$$

Equations (35) to (37) assume a linear temperature dependence of the sample's, Cu and CuNi Seebeck coefficients. However, because this is rarely the case for the Seebeck coefficient of TE materials, there should therefore $T_2 - T_1 \leq 10$ K during the measurement of our samples [143]. In our case, $T_2 - T_1$ was usually set between 5 and 8 K. The empirically determined deviation of the measured Seebeck value in the PSM from a reference value is reported to lie between 10 and 15%, in dependence of the sample´s thermal properties [143]. This holds for materials that have room-temperature absolute Seebeck values between 50 and 300 µV/K, which is the case for our TE materials (around 90 µV/K for the p-type, around -110 µV/K for the n-type). For materials with low Seebeck coefficient such as high-temperature thermoelectrics or metals, the deviation can reach upto 40% or more.

b) Obtaining the electrical contact resistance

As the PSM simultaneously maps the Seebeck coefficient and the electrical potential, both parameters can be linked relatively to the position on the sample. A typical line-scan on the x axis (represented by the red dotted line in in Figure 28a) is shown in Figure 29a. The TE/electrode interfaces can be spotted by the change in the Seebeck coefficient between the TE material and the metallic electrode (α close to 0). The electrical contact resistivity at one interface $r_{c,PSM}$ can be estimated using the (measured) electric potential drop between the points where the transition in Seebeck coefficient happens:

$$r_{c,PSM} = \frac{\Delta V}{j_{PSM}} = \frac{|V_{el} - V_{TE}|}{j_{PSM}} \tag{38}$$

where j_{PSM} is the current density (obtained from the known electrical current I such as $j = I/A$ with A the cross-section of the sample). ΔV is the difference in voltage between the contacting electrode V_{el} and the TE material V_{TE} at the interface.

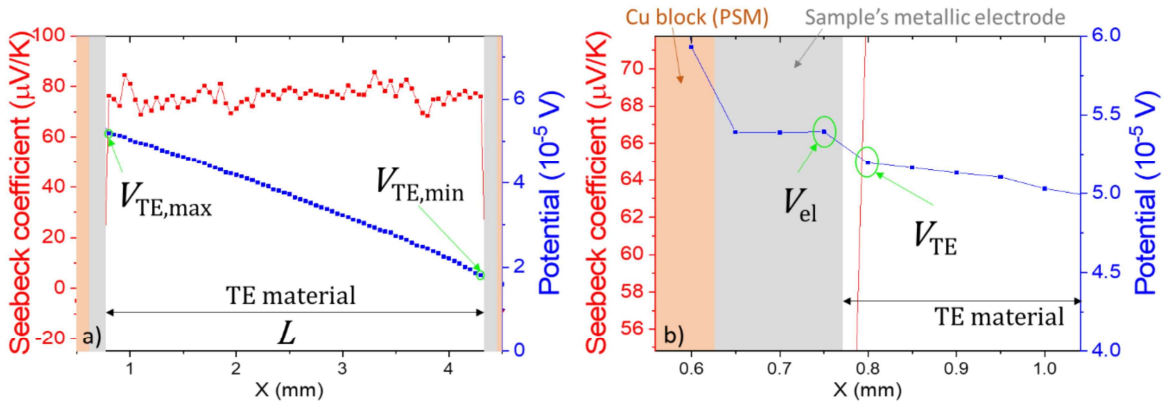

Figure 29 - a) exemplary PSM line-scan of a contacted p-type sample, adapted from [4], b) zoom-in of the left electrode/TE interface seen in a). $V_{TE,max}$ and $V_{TE,min}$ are the electrical potentials at both end points of the TE material of length L (used in equation (39)), V_{el} and V_{TE} are respectively the measured potentials in the electrode and in the TE material on the points at each side of the (here, left) interface (used in equation (38)). The interface is located at the transition between the Seebeck value of the electrode and the TE material. For the shown case $V_{TE} = V_{TE,max}$ whereas for the right electrode at X = 4.4 mm holds $V_{TE} = V_{TE,min}$.

This equation applies in the case where a homogeneous current density flows through the sample. In reality, the homogeneity of the current distribution cannot be guaranteed due to imperfections at the different interfaces. Inhomogeneity in the TE/electrode interface due to non-planar surfaces was already mentioned in section 1.3.2, but there are additional possible disturbances that will hinder the current flow, such as local contamination at those interfaces or partial delamination or an improper clamping of the sample between the Cu blocks of the PSM.

Therefore, the local current density in the sample differs in general from the mean current density deduced from the current value read by the PSM.

The PSM current is measured by evaluating the voltage drop over a 1 Ω precision shunt resistor (PBV, ISA-Plan® Isabellenhütte) which is connected in series with the Cu blocks of the sample holder.

The calculated current density j_{TE} that flows in the sample can be estimated using the known electrical resistivity of the TE material ρ_{TE} (measured with the HT-*S*-σ, see section 2.2.2), the TE pellet geometry and the potential drop along it $\Delta V_{\mathrm{TE}} = V_{\mathrm{TE,max}} - V_{\mathrm{TE,min}}$, such as:

$$j_{\mathrm{TE}} = \frac{(V_{\mathrm{TE,max}} - V_{\mathrm{TE,min}})}{L\rho_{\mathrm{TE}}} \tag{39}$$

where L is the TE length along the *x* axis, represented in Figure 29a. $V_{\mathrm{TE,max}}$ and $V_{\mathrm{TE,min}}$ are the electrical potentials at both ends of the linear profile, as represented in Figure 29b.

Then, the corresponding contact resistance can be obtained such as:

$$r_{\mathrm{c,TE}} = \frac{|V_{\mathrm{el}} - V_{\mathrm{TE}}|}{j_{\mathrm{TE}}} \tag{40}$$

A significant difference between j_{TE} and j_{PSM} will obviously lead to a proportional difference between $r_{\mathrm{c,TE}}$ and $r_{\mathrm{c,PSM}}$, which complicates the estimation of the true value of the contact resistance. This difference can originate from poor sample clamping or impurities, cracks, pores, etc. in the TE material or in the contact area, which leads to an inhomogeneous current distribution. As the TE electrical conductivity at room temperature is known, and j_{TE} is obtained considering the potential slope inside the TE material which allows to take local irregularities on the current path into account, it is usually assumed that $r_{\mathrm{c,TE}}$ gives a more precise value of the contact resistivity.

If both values are close (similar order of magnitude), a homogeneous current distribution across the sample can be assumed and the result can be assumed to be without severe systematic error.

As shown in section 1.3.2, a value of $r_{\mathrm{c}} \leq 10$ μΩcm² is targeted for our samples. The PSM is therefore used in a first step to optimize the contacting process by monitoring the influence of several parameters on the contact resistance of the samples (see sections 3 and 4). In a second step, after the contacting process has been validated and implemented, the PSM is used prior to the TEG assembly to verify the legs contact quality and check for the presence of cracks, which

are detected by a sudden drop in potential in the TE material as seen in Figure 30, and increase the inner resistance of the TEG.

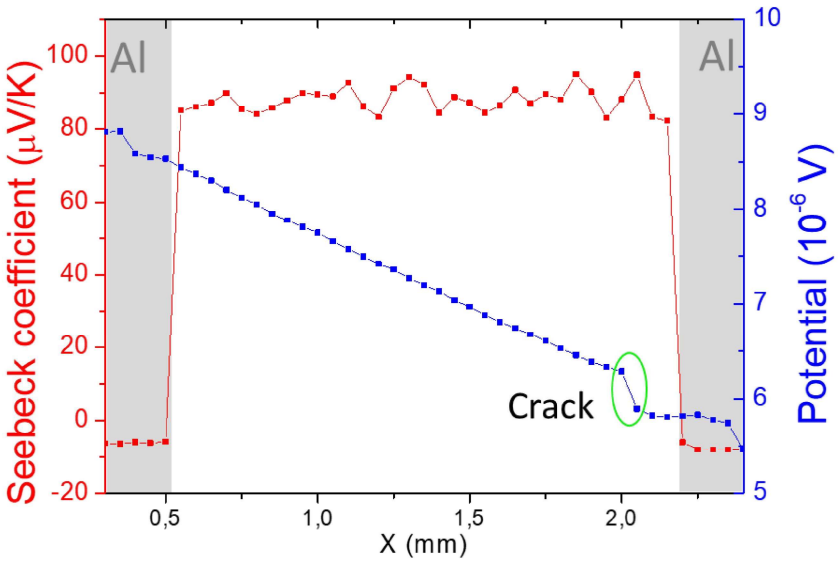

Figure 30 - PSM line scan featuring a drop in potential due to a crack in the TE material. Image adapted from [4].

2.2.4. TEGMA

a) General description

After assembly, the TEG module performance is measured using an in-house built Thermoelectric Generator Measurement Apparatus (TEGMA) reported in [145-147]. A picture of the device with indication of the components of the measuring section is shown in Figure 31. From top to bottom, the setup is made of a heater, a geometry adaptor (made of oxygen-free copper), the measured TEG module, a heat flow meter (HFM, in our case made of nickel LC992) and a cooling plate (oxygen-free copper). The cross-sections of the geometry adaptor and the HFM need to be similar to the TEG module geometry, not smaller, to ensure good heat distribution and not much larger, to reduce possible lateral radiative thermal losses. A large difference would also lead to constriction resistances and therefore a deviation from the linear temperature profile which is assumed in the heat flow measurement (see below). To ensure good heat transfer along the measuring column, graphite foils (Dr. Fritsch Sondermaschinen GmbH, 200 µm) are inserted at the interfaces. Three thermocouples (type N) are used to monitor the temperature in the geometry adaptor and are located at a distance of 1, 3, 5 mm from the TEG. Five thermocouples (type N) are spaced along the HFM at 10, 15, 20, 25, 30 mm from the TEG module-side interface.

TEGMA module characterization is conducted under vacuum to avoid convective thermal losses. Usually, the chamber is filled with wool-like thermal damming material to reduce lateral

thermal losses due to radiation, however internal tests previously showed that this was unnecessary for cold side temperatures below 50 °C (for our measurements, T_c = 25 °C). Those tests were nevertheless done on larger size TEG modules (and larger heat flow) than the ones studied in this work, for which those radiative loss may still be occurring. This will be further discussed in sections 5 and 6.1.

The measuring section is mechanically loaded by a linear actuator, which provides an axial pressure to the column to reduce thermal contact resistances between the stacked components. The force is transmitted by a spring package located underneath the cooling plate. In this work, a pressure of 2-5 MPa was applied to the TEG in the TEGMA, which can influence the thermal resistances between the components of the measurement column.

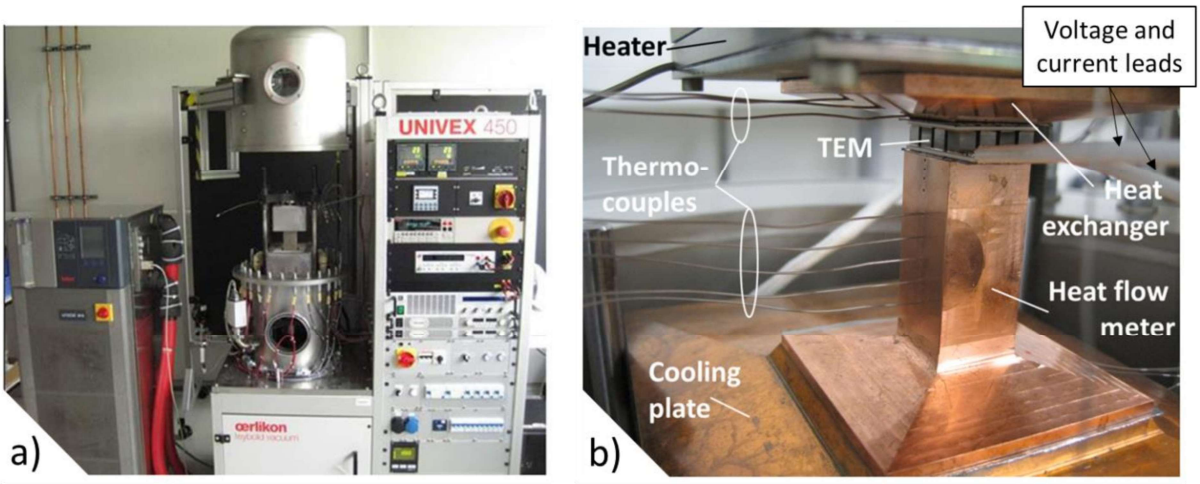

Figure 31 - a) Picture of the TEGMA device, taken from [147], b) indication of the elements of the measuring column, adapted from [146].

The full TEG measurement loop is represented in Figure 32. It shows that for fixed pressure and atmospheres (like in this thesis), each temperature step starts with a stabilization period, followed by open-loop measurements of several parameters. An electrical current is then applied though the circuit and various parameters are measured step by step for increasing current values. Finally, the next temperature conditions can be set and the loop starts again.

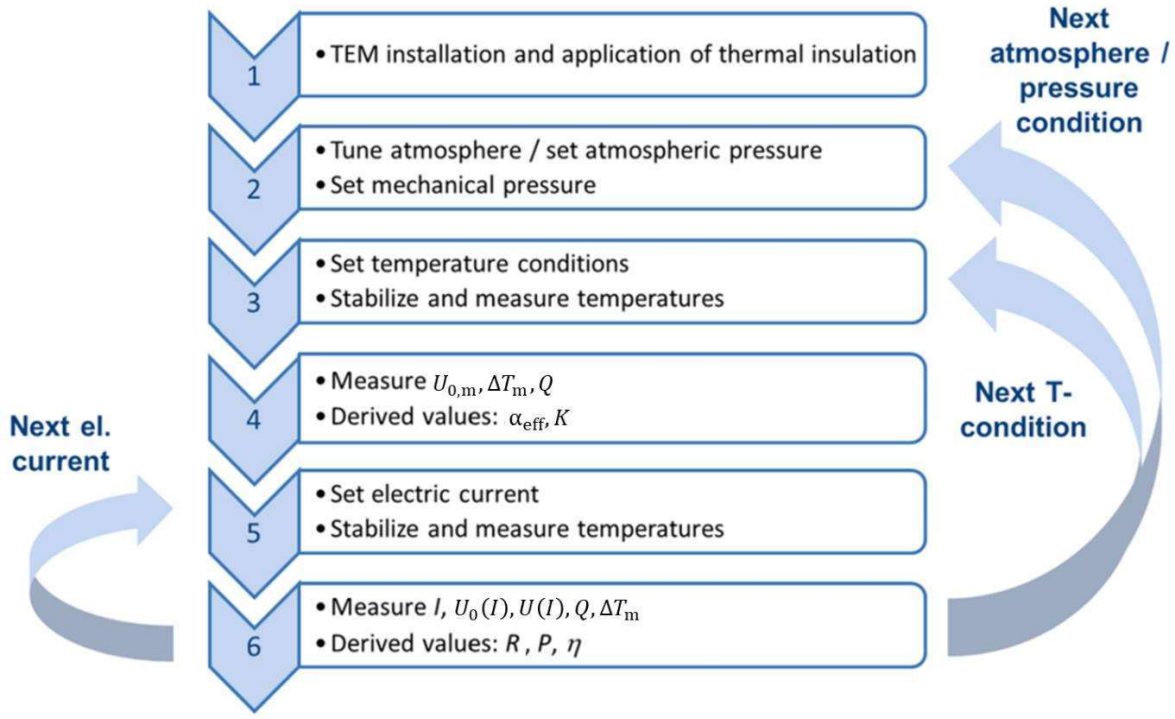

Figure 32 - Process chart for TEM characterization in the TEGMA: open circuit voltage ($U_{0,m}$), heat flow (Q), temperature difference at the hot/cold blocks (ΔT_m), effective Seebeck coefficient (α_{eff}), thermal conductance (K), electric current (I), terminal voltage (U), electric resistance (R), electric power output (P), and efficiency (η). Adapted from [145].

b) Electrical measurement

The electrical characterization is reported in [146]. A DC electronic load (EA-EL 9400–50, Elektro-Automatic) is connected to two leads at the terminals of the TEG module for adjustment of the load current I. The TEG is connected to the electric measurement circuit in a four-point scheme: close to the leads determining I, two additional sensor cables are soldered and measure the terminal voltage U. This allows to avoid taking the electric contact resistances between the supplying leads and the TEG module terminals into account in the measurement of U.

The open loop voltage $U_{0,\mathrm{m}}$ is measured after temperature stabilization at the hot and cold side of the TEG. From now on, the "m" subscript will refer to measured values (apart from T_{m} which is mean temperature). The open-circuit voltages of each single leg add up to form the module open-circuit voltage. It follows that $U_{0,\mathrm{m}}$ is defined using the number of leg pairs N within the module, the effective Seebeck coefficient per thermocouple α_{eff} and the temperature difference at the TE legs ΔT_{TE}, such as:

$$U_{0,\mathrm{m}} = \mathrm{N} \cdot \alpha_{\mathrm{eff}} \cdot \Delta T_{\mathrm{TE}} \tag{41}$$

Then, an electric direct current (DC) is applied through the TEM. The applied current range is typically chosen from open loop ($I = 0$ A) up to the short circuit current I_{SC}, which depends on

the temperature conditions and is characteristic for each TEM module (material properties and module geometry). The current I and the terminal voltage U are measured twenty times at every current set point in order to calculate measurement uncertainties and mean values and therefore average out the impact of statistical signal noise.

The resulting *I-U* behavior gives access to the internal electric resistance R of the module, since $U = U_0 - RI$. However, for $I \neq 0$, the transported Peltier heat effectively decreases the temperature difference across the TEG, which affects the value of $U_{0,\mathrm{m}}$. This change will be referred to in this thesis by "the Peltier shift". Neglecting the Peltier shift by a direct evaluation of the slope $\Delta V/\Delta I$ would lead to an overestimation of R for each fixed heater and cooler temperatures.

A Rapid-Steady-State (RSS) method is used in order to account for this change: the current is turned off and shortly on again, so that the value of $U_{0,\mathrm{m}}$ can be obtained for the temperature conditions corresponding to $I \neq 0$. Although counter-intuitive, such open-loop voltage will be labelled $U_{0,\mathrm{m}}(I)$.

R is therefore evaluated at different electrical currents I_1 and I_2 from differences between steady state terminal voltages U_1 and U_2 and corresponding values of the reduced open loop voltage $U_{0,\mathrm{m}}(I_1)$ and $U_{0,\mathrm{m}}(I_2)$:

$$R = \frac{\Delta U_1 - \Delta U_2}{I_1 - I_2} = \frac{U_{0,\mathrm{m}}(I_1) - U_1 - U_{0,\mathrm{m}}(I_2) + U_2}{I_1 - I_2} \tag{42}$$

The procedure is described in detail in [145].

A single and universal uncertainty value cannot be expressed for R, due to its dependence on voltage and current ranges, which differ with module type and application temperatures. In [146], the uncertainty was found to vary between 0.96% and 2.28% for values of R between 22.74 Ω and 0.74 Ω, respectively. Those values were obtained for commercial Bi_2Te_3-based TEM modules with total surfaces ranging between 40 × 40 mm² and 54 × 54 mm², for T_h = 200–225 °C and T_c = 50 °C.

The uncertainty of open loop voltage measurements has not been isolated so far. However, since it was needed for expression of the uncertainty of R, it is documented in the Supplementary Information of [146]. It lies between 0.06% and 0.09% for $U_{0,\mathrm{m}}$ values between 7 V and 25 V, respectively, for TEM and conditions similar to those for which the uncertainties of R_i were determined.

The TE modules presented in this thesis typically show values of $R \approx 0.012 - 0.020\ \Omega$ and $U_{0,m} \approx 0.08–0.20$ V, which lies quite far from the studied range, and the type of module is very different (TE material type, geometry, application temperature). We are exploring new grounds for which measurement uncertainties therefore still need to be established.

c) Heat flow determination

Heat flow measurement for TEM operation has remained challenging to date due to lack of guidelines and standards for testing methods. Consequently, it is difficult to obtain reliable experimental TEM conversion efficiency. An international round robin campaign was led among twelve laboratories and showed deviations of approximately 20% for all TE module properties [148]. To overcome this challenge, low uncertainty characterization methods and specific TEM reference samples have to be developed and standardized.

Generally, heat flow can be measurement with two different techniques: the absolute or the reference principles, using a guarded heater (GHP) or a non-shielded heater, respectively. The development, operation and maintenance of absolute measurement principles are usually more expensive and need long methodical experience. They also require longer stabilization times to reach thermal equilibrium. Therefore, reference measurement techniques are generally preferred as they are easier to operate, provided that repeatability and traceability of the measurement is still assessed. In this work, the reference principle was used such as shown in Figure 33, with a HFM only at the cold side.

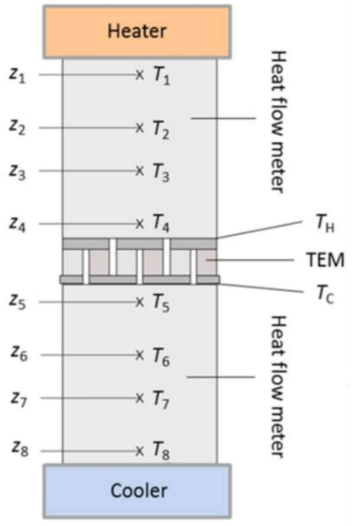

Figure 33 - Schematic of the measuring section for the reference principle of heat flow measurement. One or two heat flow meters can be used. They need to feature several temperature sensors, used to determine the temperature difference along the HFM and obtain the heat flow. Taken from [145].

The hot side temperature T_h and the cold side temperature T_c at the TEG can be set and monitored to ensure a measurement of the TEG in the desired temperature conditions. These temperatures can either be directly measured by temperature sensors placed in the direct vicinity of the TEG, or obtained by a linear extrapolation from localized temperature sensors (labelled *Z*i in Figure 33) in in the direction of heat flow within the HFM.

The one-dimensional Fourier's law states that the heat flow Q is directly proportional to the temperature gradient within the heat flow meter ∇T_{HFM}, such as:

$$Q = -A_{\mathrm{HFM}} \cdot \kappa_{\mathrm{HFM}} \cdot \nabla T_{\mathrm{HFM}} = -A_{\mathrm{HFM}} \cdot \kappa_{\mathrm{HFM}} \cdot \frac{\Delta T_{\mathrm{HFM}}}{L_{\mathrm{HFM}}} \tag{43}$$

where κ_{HFM}, A_{HFM} and L_{HFM} are the thermal conductivity, the cross-sectional area and the maximum distance between the thermocouples attached to the HFM block, respectively. ΔT_{HFM} is measured with the temperature sensors shown in Figure 33. Equation (43) assumes a constant $\nabla T_{\mathrm{HFM}} = \frac{dT_{\mathrm{HFM}}}{dx}$ and a mean value for the thermal conductivity of the HFM material. This assumption is valid if the HFM is made of a material whose thermal conductivity has a relatively flat temperature dependence in the relevant temperature range. In this thesis, the HFM was made of Ni, which is not as thermally conductive as Cu, but since the temperature difference along the block was small (<10 K, due to the small size of our TEG), assuming a mean thermal conductivity over the respective temperature interval is sufficient for good heat flow measurements.

With the reference principle, the heat flow can be measured both at the hot and cold side of the TEG, or on one side only. Measuring the heat flow on both sides allows for a verification of the measurement uncertainty, since it can be verified that $Q_{\mathrm{out}} = Q_{\mathrm{in}} + P$, where $Q_{\mathrm{out}} = Q_{\mathrm{HFM,cold}}$ and $Q_{\mathrm{in}} = Q_{\mathrm{HFM,hot}}$. This equality would not be verified in case of lateral heat losses (e.g. by radiation or convection). In this work, the heat flow was measured on the cold side only, as the temperature distribution in a small-cross-sectioned HFM is less affected by radiation compared to the hot side.

The determination of the heat flow measurement uncertainty was made on a certified reference material for the thermal conductivity from the U.K. National Physical Laboratory (Inconel 600, NPL 2I09), with installation conditions similar to TEG measurement conditions. It was found that the relative uncertainty lies between 10 and 13% [145].

2.3. Employing the CPM for TEG measurement analysis

In order to check for the reliability of the measurement and search for directions for performance improvement, calculations were made to compare theoretical values to TEG measurement results. The CPM, which was presented in section 1.2.2, was chosen as modelling method for the TEG measurement analysis for its simplicity. Its main assumption is to consider constant properties in the TE legs. Traditionally, the values were taken at the average temperature (between the hot and cold sides of the legs). This method has been shown to significantly overestimate zT and efficiency predictions, to an extent depending on the material type [149]. As specified in section 1.2.2, the temperature average $\bar{X}$ of the property $X(T)$ between T_h and T_c, is obtained using $\bar{X} = \frac{1}{\Delta T}\int_{T_\mathrm{c}}^{T_\mathrm{h}} X(T)\mathrm{d}T$ for α, ρ and κ^{-1}.

In section 1.2.2, CPM was presented for an exemplary single TE leg. However, a real TEG is composed of multiple leg pairs, which are made of n- and p-type materials with differing, asymmetric TE properties and possibly different geometries. The adaptation of thermoelectric quantities from a single leg case to multiple leg pairs is summarized in Table 6.

Table 6 - Thermoelectric quantities used in performance estimation of TEG modules with N pairs (reproduced from [12]).

Entity	**Single leg**	**pn couple**	**TEG**
Seebeck coefficient (α)	$\alpha_\mathrm{p}, \alpha_\mathrm{n}$	$\alpha_\mathrm{pn} = \alpha_\mathrm{p} + \lvert\alpha_\mathrm{n}\rvert = \alpha_\mathrm{p} - \alpha_\mathrm{n}$	$N \cdot \alpha_\mathrm{pn}$
Electrical resistance (R)	$R_\mathrm{p}, R_\mathrm{n}$	$R_\mathrm{pn} = R_\mathrm{p} + R_\mathrm{n}$	$N \cdot R_\mathrm{pn}$
Thermal conductance (K)	$K_\mathrm{p}, K_\mathrm{n}$	$K_\mathrm{pn} = K_\mathrm{p} + K_\mathrm{n}$	$N \cdot K_\mathrm{pn}$
Voltage	$U_\mathrm{p}, U_\mathrm{n}$	$U_\mathrm{pn} = U_\mathrm{p} + U_\mathrm{n}$	$N \cdot U_\mathrm{pn}$
Current	$I_\mathrm{p} = I_\mathrm{n}$	$I_\mathrm{pn} = I_\mathrm{p} = I_\mathrm{n}$	I_pn
Heat flow	$Q_\mathrm{p}, Q_\mathrm{n}$	$Q_\mathrm{pn} = Q_\mathrm{p} + Q_n$	$N \cdot Q_\mathrm{pn}$
Electrical power output	$P_\mathrm{p}, P_\mathrm{n}$	$P_\mathrm{pn} = P_\mathrm{p} + P_\mathrm{n}$	$N \cdot P_\mathrm{pn}$
Efficiency	$\eta_\mathrm{p}, \eta_\mathrm{n}$	$\eta_\mathrm{pn} = \frac{P_\mathrm{pn}}{Q_\mathrm{pn}}$	η_pn

2.3.1. Determining the temperatures at the TE legs

One important aspect which was not mentioned in section 1.2.2 is the difference between ΔT_m, ΔT_TEG and ΔT_TE, which are respectively the temperature difference applied between the edges of the heating and cooling blocks (measured by the TEGMA), the temperature difference applied to the TEG and the temperature difference at the TE legs. Those different temperatures are represented along the measuring column in Figure 34a. It can be seen that there are

temperature drops along the different coupling layers (graphite foil, ceramic plate, Cu bridges) and at each of their interfaces (contact resistances).

The difference between ΔT_{TEG} and ΔT_{TE} depends on the design of the module (substrate type), while the difference between ΔT_{m} and ΔT_{TEG} would depend on the mode of thermal coupling in the individual application case. The difference between ΔT_{m} and ΔT_{TE} on each side of the TEG are called parasitic losses, as the temperature lost "outside" of the TE legs does not contribute to power generation.

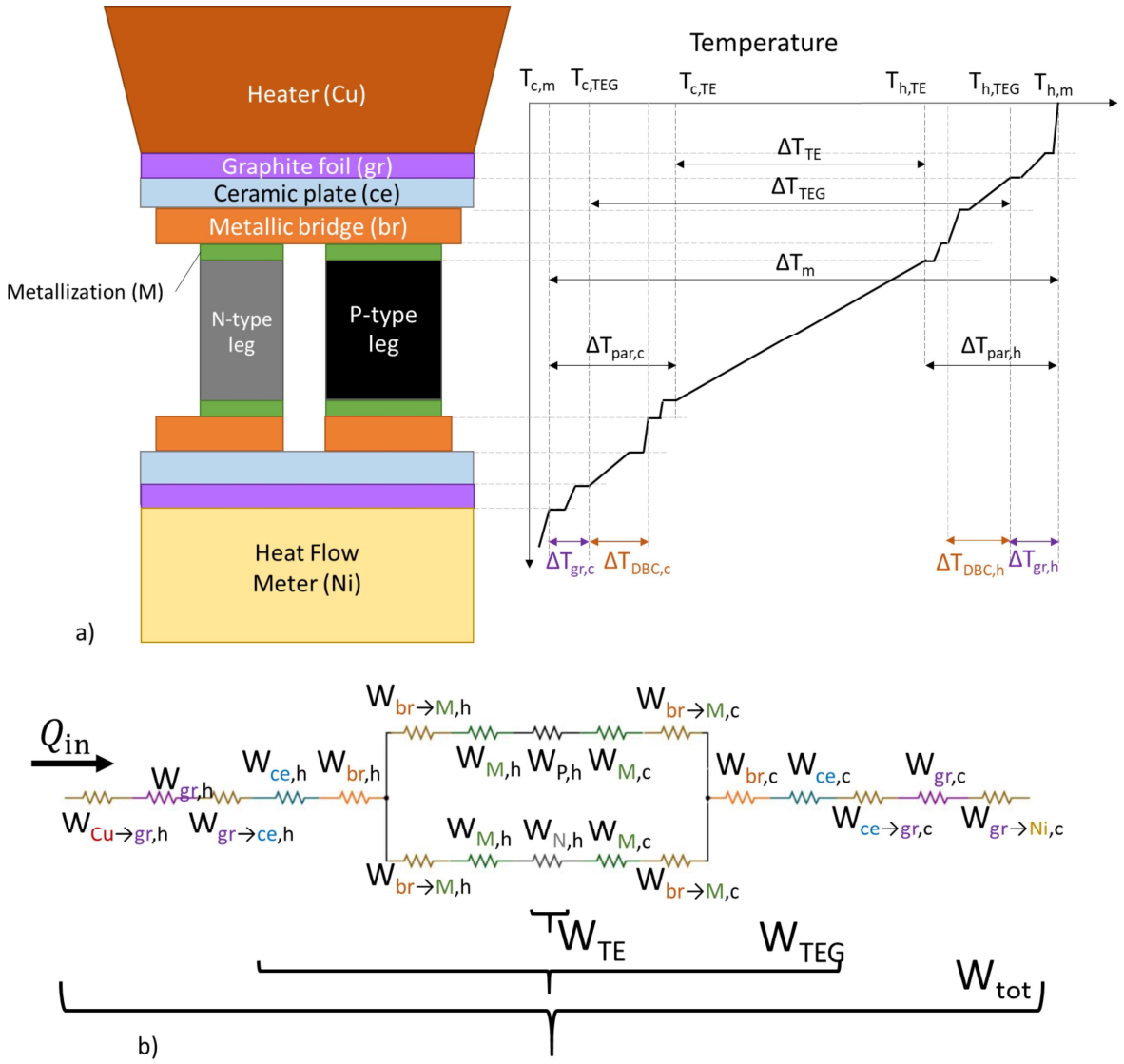

Figure 34 – a) Schematics of the elements of the measurement column surrounding the TEG and the corresponding temperature profile. The copper bridges on the outside of the TEG (between the ceramic plate and the graphite foil) are not represented. The dimensions of the components are arbitrary and the temperature drops are schematic and qualitative. $T_{c,m}$, $T_{h,m}$ – measured cold and hot side temperatures at the heat flow meter and the heater close the TEG, respectively; $T_{h,TEG}$, $T_{c,TEG}$ – temperatures at the hot and cold side of the TEG, respectively; $T_{h,TE}$, $T_{c,TE}$ – temperatures at the hot and cold side of the TE legs, respectively. Adapted from SI of [6]; b) equivalent thermal circuit of the measurement column, with the thermal resistances of each layer (W_X, (X) being labelled for each layer in a)) and the thermal contact resistances between them ($W_{X\rightarrow Y}$, contact resistance from material X to material Y). The contact resistances between the ceramic and the metallic bridges of the DBC, as well as the contact resistances between the TE materials and the metallizations are neglected in this figure, although

they do contribute to the total thermal resistance as represented in a). The c and h subscripts designate cold and hot sides, respectively.

The equivalent thermal circuit of the measurement column is represented in Figure 34b. There also are contact resistances between the ceramic plate and the direct bonded Cu bridges, as well as between the Cu bridges and the legs metallizations, but they were not included in the figure, as they are supposed to be very low and are usually neglected in modelling.

a) At open-loop conditions

The most realistic calculations can be made using the temperatures at the TE legs. They can be determined quite accurately with the measured open-loop voltage $U_{0,\mathrm{m}}$ if the TE properties of the leg are well-known. $\Delta T_{\mathrm{TE},0}$ (at open-loop) is obtained using:

$$\Delta T_{\mathrm{TE},0} = \frac{U_{0,\mathrm{m}}}{N(\alpha_{\mathrm{p}} - \alpha_{\mathrm{n}})} \tag{44}$$

The temperatures at the hot and cold side of the TE legs can then be obtained assuming a symmetrical temperature loss across graphite foils and DBC substrates such as $T_{\mathrm{h,TE},0} = T_{\mathrm{h,m},0} - 0.5(\Delta T_{\mathrm{m},0} - \Delta T_{\mathrm{TE},0})$ and $T_{\mathrm{c,TE},0} = T_{\mathrm{c,m},0} + 0.5(\Delta T_{\mathrm{m},0} - \Delta T_{\mathrm{TE},0})$, where $T_{\mathrm{c,m},0}$ and $T_{\mathrm{h,m},0}$ are the measured cold and hot side temperatures at the interfaces between the TEG and the heat flow meter and the heater (respectively), at open loop.

This equation assumes that the temperature difference at the n-type and p-type legs is the same, which would be incorrect in case of quite different thermal conductivities of the materials. This is also a 1D model while the measurement is partly affected by 3D effects.

When applying equation (44), the Seebeck coefficient averages $\alpha_{\mathrm{p}}, \alpha_{\mathrm{n}}$ are calculated in a first iteration assuming $T_{\mathrm{h,TE},0} \approx T_{\mathrm{h,m},0}$ and $T_{\mathrm{c,TE},0} \approx T_{\mathrm{c,m},0}$, which leads to some deviation in the obtained $\Delta T_{\mathrm{TE},0}$, $T_{\mathrm{c,TE},0}$ and $T_{\mathrm{h,TE},0}$. However, equation (44) is then reapplied in a second iteration with new $\alpha_{\mathrm{p}}, \alpha_{\mathrm{n}}$ average values corresponding to the temperature conditions at the TE legs obtained in the first iteration. The obtained temperatures converge in only two iterations due to the weak slope of $\alpha(T)$. An example of temperatures before and after iteration and the corresponding open-circuit voltages are reported in Table 7 and Figure 35, respectively.

Table 7 – Measured temperatures at the heater and HFM and calculated temperatures at the TE legs at open loop, for a module identical to the one reported in [6].

Input data		**First iteration**		**Second iteration**	
$T_{\mathrm{h,m,0}}$ (°C)	$T_{\mathrm{c,m,0}}$ (°C)	$T_{\mathrm{h,TE,0}}$ (°C)	$T_{c,\mathrm{TE,0}}$ (°C)	$T_{\mathrm{h,TE,0}}$ (°C)	$T_{c,\mathrm{TE,0}}$ (°C)
400.1	24.4	379.8	44.6	379.0	45.5
350.6	24.5	335.3	39.7	335.0	40.1
299.7	26.5	289.2	37.0	289.2	37.0
250.4	24.5	243.0	32.0	242.9	32.0
200.8	24.5	196.4	29.0	196.4	29.0

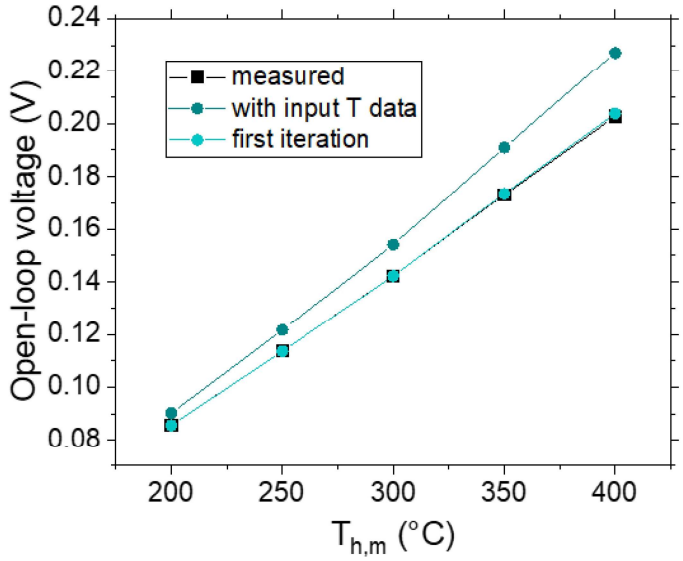

Figure 35 - Measured and calculated open-circuit voltage after two iterations, for the module reported in [6].

An obvious error in this method arises from the assumed symmetrical distribution of the parasitic temperature drop between hot and cold sides to obtain values of $T_{\mathrm{c,TE}}$ and $T_{\mathrm{h,TE}}$. In reality, the thermal resistance of the graphite and ceramic plates are temperature-dependent, those terms are therefore not symmetric, even if the physical arrangement was perfectly symmetrical (i.e. $W_{\mathrm{ce,h}} \neq W_{\mathrm{ce,c}}$ in Figure 34b). These materials are quite well-known and the varying wit temperature thermal resistance can however be estimated, as will be shown in the SI of section 5 ([6]). However, the thermal contact resistance between each layer are also temperature-dependent, but this dependence is unknown, as it also depends on the quality of the junction (surface cleanness, roughness, etc.) and the materials involved. Therefore, the overall parasitic thermal resistances on the hot and cold sides cannot be reliably estimated. Calculations with other heat loss distributions and comparison to the symmetry assumption are shown in the SI of section 5 ([6]).

This method is also sensitive to the estimates of the legs' TE properties. The experimental data used for the CPM calculations is obtained from as-sintered pellets, however, some material change can occur during the contacting, module assembly and TEGMA measurement, especially in the n-type material. The impact of change in TE properties and the computational adjustments to accommodate for it will be discussed in section 6.1.

$\Delta T_{\mathrm{TE},0}$ can be obtained via two other methods: calculating the temperature drop through the coupling considering each layer's thermal properties, and assuming the constancy of the open-circuit heat flow along the measurement column. Those methods are presented in the SI of section 5 ([6]).

b) At maximum power ($I = I_{\mathrm{opt}}$)

Due to the influence of the Peltier heat, the temperature difference at the TE legs decreases when current is flowing and most TEG parameters are relevant for $I \neq 0$. The temperatures at the TE legs $T_{\mathrm{h,TE,opt}}$ and $T_{\mathrm{c,TE,opt}}$ are determined for the current value at maximum power I_{opt} and are used to calculate other parameters, including maximum efficiency. Indeed, there is usually little difference between $I_{\mathrm{opt},\eta}$ and I_{opt} (the TEG presented in section 5 showed 1 to 7% difference), therefore, the heat flow and temperatures at the TE legs will be similar for both current conditions.

Considering $\Delta T_{\mathrm{par}} = \Delta T_{\mathrm{par,c}} + \Delta T_{\mathrm{par,h}}$, we define $\Delta T_{\mathrm{par},0} = \Delta T_{\mathrm{par}}(I = 0)$ and $\Delta T_{\mathrm{par,opt}} = \Delta T_{\mathrm{par}}(I = I_{\mathrm{opt}})$. Assuming that the thermal resistance of the parasitic layers does not vary with current, ΔT_{par} varies proportionally to the heat flow only, therefore:

$$\frac{Q_{\mathrm{opt,m}}}{Q_{0,\mathrm{m}}} = \frac{\Delta T_{\mathrm{par,opt}}}{\Delta T_{\mathrm{par},0}} = \frac{\Delta T_{\mathrm{m,opt}} - \Delta T_{\mathrm{TE,opt}}}{\Delta T_{\mathrm{par},0}} \tag{45}$$

where Q_{m} is the measured incident heat flow and "0" and "opt" subscripts respectively refer to parameters at open-loop conditions and at optimum current for maximum power. $\Delta T_{\mathrm{par},0}$ is known such as $\Delta T_{\mathrm{par},0} = \Delta T_{\mathrm{m},0} - \Delta T_{\mathrm{TE},0}$. From equation (45), $\Delta T_{\mathrm{TE,opt}}$ is obtained and corresponding $T_{\mathrm{h,TE,opt}}$ and $T_{\mathrm{c,TE,opt}}$ can be determined (assuming symmetric losses).Equation (45) holds if the heat flow is constant along the column. This is not true in case of materials with decent TE properties and $I \neq 0$, in which case a smaller temperature drop should occur at the cold side compared to the hot side since $Q_{\mathrm{in,opt}} > Q_{\mathrm{out,opt}}$. However, since the measured

efficiency of our prototypes remains quite low (<5 %), we have $Q_{\mathrm{in,opt}} \approx Q_{\mathrm{out,opt}}$ and the symmetry assumption is acceptable.

As indicated in section 2.2.4, the measured incident heat flows are determined such as $Q_{\mathrm{m}} = Q_{\mathrm{out,m}} + P_{\mathrm{m}}$.

2.3.2. Calculating TEG performance

a) Maximum power and efficiency

Adapting equations (14) and (20) (section 1.2.2), the maximum power output and maximum conversion efficiency for a N-pair TEG are given as follows:

$$P_{\max} = N\left(P_{\mathrm{n}} + P_{\mathrm{p}}\right) = \frac{N\left(\left(\alpha_{\mathrm{p}} - \alpha_{\mathrm{n}}\right)\Delta T_{\mathrm{TE,opt}}\right)^2}{2R} \tag{46}$$

$$\eta_{\max} = \frac{T_{\mathrm{h,TE,opt}} - T_{\mathrm{c,TE,opt}}}{T_{\mathrm{h,TE,opt}}} \; \frac{\sqrt{1 + ZT_{\mathrm{m}}} - 1}{\frac{T_{\mathrm{c,TE,opt}}}{T_{\mathrm{h,TE,opt}}} + \sqrt{1 + ZT_{\mathrm{m}}}} \tag{47}$$

where T_{m} is the average of $T_{\mathrm{c,TE,opt}}$ and $T_{\mathrm{h,TE,opt}}$. ZT_{m} is the device figure of merit with:

$$Z = \frac{N^2\left(\alpha_{\mathrm{p}} - \alpha_{\mathrm{n}}\right)^2}{K_{\mathrm{TE}} R} \tag{48}$$

where R is the inner electrical resistance and K_{TE} the thermal conductance of the TE legs such as:

$$R = R_{\mathrm{TE}} + R_{\mathrm{c}} = N\left[\frac{\rho_{\mathrm{p}} L}{A_{\mathrm{p}}} + \frac{\rho_{\mathrm{n}} L}{A_{\mathrm{n}}} + 2r_{\mathrm{c}}\left(\frac{1}{A_{\mathrm{p}}} + \frac{1}{A_{\mathrm{n}}}\right)\right] \tag{49}$$

$$K_{\mathrm{TE}} = N\left(\frac{\kappa_{\mathrm{p}} A_{\mathrm{p}}}{L} + \frac{\kappa_{\mathrm{n}} A_{\mathrm{n}}}{L}\right) \tag{50}$$

where R_{TE} is the total electrical resistance of the TE legs and R_{c} the total electrical contact resistance. Equation (49) neglects the resistance of the metallic layers (Al metallization, Cu metallization, Cu bridges) and the contact resistances between them, therefore R_{c} is assumed to mainly originate from the Al/TE interface. All averaged TE properties are calculated considering $T_{\mathrm{h,TE,opt}}$ and $T_{\mathrm{c,TE,opt}}$.

It is important to note that equation (48) overestimates Z by underestimating K, as only the conductance of the TE materials is considered, while in reality there is thermal bypass from the hot side to the cold side of the TEG. Here, the thermal bypass is neglected as the measurement temperature remains relatively low (≤400 °C).

For the open-loop heat flow, Q_0, equation (50) is applied for $I = 0$, using $\Delta T_{\mathrm{TE},0}$ and $T_{\mathrm{h,TE}}(I = 0)$, and K_{TE} is calculated for open-loop temperature conditions.

b) Heat flow

Within CPM the incident heat flow at maximum power Q_{opt} is calculated using the following equations:

$$Q_{\mathrm{opt}} = K_{\mathrm{TE}}\Delta T_{\mathrm{TE,opt}} + I \cdot N \cdot \left(\alpha_{\mathrm{p}} - \alpha_{\mathrm{n}}\right)T_{\mathrm{h,TE,opt}} - \frac{1}{2}I^2 R \tag{51}$$

$$I_{\mathrm{opt}} = \frac{N(\alpha_{\mathrm{p}} - \alpha_{\mathrm{n}})\Delta T_{\mathrm{TE,opt}}}{2R} \tag{52}$$

3. Chapter 3 (Paper 1): Aluminum as promising electrode for $Mg_2(Si,Sn)$-based thermoelectric devices

In this paper/chapter, we address the first step in the development of a TEG, following TE material optimization: electrode selection. Previously, moderately satisfying electrodes were reported in literature, the best candidate being Ag which showed low contact resistances but altered the properties of the n-type material [1, 2], while other tested electrodes generally led to cracking or delamination [2, 3].

In this paper, we test aluminum as an electrode for $Mg_2(Si,Sn)$, which is attractive due to its CTE close to the TE material's, its melting point which is compatible with the contacting process and its ductility. We find that Al is a promising electrode for $Mg_2(Si,Sn)$ for its mechanical and chemical stability with the TE material. No cracking nor delamination occurs in contrast to previously reported electrodes, which indicates favorable thermomechanical compatibility and contact resistivities below the set threshold of 10 $\mu\Omega cm^2$ are measured, while no change in the TE materials are observed. The interface directly after contacting is free of visible reacted areas, which start to grow with annealing without increasing the contact resistivity.

In this thesis, **the published version of the paper, following the journal´s template**, is provided. This work was published on 16th March 2021 in Materials Today Energy journal, Volume 21, page 100718.

Reference: J. Camut, N.H. Pham, D.Y. Nhi Truong, G. Castillo-Hernandez, N. Farahi, M. Yasseri, E. Mueller, J. de Boor, *Aluminum as promising electrode for Mg2(Si,Sn)-based thermoelectric devices*, Materials Today Energy, 2021, Volume 21, p. 100718, https://doi.org/10.1016/j.mtener.2021.100718.

Materials Today Energy 21 (2021) 100718

Contents lists available at ScienceDirect

Materials Today Energy

journal homepage: www.journals.elsevier.com/materials-today-energy/

Aluminum as promising electrode for $Mg_2(Si,Sn)$-based thermoelectric devices

J. Camut [a, *, e], N.H. Pham [a, b, e], D.Y. Nhi Truong [a], G. Castillo-Hernandez [a, c], N. Farahi [a], M. Yasseri [a], E. Mueller [a, c], J. de Boor [a, d, **]

[a] Institute of Materials Research, German Aerospace Center (DLR), Germany
[b] Ångström Laboratory, Uppsala University, Sweden
[c] Institute of Inorganic and Analytical Chemistry, Justus Liebig University of Giessen, Giessen, Germany
[d] Institute of Technology for Nanostructures (NST), Faculty of Engineering, University of Duisburg-Essen, Germany

ARTICLE INFO

Article history:
Received 30 November 2020
Received in revised form
26 February 2021
Accepted 11 March 2021
Available online 16 March 2021

Keywords:
Contacting
Thermoelectrics
Semiconductors
Thermoelectric generators
Electrode selection
Contact resistance

ABSTRACT

The solid solutions of magnesium silicide and magnesium stannide $Mg_2(Si,Sn)$ are high-performance thermoelectric (TE) materials with the advantage of being composed of light, cheap, and abundant elements. Therefore, they are especially attractive for the conversion of remnant heat into electricity in fields like the automotive sector or the aerospace industry. The optimization of $Mg_2(Si,Sn)$-based thermoelectric generators requires establishing a suitable electrode to ensure unhindered conduction of the electrical current through the module. We have tested aluminum for such applications and developed a technological process for joining. The obtained functionalized TE legs showed electrical contact resistances below 10 $\mu\Omega cm^2$ for both p- and n-type materials and the values are preserved or even lowered with annealing. The p-type material is found to be stable and in the n-type, there is no indication for a charge carrier compensation due to the electrode, as was previously reported e.g. for Cu and Ag. Comparison with other reported electrodes shows that aluminum is so far the most suitable electrode for an $Mg_2(Si,Sn)$-based module.

1. Introduction

As the need for green energy sources is increasing, thermoelectric generators (TEG) are of significant interest in the field of renewable energy due to their ability to convert waste heat into useable electricity. In many industries, such as aerospace and automotive, a large proportion of the energy is wasted as heat, as it cannot be directly reused in a closed-loop [1,2].

A TEG consists of p- and n-type thermoelectric (TE) elements, referred to as legs, which are arranged electrically in series and thermally in parallel using metal-bonded ceramic plates [3]. Between the TE material and the metal on the ceramic plate (bridge), a metallic layer is usually inserted, referred to as electrode. Multiple designs and arrays of TEGs exist, optimized for different applications [4].

The performance of a TEG is assessed by its power output P and its conversion efficiency Φ, which directly depends on the TE material properties and the contact resistances between the TE legs and the electrodes, as shown in the following equations [5]:

$$P = \frac{S^2\sigma}{2}\frac{NA(T_h - T_c)^2}{(l+n)} \quad (1)$$

$$\Phi = \left(\frac{T_h - T_c}{T_h}\right)\left\{2 - \frac{1}{2}\left(\frac{T_h - T_c}{T_h}\right) + \frac{4}{zT_h}\left(\frac{l+n}{l}\right)\right\}^{-1} \quad (2)$$

where, S and σ are the Seebeck coefficient and electrical conductivity of a thermoelement (a n- or p-type leg), z its figure of merit calculated as $z = \frac{S^2\sigma}{\kappa}$, where κ is the thermal conductivity. N is the number of thermoelement pairs in the module; A is the cross-sectional area of a thermoelement; T_h and T_c are the temperatures at the hot and cold sides, respectively, of the module; l is the

* Corresponding author.
** Corresponding author.
E-mail addresses: julia.camut@dlr.de (J. Camut), johannes.deboor@dlr.de (J. de Boor).
[e] Contributed equally.

https://doi.org/10.1016/j.mtener.2021.100718
2468-6069/

length of a thermoelement; $n = 2\sigma\rho_c$, where ρ_c is the electrical specific contact resistance in Ωcm^2. This equation assumes equal properties for n- and p-type materials; in the case of TEG with more than one leg and unequal properties between n- and p-type materials, the average of the electrical and thermal resistivities should be used. The equations are based on the assumption of constant, i.e. temperature-independent properties, and neglect the effect of the ceramic plates and the thermal contact resistance. They show that material optimization and contact quality improvement are key parameters to increase the TEG performance for a given temperature range. Standard requirements for industrial use of TEG suggest the use of TE materials with a high figure of merit ($zT \geq 1$) and low electrical contact resistance ($\leq$10% of the TE material resistance) [6].

The TE solid solutions $Mg_2Si_{1-x}Sn_x$ ($x \approx 0.7$) have reproducibly high thermoelectric performance with a figure of merit of up to $zT = 1.4$ for n-type and 0.6 for p-type at 450 °C [7–12]. This makes the n-type material one of the best in terms of zT in the mid-to high-temperature range, with similar performance to other materials in other temperature ranges, such as $CoSb_3$ ($zT = 1.4$ at 500 °C [13]) and SiGe ($zT = 1$ at 900 °C) [3]. The p-type material remains to be improved but lies in the zT range of other known materials used at similar temperatures, such as HMS ($zT = 0.8$ at 500 °C [14]), ZnSb ($zT = 1.2$ at 370 °C [15]) and CeFe4Sb12 ($zT = 0.8$ at 550 °C [17]), although the best p-type materials remain PbTe ($zT = 1.8$ at 600 °C [16]) and TAGS ($zT = 1.8$ at 750 °C [18]). Silicide-based materials also have the advantages of being lightweight and inexpensive, which makes them especially suitable for applications where weight plays a decisive role, like the automobile and aerospace industries. Mg_2(Si,Sn) is less costly yet providing the equivalent performance compared with half-Heusler and Skutterudites alloys, which are more prominently used in the waste heat recovery industry [3,19].

Some silicide-based modules have already been reported [20–26], showing a performance of 0.9–4% of efficiency and a maximal power density between 0.3 and 1 W/cm^2, often combining n-type Mg_2Si and p-type HMS legs. The development of a fully Mg_2(Si,Sn)-based TEG is still at an early stage. Gao reported a first attempt at building such a TEG [27], showing a maximum power output of 117 mW for $T_h = 440$ °C and $T_c = 110$ °C; however, the experimental technique used to build the module is tricky and unoptimized. Furthermore, a suitable electrode for the TE material still remains to be found. In order for the performance to be maintained, the contact of the TE material and the electrode must be physically and chemically stable with time: its contact resistance should remain low and the microstructure should not deteriorate during the TEG lifetime. Of the same importance is the preservation of TE material properties during the joining process, which usually limits the temperature and pressure range that can be used [28], while higher temperatures and pressure are usually more favorable to the establishment of a good contact [29]. Those limitations help define some criteria for potential electrode selection: the electrode and TE material should have similar coefficients of thermal expansion (CTE) to ensure mechanical stability across the application temperature range [30] and the electrode should have a melting point such as the maximum joining temperature should be between 50 and 80% of the electrode melting temperature [29,31]. Obviously, other fundamental requirements are high electrical and thermal conductivity; however since the electrode materials are usually metallic, these criteria are the most easily fulfilled.

Finding a suitable electrode for the Mg_2(Si,Sn) solids solution was attempted in a couple of studies with electrode materials such as Ni, Ag, Cu, and constantan ($Ni_{45}Cu_{55}$) [32,33]. All show rather low electrical contact resistances but are unsatisfactory due to several issues. Ni was first tested since it was previously identified as a good matching electrode for binary Mg_2Si [34–36]. However, a systematic formation of cracks is reported; which is attributed to the mismatch in CTE (13 for Ni; 16.5–18.5·10^{-6} K^{-1} for Mg_2(Si,Sn)), making this material incompatible as an electrode [32]. A similar issue is reported for constantan electrodes ($Ni_{45}Cu_{55}$) [33]. Ag and Cu are the electrodes showing the lowest contact resistances (about or below 10 $\mu\Omega cm^2$); however, they both show an altering of the n-type Seebeck coefficient of the TE material after contacting [32,33]. Ayachi et al. recently established that this was due to the formation of Ag defects in the solid solution lattice during the diffusion process, as the formation energy of those defects is lower than the formation energy of the defects responsible for the n-type conduction [37]. A similar behavior is suspected for the Cu electrodes, which also massively reacts with the TE material, occasionally causing local delamination of the electrode.

In this study, aluminum was selected as a candidate for an electrode for the Mg_2(Si,Sn) material, since it is apparently a poor dopant, unlike Ag and Cu [39,40]. This metal has the advantages of being abundant and low-priced. Its CTE is larger than the TE material's ($26 \cdot 10^{-6}$ K^{-1} for Al [41], 16.5–17.5·10^{-6} K^{-1} ($x = 0.6$) and 17.5–18.5·10^{-6} K^{-1} ($x = 0.7$) for the TE material [32,42]); however, aluminum is malleable so it is believed that this behavior will help accommodate the mechanical stresses due to the CTE difference, unlike for Ni, which is much harder. Aluminum has a melting point of 660 °C, which is low enough to allow for direct bonding to the TE material, while being high enough to guarantee the electrode's stability across the application temperature range (<500 °C). Concerning the possible reactions that could occur at the interface, the phase diagrams of Al with Si and Sn suggest the small formation of complicating intermetallic compounds (IMC) that might degrade the overall performance [43,44]. It is reported that transient liquid phase bonding of Al to Mg using Sn interlayers leads to the formation of the phase Mg_2Sn, which shows that Mg and Sn preferentially react with each other rather than with Al [45]. The association of aluminum and silicides is reported in one study from Tohei et al. [26], where Al is used as a solder to join Mg_2Si legs to Ni electrodes. The contact is established and mechanically strong. No secondary phase is reported to form at the interface. No annealing experiment is reported, nor is the evolution of the transport properties after joining. Aluminum has also been used with other silicides, such as NiSi [46] and $CrSi_2$ [47], where it did not show any reaction with Si while successful bonding was obtained.

In this paper, we show that aluminum can be successfully bonded to p-type and n-type Mg_2(Si,Sn), giving low electrical contact resistances with a clean interface, free of detrimental secondary phases. Annealing experiments confirm that the contact on the p-type material is stable, while the transport properties of the n-type material are altered with annealing time, increasing the value of the absolute Seebeck coefficient.

A comparative annealing experiment is made with a non-contacted sample, in which an increase in absolute Seebeck coefficient is also observed. This shows that the main cause for the change in the n-type TE properties is probably magnesium evaporation. It is also found that the electrical contact resistances remain low, or get even lower with annealing. In this manuscript, we show that a step forward is made toward a future TEG, as aluminum is found to be a reliable electrode for Mg_2(Si,Sn) TE materials.

2. Materials and methods

The solid solutions Mg_2(Si,Sn) pellets were prepared with the following stoichiometry: $Mg_{2.06}Si_{0.3}Sn_{0.665}Bi_{0.035}$ for n-type and either $Mg_{1.98}Li_{0.02}Si_{0.4}Sn_{0.6}$ or $Mg_{1.98}Li_{0.03}Si_{0.3}Sn_{0.7}$ for p-type

following the melting route reported in Refs. [33,38,48]. 3% excess of Mg was introduced in the n-type samples to compensate for the Mg evaporation occurring during the sintering, which lasts double the time needed for p-type samples. The p-type samples presented in this study have different compositions like the one with $x = 0.4$ that was first selected due to its higher zT; but meanwhile, the studies from Pham et al. and Ayachi et al. showed that there could be a different behavior between the n-type and the p-type samples after contacting; the work was, therefore, pursued with the $x = 0.3$ composition for both n- and p-type to make the comparison easier. The n-type pellets were sintered at 700 °C for 20 min at 66 MPa and the p-type pellets at 650 °C for 10 min at 66 MPa under vacuum.

The pellets were then manually ground to a constant thickness with a precision of ±10 μm. The joining step was made either at 450 °C or 500 °C through indirect heating, for 10 min with a pressure of 30 MPa under vacuum, at a 1 K/s heating rate. A buffer layer of Al_2O_3 powder was introduced under and on top of the pellet and foils, in order to avoid cracking of the TE pellet due to the pressure while joining. For the p-type samples, the joining at 450 °C was made with a composition of $x = 0.3$ while the joining at 500 °C was made for $x = 0.4$. The aluminum foil (99.5%; chemPUR) was ground with 4000 SiC paper before the joining process, in order to remove the native oxide layer on its surface. A combined material compaction and electrode sintering are not feasible for the chosen material combination, because the melting point of aluminum is too low compared to the temperature necessary to the good compaction and optimization of the properties of the TE material [49,50]. The joining temperatures of 450 °C and 500 °C were selected as they respect the criteria of being between 50 and 80% of the melting point of aluminum while preserving the TE material properties, which can be altered with an excessively high-temperature exposure [49].

The quality of the joining is estimated by the value of its specific contact resistance r_c and the preservation of the Seebeck coefficient of the TE material using a Potential & Seebeck Scanning Microprobe (PSM) [51], and by its microstructural and chemical composition at the interface, using scanning electron microscopy (Zeiss Ultra 55 SEM equipped with an EDX detector). After characterization, the contacted samples are annealed at 450 °C under argon atmosphere for 1 and 2 weeks (total time) with BN coating in order to investigate the stability of the contacts over time.

An experimental flowchart summing up the sintering, contacting, annealing and analysis of the samples is shown in Fig. 1.

After measuring the Seebeck coefficient, it is possible to estimate the carrier concentration and the carrier mobility after annealing using a single parabolic band model (SPB) [52]. In this model, the transport properties are obtained following the equations given by:

$$|S| = \frac{k_B}{e} * \left(\frac{2F_1(\eta)}{F_0(\eta)} - \eta \right) \tag{3}$$

$$n = 4\pi \left(\frac{2m_d^* k_B T}{h^2} \right)^{1,5} F_{\frac{1}{2}}(\eta) \tag{4}$$

where $\eta = \frac{E_F}{k_B T}$ is the reduced chemical potential, m_d^* the density of states effective mass and n the carrier concentration, k_B is the Boltzmann's constant, $F_i(\eta)$ is the Fermi integral of order i.

Using the Pisarenko plot linking S and n with an effective mass of $2.5m_0$ for n-type [53] and $1.5m_0$ for p-type [52], we deduce the carrier concentration of the samples from our measured S data. The plots are shown in Supplementary Information. The electrical conductivity σ is measured with an in-house built system, which allows the measuring of the electrical conductivity of a sample using a four-point-probe in an in-line setup [54], with 1 mm probe distance. The probes are spring-loaded tungsten carbide needles. The voltage measurement for the voltage drop across the sample and the voltage drop across a 1-Ohm reference resistance is done by lock-in-amplifiers for accuracy. The voltage at the reference resistance is needed to calculate the electrical current and thus the sample's resistance, from which the specific resistance or conductivity is calculated; the sample's geometry is taken into account by a calculated correction factor. This device has the advantage of allowing to measure samples with smaller geometries, although if the geometry is too close or smaller than the length of the 4-points distance the results are less accurate. The mobility μ is then

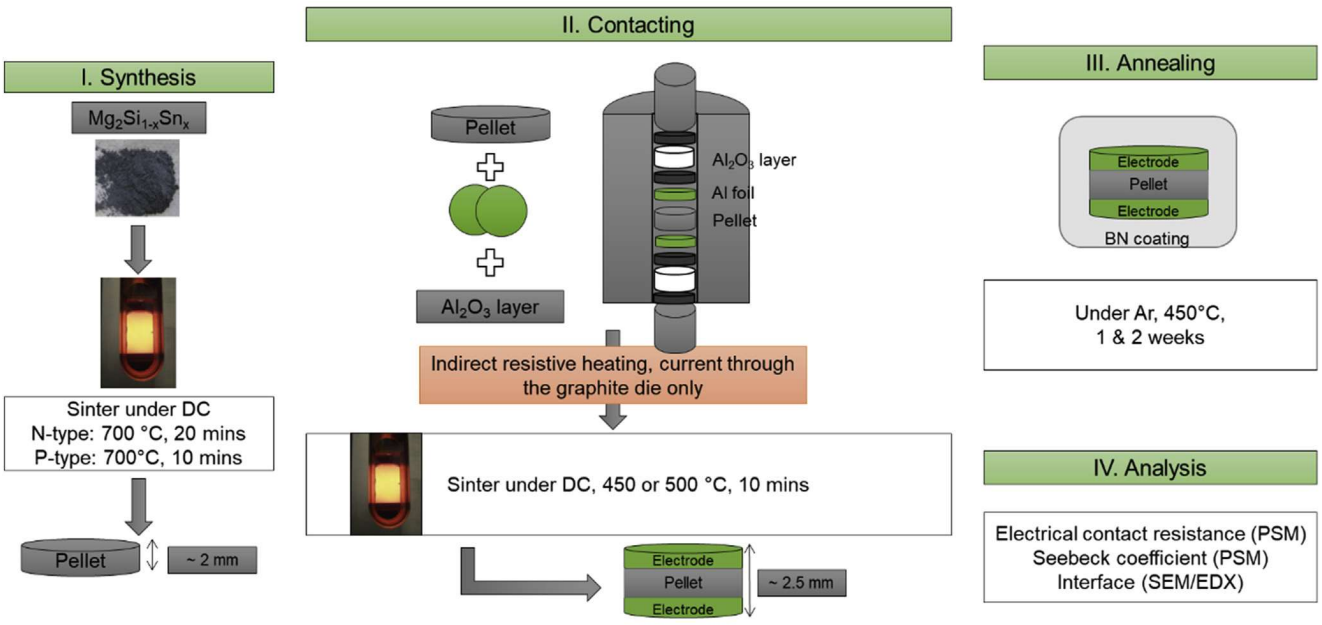

Fig. 1. Experimental flowchart from powder to the analysis of the contacted pellet.

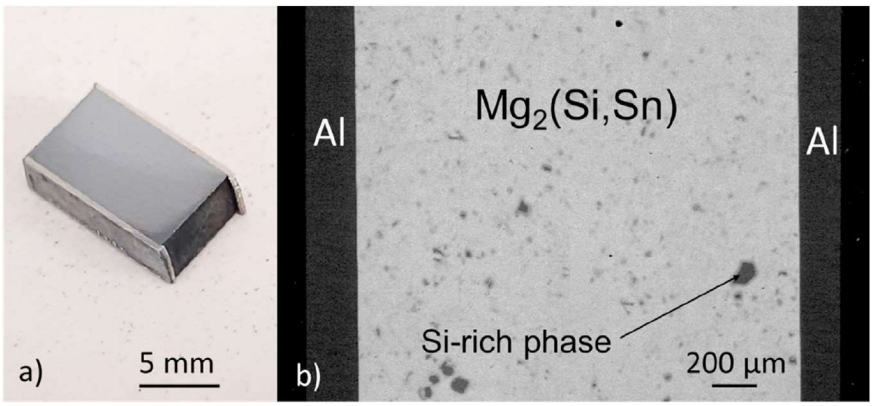

Fig. 2. a) Photo and b) SEM image of a sample after joining.

calculated using the electrical conductivity and the Seebeck coefficient estimated carrier concentration, using the following equation:

$$\sigma = ne\mu \tag{5}$$

3. Results

In general, joining the TE material with Al provides visibly good joints, as can be seen in Fig. 2. Sound contact is produced without any visible cracks or delamination either in the material or the electrode foil. The visible black dots in the TE material are a Si-rich phase due to incomplete reaction; those impurities are often seen in the material [49]. The evolution of the microstructure at the interface with joining temperature and annealing is reported in Fig. 3. It is seen for all the samples that the interface directly after joining is very flat and smooth and there is no visible indication for a chemical reaction between the aluminum electrode and the TE material. After 1 week of annealing, a few black spots at or close to the interface and a brighter layer close to the interface are visible. From EDX line scans (Fig. 4) these can be identified as aluminum grains and an Sn-rich $Mg_2(Si,Sn)$ phase at the interface. There is no drastic evolution between the first and the second week of annealing, as the secondary phases do not noticeably grow further. Note that a different piece (cut from a pellet sintered under identical conditions) was employed for each annealing experiment in order to preserve samples at different annealing stages.

From the EDX line scan in Fig. 4 the atomic % can be read, corresponding to a composition of approximately $Mg_2Si_{0.15}Sn_{0.85}$ for that newly formed phase. This phase extends on a scale from 5 to 15 μm. The size of this second phase differs between the samples. The two samples contacted at 450 °C show scarce nuclei along with the interface (diameter ≈ 5–10 μm), while the samples contacted at 500 °C show more or less continuous reaction layers (thickness ≈ 10–15 μm). This difference could be due to the difference in joining temperature, although there is no noticeable difference directly after joining. It is possible that Al has diffused more into the TE material with a higher joining temperature, allowing the reaction during annealing to progress faster. This could also simply be due to sample-to-sample variation. The small Al 'particles' found close to the interface might be due to diffusion and precipitation during the cooling process, but the exact mechanism remains unclear.

Figs. 5 and 6 show the Seebeck coefficient and potential line-scan for all the samples, p-type and n-type respectively. It can be observed that the absolute potential values differ quite dramatically for the different samples. This is due to the quality of the interface between the sample and the sample holder, which has a direct impact on the magnitude of the flowing current, roughly proportional to the potential values. This, however, does not influence the r_c measurement results.

It is seen that the p-type Seebeck coefficient is not changing with annealing, although the measurement of the sample contacted at 450 °C and annealed for 1 week shows large scattering. This can be attributed to some problem during the measurement (poorer contact to the sample holder, surface quality, or wear of the tip). This explanation is also supported by the fact that no other p-type sample shows this much scattering, which leads to the belief that this is rather due to a punctual preparation issue than to the aluminum joining. Overall, the average p-type Seebeck coefficient lies around 90 μV/K, corresponding to a carrier concentration of about 1.9×10^{20} cm^{-3}, which is in the usual range reported in the literature for optimal properties [7]. However, it is seen that the n-type Seebeck coefficient is altered through annealing. The sample contacted at 450 °C shows a Seebeck coefficient evolution from −100 to −130 and −145 μV/K after respectively 1 and 2 weeks of annealing. The sample contacted at 500 °C changes from −120 to −180 and −170 μV/K after respectively 1 and 2 weeks of annealing. The change between the first and second week of annealing in both samples can be explained by the PSM accuracy of about 10–15% [55].

It should be noted that the power factors and figure of merit for the n- and p-type samples at room temperature before annealing are in the range of previously reported high-performance samples [48,52]. The n-type sample shows power factors of about $25 \cdot 10^{-4}$ W/mK^2 at room temperature and $38 \cdot 10^{-4}$ W/mK^2 at 700 K and a figure of merit zT = 1.3 at 650 K, while the p-type sample shows power factors of about $6 \cdot 10^{-4}$ W/mK^2 at room temperature and $12 \cdot 10^{-4}$ W/mK^2 at 700 K and a figure of merit zT = 0.4 at 650 K. This confirms the good TE properties of the employed material with tested electrodes for future devices.

The specific electrical contact resistance r_c is calculated as previously reported [33], using the following equation:

$$r_c = \frac{(V_{elec} - V_{TE}) * l_{TE}}{\Delta V_{TE} * \sigma_{TE}} \tag{6}$$

where V_{elec} is the potential on the electrode at the interface and V_{TE} is the potential on the TE material at the interface, the position of the interface being located using the drop in Seebeck coefficient on the line-scan. l_{TE} is the length of the TE material (between the two electrodes), ΔV_{TE} is the drop in potential across the TE material and σ_{TE} is the electrical conductivity of the TE material, measured using a 4-probe inline technique. For the samples that were too small to

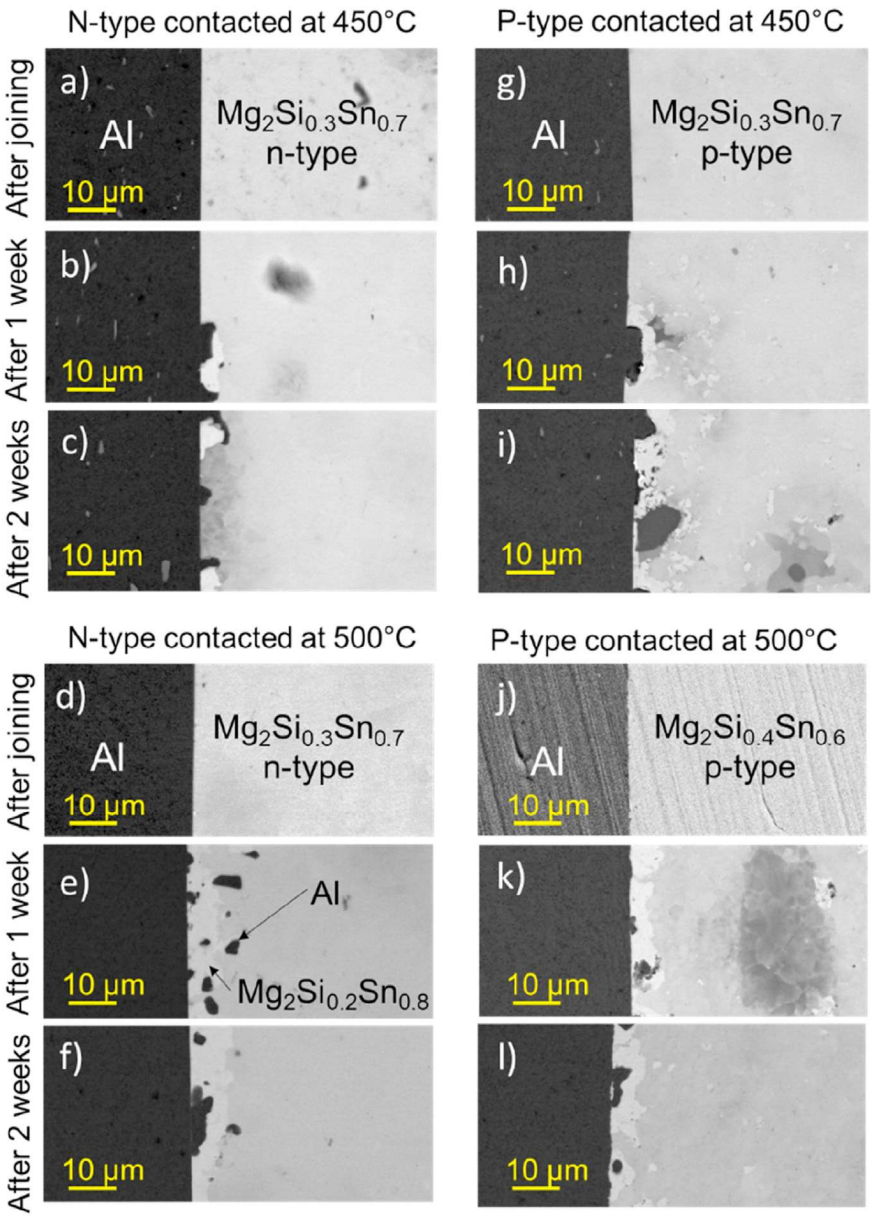

Fig. 3. SEM images of the contacted samples for difference joining temperatures: directly after joining, after 1 and 2 weeks of annealing at 450 °C under Ar atmosphere.

be measured, a constant charge carrier mobility compared to a similar sample is assumed, and the σ_{TE} is obtained using Eq. (5) by estimating the charge carrier concentration using the Pisarenko plot and the measured Seebeck coefficient. The variation in carrier concentration is then proportional to the variation in electrical conductivity.

The obtained r_c values are compared to contact resistance values obtained using the current density directly measured by the PSM, contrarily to Eq. (6) where the current density is calculated using the TE material properties:

$$r_{c\_PSM} = \frac{(V_{elec} - V_{TE})*A}{I_{PSM}} \quad (7)$$

where A is the sample cross-section and I the current measured in the device. Multiple line-scans are measured for each sample, the r_c value presented below is the average value of all the lines, given with the corresponding standard deviation.

The calculation of the electrical contact resistance according to Eq. (7) requires the assumption that the current density is homogeneous over the whole sample (along cross-section and length), while Eq. (6) only assumes a constant current density along the direction of the line-scan. The more inhomogeneous the interface, the more different are the results given by both equations.

The r_c value of each sample is reported in Table 1. All samples show a low contact resistance directly after contacting except the n-type sample contacted at 450 °C. This sample shows asymmetric r_c contact resistance, the 'left/right' designates the left and right interfaces on the PSM scan shown in Fig. 6. One of the r_c values is satisfyingly low but the other one is dramatically high (>1000 µΩcm^2). Moreover, there is a large difference between the results from Eqs. (6) and (7), meaning that the interface of the sample is highly inhomogeneous. The very same piece of sample is used for the first week of annealing and it is seen that annealing seems to 'heal' the high contact resistance, as after 1 week of annealing the sample shows symmetric and low r_c and r_{c_PSM}

values. Similarly, for the p-type sample contacted at 450 °C, the initial r_c value after joining is 17 ± 8 μΩcm^2 and is progressively decreased with annealing, until reaching a value below 10 μΩcm^2 after 2 weeks. Both samples contacted at 500 °C had an initial value <10 μΩcm^2 directly after joining, which is not altered with annealing. Overall, most r_c values are around or below 10 μΩcm^2, while most r_{c_PSM} values remain below 20 μΩcm^2, which shows acceptable homogeneity and reliability of the measurement.

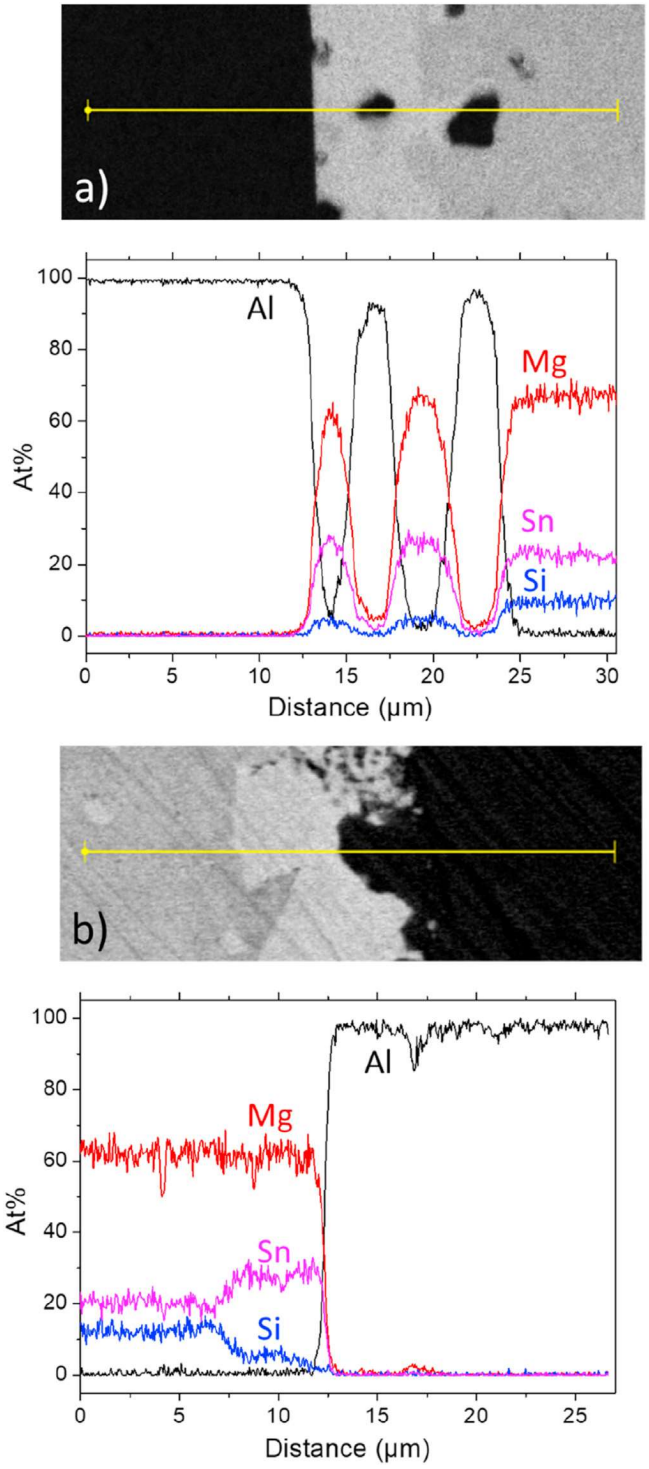

Fig. 4. EDX line-scan of the secondary phases forming at the interface. The samples are a) n-type $Mg_2Si_{0.3}Sn_{0.7}$ and b) p-type $Mg_2Si_{0.4}Sn_{0.6}$ both contacted at 500 °C.

The change in Seebeck coefficient of the n-type sample could originate from two factors: the diffusion of Al creating stable defects and changing the carrier concentration in the TE material or the evaporation of Mg due to annealing, previously reported in the literature [56]. In order to understand the origin of the change in the n-type Seebeck coefficient with annealing, the results of comparative annealing experiments are reported in Fig. 7. Several samples are compared: an electrode-free control sample and the samples contacted at 450 °C and 500 °C already presented above. All samples are coated with a BN slurry and annealed for 1 and 2 weeks at 450 °C under Ar.

The control sample is a pellet that was previously contacted with Al at 450 °C and showed very high contact resistance on both sides, indicating that the Al diffusion length into the TE material is very probably negligible. The Al was peeled off and the faces of the TE pellet were thoroughly ground (>0.1 mm). As a consequence, the sample has a similar thermal history as the other samples, while being Al-free.

It is seen that in the control experiment, the Seebeck coefficient gradually changes with annealing, increasing from −90 μV/K to −110 μV/K and −120 μV/K after respectively 1 and 2 weeks of annealing, which demonstrates the effect of Mg loss alone. With similar coating conditions, the sample contacted at 450 °C shows a Seebeck coefficient evolution from −100 μV/K to −130 μV/K and −145 μV/K: the change after each annealing step is larger than for the control experiment, presumably indicating that some of this evolution is due to the aluminum electrode. However, those changes remain within the range of error of the PSM, and must, therefore, be considered cautiously. For the experiment with the contacting at 500 °C, the Seebeck coefficient goes from −120 μV/K to −180 μV/K after one week and to −170 μV/K after 2 weeks. The decrease in |S| after the first week is within the measurement accuracy of the PSM and most likely not a physical change; we assume that the Seebeck coefficient is reaching a plateau after the first week of annealing.

Using the set of Eqs. (3)–(5), the mobility of the charge carriers in the control experiment and the sample contacted at 450 °C with different annealing times is calculated and reported in Table 2. For both samples, annealing implies a drastic decrease of the electrical conductivity, generally by a factor of 3–4. It can be seen that for the sample contacted at 450 °C, the mobility after the first week of annealing is reduced by a factor of 2, and does not change much further after the second week of annealing. The mobility of the control experiment after two weeks of annealing is also reduced by a factor of 2. The sample contacted at 500 °C and the corresponding annealed samples were too small to be reliably measured, their charge carrier mobility was, therefore, not assessed. For the same reason, the electrical conductivity after the first week of annealing for the control experiment could also not be measured.

4. Discussion

First, there is no sign of a harmful CTE mismatch impact on the pellet as no formation of cracks is observed after joining the electrode. The formation of the Sn-rich phase at the interface with annealing is also interesting in this regard, as Mg_2Sn has a CTE of $17–19 \cdot 10^{-6}$ K^{-1} [57,58], so it could act as a mechanical buffer layer between the electrode and Mg_2(Si,Sn) and enhance the mechanical stability of the joint. Moreover, the microstructure evolves slowly after the first week of annealing, as not much further growth is noticed after the second week, and therefore, the interface seems also chemically sufficiently stable.

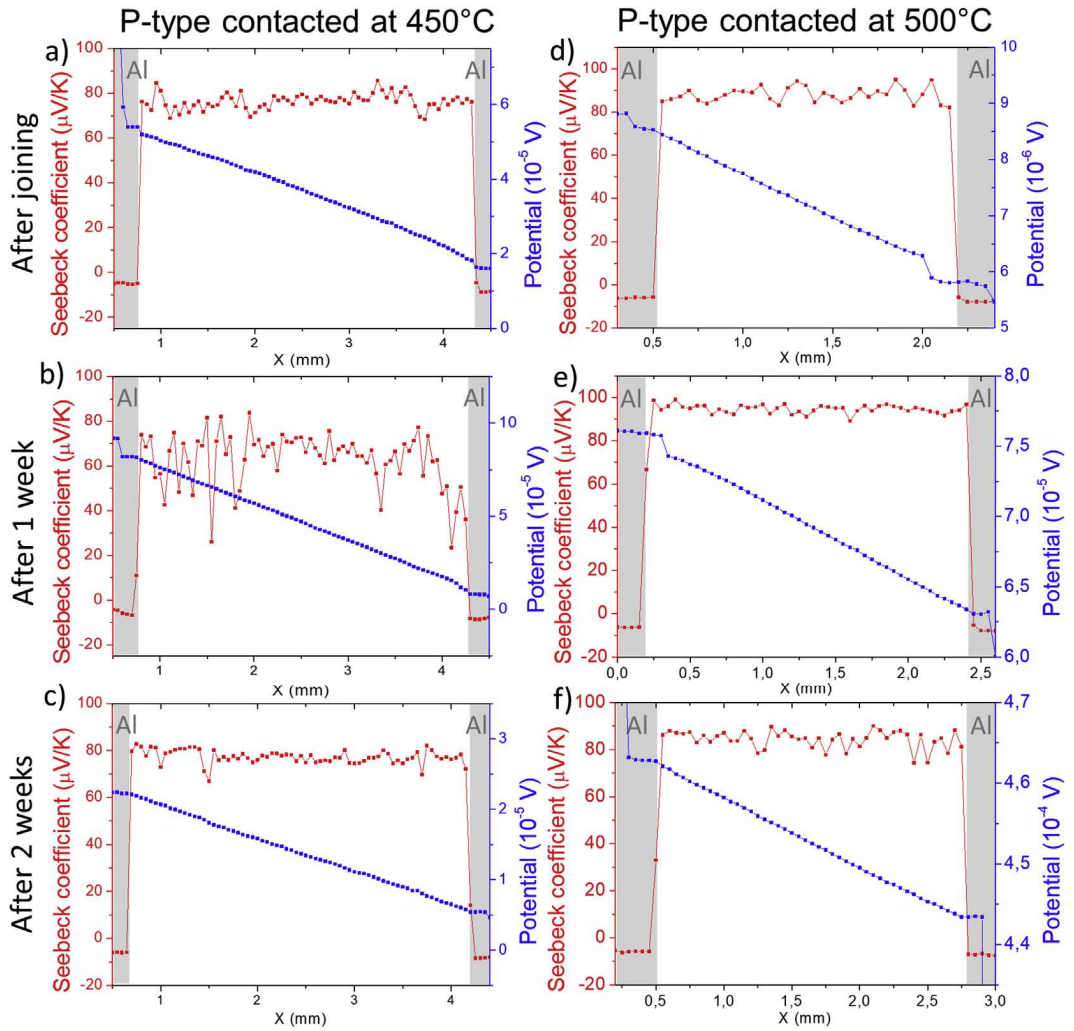

Fig. 5. Exemplary line-scans of the Seebeck coefficient and the electrical potential for p-type $Mg_2(Si,Sn)$ samples for different joining temperatures: directly after joining, after 1, and after 2 weeks of annealing at 450 °C under Ar atmosphere.

The decrease in r_c with annealing is systematic, even for samples starting with higher values, while the development of the microstructure is not uniform in all the samples. No trend can be observed between the r_c value, its standard deviation, and the regularity of the microstructure, meaning that the growth of the reaction layer is not correlated with the electrical contact resistance. Possible explanations for the decrease of r_c with annealing are the reconsolidation of nanocracks [59,60] or a dissolution of oxides at the interface, which would allow a better current transmission.

The influence of the joining temperature on the quality of the contact is not large in the investigated range. It seems that a higher joining temperature induces a thicker reaction layer at the interface with annealing, which could potentially guarantee higher mechanical stability. The n-type pellet contacted at 450 °C is the only one showing a tremendously high electrical contact resistance (on one side only), but it is believed to be rather due to a punctual lack

Table 1
Specific electrical contact resistances of the $Mg_2(Si,Sn)$ samples for difference joining temperatures: directly after joining, after 1, and after 2 weeks of annealing at 450 °C under Ar atmosphere. r_c values were calculated using Eq. (6), r_{c_psm} using Eq. (7).

	Contacted at 450 °C		Contacted at 500 °C	
	r_c ($\mu\Omega cm^2$)	r_{c_PSM} ($\mu\Omega cm^2$)	r_c ($\mu\Omega cm^2$)	r_{c_PSM} ($\mu\Omega cm^2$)
p-type				
After joining	17 ± 8	19 ± 6	9 ± 5	3 ± 2
1 week annealing	11 ± 7	13 ± 9	4 ± 2	4 ± 2
2 weeks annealing	7 ± 3	5 ± 3	9 ± 9	18 ± 18
n-type				
After joining (left/right side)	1327 ± 195/10 ± 4	9487 ± 1396/69 ± 28	3 ± 2	1 ± 1
1 week annealing	5 ± 2	8 ± 4	5 ± 6	14 ± 16
2 weeks annealing	6 ± 3	15 ± 9	5 ± 3	11 ± 8

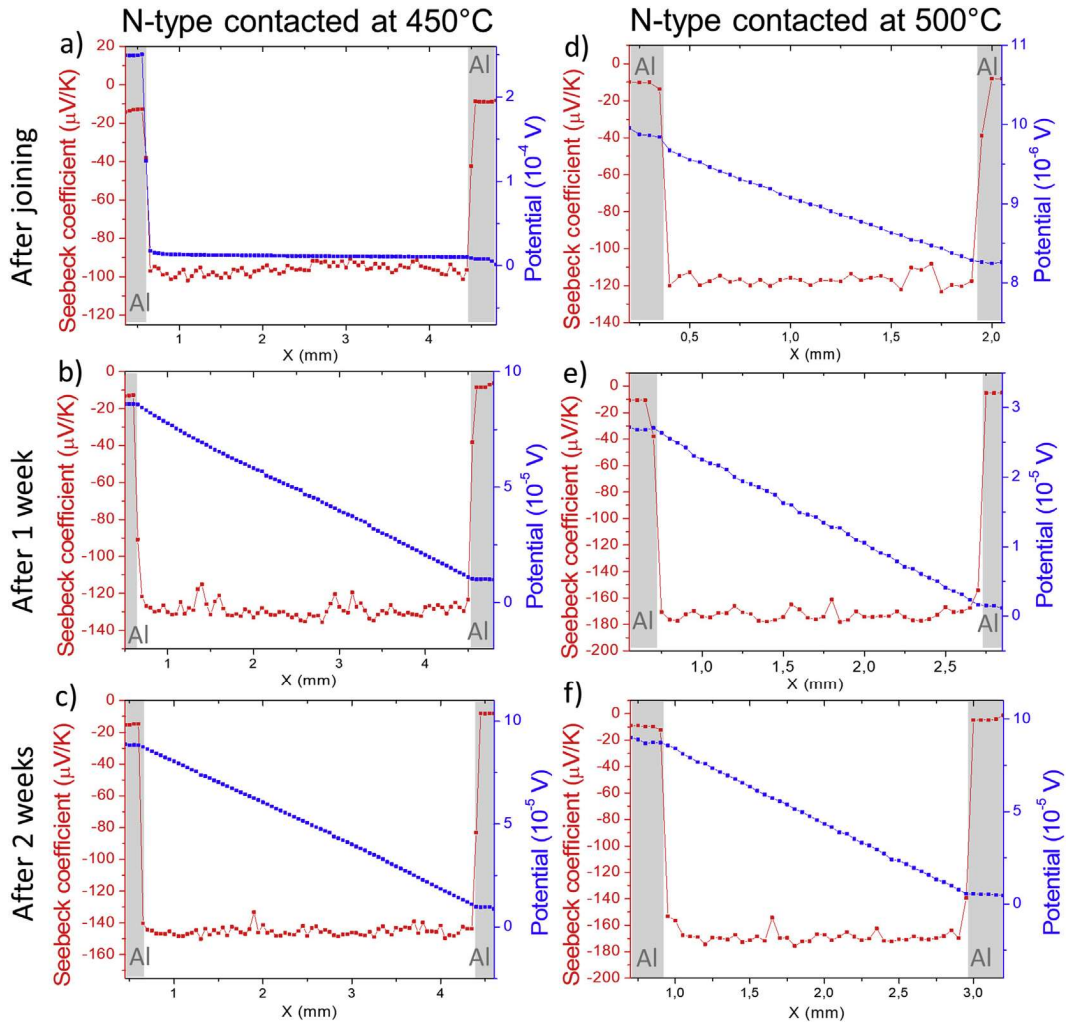

Fig. 6. Exemplary line-scans of the Seebeck coefficient and the electrical potential for the n-type $Mg_2(Si,Sn)$ samples for different joining temperatures: directly after joining, after 1, and after 2 weeks of annealing at 450 °C under Ar atmosphere.

of process control than to the joining temperature itself, as this is not observed for the p-type equivalent experiment. Nevertheless, contacting at 500 °C instead of 450 °C provided lower r_c values directly after joining, and is, therefore, found to be advantageous.

The aluminum electrode does not have any detrimental impact on the p-type Seebeck coefficient, even after 2 weeks of annealing. A significant increase is however observed in the n-type absolute Seebeck coefficient, indicating that the carrier concentration decreases with annealing. At least two factors can plausibly be at play in this change: Al diffusing into the TE material and altering its transport properties through the formation of stable compensating defects and Mg evaporation during annealing.

Liu et al. showed that in n-type Mg_2Sn and Mg_2Si, the most stable defects are Mg vacancies (−2), independently of Mg chemical potential [61]. If there is some Mg evaporation during annealing, this means that the amount of Mg vacancies increases. This should decrease the electron carrier concentration and thus increase $|S|$. A

Table 2
Measured and estimated electrical properties of the n-type TE material after joining and after 1 and 2 weeks of annealing.

	0 week	1 week	2 weeks
Control experiment			
Average Seebeck coefficient (μV/K)	−90	−105	−120
Carrier concentration (10^{20} cm^{-3})	4.1	3.2	2.5
Electrical conductivity (S/cm)	3130	–	1190
Mobility (cm^2/Vs)	48	–	30
Contacted at 450 °C			
Average Seebeck coefficient (μV/K)	−95	−130	−145
Carrier concentration (10^{20} cm^{-3})	3.8	2.1	1.7
Electrical conductivity (S/cm)	3450	1150	840
Mobility (cm^2/Vs)	57	34	31

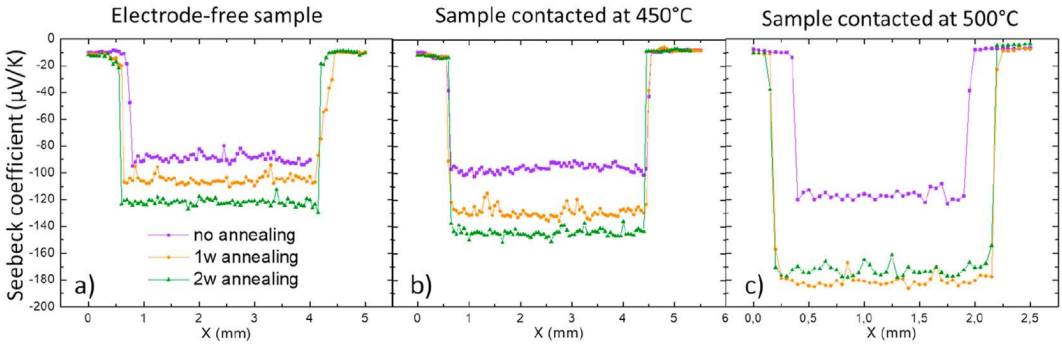

Fig. 7. Evolution of the n-type Seebeck coefficient with annealing for a) the control experiment **(sample without electrode)**, b) the sample contacted at 450 °C, c) the sample contacted at 500 °C.

Table 3
Summary of the contact resistance and limitations of potential electrodes for Mg_2Si1-xSnx with x = 0.3–0.4.

Electrode	r_c (μΩcm^2)	Evaluation after joining	Evaluation after annealing	Reference
Ni	25–50	Cracks due to CTE mismatch	No annealing experiment	[32]
Ag	9–15	Electrode-induced decrease in n-type carrier concentration	No annealing experiment	[32,37]
Cu	<10	Electrode-induced decrease in n-type carrier concentration; thick reaction layer that can cause delamination	Further decrease in n-type carrier concentration, probably both due to electrode and Mg loss	[38]
CuNi	<50	Electrode-induced decrease in n-type carrier concentration; cracks due to CTE mismatch	No annealing experiment	[38]
Al	≤10	Fine	Decrease in n-type carrier concentration, presumably due to Mg loss	This work

decrease in carrier concentration under Mg loss has already been observed experimentally for n-type material [49,56], which supports this hypothesis. One could wonder why such a behavior is not observed on the p-type samples. In this regard, it is interesting to note that the n-type material is synthesized containing excess Mg, while the p-type is not [48]. This means that during annealing, the n-type can shift from Mg-rich to Mg-poor condition, while the p-type material remains under Mg-poor conditions during all the annealing experiments. This could explain the fact that the n-type Seebeck coefficient is changing while the p-type is not.

In Fig. 7, the control experiment, without the Al electrode, shows an ongoing increase of |*S*| with annealing duration, well in line with the hypothesis that Mg loss is mainly responsible for the observed changes. For the sample contacted at 450 °C the change of |S| after one week is higher than for the control experiment, possibly indicating that an Al-TE interaction also plays a role in the decrease of carrier concentration. The further evolution is comparable to that of the control sample, and therefore, most likely an indication of ongoing Mg loss. The sample contacted at 500 °C shows a significantly larger change than the other two. This could again be due to Mg loss, with the higher change being linked to the higher joining temperature, and/or and to the interaction of the Al electrode with the TE material.

A generally possible interaction mechanism (diffusion of the electrode into the TE material) was discussed by Ayachi et al. for Ag and n-type Mg_2(Si,Sn) [37]. However, it is unlikely that the mechanism at play in our case is similar. For Ag, a *local gradient* in the Seebeck coefficient was observed from the interfaces to the center of the TE material. If Al was a faster or a similar diffuser in Mg_2(Si,Sn) compared to Ag, a change in the Seebeck coefficient would be observed directly after joining, which is not the case. If Al was a slower diffuser the formation of a gradient would be expected upon annealing time, which is in contrast to the observed constant change along with the TE material.

Moreover, Ag is well-known as a p-type dopant for Mg_2(Si,Sn), it is, therefore, plausible that its diffusion into the n-type material decreases its carrier concentration. On the other hand, Al was predicted and shown to be a rather poor dopant in Mg_2(Si,Sn) [62–66], with the data focusing on the Si-rich side of the spectrum. In our case of hypothetical uncontrolled Al-doping, the effect on carrier concentration would, therefore, be expected to be rather weak. DFT calculations similar to those made for Ag [37] should be considered for Al in order to understand the defects that it creates in the TE material and how this could affect the carrier concentration on the Sn-rich end of the composition range.

Finally, the mobility calculations in Table 2 show that the mobility is decreasing at the same time as the carrier concentration, resulting in a larger decrease of the electrical conductivity. The loss of mobility is similar for all samples. It has already been shown that one consequence of Mg loss is the decrease in charge carriers mobility [49,56], while from a simple carrier concentration reduction (by counter-doping) no loss in mobility would be expected.

All this suggests that the observed changes in the material properties are due to Mg loss rather than Al diffusion leading to a charge carrier compensation. We also note that the difference in *S* variation could also be indicating a lack of reproducibility in the BN-coating quality and thus extend of Mg evaporation. For a further confirmation of the drawn conclusions, further investigations and annealing experiments should be performed with better coating, see e.g. Refs. [67–72].

A summary of the results obtained for aluminum and the electrodes previously reported in literature can be found in Table 3. It shows that aluminum is the best electrode so far for contacting p-type and n-type Mg_2(Si,Sn) with optimal TE properties.

5. Conclusion

We found a suitable material and joining conditions to make stable and high-quality contact for a Mg_2(Si,Sn) material system.

Obtained joints are mechanically and chemically stable after 2 weeks of annealing. Contacting at 500 °C leads to low electrical contact resistances, around 10 $\mu\Omega cm^2$ for both n- and p-type materials, and no deterioration of those values is observed after annealing. The p-type properties are found to be stable, while a variable change in the n-type Seebeck coefficient is observed after annealing. It is attributed to magnesium evaporation from the TE material and presumably not due to the interaction between the electrode and the TE material, unlike previous electrodes like Ag and Cu that showed counter-doping effects [33,37]. Although it is still suggested to add a protection layer on the TE material for enhanced material stability and preserved maximum efficiency, aluminum is shown to be a very promising electrode for a future $Mg_2(Si,Sn)$-based thermoelectric generator.

Data availability statement

The raw/processed data required to reproduce these findings cannot be shared at this time due to legal or ethical reasons.

CRediT authorship contribution statement

J. Camut: Writing – original draft, Writing – review & editing, Visualization, Investigation. **N.H. Pham:** Writing – original draft, Writing – review & editing, Investigation. **D.Y. Nhi Truong:** Writing – review & editing, Investigation. **G. Castillo-Hernandez:** Writing – review & editing. **N. Farahi:** Writing – review & editing. **M. Yasseri:** Investigation. **E. Mueller:** Conceptualization, Supervision. **J. de Boor:** Conceptualization, Supervision, Project administration, Writing – review & editing.

Declaration of competing interest

The authors declare that they have no known competing financial interests or personal relationships that could have appeared to influence the work reported in this paper.

Acknowledgements

The authors would like to gratefully acknowledge the endorsement for the DLR Executive Board Members for Space Research and Technology, as well as the financial support from the Young Research Group Leader Program. M.Y. would like to thank for the financial support that is provided by the DFG via the GRK (Research Training Group) 2204 'Substitute Materials for Sustainable Energy Technologies'. G.C.H. would like to thank the financial support of the Mexican Science and Technology Ministry (CONACyT). J.C., N.H.P, D.Y.N.T., N.F and would like to thank the DAAD fellowship programs (No. 57424731, 57265854, 57370121 and 248, respectively), while JdB is partially funded by the Deutsche Forschungsgemeinschaft (DFG, German Research Foundation), project number 396709363. Lastly, we would also like to acknowledge Pawel Ziolkowski and Przemyslaw Blaschkewitz for their help and assistance with the thermoelectric measurements, as well as S. Ayachi for discussions.

Appendix A. Supplementary data

Supplementary data to this article can be found online at https://doi.org/10.1016/j.mtener.2021.100718

References

[1] S. Karellas, et al., Energetic and exergetic analysis of waste heat recovery systems in the cement industry, Energy 58 (2013) 147–156.
[2] J. Yang, F. Stabler, Automotive applications of thermoelectric materials, J. Electron. Mater. 38 (2) (2009) 1245–1251.
[3] G.J. Snyder, E.S. Toberer, Complex thermoelectric materials, in: Materials for Sustainable Energy: a Collection of Peer-Reviewed Research and Review Articles from Nature Publishing Group, World Scientific, 2011, pp. 101–110.
[4] R. He, G. Schierning, K. Nielsch, Thermoelectric devices: a review of devices, architectures, and contact optimization, Adv. Mater. Technol. 3 (4) (2018) 1700256.
[5] D. Rowe, G. Min, Design theory of thermoelectric modules for electrical power generation, IEE Proc.-Sci., Meas. 143 (6) (1996) 351–356.
[6] D. Rowe, Conversion efficiency and figure-of-merit, in: CRC Handbook of Thermoelectrics, CRC press, 1995, pp. 31–37.
[7] J. de Boor, et al., Recent progress in p-type thermoelectric magnesium silicide based solid solutions, Mater Today Energy 4 (2017) 105–121.
[8] M.B.A. Bashir, et al., Recent advances on Mg2Si1− xSnx materials for thermoelectric generation, Renew. Sustain. Energy Rev. 37 (2014) 569–584.
[9] J. de Boor, et al., Thermoelectric performance of Li doped, p-type Mg2 (Ge, Sn) and comparison with Mg2 (Si, Sn), Acta Mater. 120 (2016) 273–280.
[10] V. Zaitsev, et al., Highly effective Mg2Si1−xSnx thermoelectrics, Phys. Rev. B 74 (4) (2006), 045207.
[11] M.I. Fedorov, V.K. Zaitsev, G.N. Isachenko, High effective thermoelectrics based on the Mg2Si-Mg2Sn solid solution, in: Solid State Phenomena, Trans Tech Publ, 2011.
[12] W. Liu, et al., Convergence of conduction bands as a means of enhancing thermoelectric performance of n-type Mg2Si1−xSnx solid solutions, Phys. Rev. Lett. 108 (16) (2012) 166601.
[13] V. Trivedi, et al., Microstructure and doping effect on the enhancement of the thermoelectric properties of Ni doped Dy filled CoSb 3 skutterudites, Sustain. Energy Fuels 2 (12) (2018) 2687–2697.
[14] S. Muthiah, et al., Significant enhancement in thermoelectric performance of nanostructured higher manganese silicides synthesized employing a melt spinning technique, Nanoscale 10 (4) (2018) 1970–1977.
[15] A. Ostovari Moghaddam, et al., Ge-Doped ZnSb/β-Zn4Sb3 nanocomposites with high thermoelectric performance, Adv. Mater. Interfaces 6 (18) (2019) 1900467.
[16] P. Jood, et al., Na doping in PbTe: solubility, band convergence, phase boundary mapping, and thermoelectric properties, J. Am. Chem. Soc. 142 (36) (2020) 15464–15475.
[17] K.-M. Song, et al., Synthesis and Thermoelectric Properties of Ce 1− z Pr z Fe 4− x Co x Sb 12 Skutterudites, J. Electron. Mater. 46 (5) (2017) 2634–2639.
[18] S. Yang, et al., Thermal stability study of melt spun TAGS-80 thermoelectric bulks, J. Mater. Sci.: Mater. Electron. 28 (20) (2017) 15279–15283.
[19] J.-i. Tani, H. Kido, Fabrication and thermoelectric properties of Mg2Si-based composites using reduction reaction with additives, Intermetallics 32 (2013) 72–80.
[20] G. Skomedal, et al., Design, assembly and characterization of silicide-based thermoelectric modules, Energy Convers. Manag. 110 (2016) 13–21.
[21] A. de Padoue Shyikira, G. Skomedal, P.H. Middleton, Performance evaluation and stability of silicide-based thermoelectric modules, Mater. Today: Proc (2020), https://doi.org/10.1016/j.matpr.2020.05.193.
[22] H. Kaibe, et al., Development of thermoelectric generating stacked modules aiming for 15% of conversion efficiency, in: ICT 2005. 24th International Conference on Thermoelectrics, IEEE, 2005, 2005.
[23] K.R. Tarantik, et al., Thermoelectric modules based on silicides–development and characterization, Mater. Today: Proc 2 (2) (2015) 588–595.
[24] T. Nakamura, et al., Power-Generation performance of a π-structured thermoelectric module containing Mg 2 Si and MnSi 1.73, J. Electron. Mater. 44 (10) (2015) 3592–3597.
[25] H.S. Kim, et al., Design of segmented thermoelectric generator based on cost-effective and light-weight thermoelectric alloys, Mater. Sci. Eng., B 185 (2014) 45–52.
[26] T. Tohei, et al., Bondability of Mg2Si element to Ni electrode using Al for thermoelectric modules, in: IOP Conference Series. Materials Science and Engineering (Online), 2014.
[27] P. Gao, Mg2(Si, Sn)-Based Thermoelectric Materials and Devices, Michigan State University, 2016, p. 128.
[28] G. Skomedal, et al., High temperature oxidation of Mg2 (Si-Sn), Corrosion Sci. 111 (2016) 325–333.
[29] A. Shirzadi, H. Assadi, E. Wallach, Interface evolution and bond strength when diffusion bonding materials with stable oxide films, Surf. Interface Anal. 31 (7) (2001) 609–618.
[30] S.-L. Li, et al., Thermo-mechanical analysis of thermoelectric modules, in: 2010 5th International Microsystems Packaging Assembly and Circuits Technology Conference, IEEE, 2010.
[31] J.J. D'Angelo, et al., Electrical contact fabrication and measurements of metals and alloys to thermoelectric materials, Mater. Res. Soc. Symp. Proc. 1044 (2008) 449–455.
[32] N.H. Pham, et al., Ni and Ag electrodes for magnesium silicide based thermoelectric generators, Mater Today Energy 11 (2019) 97–105.
[33] S. Ayachi, et al., Developing contacting solutions for Mg2Si1−x Sn x-based thermoelectric generators: Cu and Ni45Cu55 as potential contacting electrodes, ACS Appl. Mater. Interfaces 11 (43) (2019) 40769–40780.
[34] J. de Boor, et al., Fabrication and characterization of nickel contacts for magnesium silicide based thermoelectric generators, J. Alloys Compd. 632 (2015) 348–353.

[35] J. de Boor, et al., Thermal stability of magnesium silicide/nickel contacts, J. Electron. Mater. 45 (10) (2016) 5313–5320.
[36] K. Mitra, S. Mahapatra, T. Dasgupta, Fabrication of nickel contacts for Mg 2 Si based thermoelectric generators via an induction assisted rapid monoblock sintering technique, J. Electron. Mater. 48 (3) (2019) 1754–1757.
[37] S. Ayachi, et al., On the relevance of point defects for the selection of contacting electrodes: Ag as an example for Mg2(Si,Sn)-based thermoelectric generators, Mater. Today Phys. 16 (2021) 100309.
[38] S. Ayachi, et al., Contacting Cu electrodes to Mg 2 Si 0.3 Sn 0.7: direct vs. Indirect resistive heating, Semiconductors 53 (13) (2019) 1825–1830.
[39] P. Zwolenski, J. Tobola, S. Kaprzyk, A theoretical search for efficient dopants in Mg 2 X (X= Si, Ge, Sn) thermoelectric materials, J. Electron. Mater. 40 (5) (2011) 889–897.
[40] J.-i. Tani, H. Kido, First-principles and experimental studies of impurity doping into Mg2Si, Intermetallics 16 (3) (2008) 418–423.
[41] F. Nix, D. MacNair, The thermal expansion of pure metals: copper, gold, aluminum, nickel, and iron, Phys. Rev. 60 (8) (1941) 597.
[42] Y. Gelbstein, et al., Physical, mechanical, and structural properties of highly efficient nanostructured n-and p-silicides for practical thermoelectric applications, J. Electron. Mater. 43 (6) (2014) 1703–1711.
[43] J. Murray, A. McAlister, The Al-Si (aluminum-silicon) system, Bull. Alloy Phase Diagrams 5 (1) (1984) 74.
[44] A. McAlister, D. Kahan, The Al-Sn (aluminum-tin) system, Bull. Alloy Phase Diagrams 4 (4) (1983) 410–414.
[45] Z. Li, et al., Control of Mg2Sn formation through ultrasonic-assisted transient liquid phase bonding of Mg to Al, J. Mater. Process. Technol. 255 (2018) 524–529.
[46] M. Bartur, M.-A. Nicolet, Aluminum contact to nickel silicide using a thin tungsten barrier, Thin Solid Films 91 (2) (1982) 89–98.
[47] T. Kajikawa, et al., Thermoelectric properties and electrode bonding performance for metal silicides, in: Proceedings ICT2001. 20 International Conference on Thermoelectrics (Cat. No. 01TH8589), IEEE, 2001.
[48] N. Farahi, et al., High efficiency Mg 2 (Si, Sn)-based thermoelectric materials: scale-up synthesis, functional homogeneity, and thermal stability, RSC Adv. 9 (40) (2019) 23021–23028.
[49] A. Sankhla, et al., Analyzing thermoelectric transport in n-type Mg2Si0. 4Sn0. 6 and correlation with microstructural effects: an insight on the role of Mg, Acta Mater. 199 (2020) 85–95, https://doi.org/10.1016/j.actamat.2020.07.045. ISSN 1359-6454.
[50] H. Kamila, et al., Synthesis of p-type Mg2Si1-xSnx with x= 0-1 and optimization of the synthesis parameters, Mater. Today: Proc 8 (2019) 546–555.
[51] D. Platzek, et al., Potential-Seebeck-microprobe (PSM): measuring the spatial resolution of the Seebeck coefficient and the electric potential, in: ICT 2005. 24th International Conference on Thermoelectrics, IEEE, 2005.
[52] H. Kamila, et al., Analyzing transport properties of p-type Mg 2 Si–Mg 2 Sn solid solutions: optimization of thermoelectric performance and insight into the electronic band structure, J. Mater. Chem. 7 (3) (2019) 1045–1054.
[53] N. Farahi, et al., Nano-and microstructure engineering: an effective method for creating high efficiency magnesium silicide based thermoelectrics, ACS Appl. Mater. Interfaces 8 (50) (2016) 34431–34437.
[54] D.K. Schroder, Semiconductor Material and Device Characterization, John Wiley & Sons, 2015.
[55] P. Ziolkowski, et al., Probing thermopower on the microscale, Phys. Status Solidi 210 (1) (2013) 89–105.
[56] D. Kato, et al., Control of Mg content and carrier concentration via post annealing under different Mg partial pressures for Sb-doped Mg2Si thermoelectric material, J. Solid State Chem. 258 (2018) 93–98.
[57] H. Kasai, et al., Multi-temperature structure of thermoelectric Mg2Si and Mg2Sn, Acta Crystallogr. B: Struct. Sci., Crystal Eng. Mater. 73 (6) (2017) 1158–1163.
[58] M. Rittiruam, et al., Predication of thermal conductivity of Mg2X (X= Ge and Sn) by molecular dynamics, Integrated Ferroelectrics Int. J. 165 (1) (2015) 61–72.
[59] A. Evans, E. Charles, Strength recovery by diffusive crack healing, Acta Metall. 25 (8) (1977) 919–927.
[60] I.A. Chou, H.M. Chan, M.P. Harmer, Effect of annealing environment on the crack healing and mechanical behavior of silicon carbide-reinforced alumina nanocomposites, J. Am. Ceram. Soc. 81 (5) (1998) 1203–1208.
[61] X. Liu, et al., Significant roles of intrinsic point defects in Mg2X (X= Si, Ge, Sn) thermoelectric materials, Adv. Electron. Mater. 2 (2) (2016) 1500284.
[62] P. Vivekanandhan, et al., Structural features and thermoelectric properties of spark plasma assisted combustion synthesised Magnesium silicide doped with Aluminium, Mater. Chem. Phys. 241 (2020) 122407.
[63] J.-i. Tani, H. Kido, Thermoelectric properties of Al-doped Mg2Si1−xSnx (x≦ 0.1), J. Alloys Compd. 466 (1–2) (2008) 335–340.
[64] X. Hu, M.R. Barnett, A. Yamamoto, Synthesis of Al-doped Mg2Si1−xSnx compound using magnesium alloy for thermoelectric application, J. Alloys Compd. 649 (2015) 1060–1065.
[65] G. Kim, et al., Co-doping of Al and Bi to control the transport properties for improving thermoelectric performance of Mg2Si, Scripta Mater. 116 (2016) 11–15.
[66] A. Kato, T. Yagi, N. Fukusako, First-principles studies of intrinsic point defects in magnesium silicide, J. Phys. Condens. Matter 21 (20) (2009) 205801.
[67] S. Battiston, et al., Multilayered thin films for oxidation protection of Mg2Si thermoelectric material at middle–high temperatures, Thin Solid Films 526 (2012) 150–154.
[68] F. D'Isanto, et al., Oxidation protective glass coating for magnesium silicide based thermoelectrics, Ceram. Int. 46 (15) (2020) 24312–24317.
[69] F. Gucci, et al., Oxidation protective hybrid coating for thermoelectric materials, Materials 12 (4) (2019) 573.
[70] P. Nieroda, et al., New high temperature amorphous protective coatings for Mg2Si thermoelectric material, Ceram. Int. 45 (8) (2019) 10230–10235.
[71] Y. Sadia, D. Ben-Ayoun, Y. Gelbstein, PbO–SiO2-based glass doped with B2O3 and Na2O for coating of thermoelectric materials, J. Mater. Res. 34 (20) (2019) 3563–3572.
[72] J.-i. Tani, M. Takahashi, H. Kido, Fabrication of oxidation-resistant β-FeSi2 film on Mg2Si by RF magnetron-sputtering deposition, J. Alloys Compd. 488 (1) (2009) 346–349.

Supplementary Information

It is possible to plot the dependence between the Seebeck coefficient and the carrier concentration of a thermoelectric material, using a single parabolic band model (SPB) [1]. In this model, the transport properties are obtained following the equations given by:

$$|S| = \frac{k_B}{e} * \left(\frac{2F_1(\eta)}{F_0(\eta)} - \eta\right) \quad (3)$$

$$n = 4\pi \left(\frac{2m_d^* k_B T}{h^2}\right)^{1,5} F_{\frac{1}{2}}(\eta) \quad (4)$$

Where $\eta = \frac{E_F}{k_B T}$ is the reduced chemical potential, m_d^* the density of states effective mass and *n* the carrier concentration, k_B is the Boltzmann's constant, $F_i(\eta)$ is the Fermi integral of order i. The effective mass of the materials are $2.5\ m_0$ for n-type [2] and $1.5\ m_0$ for p-type [1].

These plots, called Pisarenko plots, are shown in Figure 1. They can be used to deduce charge carrier mobility, providing measured data of the Seebeck coefficient and electrical conductivity is available.

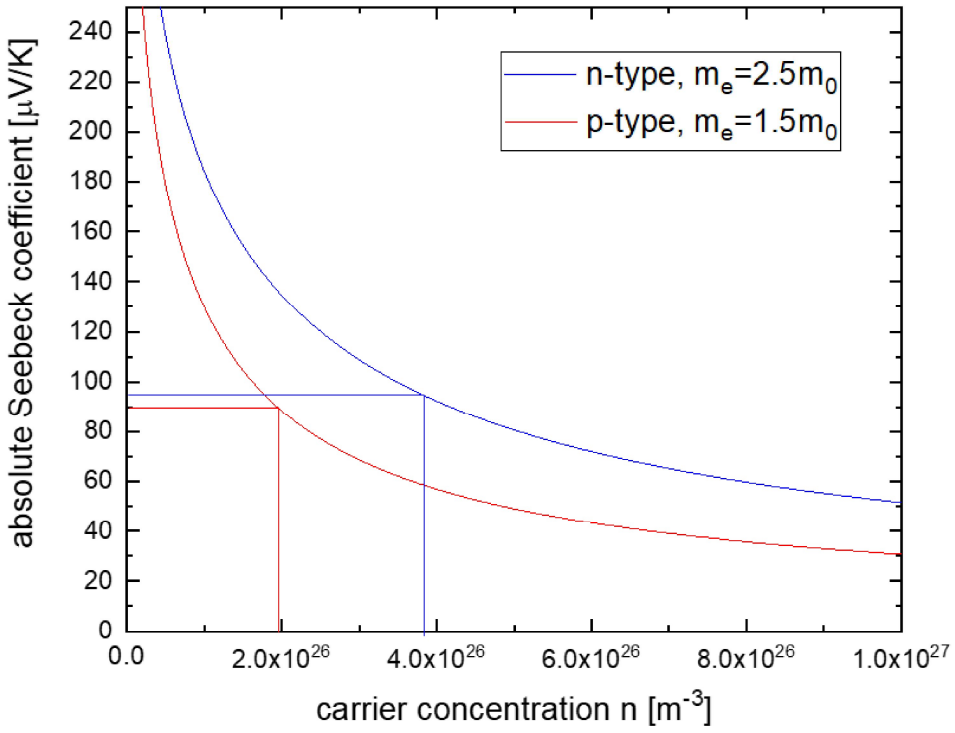

Figure 1 – Pisarenko plots for n- and p-type $Mg_2(Si,Sn)$, with marked respective values for Seebeck coefficients before contacting and annealing

1. Kamila, H., et al., *Analyzing transport properties of p-type Mg 2 Si–Mg 2 Sn solid solutions: optimization of thermoelectric performance and insight into the electronic band structure.* Journal of Materials Chemistry A, 2019. **7**(3): p. 1045-1054.
2. Farahi, N., et al., *Nano-and microstructure engineering: an effective method for creating high efficiency magnesium silicide based thermoelectrics.* ACS Applied Materials Interfaces, 2016. **8**(50): p. 34431-34437.

4. Chapter 4 (Paper 2): Overcoming Asymmetric Contact Resistances in Al-Contacted $Mg_2(Si,Sn)$ Thermoelectric Legs

In this paper/chapter, we discuss a strategy to optimize Al contacting to $Mg_2(Si,Sn)$, increasing reproducibility of the process and the results.

It is pointed out that the main drawback of using Al as electrode for $Mg_2(Si,Sn)$ is the lack of reproducibility of electrical contact resistances. While some samples have satisfyingly low contact resistivities, significant asymmetry in contact resistivity values between both interfaces of the samples is frequently occurring. In this paper, we show that this asymmetry originates from the dicing step. As the dicing step is unavoidable in the current leg fabrication process (direct bonding of metallic foil), finding a way to ensure low contact resistivities on both sides of the samples was necessary.

It is found that using ion etching on the Al foils before sputtering a layer of oxidation barrier is an effective strategy to maintain symmetrically low contact resistivities after the dicing step. Zn is used as a "sacrificial" oxidation barrier material, meant to melt during the contacting step, after which protecting the Al from oxidation is no longer needed. Zn is chosen due to its low melting point and its high solubility in Al at the temperatures used in the process.

The diffusion of Zn leads to the appearance of a gradient in the Seebeck coefficient from the interfaces towards the middle of the n-type material (similarly to Ag) while no effect is observed on the p-type material.

In this thesis, **the published version of the paper, following the journal´s template,** is provided. This work was published on 10 November 2021 in Materials journal, Volume 14, page 6774.

Reference: J. Camut, S. Ayachi, S.; G. Castillo-Hernández, S. Park, B. Ryu, S. Park, A. Frank, C. Stiewe, E. Müller, J. de Boor, *Overcoming Asymmetric Contact Resistances in Al-Contacted Mg2(Si,Sn) Thermoelectric Legs*, Materials, 2021, 14, 6774, https://doi.org/10.3390/ma14226774

materials

MDPI

Article

Overcoming Asymmetric Contact Resistances in Al-Contacted $Mg_2(Si,Sn)$ Thermoelectric Legs

Julia Camut [1,*], Sahar Ayachi [1], Gustavo Castillo-Hernández [1], Sungjin Park [2], Byungki Ryu [2], Sudong Park [2], Adina Frank [1], Christian Stiewe [1], Eckhard Müller [1,3] and Johannes de Boor [1,4,*]

1 Department of Thermoelectric Materials and Systems, Institute of Materials Research, German Aerospace Center, 51147 Cologne, Germany; sahar.ayachi@dlr.de (S.A.); gustavo.castillo-hernandez@dlr.de (G.C.-H.); adina.frank@dlr.de (A.F.); christian.stiewe@dlr.de (C.S.); Eckhard.mueller@dlr.de (E.M.)
2 Energy Conversion Research Center, Korea Electrotechnology Research Institute (KERI), 12, Jeongiui-gil, Seongsan-gu, Changwon-si 51543, Gyengsangnam-do, Korea; sjinpark@keri.re.kr (S.P.); byungkiryu@keri.re.kr (B.R.); john@keri.re.kr (S.P.)
3 Institute of Inorganic and Analytical Chemistry, JLU Giessen, 35390 Giessen, Germany
4 Institute of Technology for Nanostructures (NST), Faculty of Engineering, University of Duisburg-Essen, 47057 Duisburg, Germany
* Correspondence: julia.camut@dlr.de (J.C.); Johannes.deboor@dlr.de (J.d.B.)

Abstract: Thermoelectric generators are a reliable and environmentally friendly source of electrical energy. A crucial step for their development is the maximization of their efficiency. The efficiency of a TEG is inversely related to its electrical contact resistance, which it is therefore essential to minimize. In this paper, we investigate the contacting of an Al electrode on $Mg_2(Si,Sn)$ thermoelectric material and find that samples can show highly asymmetric electrical contact resistivities on both sides of a leg (e.g., 10 $\mu\Omega\cdot cm^2$ and 200 $\mu\Omega\cdot cm^2$). Differential contacting experiments allow one to identify the oxide layer on the Al foil as well as the dicing of the pellets into legs are identified as the main origins of this behavior. In order to avoid any oxidation of the foil, a thin layer of Zn is sputtered after etching the Al surface; this method proves itself effective in keeping the contact resistivities of both interfaces equally low (<10 $\mu\Omega\cdot cm^2$) after dicing. A slight gradient is observed in the n-type leg's Seebeck coefficient after the contacting with the Zn-coated electrode and the role of Zn in this change is confirmed by comparing the experimental results to hybrid-density functional calculations of Zn point defects.

Keywords: thermoelectrics; thermoelectric generator; contacting; contact resistance; electrode; silicides; process

Citation: Camut, J.; Ayachi, S.; Castillo-Hernández, G.; Park, S.; Ryu, B.; Park, S.; Frank, A.; Stiewe, C.; Müller, E.; de Boor, J. Overcoming Asymmetric Contact Resistances in Al-Contacted $Mg_2(Si,Sn)$ Thermoelectric Legs. *Materials* **2021**, *14*, 6774. https://doi.org/10.3390/ma14226774

Academic Editors: Zihang Liu and Takao Mori

Received: 6 October 2021
Accepted: 5 November 2021
Published: 10 November 2021

1. Introduction

With their ability to convert waste heat into electricity, thermoelectric generators (TEG) are a promising source of renewable energy. They have no moving parts, making their maintenance easy, and they have the advantage of being lightweight and reliable, which makes them relevant in fields such as the aerospace and the automotive industries [1–3].

A TEG is typically composed of n- and p-type thermoelectric (TE) legs, which are connected to metal-bonded ceramic plates electrically in series and thermally in parallel [4]. The legs are usually functionalized: they are contacted with a metallic layer, referred to as electrode, that will be then soldered to the metallic bridges, which interconnects the legs in an electrical circuit. This electrode can have a barrier diffusion function or be combined with another layer that plays this role, and is also applied to facilitate the bonding of the TE elements to the bridges. The establishment of a good electrical contact between metals, which are indeed simpler. Applying solders directly between the bridges and the TE legs could alter the TE properties due to diffusion processes. The design of the legs and the choice of the TE materials in TEGs can vary in order to suit their different applications [5].

To assess the performance of a TEG, its power output P and its conversion efficiency η can be calculated, using the TE material properties and the contact resistances between the TE legs and the electrodes. The equations for a TEG containing N pairs of thermoelectric legs are shown in the following equations [6]:

$$P = \frac{S^2\sigma}{2}\frac{NA(T_h - T_c)^2}{(l+n)} \quad (1)$$

$$\eta = \left(\frac{T_h - T_c}{T_h}\right)\left\{2 - \frac{1}{2}\left(\frac{T_h - T_c}{T_h}\right) + \frac{4}{zT_h}\left(\frac{l+n}{l}\right)\right\}^{-1} \quad (2)$$

where S and σ are the Seebeck coefficient and electrical conductivity of a pair of n-type and p-type legs, z its figure of merit calculated as $z = \frac{S^2\sigma}{\kappa}$, where κ is the thermal conductivity. In this equation, equal properties for n- and p-type materials are assumed; in the case of unequal properties and cross-sections, the average of the Seebeck coefficients, of the electrical resistances and of the thermal conductances should be used. N is the number of leg pairs in the module; A is the cross-sectional area of a leg; T_h and T_c are, respectively, the temperatures at the hot and cold sides of the TE legs; l is the length of a TE leg; $n = 2\sigma\rho_c$, where ρ_c is the electrical specific contact resistance. The equations assume temperature independent properties and also neglect 2D or 3D effects.

These equations show that, for a given temperature range, material optimization and contact quality improvement are crucial to increase the TEG performance. Low electrical contact resistance ($\leq$10% for each TE leg) and TE materials with a high figure of merit ($zT \geq 1$) are standard requirements for industrial use of TEG [7].

The TE solid solutions $Mg_2Si_{1-x}Sn_x$ ($x \approx 0.6$–0.7) have reproducibly high thermoelectric properties with a figure of merit of up to zT = 0.6 for p-type and 1.4 for n-type at 450 °C [8–14]. On top of being lightweight, this material has the advantage of being inexpensive and non-toxic. Mg_2X has a cubic anti-flourite $Fm\bar{3}m$ crystal structure [15,16].

A few silicide-based modules combining n-type Mg_2Si and p-type HMS (High-Manganese Silicide) legs were already reported [17–24]. However, the development of a fully $Mg_2(Si,Sn)$-based TEG remains at an early stage. Gao reported a first attempt at building such a TEG [25], showing a maximum power output of 117 mW for T_h = 440 °C and T_c = 110 °C. Recently, Goyal et al. reported a power density of 0.52 W/cm^2 and a computed predicted maximum efficiency of 5% for a fully $Mg_2(Si,Sn)$-based TEG [26].

A first step in the development of a fully $Mg_2(Si,Sn)$-based TEG is the electrode selection. Several attempts were reported with only partially promising results, as the electrodes provided low electrical contact resistance but also led to cracking (Ni, constantan) or altering of the TE material's Seebeck coefficient (Cu, Ag) [27–29]. Most recently, aluminum was reported as the best electrode for this TE material system, showing low electrical contact resistance and good thermal and chemical stability of the interface also through annealing [30]. In that work, one of the reported samples showed asymmetric electrical contact resistances at the two contacting faces before annealing. The difference between the two sides was of several orders of magnitude and, although the highly resistive contact seemed to heal with annealing, the reason for this initial asymmetry could not be given. A similar case can also be found with silver electrodes [29], and we also encountered this issue with Ag and Ni electrodes, as shown in Supplementary Information. No similar phenomenon seems to have been reported in the thermoelectrics or even in the broader electronics field.

A high electrical contact resistance, even if only located on one side of the TE leg, is detrimental to a TEG performance. Even in the case of a reduction of the electrical contact resistance with annealing, which could happen during the lifetime of the TEG, this would create a consequent delay in optimal performance. A high electrical contact resistance could also potentially indicate a poor physical adhesion, which could lead to an early mechanical failure of a working device composed of such kind of legs. Since the

technological steps towards TEG have not yet been thoroughly studied nor reported, it is likely that this asymmetry in contact resistances was or will be encountered in other studies.

This paper is focused on the study of this asymmetry phenomenon using aluminum electrodes, as previously reported. Based on the statistics of various samples, the influence of the typically most relevant processing parameters for contacting can be ruled out (e.g., temperature, pressure…). However, it was found that the asymmetry in contact resistances appears during the dicing step, as the high electrical contact resistance is systematically observed on the sample side, which is at the bottom, attached to the sample holder, during dicing. A strategy consisting in etching the Al foil and protecting it with a sputtered Zn layer as oxidation barrier prior to contacting is shown to effectively avoid the asymmetry in electrical contact resistances after dicing. This indicates that the rise in the bottom side electrode's electrical resistivity during dicing is probably due to the presence of the native oxidation layer on Al foils prior to contacting. The added Zn layer does not trigger any chemical reaction detrimental to the interface adhesion, and does not alter the p-type Seebeck coefficient. A slight gradient in the Seebeck coefficient is observed for the n-type sample, but its magnitude is low enough to preserve future TEG's performance. In this manuscript, we show an efficient way to overcome a technical challenge for the fabrication of a Mg_2(Si,Sn)-based TEG.

2. Materials and Methods

2.1. Experimental

The solid solution Mg_2(Si,Sn) pellets were prepared similarly to what was reported in previously published papers [27,30–32], with the following nominal stoichiometry: $Mg_{2.06}Si_{0.3}Sn_{0.665}Bi_{0.035}$ for n-type and $Mg_{1.98}Li_{0.03}Si_{0.3}Sn_{0.7}$ for p-type. The n-type composition contains Mg with an excess of 3% in order to compensate for the Mg evaporation occurring during the sintering, due to its longer duration compared to p-type samples. The pellets' preparation prior to contact as well as the contacting parameters are also identical to what was previously published [30]. Unless specified otherwise, the contacting temperature for the samples presented in this paper is 475 °C. After contacting, the pellets are diced into legs using a Disco DAD321 Automatic Dicing Saw). The cutting speed through the sample was 0.3 mm/s with an angular speed of 30,000 blade rotations per minute and each cut was made in two passes, keeping the mechanical stress to the sample by the blade´s displacement as low as possible.

The quality of the joining is estimated by the value of its specific contact resistance rc and the preservation of the Seebeck coefficient of the TE material using a Potential & Seebeck Scanning Microprobe (PSM) [33]; and by its microstructural and chemical composition at the interface using scanning electron microscopy (Zeiss Ultra 55 SEM equipped with an EDX detector). Two r_c values are obtained for each contact with two different calculation methods, using the TE material´s electrical conductivity to calculate the current density ($r_{c,j(TE)}$), or using the current passing through the sample as measured by the PSM ($r_{c,j(PSM)}$), as reported in previously published papers [27,30]. The two specific electrical contact resistances are calculated using the following equations:

$$r_{c,j(TE)} = \frac{(V_{elec} - V_{TE}) \times l_{TE}}{\Delta V_{TE} \times \sigma_{TE}} \quad (3)$$

$$r_{c,j(PSM)} = \frac{(V_{elec} - V_{TE}) \times A}{I_{PSM}} \quad (4)$$

where V_{elec} is the potential on the electrode (metallic) at the interface and V_{TE} is the potential on the TE material at the interface, the position of interface being located using the drop in Seebeck coefficient on the line-scan. The difference $V_{elec} - V_{TE}$ corresponds, therefore, to the drop of potential across the electrode-TE interface. l_{TE} is the length of the TE material (between the two electrodes), ΔV_{TE} is the drop of potential across the TE material and σ_{TE}

is the electrical conductivity of the TE material, measured using a 4-probe inline technique, A is the sample cross-section and I_{PSM} the current measured in the device.

Multiple line-scans are measured for each sample, each r_c value presented below is the average value of all the lines, given with the corresponding standard deviation.

The calculation of the electrical contact resistance according to Equation (4) requires the assumption that the current density is homogeneous over the whole sample (along cross-section and length), while Equation (3) only assumes a constant current density along the direction of the line-scan. The more inhomogeneous the interface, the more different are the results given by both equations. The comparison of those two values allows to assess the reliability of the measurement and the quality of the Al/TE interface.

The Zn coating suggested as an oxidation barrier was applied by magnetron sputtering using an AXPLORER 4375 S3E1 PVD machine. An ion etching process was performed on the Al foil surface prior to the Zn coating in order to remove the oxide layer on the Al surface. The coating was deposited at room temperature on a substrate rotating at 10 min^{-1} with a starting vacuum of 5×10^{-6} mbar. The duration of the coating was 90 min with a growth rate of 1.3 nm/s. The Zn target used for this process was provided by EvoChem (purity 99.99%).

2.2. Computational Method

First-principles calculations were performed to study the defect stability of Zn related point defects in Mg_2Si and Mg_2Sn using hybrid-density functional calculations [34]. The planewave basis set and the projector-augmented wave pseudopotentials [35] were used, as implemented in the Vienna Ab initio Simulation Package (VASP) code [36]. For the exchange-correlation functional, the Perdew–Burke–Ernzerhof parameterized generalized gradient approximation [37] was used. For hybrid calculations, the HSE06 is used with the exact mixing fraction of 25% and the screening parameter of 0.208 $Å^{-1}$ [34].

For the defect stability, the charged defect formation energy of defect D with charge state q (D^q), where q is +2, +1, 0, −1, −2, was calculated using the following equation [38]

$$E_{Form}[D^q] = E_{tot}[D^q] - E_0 - \Sigma_i \, (\, \mu_i \, \delta n_i) + q(E_F) \quad (5)$$

where $E_{tot}[D^q]$ and E_0 are total energies with and without defects, subscript i indicates the atomic element, μ_i is the atomic chemical potential, δn_i is the change of number of i-th element in the defective supercell with respect to the pristine one, and E_F is the Fermi level of the system. Detailed information can be found in our previous work [39–41].

The defect density of D^q in Mg_2Si or Mg_2Sn can be estimated using the defect formation energy and the Boltzmann factor for a given material synthesis temperature.

3. Results

Figure 1 shows the ratio of the electrical contact resistance of both sides of the functionalized leg. It displays a quite large range of r_{c1}/r_{c2} (factor of 1 to 100) extracted from more than 30 Al-contacted samples and various combinations of experimental parameters. It can be seen that a minority of the samples actually have symmetric contact resistances, such as those shown in the study about aluminum contacting [30]. Some experimental factors, such as contacting temperature, pressure and TE pellet length, were suspected as more likely to be the causes for the asymmetry. However, when plotted accordingly, none of them shows a significant correlation with the asymmetry, as can be seen in Figure 1.

Other factors—carrier type, TE pellet geometry (diameter of 15 or 30 mm), presence or absence of a buffer layer during contacting, direct vs. indirect setup—did not show a clear correlation either, see Table S2 in the SI. Indeed, asymmetrically contacted samples could be randomly found for all "configurations" of those factors.

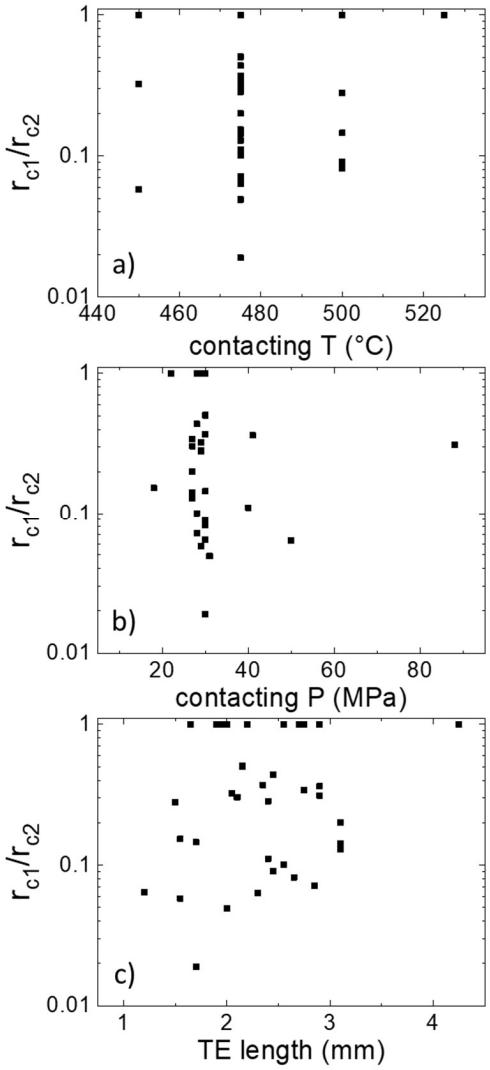

Figure 1. Ratio of the two electrical contact resistances of the same sample (smaller/larger) depending on various experimental parameters: (**a**) contacting temperature, (**b**) contacting pressure, (**c**) TE length before contacting. The samples are all $Mg_2(Si,Sn)$ with Al electrodes.

In order to determine if this asymmetry phenomenon is linked to the joining or the dicing step in the leg fabrication process, two differential experiments were designed. In the first one, the side of the sample which is at the top during the contacting step is also on the top during the dicing step, while in the second one, the sides are switched (the top side during contacting goes at the bottom during dicing). The experiments are labelled "X/Y" with X being the position of one side during contacting and Y the position of that same side during dicing. After contacting, the pellets are cut in 9 square-based legs. The results of the top/top experiment are shown in Table 1**.** while the results of the top/bottom experiment are shown in Table 2. The two contact resistivity values are obtained using the Equations (3) and (4). Exemplary line scans of the potential and the Seebeck coefficient are shown in Figure S4 in SI for each experiment.

The most important observation from both tables is that the side with the higher specific contact resistance is always the side at the bottom during cutting, which indicates that the asymmetry is not linked to the contacting but to the dicing step.

Table 1. Specific electrical contact resistances r_c on both sides of several legs, diced from a pellet contacted with Al foils. Leg 6 is missing as it broke during preparation, and leg 1 was cracked, which led to a massive potential drop, therefore the corresponding values are not reported.

Top/Top		Leg 2	Leg 3	Leg 4	Leg 5	Leg 7	Leg 8	Leg 9	Average
Side on top during dicing	$r_{c,j(TE)}$ ($\mu\Omega\cdot cm^2$)	12 ± 8	8 ± 5	5 ± 2	9 ± 5	25 ± 13	7 ± 4	9 ± 4	10.7
	$r_{c,j(PSM)}$ ($\mu\Omega\cdot cm^2$)	14 ± 9	7 ± 4	9 ± 5	11 ± 6	18 ± 9	5 ± 3	10 ± 4	10.6
Side on bottom during dicing ($\mu\Omega\cdot cm^2$)	$r_{c,j(TE)}$ ($\mu\Omega\cdot cm^2$)	368 ± 246	380 ± 57	702 ± 90	256 ± 100	305 ± 19	396 ± 80	298 ± 50	386.4
	$r_{c,j(PSM)}$ ($\mu\Omega\cdot cm^2$)	417 ± 278	301 ± 45	1435 ± 184	306 ± 120	218 ± 13	313 ± 64	350 ± 59	477.1

Table 2. Specific electrical contact resistances r_c on both sides of a pellet contacted with Al foils, after dicing into several legs. legs 1, 2 and 3 broke during grinding. Legs 4 and 6 got detached from the sample holder and are therefore not identifiable.

Top/Bottom		Leg 5	Leg 7	Leg 8	Leg 9	Average
Side on top during dicing	$r_{c,j(TE)}$ ($\mu\Omega\cdot cm^2$)	7 ± 5	15 ± 7	6 ± 2	7 ± 5	7.5
	$r_{c,j(PSM)}$ ($\mu\Omega\cdot cm^2$)	8 ± 6	12 ± 5	7 ± 3	9 ± 6	8.8
Side on bottom during dicing ($\mu\Omega\cdot cm^2$)	$r_{c,j(TE)}$ ($\mu\Omega\cdot cm^2$)	581 ± 101	199 ± 22	100 ± 46	107 ± 25	258.2
	$r_{c,j(PSM)}$ ($\mu\Omega\cdot cm^2$)	699 ± 122	156 ± 17	115 ± 53	144 ± 34	317.7

It can also be seen that some legs have a very high standard deviation. This typically indicates non-uniform interfaces in a sample: as the potential drop at the interface is greatly varying line to line due to varying contact quality, the resulting variation in the contact resistivity for one sample is higher. The asymmetry is generally more pronounced (higher r_c values at the bottom during dicing) for the top/top sample (Table 1) than for the top/bottom sample (Table 2). It is seen for both kinds of samples that the magnitude of the low r_c does not vary a lot, as it mostly remains below 15 $\mu\Omega\cdot cm^2$, while high r_c values vary more leg to leg.

In Figure S1 in SI, EDX line scans of the Al/TE interface are presented. It can be seen that for higher r_c, a peak of oxygen is observed at the junction. This peak is much weaker for interfaces with lower r_c, indicating a correlation between the initial presence or absence of oxidation on the Al foil and the magnitude of the specific electrical contact resistance.

Aluminum is known to oxidize quickly and to form a very stable oxide, Al_2O_3. Before joining, the Al foils are polished with SiC paper in order to diminish the thickness of the oxide layer. As this is a manual process, its reproducibility is limited (wear of the paper due to prior grinding of other foils, varying exposure time to air before the start of the joining process). This method also does not completely prevent the presence of an oxide layer, as a new, fresh Al_2O_3 layer forms within less than seconds under air. It is therefore suspected that the presence of oxide prior to contacting could play a role in the appearance of the high contact resistance during dicing, where the pulling forces would damage those areas with weaker adhesion.

To test this hypothesis, the Al foils were ion-etched under Ar in the PVD, with subsequent sputtering of an 8 µm Zn layer as oxidation protection. SEM pictures of the coating and a picture of a contacted pellet are shown in Figures S2 and S3 in SI. After Al/TE contacting with the coated foils, the functionalized pellets were cut similarly to the previous samples. The specific contact resistances for all legs are reported in Table 3. Zn was chosen due to its known solubility in Al [42,43]. Zn can still oxidize under air, which is why the foils are stored under Ar before contacting. However, a thickness of 8 µm is enough to protect the Al for at least the time necessary until the contacting process. Moreover, Zn has a low melting point which allows it to act as a solder during contacting and to break the oxide layer which might have formed at its surface.

Table 3. Specific electrical contact resistances r_c on both sides of legs cut from a pellet contacted with Zn-coated Al foils. No leg from this sample broke.

Zn-Sputtering		Leg 1	Leg 2	Leg 3	Leg 4	Leg 5	Leg 6	Leg 7	Leg 8	Leg 9	Average
Side on top during dicing	$r_{c,j(TE)}$ ($\mu\Omega\cdot cm^2$)	3 ± 1	5 ± 4	3 ± 1	3 ± 1	7 ± 7	3 ± 1	2 ± 1	3 ± 1	4 ± 2	3.7
	$r_{c,j(PSM)}$ ($\mu\Omega\cdot cm^2$)	3 ± 1	7 ± 6	3 ± 2	5 ± 1	15 ± 14	4 ± 1	2 ± 1	4 ± 1	7 ± 5	5.6
Side on bottom during dicing ($\mu\Omega\cdot cm^2$)	$r_{c,j(TE)}$ ($\mu\Omega\cdot cm^2$)	10 ± 7	12 ± 4	3 ± 1	3 ± 1	9 ± 5	3 ± 1	4 ± 1	46 ± 8	3 ± 2	10.3
	$r_{c,j(PSM)}$ ($\mu\Omega\cdot cm^2$)	20 ± 12	18 ± 7	4 ± 2	5 ± 2	19 ± 9	4 ± 1	5 ± 1	59 ± 10	6 ± 3	15.6

After dicing, most legs have low and symmetric r_c, which indicates that removing oxidation from the Al foil is an effective strategy to avoid asymmetric electrical contact resistances. A possible explanation for the asymmetry behavior could therefore be that local oxidation spots are present at the interface. During cutting, the interface around those points could be pulled apart more easily due to a concentration of stress, which would increase r_c.

An SEM picture of the interface, the corresponding EDX points analysis as well as an EDX mapping are respectively reported in Figure 2, Table 4 and Figure 3.

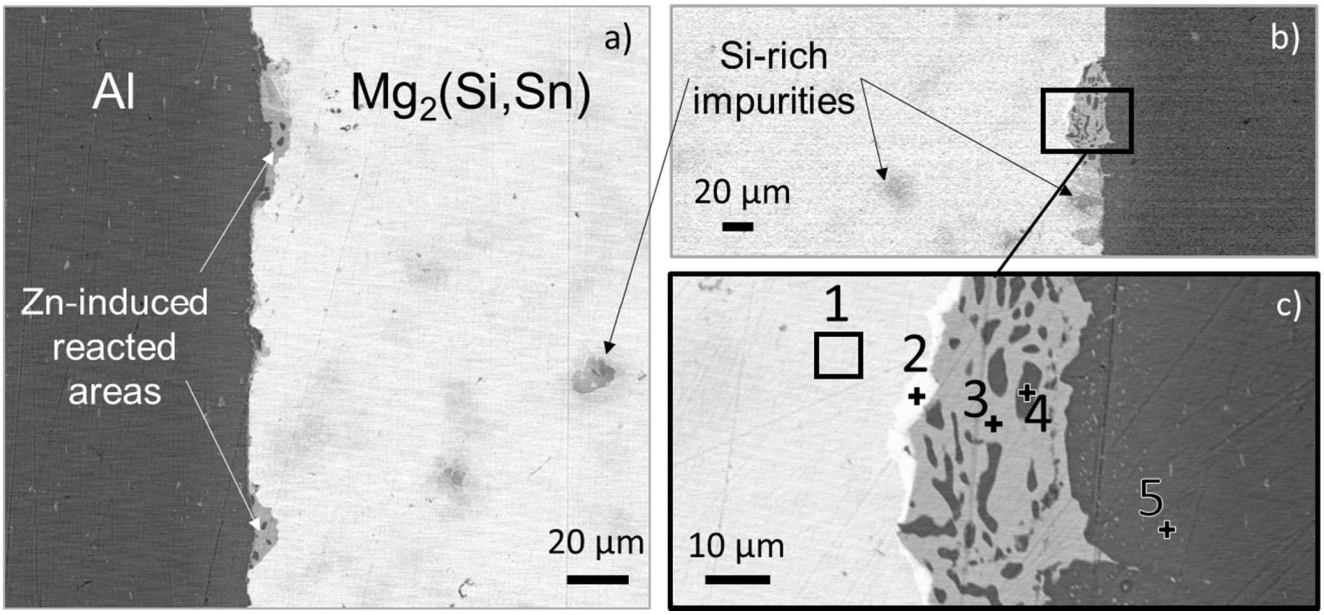

Figure 2. SEM images of different areas of the interface after contacting of a Zn-coated Al foil with a $Mg_2(Si,Sn)$ pellet: (**a**) first side interface, (**b**) second side interface, (**c**) zoom-in and point analysis of the reacted area in (**b**).

Table 4. EDX analysis of the points indicated in Figure 2. The quantities are given in at%.

Point	%Mg	%Si	%Sn	%Bi	%Zn	%Al
1	64.4	8.8	25.6	1.2	-	-
2	63.6	9.0	21.7	5.7	-	-
3	33.2	-	-	-	41.9	24.9
4	2.3	-	-	-	3.4	94.2
5	1.5	-	-	-	3.6	94.9

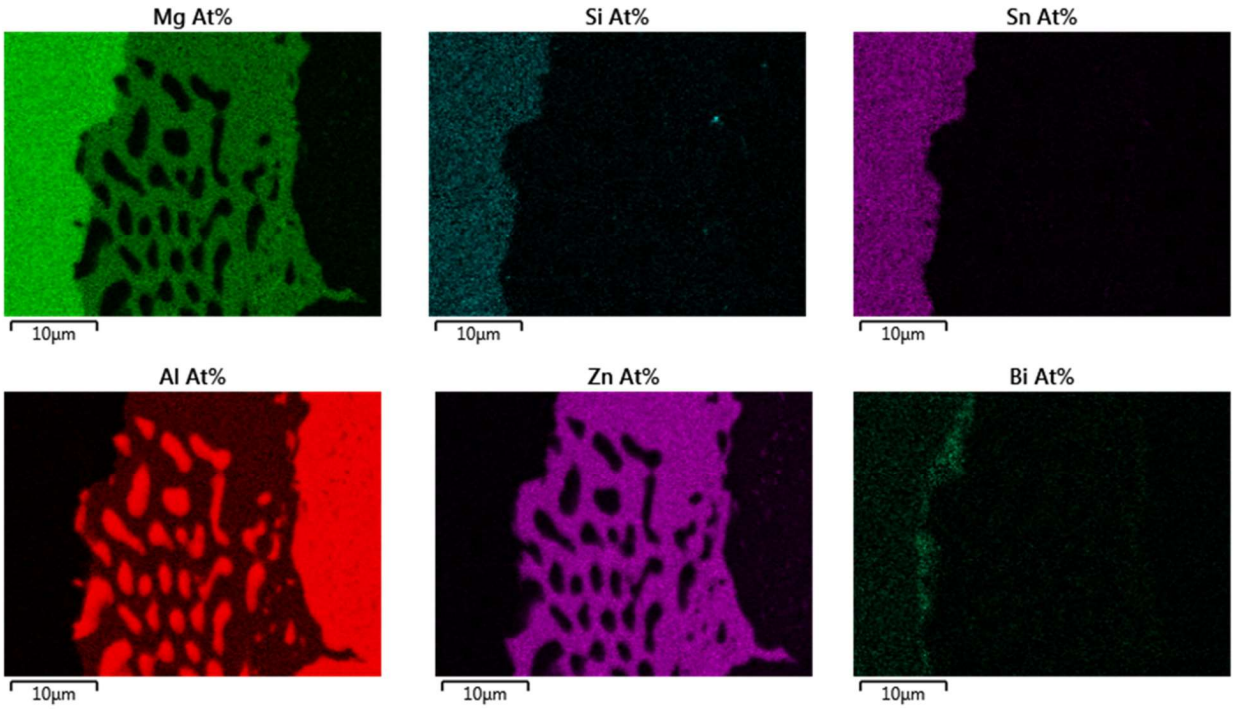

Figure 3. EDX mapping of a reaction area between Al, Zn and the $Mg_2(Si,Sn)$ TE material.

It was previously shown that there was no reaction at the interface between Al and $Mg_2(Si,Sn)$ directly after contacting [30]. Here, with the Zn coating, the interconnection zone contains scarce small areas with newly formed phases, of a diameter of 20–40 µm. They are mostly composed of a ternary alloy (Zn; Mg; Al) containing pure Al dots. At the interface between the interconnection zone and the $Mg_2(Si,Sn)$ matrix, a very bright Bi-rich phase is formed. From the mapping, it can be seen that, similarly to experiments with uncoated Al foils [30], there is no composition gradient neither in Al electrode, nor in the TE material next to the nuclei.

Contacting an electrode with a Zn layer implies that some Zn could diffuse into the TE material. This can potentially have detrimental effects on the TE properties (and potentially also on the thermal stability of the material) as was already observed with other electrodes such as Ag and Cu [29,32,39]. In order to check for those effects, Seebeck coefficient measurements were performed and reported in Figure 4. The results are from measurements after sintering (in black) and after contacting (in red).

For the p-type sample, the Seebeck coefficient changes by less than 10% between the sintered and the contacted states, which is negligible and could be attributed to the wear of the tip of the PSM. For the n-type sample, a gradient in the Seebeck coefficient appears after contacting. There is a difference of about 20 µV/K from the TE material-electrode interface to the center of the n-type material (−110 µV/K at the interface, −90 µV/K in the middle). The appearance of a gradient after contacting is similar to what was reported on contacting with Ag electrodes, in which case the gradient was explained by charge carrier compensation due to Ag diffusion into the TE material [29,39]. This hypothesis was supported by the relatively low formation energies of electrode-related point defects compared to the intrinsic and dopant-induced point defects.

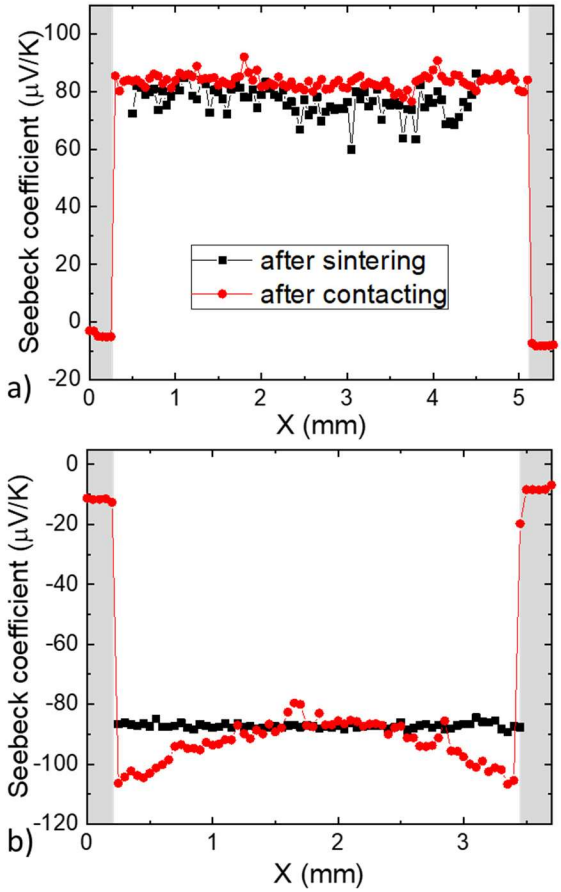

Figure 4. Seebeck scans along the (**a**) p-type, (**b**) n-type $Mg_2(Si,Sn)$ pellet contacted with Zn-coated Al foils after sintering and directly after contacting at 475 °C.

In order to verify if the same mechanism can explain our experimental results, hybrid-DFT calculations were performed to study the defect stability of Zn-related defects in Mg_2Si and Mg_2Sn. The possible formation of Zn-related point defects is confirmed by comparing the formation energies of the Zn-related point defects to those of intrinsic and extrinsic (Bi and Li) defects from previous papers [39,40]. As the samples of interest presented in this paper are Sn-rich $Mg_2(Si,Sn)$ solid solutions, only the results of Mg_2Sn are shown in Figure 5, while the results for Mg_2Si are shown in Figure S5 in SI. In these calculations, both Mg-poor and Mg-rich chemical potential environments were considered. In fact, the experimental n-type samples were synthesized with 3 at.% excess Mg, which means an initially Mg rich environment. However, after sintering and joining, Mg loss is very probable due to Mg evaporation and Mg diffusion. Therefore, it makes sense to also investigate the defect formation energies under Mg poor conditions. The case of p-type Li-doped Mg_2Sn under Mg-rich conditions will not be discussed. Indeed, Li doping is aimed at Mg sites in the Mg_2X material; however, it was found that, although Li on Mg site defects are stable, Li interstitials are even more stable defects [39]. This means that the Li-doped material will always contain a certain proportion of Mg vacancies and Mg-rich conditions will not be obtained. For simplicity, only the most stable defects (with $E_{form} < 1$ eV) are presented in the figure below and discussed. Note that if the defect formation energy difference is larger than 1 eV, the defect number density is negligible due to its exponential dependence on the defect formation energy [40].

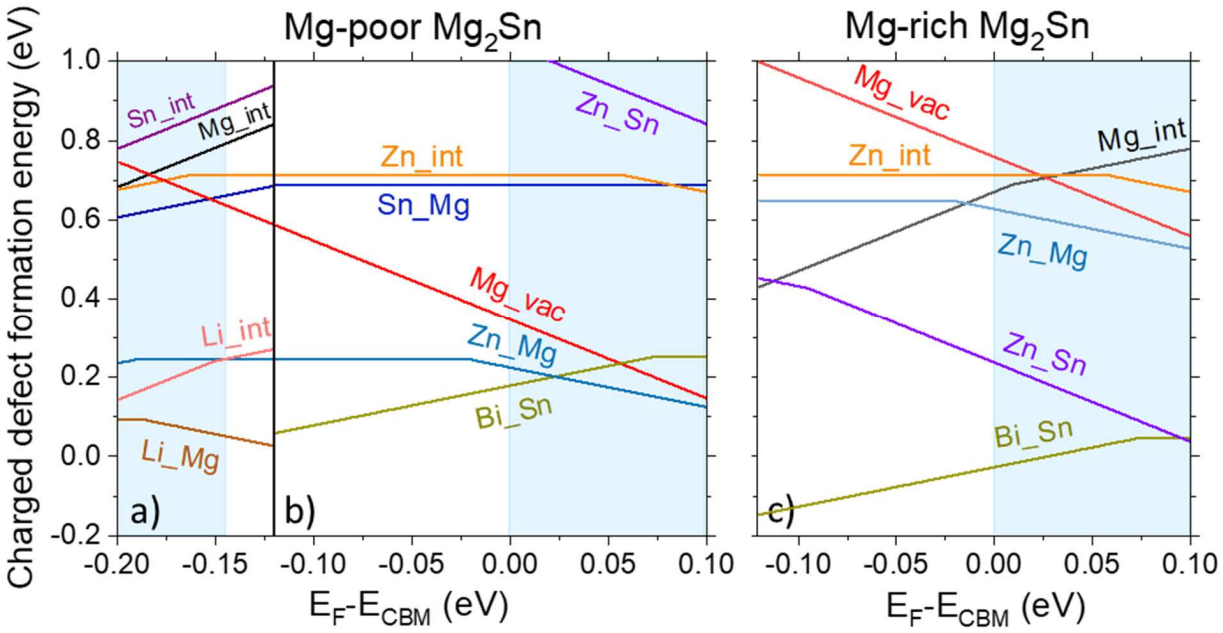

Figure 5. Charged defect formation energies for Zn defects in: (**a**) Li-doped (**b**) Bi-doped Mg_2Sn under Mg-poor conditions (**c**) Bi-doped Mg_2Sn under Mg-rich conditions. For simplicity, the results relevant for the Li-doped samples are represented in the Fermi level region around VBM only.

Figure 5 shows the charged defect formation energy as a function of the Fermi level for various defects in the case of Zn diffusion in Bi- and Li-doped Mg_2Sn. Here, we considered the Zn interstitial (Zn_int, or I_{Zn}), Zn substitutional at Mg (Zn_Mg or Zn_{Mg}), and Zn substitutional at Sn site (Zn_Sn or Zn_{Sn}).

Figure 5a,b show the defect formation energies of Zn in p- and n-type, respectively, Mg-poor Mg_2Sn. It is seen that in the p-type material, the Li_{Mg} (Li_Mg) defect (p-type dopant) is more stable than the most stable defect brought by Zn, meaning that no charge compensation is to be expected. For the n-type, the Zn_{Mg} defect is the most stable Zn-defect in Sn-rich Mg_2Sn and the corresponding defect formation energy is only 0.25 eV. As Zn and Mg have the same number of valence electrons, the Zn_{Mg} is an isovalent defect, which does not donate any hole or electron carrier if the Fermi level is at the middle of the bandgap. However, when the Fermi level is at the CBM, the charge state of Zn_{Mg} can be negative, indicating a possible electron trapping by Zn_{Mg}. This can be explained by the fact that, although Zn is isovalent to Mg, it can attract electrons as it has higher electronegativity compared to Mg. Similarly, conduction band subgap states acting as electron trap induced by metal cation disorder or anion isovalent doping were reported for oxide semiconductors [44] and GaAs [45].

Under Mg-rich conditions, Zn_{Sn} is the most stable Zn-related point defect and its charge state is always negative over the whole E_F range inside the band gap, as shown in Figure 5c.

From the above-charged defect formation energies, we elucidate that the Zn-related defects in Mg_2Sn can be electron trap centers in n-type Mg_2Sn. Ayachi et al., reported that Ag or Mg-related native defects diffuse easily in Mg_2Si and Mg_2Sn [39]. Similarly, we may expect that the Zn in the surface of Zn-coated Al electrode can diffuse towards Mg_2Sn. The Zn_{Sn} and Zn_{Mg} double electron killers can be generated inside the Mg-rich or Sn-rich n-type Mg_2Sn, respectively. As they can easily trap the electrons in the n-type Mg_2Sn where E_F is near the CBM, a charge compensation would occur.

These predictions of the hybrid-DFT calculations match with the experimental results obtained in Figure 4. Indeed, we see no change in the p-type carrier concentration and a decrease of n-type carrier concentration close to the contacts, indicated by the Seebeck

coefficient as S is inversely related to n. Diffusion of the sputtered Zn is therefore strongly suspected to be the origin of the change in TE properties.

4. Discussion

Although Al was found to be a promising electrode for the $Mg_2(Si,Sn)$ material system [30], the phenomena of asymmetry in electrical contact resistances on a functionalized leg was repeatedly observed on multiple $Mg_2(Si,Sn)$ samples contact to Al electrodes with various experimental parameters. No correlation could be found between the ratio of electrical contact resistivities and the contacting parameters. Furthermore, the contacting-dicing experiment of this work showed that the high r_c was systematically found at the bottom side from the dicing step, which indicates that the asymmetry does not originate from the contacting but from the dicing process.

The presence of an oxygen peak on the EDX line scans at the Al/TE interfaces with high electrical contact resistances (SI), as well as the disappearance of the asymmetry when oxidation is avoided on the Al foil, indicates that the native oxide layer of the Al electrode could be the origin of the phenomenon. The oxide can prevent proper adhesion [46], which creates areas where the contact between the TE material and Al is weak and more sensitive to the mechanical stress applied during dicing [47].

Using ion-etching and Zn sputtering as an oxidation barrier is shown to be an efficient method to ensure low and symmetric electrical contact resistivities after dicing. A gradient in the Seebeck coefficient is observed after contacting on the n-type sample, indicating a decrease in carrier concentration in the TE material close to the interfaces. This behavior shows that the diffusion of one or several elements changes the defect concentrations, which alters the local carrier concentration. Given the low magnitude of this gradient, the corresponding change in carrier concentration should be minor and there should not be any significant impact on the performance of the leg in a TEG. Indeed, supposing that the whole leg's Seebeck coefficient changed from -90 µV/K to -110 µV/K (instead of only the areas close to the contacts), it can be deducted, using the Pisarenko plot in Figure S7 in SI, that the carrier concentration would change from $n = 3.1 \times 10^{26}$ m^{-3} to $n = 2.2 \times 10^{26}$ m^{-3}. It is known that for many material systems, including $Mg_2(Si,Sn)$ solid solutions, the zT, and therefore the efficiency, are not so sensitive to such a change in carrier concentration, as its peak extends on a broad n range [48].

The formation of small islands with new phases at the interface shows an affinity between Zn, Al, Mg and Bi, as a new (Mg;Al;Zn) phase is formed and Bi is segregated at the edge of this new phase. This might indicate that the change in carrier concentration may not, as discussed above, be due to the creation of Zn-related defects in $Mg_2(Si,Sn)$, but rather to the diffusion of Mg or Bi out of $Mg_2(Si,Sn)$. With the employed microstructural techniques, no gradient for one of the elements is discernable, we can therefore not differentiate between both options nor exclude a combination of both.

The case of Al diffusion into n-type $Mg_2(Si,Sn)$ was already discussed in a previous work, where no gradient was found after contacting with non-coated Al foils [30], similarly to the first results in this work (see line scans in SI). It also appears that Al is a poor dopant for this material system as shown in [49–53]. It is, therefore, unlikely that the diffusion of Al into the n-type TE material is at the origin of the change in carrier concentration.

The effect of Zn is investigated by hybrid-DFT calculations, which predicts no change in carrier concentration of the Li-doped p-type material and a probable change of the Bi-doped n-type material, due to quite stable Zn_{Mg} and Zn_{Sn} defects which are electron killers. In literature, the effect of Zn on n-type $Mg_2(Si,Sn)$ was studied by Andersen et al., who also reported an increase in absolute n-type Seebeck coefficient in Zn-doped $Mg_2Si_{0.4}Sn_{0.6}$ [54]. Although this does not completely dismiss the effect of the other elements suggested above, it suggests the clear and major role of Zn in the gradient observed in the samples with Zn-coated Al electrodes.

It was mentioned above that the gradient in Seebeck coefficient due to Zn diffusion is light and not detrimental to a TEG performance. It would, however, be possible to avoid

this gradient altogether by finding a different oxidation barrier that would not create stable defects in the n-type material, using DFT calculations for the barrier selection [39]. Nevertheless, a far more important point to ensure long-term TEG performance is the material stability. It has been already shown that the n-type TE properties are very sensitive to Mg evaporation, which greatly alters the carrier concentration [27,30,55–57]. The investigation of suitable coating and annealing conditions should therefore be prioritized for further TEG development, see, e.g., Refs. [58–63].

5. Conclusions

We reported a technological difficulty related to the making of functionalized thermoelectric legs: asymmetry in electrical contact resistances. This issue could be commonly encountered in the field of thermoelectric materials in the present and future, as it appears during a widely used preparation process (pellet metallization followed by leg dicing). We investigated its origins and searched for an efficient solution to avoid it. It is found that it is crucial to avoid the presence of oxidation on the foil to be contacted as electrode, as this will tend to cause asymmetric contacts during the dicing step by the mechanical stress applied to the electrode/TE interface. An effective way for this is to ion-etch the metallic foil and coat the oxide-free surface with an oxidation protecting layer. In this work, the method was tested with Zn as oxidation barrier for Al on $Mg_2(Si,Sn)$. It successfully suppressed the contact asymmetry, allowing to reach low specific contact resistances on both sides of the samples (<10 $\mu\Omega\cdot cm^2$). A slight gradient in n-type Seebeck coefficient is observed close to the Al/TE interfaces due to the Zn diffusion, which should not be detrimental to the leg performance in a TEG. In this study, an efficient method to ensure low and symmetric electrical contact resistivities between Al and $Mg_2(Si,Sn)$ was found. It may also be transferable to other material systems, thus making one more step towards TEG development.

Supplementary Materials: The following are available online at https://www.mdpi.com/article/10.3390/ma14226774/s1, Table S1—Asymmetric electrical contact resistivities for several electrodes on Mg_2X materials; Table S2—List of symmetric and asymmetric samples with varying contacting parameters; Figure S1—Linescans of Al/$Mg_2(Si,Sn)$ interfaces. (a) left of sample 1, (b) right of sample 1, (c) left of sample 2, (d) right of sample 2; Table S3—Electrical contact resistivities of the Al/$Mg_2(Si,Sn)$ interfaces presented in Figure S1; Figure S2—BsE and SE2 observations of the Zn coating on the Al foil after ion etching; Figure S3—picture of a $Mg_2(Si,Sn)$ pellet after contacting with Zn-coated electrodes; Figure S4—Exemplary line scans of the potential and Seebeck coefficients for the reported experiments (a) top/bottom experiment, side at the top during cutting (leg7), (b) top/bottom experiment, side at the bottom during cutting (leg 7), (c) top/top experiment (leg 4), (d) experiment with Zn-coated Al foils (leg 5). The Cu layer indicated in (a) and (b) corresponds to the sample holder of the PSM.; Figure S5—Charged defect formation energies for Zn defects in: (a) Li-doped and (b) Bi-doped Mg_2Si under Mg-poor conditions (c) Bi-doped Mg_2Si under Mg-rich conditions, (d) Li-doped Mg_2Sn under Mg-poor conditions. For simplicity, the Li-doped Mg_2Si and Mg_2Sn are only represented in the Fermi level region around VBM, while the Bi-doped samples are represented in the Fermi level region around CBM.; Figure S6—Pisarenko plot for n-type $Mg_2(Si,Sn)$, with an effective mass of $2.1m_0$.

Author Contributions: Conceptualization, E.M. and J.d.B.; Formal analysis, S.P. (Sungjin Park), B.R. and S.P. (Sudong Park); Investigation, J.C., G.C.-H. and A.F.; Supervision, E.M. and J.d.B.; Writing—original draft, J.C.; Writing—review & editing, J.C., S.A., G.C.-H., B.R., C.S., E.M. and J.d.B. All authors have read and agreed to the published version of the manuscript.

Funding: The authors would like to gratefully acknowledge the endorsement for the DLR executive Board Members for Space Research and Technology, as well as the financial support from the Young Research Group Leader Program. G.C.H would like to thank the financial support of the Mexican Science and Technology Ministry (CONACyT). J.C. would like to thank the DAAD fellowship programs No. 57424731. J.d.B acknowledges support by the Deutsche Forschungsgemeinschaft (DFG, German Research Foundation), project number 396709363. A.F. acknowledges support by the DFG via the GRK (Research Training Group) 2204 "Substitute Materials for Sustainable En-

ergy Technologies". This work was also supported by the KETEP and MOTIE of the Republic of Korea: Grant No. 20188550000290, "Development of Meta-Silicide Thermoelectric Semiconductor and Metrology Standardization Technology of Thermoelectric Power Module". The authors from the Korea Electrotechnology Research Institute (KERI) were also supported by the KERI Primary Research Program by MSIT/NST of the Republic of Korea: Grant No. 21A01003, "Research on High-Power Low-Mid Temperature Thermoelectric Power Generator via Thermoelectric Data Manifold Exploration and Expedition".

Institutional Review Board Statement: Not applicable.

Informed Consent Statement: Not applicable.

Data Availability Statement: The data presented in this study are openly available in FigShare at [10.6084/m9.figshare.16751998].

Acknowledgments: The authors would also like to acknowledge Pawel Ziolkowski and Przemyslaw Blaschkewitz for their help and assistance with the thermoelectric measurements.

Conflicts of Interest: The authors declare no conflict of interest.

References

1. Karellas, S.; Leontaritis, A.-D.; Panousis, G.; Bellos, E.; Kakaras, E. Energetic and exergetic analysis of waste heat recovery systems in the cement industry. *Energy* **2013**, *58*, 147–156. [CrossRef]
2. Yang, J.; Stabler, F.R. Automotive Applications of Thermoelectric Materials. *J. Electron. Mater.* **2009**, *38*, 1245–1251. [CrossRef]
3. Jaziri, N.; Boughamoura, A.; Müller, J.; Mezghani, B.; Tounsi, F.; Ismail, M. A comprehensive review of Thermoelectric Generators: Technologies and common applications. *Energy Rep.* **2020**, *6*, 264–287. [CrossRef]
4. Snyder, G.J.; Toberer, E.S. Complex thermoelectric materials. In *Materials for Sustainable Energy: A Collection of Peer-Reviewed Research and Review Articles from Nature Publishing Group*; World Scientific: Singapore, 2011; pp. 101–110.
5. He, R.; Schierning, G.; Nielsch, K. Thermoelectric Devices: A Review of Devices, Architectures, and Contact Optimization. *Adv. Mater. Technol.* **2018**, *3*, 1700256. [CrossRef]
6. Rowe, D.; Min, G. Design theory of thermoelectric modules for electrical power generation. *IEE Proc. Sci. Meas. Technol.* **1996**, *143*, 351–356. [CrossRef]
7. Rowe, D. Conversion efficiency and figure-of-merit. In *CRC Handbook of Thermoelectrics*; CRC Press: Boca Raton, FL, USA, 1995; pp. 31–37.
8. de Boor, J.; Dasgupta, T.; Saparamadu, U.; Müller, E.; Ren, Z. Recent progress in p-type thermoelectric magnesium silicide based solid solutions. *Mater. Today Energy* **2017**, *4*, 105–121. [CrossRef]
9. Bashir, M.B.A.; Said, S.M.; Sabri, M.F.M.; Shnawah, D.A.; Elsheikh, M.H. Recent advances on $Mg_2Si_{1-x}Sn_x$ materials for thermoelectric generation. *Renew. Sustain. Energy Rev.* **2014**, *37*, 569–584. [CrossRef]
10. de Boor, J.; Saparamadu, U.; Mao, J.; Dahal, K.; Müller, E.; Ren, Z. Thermoelectric performance of Li doped, p-type Mg_2 (Ge,Sn) and comparison with Mg_2 (Si,Sn). *Acta Mater.* **2016**, *120*, 273–280. [CrossRef]
11. Zaitsev, V.K.; Fedorov, M.I.; Gurieva, E.A.; Eremin, I.S.; Konstantinov, P.P.; Samunin, A.Y.; Vedernikov, M.V. Highly effective $Mg_2Si_{1-x}Sn_x$ thermoelectrics. *Phys. Rev. B* **2006**, *74*, 045207. [CrossRef]
12. Fedorov, M.I.; Zaitsev, V.K.; Isachenko, G.N. High effective thermoelectrics based on the Mg_2Si-Mg_2Sn solid solution. In *Solid State Phenomena*; Trans Tech Publications Ltd.: Stafa-Zurich, Switzerland, 2011.
13. Liu, W.; Tan, X.; Yin, K.; Liu, H.; Tang, X.; Shi, J.; Zhang, Q.; Uher, C. Convergence of conduction bands as a means of enhancing thermoelectric performance of n-type $Mg_2Si_{1-x}Sn_x$ solid solutions. *Phys. Rev. Lett.* **2012**, *108*, 166601. [CrossRef]
14. Kamila, H.; Sankhla, A.; Yasseri, M.; Hoang, N.; Farahi, N.; Mueller, E.; de Boor, J. Synthesis of p-type $Mg_2Si_{1-x}Sn_x$ with x = 0–1 and optimization of the synthesis parameters. *Mater. Today Proc.* **2019**, *8*, 546–555. [CrossRef]
15. Liu, X.; Xi, L.; Qiu, W.; Yang, J.; Zhu, T.; Zhao, X.; Zhang, W. Significant Roles of Intrinsic Point Defects in Mg_2X(X= Si, Ge, Sn) Thermoelectric Materials. *Adv. Electron. Mater.* **2016**, *2*, 1500284. [CrossRef]
16. Sankhla, A.; Patil, A.; Kamila, H.; Yasseri, M.; Farahi, N.; Mueller, E.; De Boor, J. Mechanical Alloying of Optimized Mg_2(Si,Sn) Solid Solutions: Understanding Phase Evolution and Tuning Synthesis Parameters for Thermoelectric Applications. *ACS Appl. Energy Mater.* **2018**, *1*, 531–542. [CrossRef]
17. Skomedal, G.; Holmgren, L.; Middleton, H.; Eremin, I.; Isachenko, G.; Jaegle, M.; Tarantik, K.; Vlachos, N.; Manoli, M.; Kyratsi, T.; et al. Design, assembly and characterization of silicide-based thermoelectric modules. *Energy Convers. Manag.* **2016**, *110*, 13–21. [CrossRef]
18. Shyikira, A.D.P.; Skomedal, G.; Middleton, P.H. *Performance Evaluation and Stability of Silicide-Based Thermoelectric Modules*; Elsevier: Amsterdam, The Netherlands, 2021; Volume 44, pp. 3467–3474.

19. Kaibe, H.; Aoyama, I.; Mukoujima, M.; Kanda, T.; Fujimoto, S.; Kurosawa, T.; Ishimabushi, H.; Ishida, K.; Rauscher, L.; Hata, Y.; et al. Development of thermoelectric generating stacked modules aiming for 15% of conversion efficiency. In Proceedings of the ICT 2005 24th International Conference on Thermoelectrics, Clemson, SC, USA, 19–23 June 2005; Institute of Electrical and Electronics Engineers (IEEE): Piscataway, NJ, USA, 2005; pp. 242–247.
20. Tarantik, K.R.; König, J.D.; Jägle, M.; Heuer, J.; Horzella, J.; Mahlke, A.; Vergez, M.; Bartholomé, K. Thermoelectric Modules Based on Silicides-Development and Characterization. *Mater. Today Proc.* **2015**, *2*, 588–595. [CrossRef]
21. Nakamura, T.; Hatakeyama, K.; Minowa, M.; Mito, Y.; Arai, K.; Iida, T.; Nishio, K. Power-Generation Performance of a π-Structured Thermoelectric Module Containing Mg_2Si and $MnSi_{1.73}$. *J. Electron. Mater.* **2015**, *44*, 3592–3597. [CrossRef]
22. Kim, H.S.; Kikuchi, K.; Itoh, T.; Iida, T.; Taya, M. Design of segmented thermoelectric generator based on cost-effective and light-weight thermoelectric alloys. *Mater. Sci. Eng. B* **2014**, *185*, 45–52. [CrossRef]
23. Tohei, T.; Fujiwara, S.; Jinushi, T.; Ishijima, Z. Bondability of Mg_2Si element to Ni electrode using Al for thermoelectric modules. In Proceedings of the International Symposium on Interfacial Joining and Surface Technology (IJST2013), Osaka, Japan, 27–29 November 2013; IOP Publishing: Bristol, UK, 2014; Volume 61.
24. Graff, J.S.; Schuler, R.; Song, X.; Castillo-Hernandez, G.; Skomedal, G.; Enebakk, E.; Wright, D.N.; Stange, M.; de Boor, J.; Løvvik, O.M.; et al. Fabrication of a Silicide Thermoelectric Module Employing Fractional Factorial Design Principles. *J. Electron. Mater.* **2021**, *50*, 4041–4049. [CrossRef]
25. Gao, P. *Mg_2 (Si,Sn)-Based Thermoelectric Materials and Devices*; Michigan State University: East Lansing, MI, USA, 2016; p. 128.
26. Goyal, G.K.; Dasgupta, T. Fabrication and testing of $Mg_2Si_{1-x}Sn_x$ based thermoelectric generator module. *Mater. Sci. Eng. B* **2021**, *272*, 115338. [CrossRef]
27. Ayachi, S.; Castillo Hernandez, G.; Pham, N.H.; Farahi, N.; Müller, E.; de Boor, J. Developing Contacting Solutions for $Mg_2Si_{1-x}Sn_x$-Based Thermoelectric Generators: Cu and Ni45Cu55 as Potential Contacting Electrodes. *ACS Appl. Mater. Interfaces* **2019**, *11*, 40769–40780. [CrossRef] [PubMed]
28. de Boor, J.; Gloanec, C.; Kolb, H.; Sottong, R.; Ziolkowski, P.; Müller, E. Fabrication and characterization of nickel contacts for magnesium silicide based thermoelectric generators. *J. Alloys Compd.* **2015**, *632*, 348–353. [CrossRef]
29. Pham, N.H.; Farahi, N.; Kamila, H.; Sankhla, A.; Ayachi, S.; Müller, E.; de Boor, J. Ni and Ag electrodes for magnesium silicide based thermoelectric generators. *Mater. Today Energy* **2019**, *11*, 97–105. [CrossRef]
30. Camut, J.; Pham, N.; Truong, D.N.; Castillo-Hernandez, G.; Farahi, N.; Yasseri, M.; Mueller, E.; de Boor, J. Aluminum as promising electrode for Mg_2(Si,Sn)-based thermoelectric devices. *Mater. Today Energy* **2021**, *21*, 100718. [CrossRef]
31. Farahi, N.; Stiewe, C.; Truong, D.Y.N.; de Boor, J.; Müller, E. High efficiency Mg_2(Si,Sn)-based thermoelectric materials: Scale-up synthesis, functional homogeneity, and thermal stability. *RSC Adv.* **2019**, *9*, 23021–23028. [CrossRef]
32. Ayachi, S.; Hernandez, G.C.; Müller, E.; de Boor, J. Contacting Cu Electrodes to $Mg_2Si_{0.3}$ $Sn_{0.7}$: Direct vs. Indirect Resistive Heating. *Semiconductors* **2019**, *53*, 1825–1830. [CrossRef]
33. Platzek, D.; Karpinski, G.; Stiewe, C.; Ziolkowski, P.; Drasar, C.; Muller, E. Potential-Seebeck-microprobe (PSM): Measuring the spatial resolution of the Seebeck coefficient and the electric potential. In Proceedings of the ICT 2005 24th International Conference on Thermoelectrics, Clemson, SC, USA, 19–23 June 2005; IEEE: Piscataway, NJ, USA, 2005; pp. 13–16.
34. Krukau, A.V.; Vydrov, O.A.; Izmaylov, A.F.; Scuseria, G.E. Influence of the exchange screening parameter on the performance of screened hybrid functionals. *J. Chem. Phys.* **2006**, *125*, 224106. [CrossRef] [PubMed]
35. Kresse, G.; Joubert, D. From ultrasoft pseudopotentials to the projector augmented-wave method. *Phys. Rev. B* **1999**, *59*, 1758. [CrossRef]
36. Kresse, G.; Furthmüller, J. Efficient iterative schemes for ab initio total-energy calculations using a plane-wave basis set. *Phys. Rev. B* **1996**, *54*, 11169. [CrossRef]
37. Perdew, J.P.; Burke, K.; Ernzerhof, M. Generalized Gradient Approximation Made Simple. *Phys. Rev. Lett.* **1996**, *77*, 3865. [CrossRef]
38. Zhang, S.B.; Northrup, J.E. Chemical potential dependence of defect formation energies in GaAs: Application to Ga self-diffusion. *Phys. Rev. Lett.* **1991**, *67*, 2339–2342. [CrossRef]
39. Ayachi, S.; Deshpande, R.; Ponnusamy, P.; Park, S.; Chung, J.; Park, S.; Ryu, B.; Müller, E.; de Boor, J. On the relevance of point defects for the selection of contacting electrodes: Ag as an example for Mg_2(Si,Sn)-based thermoelectric generators. *Mater. Today* **2021**, *16*, 100309. [CrossRef]
40. Ryu, B.; Choi, E.-A.; Park, S.; Chung, J.; de Boor, J.; Ziolkowski, P.; Müller, E.; Park, S. Native point defects and low p-doping efficiency in Mg_2(Si,Sn) solid solutions: A hybrid-density functional study. *J. Alloys Compd.* **2021**, *853*, 157145. [CrossRef]
41. Ryu, B.; Park, S.; Choi, E.-A.; De Boor, J.; Ziolkowski, P.; Chung, J.; Park, S.D. Hybrid-Functional and Quasi-Particle Calculations of Band Structures of Mg_2Si, Mg_2Ge, and Mg_2Sn. *J. Korean Phys. Soc.* **2019**, *75*, 144–152. [CrossRef]
42. Murray, J.L.; McAlister, A.J. The Al-Si (Aluminum-Silicon) system. *Bull. Alloy. Phase Diagr.* **1984**, *5*, 74–84. [CrossRef]
43. Salinas, D.R.; García, S.G.; Bessone, J.B. Influence of alloying elements and microstructure on aluminium sacrificial anode performance: Case of Al–Zn. *J. Appl. Electrochem.* **1999**, *29*, 1063–1071. [CrossRef]
44. Han, W.H.; Chang, K.J. Subgap States near the Conduction-Band Edge Due to Undercoordinated Cations in Amorphous In-Ga-Zn-O and Zn-Sn-O Semiconductors. *Phys. Rev. Appl.* **2016**, *6*, 044011. [CrossRef]
45. Shan, W.; Yu, K.M.; Walukiewicz, W.; Wu, J.; Ager, J.; Haller, E.E. Band anticrossing in dilute nitrides. *J. Phys. Condens. Matter* **2004**, *16*, S3355–S3372. [CrossRef]

46. Shirzadi, A.A.; Assadi, H.; Wallach, E.R. Interface evolution and bond strength when diffusion bonding materials with stable oxide films. *Surf. Interface Anal.* **2001**, *31*, 609–618. [CrossRef]
47. Gross, D.; Seelig, T. *Fracture Mechanics: With an Introduction to Micromechanics*; Springer: Berlin/Heidelberg, Germany, 2017.
48. Ponnusamy, P.; Kamila, H.; Müller, E.; de Boor, J. Efficiency as a performance metric for material optimization in thermoelectric generators. *J. Phys. Energy* **2021**, *3*, 044006. [CrossRef]
49. Vivekanandhan, P.; Murugasami, R.; Kumar, S.A.; Kumaran, S. Structural features and thermoelectric properties of spark plasma assisted combustion synthesised Magnesium silicide doped with Aluminium. *Mater. Chem. Phys.* **2020**, *241*, 122407. [CrossRef]
50. Tani, J.I.; Kido, H. Thermoelectric properties of Al-doped $Mg_2Si_{1-x}Sn_x$ ($x \leqq 0.1$). *J. Alloys Compd.* **2008**, *466*, 335–340. [CrossRef]
51. Hu, X.; Barnett, M.R.; Yamamoto, A. Synthesis of Al-doped $Mg_2Si_{1-x}Sn_x$ compound using magnesium alloy for thermoelectric application. *J. Alloys Compd.* **2015**, *649*, 1060–1065. [CrossRef]
52. Kim, G.; Kim, J.; Lee, H.; Cho, S.; Lyo, I.; Noh, S.; Kim, B.-W.; Kim, S.W.; Lee, K.H.; Lee, W. Co-doping of Al and Bi to control the transport properties for improving thermoelectric performance of Mg_2Si. *Scr. Mater.* **2016**, *116*, 11–15. [CrossRef]
53. Kato, A.; Yagi, T.; Fukusako, N. First-principles studies of intrinsic point defects in magnesium silicide. *J. Phys. Condens. Matter* **2009**, *21*, 205801. [CrossRef] [PubMed]
54. Andersen, H.L.; Zhang, J.; Yin, H.; Iversen, B.B. Structural stability and thermoelectric properties of cation- and anion-doped $Mg_2Si0.4Sn0.6$. *Inorg. Chem. Front.* **2017**, *4*, 456–467. [CrossRef]
55. Kato, D.; Iwasaki, K.; Yoshino, M.; Yamada, T.; Nagasaki, T. Control of Mg content and carrier concentration via post annealing under different Mg partial pressures for Sb-doped Mg_2Si thermoelectric material. *J. Solid State Chem.* **2018**, *258*, 93–98. [CrossRef]
56. Sankhla, A.; Kamila, H.; Kelm, K.; Mueller, E.; de Boor, J. Analyzing thermoelectric transport in n-type $Mg_2Si0.4Sn0.6$ and correlation with microstructural effects: An insight on the role of Mg. *Acta Mater.* **2020**, *199*, 85–95. [CrossRef]
57. Sankhla, A.; Kamila, H.; Naithani, H.; Mueller, E.; de Boor, J. On the role of Mg content in Mg_2(Si,Sn): Assessing its impact on electronic transport and estimating the phase width by in situ characterization and modelling. *Mater. Today Phys.* **2021**, *21*, 100471. [CrossRef]
58. Battiston, S.; Boldrini, S.; Fiameni, S.; Famengo, A.; Fabrizio, M.; Barison, S. Multilayered thin films for oxidation protection of Mg_2Si thermoelectric material at middle–high temperatures. *Thin Solid Films* **2012**, *526*, 150–154. [CrossRef]
59. D'Isanto, F.; Smeacetto, F.; Reece, M.J.; Chen, K.; Salvo, M. Oxidation protective glass coating for magnesium silicide based thermoelectrics. *Ceram. Int.* **2020**, *46*, 24312–24317. [CrossRef]
60. Gucci, F.; D'Isanto, F.; Zhang, R.; Reece, M.J.; Smeacetto, F.; Salvo, M. Oxidation Protective Hybrid Coating for Thermoelectric Materials. *Materials* **2019**, *12*, 573. [CrossRef] [PubMed]
61. Nieroda, P.; Mars, K.; Nieroda, J.; Leszczyński, J.; Król, M.; Drożdż, E.; Jeleń, P.; Sitarz, M.; Kolezynski, A. New high temperature amorphous protective coatings for Mg_2Si thermoelectric material. *Ceram. Int.* **2019**, *45*, 10230–10235. [CrossRef]
62. Sadia, Y.; Ben-Ayoun, D.; Gelbstein, Y. PbO–SiO_2-based glass doped with B_2O_3 and Na_2O for coating of thermoelectric materials. *J. Mater. Res.* **2019**, *34*, 3563–3572. [CrossRef]
63. Tani, J.I.; Takahashi, M.; Kido, H. Fabrication of oxidation-resistant β-$FeSi_2$ film on Mg_2Si by RF magnetron-sputtering deposition. *J. Alloys Compd.* **2009**, *488*, 346–349. [CrossRef]

Supplementary Information

Studying the asymmetry of the electrical contact resistivities

The phenomenon of asymmetry in electrical contact resistances has been observed with other electrodes than aluminum, as can be seen in Supplementary Table S1. Although the magnitudes are different, this behavior also appears with Ni and Ag electrodes on Mg2X materials. The Ag electrodes were contacted at 450°C and 30 MPa for 10 min and the Ni electrodes at 600°C and 30 MPa for 10 min. This shows that this issue is not specific to Al and can even be encountered with electrodes that are less prone to oxidation.

Supplementary Table S1 - Asymmetric electrical contact resistivities for several electrodes on Mg_2X materials

Electrode/TE	**Symmetric sample r_c (μΩcm²)**	**Asymmetric sample (low // high r_c) (μΩcm²)**
Al/Mg_2(Si,Sn)	4 ± 2	15 ± 19 // 792 ± 181
Ni/Mg_2Si	4 ± 3	7 ± 7 // 179 ± 116
Ag/Mg_2(Si,Sn)	9 ± 1	9 ± 5 // 40 ± 36

Supplementary Table S2 also shows cases of symmetric and asymmetric samples for various factors, such as the carrier type, TE pellet geometry (diameter of 15 or 30 mm), presence or absence of a buffer layer during contacting and direct vs indirect current heating setup. The presence of both symmetric and asymmetric samples for all configurations of these factors indicates that they do not seem to play a decisive role in this asymmetry phenomenon.

Supplementary Table S2 - List of symmetric and asymmetric samples with varying contacting parameters

Sample	Low r_c (μΩcm²)	High r_c (μΩcm²)	Carrier type	Pellet diameter (mm)	Direct/ Indirect current	Buffer layer
1119JCA04	3 ± 2	symmetric	n	15	indirect	yes
1119JCA78	18 ± 7	220 ± 180	n	15	indirect	yes
1119JCA20	54 ± 26	107 ± 40	n	30	indirect	yes
1118NT20	5 ± 4	Symmetric	n	30	indirect	yes
1118NT71	7 ± 2	98 ± 13	p	15	indirect	yes

1118NT76	11 ± 4	symmetric	p	15	indirect	yes
1117NP33	9 ± 5	symmetric	p	15	indirect	no
1119JCA86	4 ± 2	Symmetric	n	15	direct	no
1120JCA09	49 ± 27	319 ± 318	n	15	direct	no

EDX line scans at the Al-TE interface of a symmetric and an asymmetric sample are shown in Supplementary Figure S1 and the respective contact resistivities are reported in Supplementary Table S3. Both samples went through the same preparation and process steps. Although the resolution of the images is not optimal due to a deficient polishing preparation, the EDX line scans show oxygen peaks at the interfaces of the asymmetric sample, with a rough correlation between peak height and r_c. Such peaks are not observed on the symmetric sample. The O peak could correspond to a very thin Al_2O_3 layer, which cannot be distinguished on the curves due to the scale.

Al_2O_3 could indicate that there was an oxide layer on the foils of the asymmetric sample before contacting and could be the origin of the asymmetry. Given that both samples were identically prepared and processed, this would indicate how variable and non-reproducible the manual foil preparation is. It is also possible that the Al_2O_3 was formed after contacting and dicing, as the dicing could have pulled on the interface or cracks could have nucleated, making a way for oxygen to diffuse at the interface and oxidize the Al electrode.

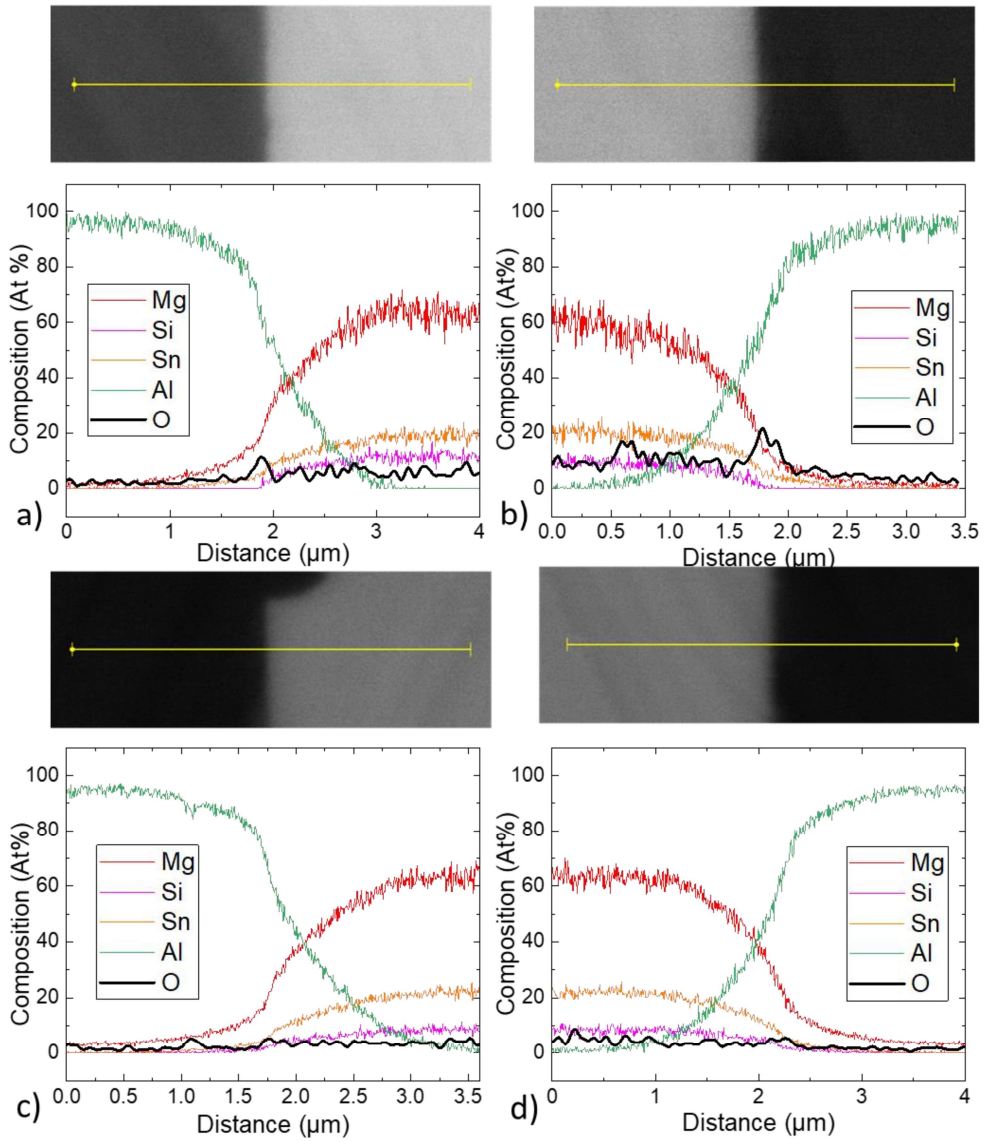

Supplementary Figure S1 - Linescans of Al/Mg_2(Si,Sn) interfaces. a) left of sample 1, b) right of sample 1, c) left of sample 2, d) right of sample 2

Supplementary Table S3 - Electrical contact resistivities of the Al/Mg2(Si,Sn) interfaces presented in Supplementary Figure S1

	interface r_c value (µΩcm²)
a	5 ± 19
b	792 ± 181
c	4 ± 3
d	4 ± 3

Zn coating and contacting experiment

Supplementary Figure S2 shows SEM images of the Zn coating on the Al foil after ion etching in the PVD. The Zn layer looks dense and continuous and is ~8 µm thick. It should therefore ensure an efficient protection against air to the Al foil. Supplementary Figure S3 shows a picture of the contacted pellet. It is seen that a large proportion of the Zn melted and got evacuated on the sides of the pellet due to the applied pressure.

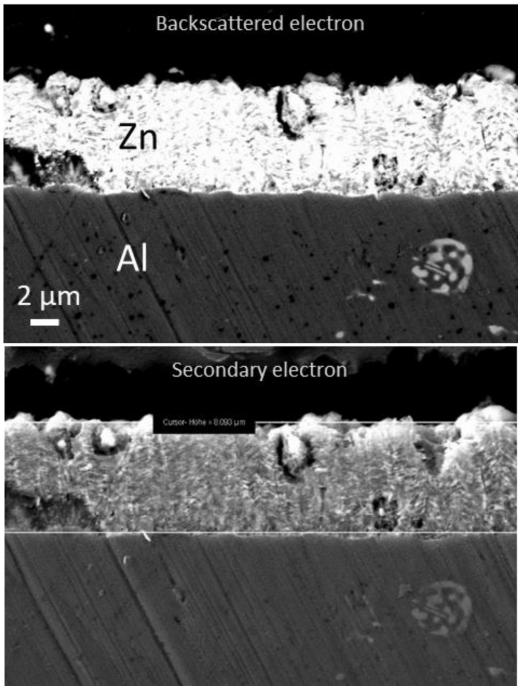

Supplementary Figure S2 - BsE and SE2 observations of the Zn coating on the Al foil after ion etching

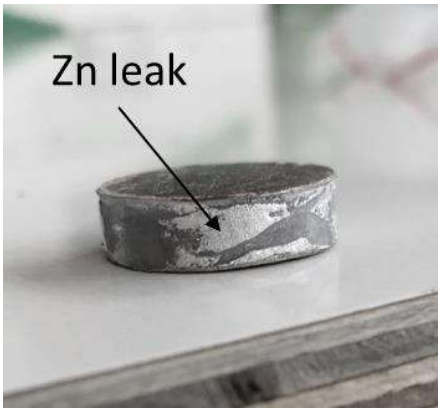

Supplementary Figure S3 - picture of a $Mg_2(Si,Sn)$ pellet after contacting with Zn-coated electrodes

Supplementary Figure S4 shows exemplary line scans of the samples presented in Tables 1, 2 and 3 of the paper. As each pellet was cut into 9 legs, and a full line scan characterization is very lengthy, most legs were measured with local line scans which focus on each interface on a scale

of 1-2 mm, separately. This is the case of the top/bottom leg presented below (Supplementary Figure S4a and b).

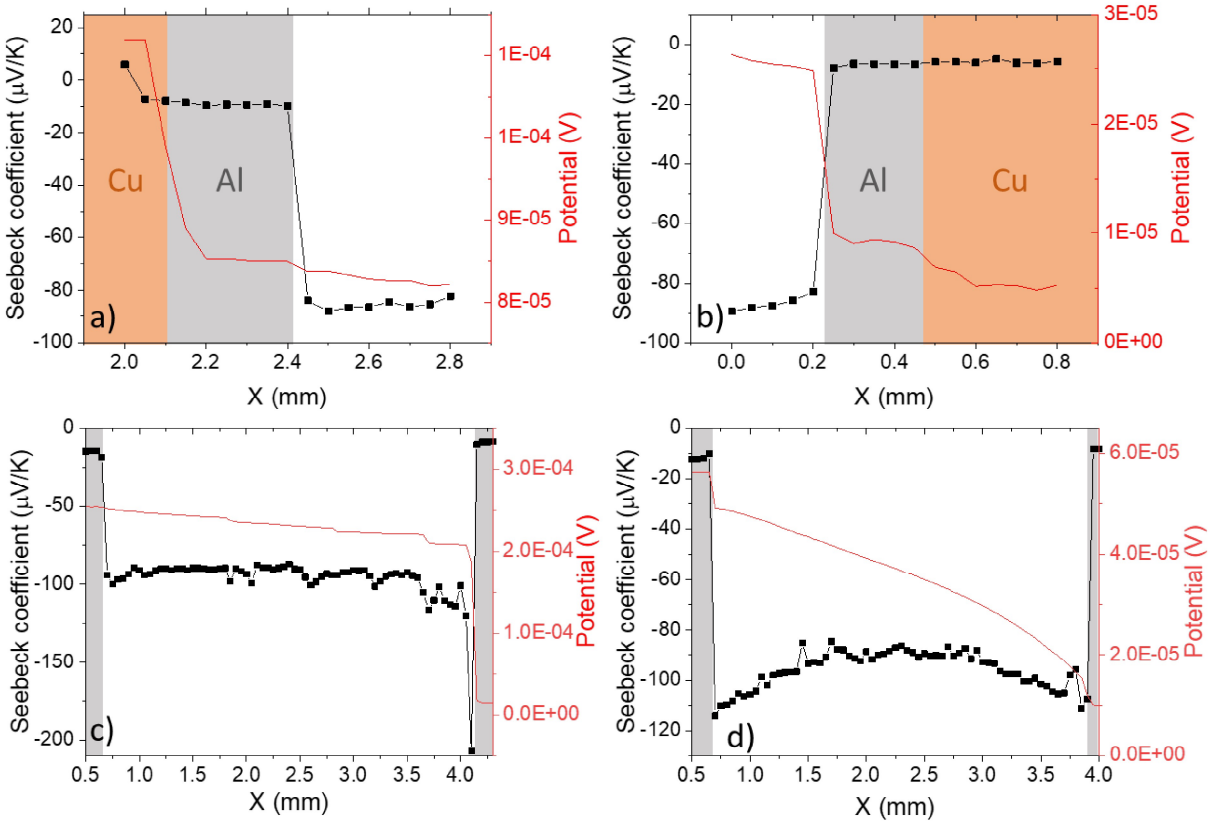

Supplementary Figure S4 - Exemplary line scans of the potential and Seebeck coefficients for the reported experiments a) top/bottom experiment, side at the top during cutting (leg7), b) top/bottom experiment, side at the bottom during cutting (leg 7), c) top/top experiment (leg 4), d) experiment with Zn-coated Al foils (leg 5). The Cu layer indicated in a) and b) corresponds to the sample holder of the PSM.

Additional hybrid-DFT calculations

In order to compare with experimental results of the Zn contacting experiments, hybrid-DFT calculations were made to investigate the defects formation energies of Zn-related defects in Mg_2X systems. Supplementary Figure S5 shows the defect formation energy calculations in Li and Bi-doped Mg_2Si. Bi-doped samples are discussed under both Mg-poor and Mg-rich conditions, while for Li-doping only the Mg-poor conditions are discussed. Indeed, Li doping is aimed at Mg sites in the Mg_2X material while it was found that, although Li on Mg site defects are indeed stable, Li interstitials are even more stable defects [1]. This means that the Li-doped material will always contain a certain proportion of Mg vacancies and Mg-rich conditions will not be obtained. In Supplementary Figure S5, only the defects with formation energies < 1 eV are presented.

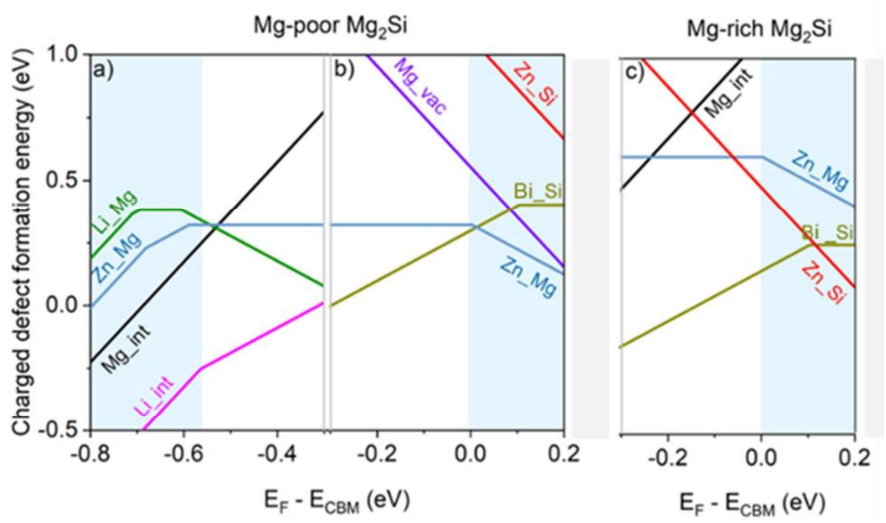

Supplementary Figure S5 - Charged defect formation energies for Zn defects in: a) Li-doped and b) Bi-doped Mg2Si under Mg-poor conditions c) Bi-doped Mg2Si under Mg-rich conditions, d) Li-doped Mg_2Sn under Mg-poor conditions. For simplicity, the Li-doped Mg2Si and Mg2Sn are only represented in the Fermi level region around VBM while the Bi-doped samples are represented in the Fermi level region around CBM.

In Supplementary Figure S5a where the results of Li-doped Mg_2Si are presented, the most relevant Zn defect in the vicinity of the valence band maxima (VBM) is Zn_{Mg} (Zn_Mg). This defect has a charge transition level (CTL) from q = 1+ to q = 0 at E_F = − 0.59 eV, below the VBM. For E_F between – 0.68 and – 0.59 eV where Zn_{Mg} is a donor defect with the charge q = 1+, the electron contribution to the charge carrier concentration is not expected to be very significant, owing to its high formation energy (E_{form} = 0.22 ~ 0.32 eV) compared to other more stable donor defects, namely I_{Li} (Li_int) and I_{Mg} (Mg_int). Nevertheless, as the intendent conduction here is p-type, the occurrence of the Zn_{Mg} defect would make it even harder to achieve such conduction, as it is yet another donor defect with a formation energy lower than that of Li_{Mg} (Li_Mg), which is the major acceptor defect.

For Bi-doped Mg_2Si under Mg-poor conditions, as presented in Supplementary Figure S5b, the relevant Zn defects are Zn_{Mg} and Zn_{Si} (Zn_Si). Zn_{Mg} is a neutral defect across the band gap and has a charge transition level above the conduction band minima (CBM) (at E_F = 0.003 eV). Above this CTL, Zn_{Mg} becomes an acceptor defect of charge q = 1-. If we take the example of highly doped sample with E_F = 0.05 eV, one can see that the main electron donor defect Bi_{Si} and the Zn_{Mg} defect have very comparable formation energies: 0.35 eV for the former, 0.27 eV for the latter. Using $n\,(D^q)=\theta_{\mathrm{deg}} n_{\mathrm{latt}} \exp(-\frac{E_{\mathrm{form}}}{k_B T})$ where k_B = 8.62 × 10^{-5} eV/K, n_{latt}= 1.6 × 10^{22} cm^{-3} for a defect on Si or Sn site in Mg_2Si and 3.1 × 10^{22} cm^{-3} for a defect on Mg sites and T = 475 °C, the

defect density for the Bi_{Si} (Bi_Si) and the Zn_{Mg} defects would respectively be 7.0×10^{19} cm^{-3} and 4.7×10^{20} cm^{-3}, which corresponds to a compensation in $n \sim 4 \times 10^{20}$ cm^{-3}. Therefore, Zn_{Mg} is expected to cause a significant compensation of the conduction electrons provided by Bi_{Si} for the Mg_2Si system under Mg poor conditions. Experimentally, this would translate to a variation in the Seebeck coefficient.

As for the second Zn-related defect in this case, Zn_{Si}, it is not expected to play an important role in determining the system´s carrier concentration because its high formation energy results in a low density. Therefore, the effect of the Zn_{Si} defect can be disregarded.

For Bi-doped Mg_2Si under Mg-rich conditions, as presented in Supplementary Figure S5c, the relevant Zn defects are also Zn_{Mg} and Zn_{Si}, however with different formation energies. Zn_{Mg} is a much less stable defect than under Mg-poor conditions with E_{form} = 0.61 eV at CBM. Therefore, it is not expected to notably influence the charge carrier concentration. On the other hand, the Zn_{Si} defect is much more stable under Mg-rich (Si-poor). Zn_{Si} is an acceptor defect of charge q = 2- in the whole chemical potential of interest region. It has a formation energy E_{form} = 0.39 eV at E_F = 0.05 eV. At this second E_F region, the formation energies of Zn_{Si} and Bi_{Si} are close, and get closer the higher the energy level. Bi_{Si} has a formation energy E_{form} = 0.20 eV at E_F = 0.05 eV. If we calculate the defect density for both defects, it would be 3.8×10^{19} cm^{-3} for Zn_{Si} and 7.2×10^{20} cm^{-3} for Bi_{Si}, which corresponds to a compensation in $n \sim 7 \times 10^{20}$ cm^{-3}. Experimentally, a variation in the carrier concentration would be expected under Mg-rich conditions.

As a conclusion, the predicted changes in carrier concentration due to Zn diffusion are similar for both Mg_2Si and Mg_2Sn. For both systems, the most stable Zn-related defect is Zn_{Mg} for Mg-poor conditions and Zn_X (X=Si or Sn) for Mg-rich conditions and all are electron killers in the n-type materials. As a consequence, the observed experimental results also match with the DFT defects calculation for n- and p-type Mg_2Si: no change is seen for p-type and a decrease in carrier concentration is observed for n-type.

Obtaining the carrier concentration from the Seebeck coefficient

Supplementary Figure S6 shows the dependence of the Seebeck coefficient with carrier concentration (Pisarenko plot) according to the single parabolic band model (SPB) [2]. In this model, the transport properties are obtained following the equations given by:

$$|S| = \frac{k_B}{e} * \left(\frac{2F_1(\eta)}{F_0(\eta)} - \eta \right)$$

$$n = 4\pi\left(\frac{2m_{\mathrm{d}}^{*}k_{\mathrm{B}}T}{h^2}\right)^{1,5} F_{\frac{1}{2}}(\eta)$$

Where $\eta = \frac{E_{\mathrm{F}}}{k_{\mathrm{B}}T}$ is the reduced chemical potential, m_{d}^{*} the density of states effective mass and n the carrier concentration, k_{B} is the Boltzmann's constant, $F_i(\eta)$ is the Fermi integral of order i. The value of $2.1\,m_0$ was taken for the effective mass after analyzing the transport properties of the material.

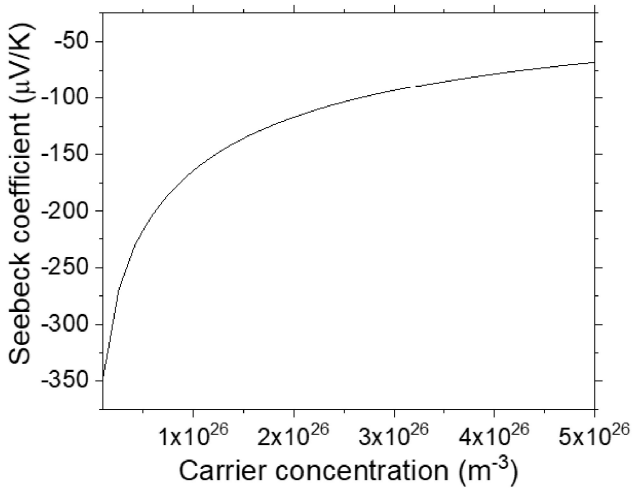

Supplementary Figure S6 - Pisarenko plot for n-type Mg2(Si,Sn), with an effective mass of 2.1m$_0$

References

1. Ayachi, S., et al., *On the Relevance of Point Defects for the Selection of Contacting Electrodes: Ag as an Example for Mg2(Si,Sn)-based Thermoelectric Generators.* Materials Today Physics, 2021. **16**: p. 100309.
2. Kamila, H., et al., *Analyzing transport properties of p-type Mg 2 Si–Mg 2 Sn solid solutions: optimization of thermoelectric performance and insight into the electronic band structure.* Journal of Materials Chemistry A, 2019. **7**(3): p. 1045-1054.

5. Chapter 5 (Paper 3): Efficiency Measurement and Modeling of a High-Performance $Mg_2(Si,Sn)$-Based Thermoelectric Generator

In this paper/chapter, we build and characterize the third ever full $Mg_2(Si,Sn)$-based TEG (a single one was reported at the start of the thesis work [127]).

We report the first efficiency measurement of such a module and measure a high power density, which scales with comparable silicide-based TEG already reported in literature [84, 128] despite its mechanical degradation. Two measurement cycles are performed and, besides some changes in the first heating discussed below, the TEG performance stayed relatively stable, excepted for an increase in the electrical inner resistance. This degradation is very likely due to thermally induced stress which led to cracking and it is imputed to the Al_2O_3 plate of the DBC substrates used in the TEG design.

We use CPM to compare theoretical calculations to the measurements. Measurement-calculations deviations below 5% are obtained for current at maximum power and maximum power. It is found that both efficiency and power output could be realistically increased by 30% by improving the mechanical stability of the module.

In this thesis, **the published version of the paper, following the journal´s template,** is provided. This work was published on 7 July 2022 in Advanced Engineering Materials journal, page 2200776.

Reference: J. Camut, P. Ziolkowski, P. Ponnusamy, C. Stiewe, E. Mueller, J. de Boor, *Efficiency Measurement and Modeling of a High-Performance Mg2(Si,Sn)-Based Thermoelectric Generator*, Adv. Eng. Mater., 2022, 2200776. https://doi.org/10.1002/adem.202200776

RESEARCH ARTICLE

ADVANCED ENGINEERING MATERIALS

www.aem-journal.com

Efficiency Measurement and Modeling of a High-Performance $Mg_2(Si,Sn)$-Based Thermoelectric Generator

Julia Camut, Pawel Ziolkowski, Prasanna Ponnusamy, Christian Stiewe, Eckhard Mueller, and Johannes de Boor**

$Mg_2(Si,Sn)$ is an attractive material class due to its excellent thermoelectric (TE) properties, its eco-friendly constituents, its low mass density, and its low price. A lot of research has been done on optimizing its TE properties; however, works on its use in thermoelectric generators (TEG) are scarce. Herein, the first conversion efficiency measurement of a functional, fully $Mg_2(Si,Sn)$-based TEG, approaching a maximum value of 4% for an applied $\Delta T = 375$ °C, is shown. A maximum power density of 0.9 W cm^{-2} (related to the cross-sectional area of the TE legs) at ΔT=375 °C is also reported, which is among the highest performance of silicide-based modules reported in literature. Efficiency measurements can be tricky due to the uncertainty of heat flow measurement and parasitic heat losses; therefore, assessing the measurement reliability by confronting it to theoretical calculations is necessary. TEG device simulation in a constant property model is used to compare measured data to expected values and a good match is found (<1% deviation for current at maximum power, <4% difference for maximum power output, deviation within measurement uncertainty range for heat flows and efficiency). The significant discrepancy between measurement and calculations of the inner electrical resistance reveals room for improvement. Cracks form due to thermally induced mechanical stress, which dramatically increase the inner electrical resistance. It is shown that by avoiding those cracks, the maximum power output and conversion efficiency of the TEG could be improved by 30%.

1. Introduction

In the context of the increasing need for green sources of electrical energy, thermoelectric (TE) materials have gained a lot of interest over the past decades.[1] Their ability to convert heat flow into electrical power makes them highly attractive as, globally, about 60% of the primary energy is lost as waste heat.[2] Although their efficiency is not as high as other green energy sources, TE devices have the advantages of being reliable and needing no maintenance due to their lack of moving parts. This has made them an interesting energy source in various fields such as the aerospace industry, where radioisotope thermoelectric generators (RTGs) convert the heat released by the natural decay of radioactive materials into electricity supply of space missions.[3] Exhaust heat conversion to electricity in the automotive and in industrial processes is also among the most popular application.[3–5] On a smaller scale, thermoelectric technology is also considered to power wearable medical devices,[6–8] mobile storage of pharmaceuticals, and electronic devices.[3]

A thermoelectric generator (TEG) is a device in which semiconducting n- and p-type TE elements, called legs, are connected electrically in series and thermally in parallel. Over the last decades, a large majority of the research in thermoelectrics has been focused on the optimization of the TE properties of various material classes as the first, very challenging step in the development chain of a TEG.[9–18] As a consequence, many material systems have not reached the TEG development stage yet and research on contacting techniques and on TE module building remained relatively scarce.[19]

Commercial TEGs based on Bi_2Te_3, the most mature material, are reported to reach an efficiency of 7.2% between room temperature and 250 °C in continuous use.[20] However, the temperature range of stable Bi_2Te_3 operation is bound to this upper limit, whereas the largest fraction of available waste heat is lost above,[21] which is why research focuses on materials and TEG operating at higher temperatures. High-performance modules using various materials were reported, such as half-Heusler compounds (8.3% efficiency and 2.11 W cm^{-2} power density when operating between 342 and 997 K[22]), Skutterudites (10.2% efficiency and 1.6 W cm^{-2} power density between 298 and 872 K[23]),

J. Camut, P. Ziolkowski, P. Ponnusamy, C. Stiewe, E. Mueller, J. de Boor
Institute of Materials Research
Department of Thermoelectric Materials and Systems
German Aerospace Center
51147 Cologne, North Rhein-Westphalia, Germany
E-mail: julia.camut@dlr.de; johannes.deboor@dlr.de

E. Mueller
Institute of Inorganic and Analytical Chemistry
JLU Giessen
35390 Giessen, Hessen, Germany

J. de Boor
Faculty of Engineering, Institute of Technology for Nanostructures (NST)
University of Duisburg-Essen
47057 Duisburg, Germany

The ORCID identification number(s) for the author(s) of this article can be found under https://doi.org/10.1002/adem.202200776.

DOI: 10.1002/adem.202200776

and PbTe (9% efficiency and 3.6 W cm^{-2} power density between 283 and 873 K[24]). PbTe/TAGS-based TEGs with up to 12% efficiency are also commercially available for temperatures between 200 and 600 °C. However, the main disadvantage of those high-performance TE materials is that they are made of toxic and/or rare and expensive compounds, while their stability under test is quite low.[25] Their toxicity and scarcity make them unsuitable for mass applications, which hinders the breakthrough of TE technology beyond space and cooling applications.

In this study, the solid-solution $Mg_2Si_{0.3}Sn_{0.7}$ was chosen as the chemical composition for both p- and n-type materials of the TEG. The n-type material exhibits a high reproducible figure of merit of up to $zT = 1.4$.[26] The figure of merit is the main parameter indicating a TE material's performance; it is defined as $zT = \frac{\alpha^2\sigma}{\kappa}T$ where α is the Seebeck coefficient, σ the electrical conductivity, and κ the thermal conductivity. This value is among the best TE performance values in the mid-to-high temperature range, compared with other materials in a similar temperature range.[14,27] P-type $Mg_2Si_{1-x}Sn_x$ has seen significant improvement over the last years with maximum zT rising from <0.1 before 2010[28] to 0.6,[13] approaching that of other material classes that might or have been used together in a TEG with n-type $Mg_2Si_{1-x}Sn_x$, such as higher-mangenese silicides (HMS), ZnSb, and $CeFe_4Sb_{12}$.[18,29,30] p-type $Mg_2Si_{1-x}Sn_x$ was also chosen due to the advantages of using similar materials for both n- and p-type legs, which are explained below. This material system also has the important advantage of not being composed of toxic nor rare elements, unlike other materials presented above. It is also lightweight, which is advantageous for mobile applications, in particular for cars and aerospace.

Following the optimization of the TE properties, the next step toward TEG device development is applying a suitable electrode. The electrode, also referred to as metallization, is a metallic layer applied between the TE leg and the bridge. It can act as a diffusion barrier,[31] mechanical buffer, and/or as an agent to facilitate soldering/joining the leg to the bridge. Aluminum was previously shown to be a compatible electrode for p- and n-type $Mg_2(Si,Sn)$,[32,33] and it was therefore used in this work as metallization layer. Using chemically similar p- and n-type materials can improve the mechanical stability of the module, even more if the same electrode is used for all legs, as the differential thermal expansion will be similar for all legs.[34] Some stress due to the remaining coefficient of thermal expansion (CTE) mismatch cannot be avoided; therefore, having the same material combination for all legs can also allow to find means to relieve this stress more easily.

Although silicides have been extensively studied in the field of TE properties optimization, not much work has yet been reported on the technological aspect of using them to build modules. Different studies have investigated Mg_2Si-based n-type unileg TEG, with limited performance.[35–38] Mg_2Si was also paired with Si–Ge, which gave a power density of 1.8 W cm^{-2} (with respect to the area of the TE legs) for $T_h = 650$ °C and $T_c = 30$ °C.[39]

Some studies also focused on the $Mg_2(Si,Sn)$/HMS combination for TEG.[29,40–42] Skomedal et al. reported a maximum power density of 3 W cm^{-2} (TE area) and predicted an efficiency of 5.3% for a possibly unrealistic $T_h = 735$ °C[41] with $Mg_2(Si,Sn)$ as n-type. In a TEG cascaded with BiTe,[42] the Mg_2Si/HMS module alone reached a maximum efficiency of 8.5%, for $T_h = 550$ °C and $T_c = 30$ °C. Finally, a segmented TEG made of BiTe and Mg_2Si/HMS gave a maximum power density 0.8 W cm^{-2} (TE area) for $\Delta T = 498$ K and an efficiency up to 5% for $\Delta T = 500$ °C and $T_c = 25$ °C.[29]

Two fully $Mg_2(Si,Sn)$-based TEGs were reported previously. Gao's thesis reported a first attempt showing a maximum power output of 117 mW for $T_h = 440$ °C and $T_c = 110$ °C.[43] More recently, Goyal et al. reported a power density of 0.52 W cm^{-2} (TE area) and calculated a predicted maximum efficiency of 5%.[44] However, no measured efficiency was reported for such a TEG so far.

Measuring the heat flow (and with it the conversion efficiency) for small TEG prototypes is difficult due to the small heat flow it requires, as this amplifies, for geometrical reasons, the uncertainty related to thermal bypass. In this work, we present the first full characterization of a fully $Mg_2(Si,Sn)$-based TEG, including its conversion efficiency measurement. The reliability of the measurement is tested through comparison with calculations using the constant property model (CPM), which has the advantages of being simple but often precise enough, given the considerable experimental uncertainties.[45] Open-circuit voltage, inner electrical resistance, heat flow for open circuit and maximum power conditions, current for maximum power, maximum power output and maximum conversion efficiency are calculated and compared. Satisfying match is found for most parameters except the inner electrical resistance, which indicates some defects in the TEG and allows to identify room for improvement. The calculations are also used to analyze the cycling behavior of the TEG (over two measuring cycles) to understand changes at material and device level. Estimations of performance for improved contact qualities are provided for a technologically realistic range of achievable inner resistance of the TEG.

2. Experimental Section

2.1. Experimental

2.1.1. Legs Preparation

Pellets of $Mg_2(Si,Sn)$ solid solutions were prepared similarly to what were reported in previously published papers, with the following nominal stoichiometry: $Mg_{2.06}Si_{0.3}Sn_{0.665}Bi_{0.035}$ for n-type (including excess Mg to compensate for Mg evaporation) and $Mg_{1.98}Li_{0.03}Si_{0.3}Sn_{0.7}$ for p-type.[26,46,47]

The electrodes consisted of Al foil (Alfa Aesar, 99.99% purity) directly in contact with the TE pellet and a Cu foil (ChemPUR, 99.995% purity) on the outside of the pellets such as that shown in **Figure 1**. The Al foil is Ar etched and coated on both sides with a ≈8 μm Zn layer, as it was previously shown that it was necessary to protect the Al surface with an oxidation barrier coating after etching to have high-quality electrical contacts.[33] The Ar-ion etching, Zn coating, and contacting process were similar to what was reported in this previous work.

After contacting, the pellets were diced into legs using a Disco DAD321 Automatic Dicing Saw. The cutting speed through the sample was 0.3 mm s^{-1} with an angular speed of 30 000 blade rotations per minute and each cut was made in a single pass. The whole process is summed up in Figure 1.

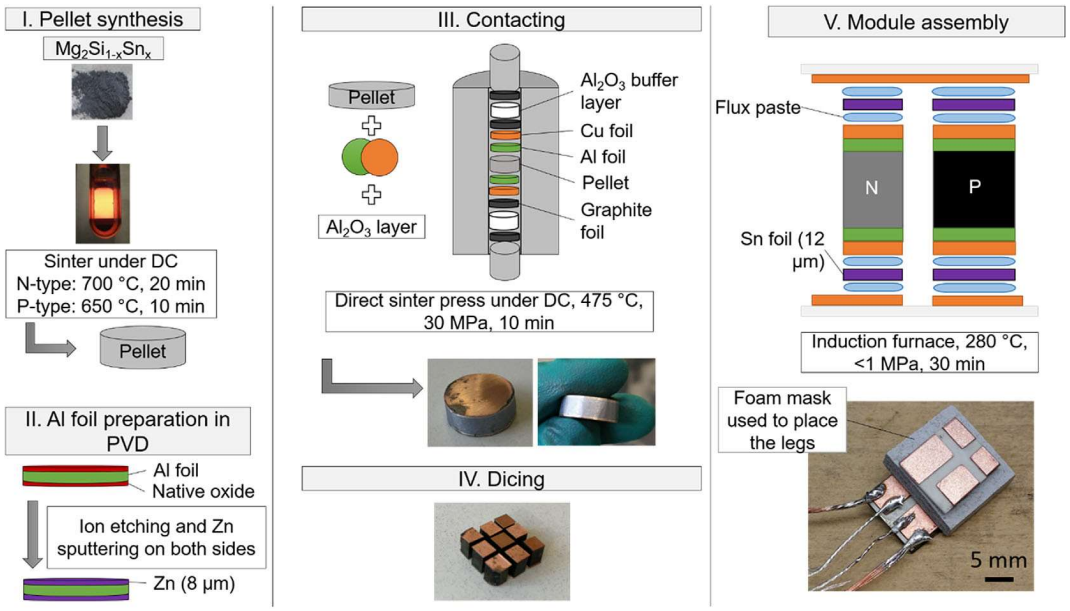

Figure 1. Preparation process from pellet fabrication over metallized legs to the thermoelectric module lab prototype. The foam mask used as leg spacer is made of Porotherm delivered by TECHNO-PHYSIK Engineering GmbH, Essen, Germany.

The quality of the joining between the metallization and the TE legs was gauged by the value of its specific contact resistance r_c, which could be measured using a potential and Seebeck scanning microprobe (PSM).[48,49] Two r_c values were obtained for each contact with two different calculation methods, using the TE material's known electrical conductivity to calculate the current density ($r_{c,j(TE)}$) or using the current passing through the sample as measured on a shunt resistor by the PSM ($r_{c,j(PSM)}$), as reported in previously published papers.[32,46] The two specific electrical contact resistances were calculated using the following equations.

$$r_{c,j(TE)} = \frac{(V_{elec} - V_{TE}) * L}{\Delta V_{TE} * \sigma_{TE}} \quad (1)$$

$$r_{c,j(PSM)} = \frac{(V_{elec} - V_{TE}) * A}{I_{PSM}} \quad (2)$$

Here, $V_{elec} - V_{TE}$ is the drop in electrical potential at the interface between the electrode and the TE material and the position of interface being localized using the drop in Seebeck coefficient on the line scan. L is the length of the TE material (between the two electrodes), ΔV_{TE} is the drop of potential along the TE material and σ_{TE} is the electrical conductivity of the TE material, A is the leg cross-section, and I_{PSM} the current measured in the device.

Evaluation of contact resistivities was conducted for the electrodes on each side of every leg. The r_c values obtained for the legs used to build the module studied in this work are reported in **Table 1**.

It can be seen that the electrical contact resistivities from both evaluation methods lie close to each other and within the limits of individual statistical distributions. Furthermore, contact resistivities are symmetric and low ($<10\,\mu\Omega\,cm^2$), meaning that the contact between the TE material and the metallization should not impede the performance of the module.[50] For the following calculations, an average value of $5\,\mu\Omega\,cm^2$ was considered for each TE/Al interface. The r_c value is also considered to be constant with temperatures, as the temperature dependence of the contact resistance between Ni electrodes and Mg_2Si was previously shown to be weak.[51] Therefore, the same value applies to both hot and cold sides of the TEG for following calculations.

Table 1. Specific contact resistances (mean value ± standard deviation) of the legs used to build the module. Each interface of each leg is reported to check for symmetry.

Leg	n-type		p-type	
Interface	Side 1	Side 2	Side 1	Side 2
$r_{c,j(TE)}$ [$\mu\Omega\,cm^2$]	3 ± 2	2 ± 1	6 ± 2	5 ± 2
$r_{c,j(PSM)}$ [$\mu\Omega\,cm^2$]	6 ± 4	4 ± 2	5 ± 2	5 ± 1

Table 2. Details of the legs used for the module fabrication.

	n-type	p-type
Effective composition	$Mg_2Si_{0.3}Sn_{0.665}$ $Bi_{0.035}$	$Mg_{1.97}Li_{0.03}$ $Si_{0.3}Sn_{0.7}$
Cross section [mm × mm]	3.4 × 3.4	4.5 × 4.5
TE length before contacting [mm]	4.05	3.96
Total leg length (including electrodes) [mm]	4.30	

2.1.2. Module Fabrication

The details of the legs used for the fabrication of the module are reported in **Table 2**.

The module consisted of two unicouples and was assembled and joined in an induction furnace. The top and bottom substrates were standard commercial direct-bonded copper (DBC) plates obtained from HHI Industrievertretungen. The legs were soldered to the DBC using Sn foil (12.5 μm) as a solder. Flux paste was applied to both sides of the solder foil, as shown in Figure 1. The joining parameters were 280 °C for 30 min with a heating rate of 25 °C min^{-1} and a load of 4 kg (0.6 MPa) under partial Ar atmosphere. The module had a filling factor of 31%, with respect to the area of the top DBC plate (top DBC: $15 \times 13\ mm^2$; bottom DBC: $14 \times 25\ mm^2$).

2.1.3. Module Testing

After assembly, the module performance was measured using an in-house built thermoelectric generator measurement apparatus (TEGMA) reported in other studies.[52–54] The measuring section of the setup was made of a heater, a geometry adaptor (copper), which distributed the heat flow on the hot side of the TEG over an appropriate cross section, the measured TEG, a nickel block (nickel LC992) that was used as a heat flow meter (HFM), and a cooling plate as a heat sink at the bottom of the configuration. To ensure good heat transfer between all components of the measuring section, graphite foils (Dr. Fritsch Gerätebau GmbH, 200 μm thickness) were inserted at all interfaces. The cold side temperature at the TEG was kept constant at 25 °C, while the hot side temperature was varied within the range from 200 to 400 °C. These values corresponded to interface temperatures of the coupling zones of the TEG, which were determined from an extrapolation of temperature profiles of the components adjacent to the TEG inside the measuring section.[38] Consequently, cold and hot side temperatures was not equal to effective temperatures at the TE legs but included temperature drops across graphite foils and DBC substrates. A schematic of the different temperatures along the measurement column is shown in the Supporting Information (Figure S2). The axial pressure applied to the TEG was about 3.9 MPa. The measurement was done under vacuum to eliminate convective heat losses, which could interfere with the heat flow measurement.

Measurement uncertainties of the TEGMA were determined for larger prototype and commercial TEG having significantly different properties compared with the module studied in this work. The uncertainty of open-circuit voltage was found to be 0.06% (for a measured value of 7.2 V)[53] (Supporting Information); the inner resistance had an uncertainty of 2.28% (for a measured value of 0.74 Ω)[53]; the heat flow had an uncertainty of 12% for a measured value of 100 W[52]; the power output had an uncertainty of 1.25% for a measured value of 2.5 W and the efficiency an uncertainty of 15.7% for a measured value of 4%.[55] Besides the choice of TE materials and contacting schemes, these deviations relate to the number of installed TE legs, their geometries, and the filling factor. Therefore, comparability to our TEG prototype is limited.

3. Theory and Evaluation

In order to check for the reliability of the measurement and identify loss mechanisms that impair module performance, model calculations on TEG performance were made to compare simulation results to measurements of the module performance. For the sake of simplicity, the constant properties model (CPM) was used, which assumes temperature-independent (averaged) properties along the TE legs using a method detailed (Equation (3)). Hence, the CPM approach neglects minor effects on the operation characteristics of TEGs such as Thomson heat and asymmetric distribution of Joule heat to the hot and cold sides of the leg. Furthermore, symmetric electric and thermal contact resistance between hot and cold side as well as between p- and n-type legs and the absence of parasitic heat bypass by radiation or convection were assumed.[56]

3.1. TE Properties and Temperature Average

In the CPM, average properties are assumed for the TE legs. While spatial averaging of electrical and thermal resistivities is physically appropriate, it was shown by Ponnusamy et al. that temperature averaging is satisfyingly reliable for the Mg_2X materials in terms of efficiency prediction (with an uncertainty <2%, which is much smaller than the measurement uncertainty).[45] This method determines an averaged property $\overline{X}$ between T_c and T_h such as

$$\overline{X} = \frac{1}{\Delta T}\int_{T_c}^{T_h} X(T)\mathrm{d}T \tag{3}$$

All TE properties (α, ρ, thermal resistivity $\frac{1}{\kappa}$) used in the following and previous CPM equations refer to temperature averages calculated using Equation (3). In particular, κ is calculated as the reciprocal of the average thermal resistivity such as $\overline{\kappa} = \left(\frac{1}{\Delta T}\int_{T_c}^{T_h}\frac{1}{\kappa(T)}\mathrm{d}T\right)^{-1}$.

The TE properties data used for the calculations are shown in **Figure 2**. This experimental data was obtained from samples synthesized using the melting route described in previous work. It is reproducible and in the range of state-of-the-art values.[13,26]

Due to the contacting procedure involving Zn, a slight gradient in the Seebeck coefficient appears in n-type legs spreading from the contact faces. An exemplary PSM linescan is shown in Supporting Information (Figure S1) and another example can be also seen in the study by Camut et al.[33]. Given the limited magnitude of the change (≤11%, locally), this should have only minor impact on the module properties.

3.2. Determining the Temperature Conditions at the TE Legs

In order to make precise calculations, the effective temperatures at the TE legs had to be determined, as there were parasitic temperature drops across the elements of the measurement column, as represented in Supporting Information (Figure S2), and only the temperatures at the interface between the TEG and the elements of the column are measured. The effective hot and cold side temperatures at the TE legs are defined by $T_{h,TE}$ and $T_{c,TE}$,

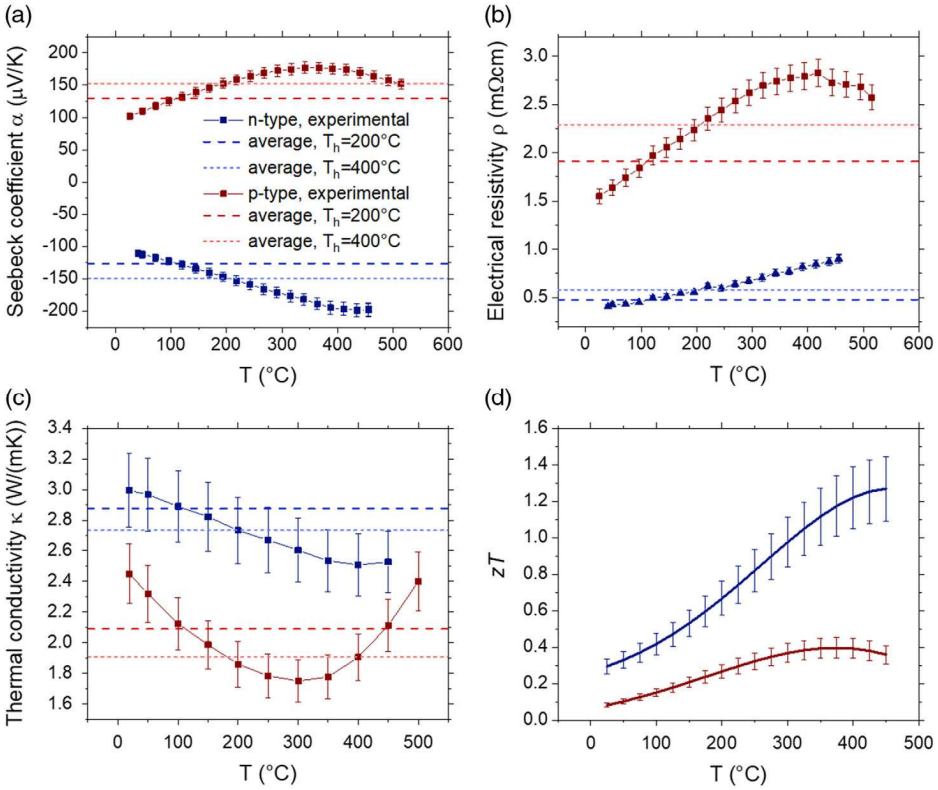

Figure 2. Measured properties of $Mg_2Si_{0.3}Sn_{0.665}Bi_{0.035}$ (n-type) and $Mg_{1.97}Li_{0.03}Si_{0.3}Sn_{0.7}$ (p-type) materials used as input for the CPM calculations: a) Seebeck coefficient, b) electrical resistivity, c) thermal conductivity, d) figure of merit. Uncertainties of the Seebeck coefficient and electrical conductivity measurement are 5% of the thermal conductivity 8%. The resulting uncertainty of zT is 14%. Exemplary temperature averages of each property for temperatures at the TE legs are given, for hot side temperatures of 200 and 400 °C and a cold side temperature of 25 °C. The legend in (a) also applies for (b), (c), and (d).

respectively, and we define the temperature difference at the TE legs such as $\Delta T_{\mathrm{TE}} = T_{\mathrm{h,TE}} - T_{\mathrm{c,TE}}$.

The open-circuit voltage is the thermovoltage generated by the TEG due to the Seebeck effect by applying a temperature difference to the legs.[57] Using the measured open-circuit voltage $U_{0,\mathrm{m}}$, the effective temperature difference at the TE legs at open loop $\Delta T_{\mathrm{TE},0} = \Delta \mathrm{T_{TE}}(\mathrm{I} = 0)$ can be obtained from the number of unicouples (N) and their Seebeck coefficient averages (α_{n}, α_{p}) such as

$$\Delta T_{\mathrm{TE},0} = \frac{U_{0,\mathrm{m}}}{N(\alpha_{\mathrm{p}} - \alpha_{\mathrm{n}})} \tag{4}$$

n and p subscripts designate n-type and p-type materials (for all following equations as well). Then, the temperatures at the hot and cold side of the TE legs can be obtained assuming a symmetrical temperature loss across graphite foils and DBC substrates such as $T_{\mathrm{h,TE}} = T_{\mathrm{h,m}} - 0.5 \times (\Delta T_{\mathrm{m}} - \Delta T_{\mathrm{TE}})$ and $T_{\mathrm{c,TE}} = T_{\mathrm{c,m}} + 0.5 \times (\Delta T_{\mathrm{m}} - \Delta T_{\mathrm{TE}})$, where $T_{\mathrm{c,m}}$ and $T_{\mathrm{h,m}}$ are the measured cold and hot side temperatures at the interfaces between the TEG and the heat flow meter and the heater, respectively.

When applying Equation (4), the Seebeck coefficient averages $\alpha_{\mathrm{p}}, \alpha_{\mathrm{n}}$ are calculated in a first iteration assuming $T_{\mathrm{h,TE}} \approx T_{\mathrm{h,m}}$ and $T_{\mathrm{c,TE}} \approx T_{\mathrm{c,m}}$, which leads to some error in the obtained ΔT_{TE}, $T_{\mathrm{c,TE}}$, and $T_{\mathrm{h,TE}}$. However, Equation (4) was reapplied in a second iteration with new $\alpha_{\mathrm{p}}, \alpha_{\mathrm{n}}$ average values corresponding to the temperature conditions at the TE legs obtained in the first iteration. The obtained temperatures converge in only two iterations due to the weak slope of $\alpha(T)$.

An obvious error in this method arises from the assumed symmetrical distribution of the parasitic temperature drop between hot and cold sides to obtain values of $T_{\mathrm{c,TE}}$ and $T_{\mathrm{h,TE}}$. In reality, the distribution is likely not symmetrical as there is a temperature dependence of the thermal contact resistance between each layer as well as of the thermal resistance of the graphite and ceramic plates. Calculations with other heat loss distributions are shown in Supporting Information (see Figure S5) and it will be shown in this paper that good match is still found with the symmetry assumption.

Other methods shown in the Supporting Information can be used for determination of the effective temperature conditions at the TE legs using the measured heat flow. However, as the measurement uncertainty of the heat flow is larger, especially at higher temperatures, we find them to be less reliable.

3.3. Temperatures at the TE Legs for $I \neq 0$

The temperatures at the TE legs obtained as described above only apply in case of open-loop conditions. However, due to the

influence of the Peltier heat, the temperature difference at the TE legs decreases when current is flowing and most TEG parameters are relevant for $I \neq 0$.

The parasitic temperature drop at the coupling zones between the TE legs and the HFM/heater, $\Delta T_{\mathrm{par,h}}$ and $\Delta T_{\mathrm{par,c}}$ respectively, are represented in Supporting Information (Figure S2). Considering $\Delta T_{\mathrm{par}} = \Delta T_{\mathrm{par,c}} + \Delta T_{\mathrm{par,h}}$, we define $\Delta T_{\mathrm{par,0}} = \Delta T_{\mathrm{par}}(I = 0)$ and $\Delta T_{\mathrm{par,opt}} = \Delta T_{\mathrm{par}}(I = I_{\mathrm{opt}})$, where I_{opt} is the current at maximum power output. Assuming that the thermal resistance of the parasitic layers does not vary with current, ΔT_{par} varies proportionally to the heat flow only, therefore

$$\frac{Q_{\mathrm{opt,m}}}{Q_{\mathrm{0,m}}} = \frac{\Delta T_{\mathrm{par,opt}}}{\Delta T_{\mathrm{par,0}}} = \frac{\Delta T_{\mathrm{m,opt}} - \Delta T_{\mathrm{TE,opt}}}{\Delta T_{\mathrm{par,0}}} \tag{5}$$

where Q is the measured incident heat flow and "0" and "opt" subscripts respectively refer to parameters at open-loop conditions and at optimum current for maximum power. $\Delta T_{\mathrm{par,0}}$ is known such as $\Delta T_{\mathrm{par,0}} = \Delta T_{\mathrm{m,0}} - \Delta T_{\mathrm{TE,0}}$. From Equation (5), $\Delta T_{\mathrm{TE,opt}}$ is calculated and the corresponding hot and cold side temperatures, $T_{\mathrm{h,TE,opt}}$ and $T_{\mathrm{c,TE,opt}}$, can be determined assuming symmetric losses.

Incident heat flows are not directly measured by the used configuration of the TEGMA, since a heat flow meter has been used at the cold side of the TEG only. Thus, Q_{m} is obtained by adding the measured values of the heat flow exiting at the cold side of the TEG ($Q_{\mathrm{out,m}}$) to the power output (P_{m}) at a given current, such as $Q_{\mathrm{m}} = Q_{\mathrm{out,m}} + P_{\mathrm{m}}$.

3.4. Heat Flows

Within CPM the heat flow at maximum power Q_{opt} is calculated using the following equations.

$$Q_{\mathrm{opt}} = K_{\mathrm{TE}} \Delta T_{\mathrm{TE,opt}} + I \cdot N \cdot (\alpha_{\mathrm{p}} - \alpha_n) T_{\mathrm{h,TE,opt}} - \frac{1}{2} I^2 R \tag{6}$$

$$I_{\mathrm{opt}} = \frac{N(\alpha_{\mathrm{p}} - \alpha_n) \Delta T_{\mathrm{TE,opt}}}{2R} \tag{7}$$

where R is the inner electrical resistance and K_{TE} the thermal conductance of the TE legs such as

$$R = R_{\mathrm{TE}} + R_{\mathrm{c}} = N\left[\frac{\rho_{\mathrm{p}} L}{A_{\mathrm{p}}} + \frac{\rho_n L}{A_n} + 2r_{\mathrm{c}}\left(\frac{1}{A_{\mathrm{p}}} + \frac{1}{A_n}\right)\right] \tag{8}$$

$$K_{\mathrm{TE}} = N\left(\frac{\kappa_{\mathrm{p}} A_{\mathrm{p}}}{L} + \frac{\kappa_n A_n}{L}\right) \tag{9}$$

where R_{TE} is the total electrical resistance of the TE legs and R_{c} the total electrical contact resistance. Equation (8) neglects the resistance of the metallic layers (Al metallization, Cu metallization, Cu bridges) and the contact resistances between them and R_{c} is assumed to mainly originate from the Al/TE interface.

For the open-loop heat flow, Q_0, Equation (6) is applied for $I = 0$, using $\Delta T_{\mathrm{TE,0}}$ and $T_{\mathrm{h,TE}}(I = 0)$, and K_{TE} is calculated for open-loop temperature conditions.

3.5. TEG Performance

For all following parameters, temperature conditions at maximum power are considered, even for maximum efficiency. Indeed, our measurement shows that there is between 1% and 2% difference between $I_{\mathrm{opt},\eta}$ (current at maximum efficiency) and I_{opt}; therefore, the heat flow and temperatures at the TE legs will be similar for both current conditions (see Figure S6 in Supporting Information).

The performance of a TEG is mainly assessed by its power output and conversion efficiency. The maximum power output is generally given by[58]

$$P_{\mathrm{max}} = N(P_n + P_{\mathrm{p}}) = \frac{(N(\alpha_{\mathrm{p}} - \alpha_{\mathrm{n}}) \Delta T_{\mathrm{TE,opt}})^2}{4R} \tag{10}$$

The maximum efficiency η_{max} of a TEG in the CPM can be obtained using the following equation.

$$\eta_{\mathrm{max}} = \frac{T_{\mathrm{h,TE,opt}} - T_{\mathrm{c,TE,opt}}}{T_{\mathrm{h,TE,opt}}} \frac{\sqrt{1 + ZT_{\mathrm{m}}} - 1}{\frac{T_{\mathrm{c,TE,opt}}}{T_{\mathrm{h,TE,opt}}} + \sqrt{1 + ZT_{\mathrm{m}}}} \tag{11}$$

where T_{m} is the average of $T_{\mathrm{c,TE,opt}}$ and $T_{\mathrm{h,TE,opt}}$. ZT_{m} is the device figure of merit with

$$Z = \frac{N^2(\alpha_{\mathrm{p}} - \alpha_n)^2}{K_{\mathrm{TE}} R} \tag{12}$$

In Equation (11) and (12), the temperatures at the TE legs are considered for more precision. In literature, the measured temperatures at the outside of the TEG are more commonly applied.

3.6. Inner Electrical Resistance

The inner electrical resistance of the TEG is calculated using Equation (8). Two leads are soldered to each TEG terminal in order to conduct a four-point measurement, which allows to neglect the resistance contributions of the current leads and potential probes. The detailed description of the procedure for measuring R is given in other studies.[39,40]

4. Results

Figure 3a shows the result of the two-cycles measurement for the open-circuit voltage. A significant increase of 12% is observed in the measured open-circuit voltage between the start and end of the first cycle, which is followed by an increase of up to 2% in the second cycle. This change will be compared to the change of other properties and commented.

The first-cycle cooling data is used for calculation of temperatures at the TE legs on the hot and cold side for $I = 0$ and I_{opt}. If we calculate the ratio $\Delta T_{\mathrm{TE}}/\Delta T_{\mathrm{m}}$, it is found that respectively 5–11% (corresponding to 7 to 41 K) and 5–12% of the temperature difference is lost through the coupling, rising with increasing hot side temperature, as shown in Figure 3b.

Figure 3c–f shows the two-cycle measurement and calculations of other parameters: the inner resistance, heat flows (for open circuit and maximum power), and the current for

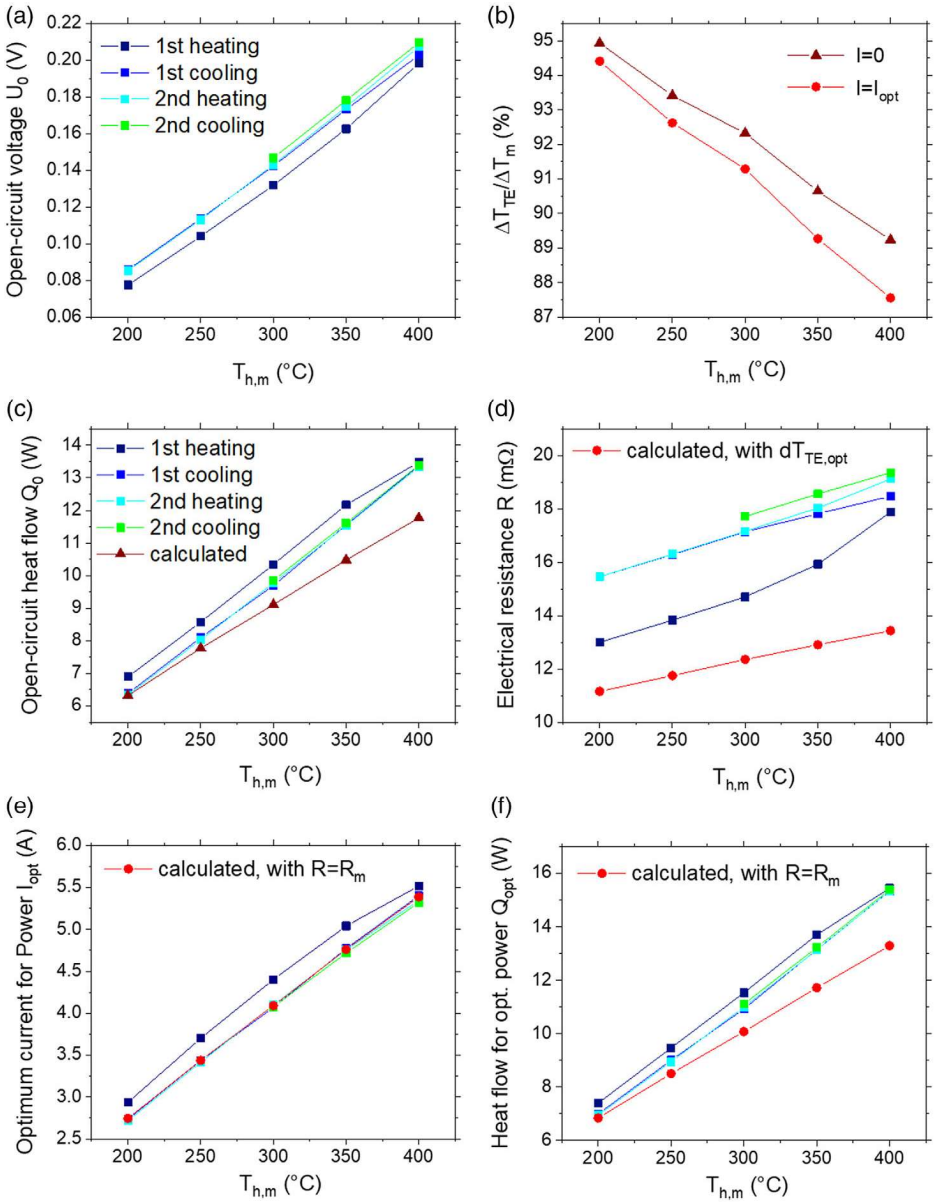

Figure 3. a) Two-cycles measurement of open-circuit voltage and b) ratio of the temperature differences at the TE legs and across the device for $I = 0$ and $I = I_{opt}$. Two-cycles measurement and calculations of: c) heat flow at open circuit, d) inner electrical resistance, e) optimum current for maximum power, and f) heat flow at maximum power. The calculated data was obtained data from the first cooling step. R_m is the measured electrical resistance. The legend of the measured data (blue to green hues, indicated in a)) also applies in (d), (e), and (f).

maximum power. It can be seen that a significant change occurs for all quantities during the first heating and cooling periods, followed by a more stable behavior in the next cycle, similar to what was observed for open-circuit voltage in Figure 3a. Changes during cycling can usually be attributed to three main factors: coupling quality (thermal transfer between TEG and TEGMA components), material change, and crack formation.

The decrease in heat flow (7% for Q_0) could indicate that the coupling quality degraded during the first heating step. This is opposed to the observed increase in open-loop voltage, as a lesser thermal transfer would rather decrease ΔT_{TE}. The increase in open-circuit voltage despite a decrease of ΔT_{TE} could be due to an increase of Seebeck coefficient. However, comparative line-scans of the Seebeck coefficient of an n-type and p-type leg are shown in Supporting Information (Figure S1). This magnitude of change (<7% for the n-type leg, <4% for the p-type) can alone explain only a minor fraction of the observed variation in the open-loop voltage. Similarly, the expected increase in material resistance is <10% (estimated using an single parabolic band model), way smaller than the observed increase, which therefore likely indicates the formation of cracks. If the cracks are located inside the TE legs (not at the interfaces with the metallization), it

would lead to an increase of ΔT_{TE} and therefore the open-loop voltage, as we observe.

Figure 3d shows the comparison between calculated and measured values of the total inner resistance. At the start of the measurement, the difference between measurement and calculation was 15%; by the end of the first cooling step, it increased to 28%. The calculated data sums the resistance of the TE legs and the contact resistances using the specific resistivity reported in Table 2. The considered contact resistance represents 2% of the calculated total inner resistance. The far larger measured R indicates that there is additional resistance in the electrical circuit, which was not yet accounted for, and that it increases with cycling (large increase in the first cycle, smaller in the second). This could come from additional contact resistance (poor soldering, progressive delamination of metallization) or from crack formation, which would hinder the current flow.

The optimum current for maximum power shows a deviation <1% between measurement (first cooling) and calculation (using the measured R). This slight deviation could come from the small change in n-type Seebeck coefficient.

The temperature profile in the cold side heat flow meter is shown in Figure S7 in the Supporting Information. It can be seen that there is a 5–12 K temperature difference, for a heater temperature of 200 °C and 400 °C respectively, which is sufficiently large for reliable estimation of the heat flow. The measured open-circuit heat flow (first cooling) is 1–14% higher than the calculated value with increasing hot side temperature, similar to the heat flow for optimum power, which shows a difference of 2–15%. This is in the range of measurement uncertainty reported in the study by Ziolkowski et al.,[52] except for the highest temperature for which the deviation is higher than the uncertainty threshold. This threshold was however determined for commercial-scale TEG (more legs, larger filling factor) and therefore does not necessarily apply to our prototype.

The similarity between observed differences for open-loop and nonzero current conditions indicates that the deviation between measurement and calculation does not highly depend on electric current flow and associated effects like Joule, Thomson, and Peltier heat and their asymmetry. Although there could be compensating effects, it gives a good hint that the CPM is applicable. Said deviation would rather originate from discrepancies between true and supposed TE properties, temperature conditions, and of course from cracks and possible TEG-internal heat bypasses, not considered in the CPM. The increase of the difference with increasing temperature indicates that the deviation is likely due to the increase of the heat bypass inside the TEG by means of radiation.

Figure 4 shows the comparison of two-cycles measurement and calculations for maximum power output and efficiency. The increase of both open-circuit voltage and inner resistance compensates such that the maximum power remains relatively stable throughout cycling (<3.5% change between cycling steps). An increase in maximum efficiency is observed between the first heating and cooling, due to the corresponding decrease in heat flow.

The higher measured electrical resistance R_m will have an impact on the deviations of further calculations which depend on this parameter. Independently from the cause of this increased resistance (contacts or cracks), the increase can be considered analytically as "effective" contact resistance such as

$$r_{c,m} = \frac{(R_m - R_{legs})A_n}{2N\left(1 + \frac{A_n}{A_p}\right)} \tag{13}$$

The obtained values for $r_{c,m}$ evolve from 85 to 99 μΩ cm^2 with increasing hot side temperature.

The power output and efficiency measurements give a maximum power of 0.55 W (density 0.9 W cm^{-2} with respect to the total TE leg area) and a maximum efficiency of 3.6%. The calculations are made using both $r_{c,m}$ and the initial $r_c = 5$ μΩ cm^2 measured between the TE material and the metallization, before the TEG assembly. Therefore, the calculations using $r_{c,m}$ represent the actual TEG while the calculations using r_c represent a realistic goal, without cracks and with the in-principle achievable low-contact resistances. The difference between measurement and $r_{c,m}$ calculations is 2–4% for maximum power and 1–10% for maximum efficiency. The larger difference of the latter is due to the deviation between calculated and measured heat flow.

To trace the origin of the observed high electrical resistance, scanning electron microscopy (SEM) investigation was performed. However, as this implied to embed the TEG for

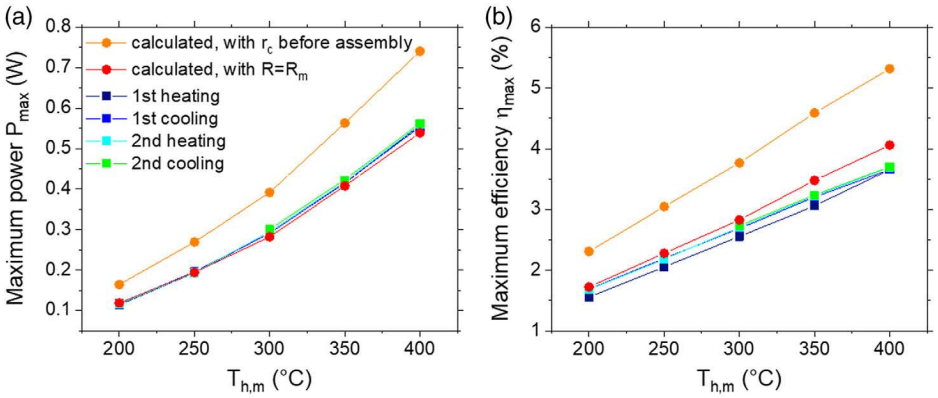

Figure 4. Comparison between measurement, calculations using contact resistance measured on the metallized legs before TEG assembly, and using contact resistance obtained from measured inner resistance, for: a) maximum power output and b) maximum efficiency. The legend in (a) also applies to (b).

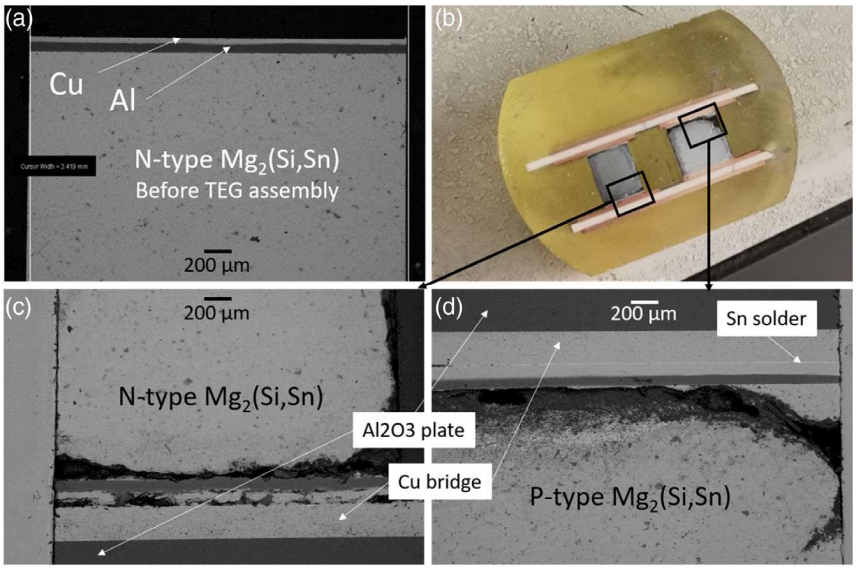

Figure 5. a) Representative SEM observation of a metallized leg before TEG assembly, b) photograph of a TEG unicouple made under identical conditions as the prototype measured and shown in Figure 3 and 4, c) SEM close-up of the junction between n-type leg and bridge indicated in (b), and (d) SEM close-up of the junction between p-type leg and bridge indicated in (b).

preparing a polished section, which would prevent any further characterization, we set up another unicouple prototype under identical conditions especially for SEM investigations; the results are shown in **Figure 5**. As this unicouple has been assembled with an identical procedure as the TEG discussed in this paper, it can give some hints on the state of the measured TEG, at least prior to its performance measurement. However, as TEG fabrication is a multistep process, there is of course some variability which limits the similarity of this unicouple analysis to the measured TEG.

It can be observed in Figure 5a that prior to assembly, no crack can be seen between the different components of the metallized leg. However, after the TEG assembly step (280 °C, 30 min, 0.6 MPa), cracks formed in the TE material next to the metallization layer. Such cracks are definitely a source of increased inner electrical resistance in a module, especially given that the hot side temperature during the measurement goes beyond 280 °C, so crack formation is even more likely. It is however supposed that the cracks in the measured TEG are not that wide as in the embedded TEG (possibly due to applied pressure in the measurement or due to a possible widening during the embedding process), as no current would flow through cracks like observed in Figure 5.

It can also be seen in Figure 5c that the Cu–Cu junction (between leg and bridge) looks suboptimal, while the other Cu–Cu interface shown in Figure 5d looks very clean. The visual quality of those contacts seems variable; it is therefore hard to conclude on the quality of the actual interfaces in the cycled TEG and on their impact on the electrical resistance.

5. Discussion

The TEG was measured for two cycles with a cold side temperature at 25 °C and a hot side temperature varying between 200 and 400 °C. After successfully assembling and characterizing the TEG, the reliability of the experimental data must be assessed by comparison to theoretical calculations. The CPM was chosen for its simplicity. The open-circuit voltage was used to determine the temperature conditions at the TE legs, which lead to low deviations between measurement and calculations for heat flows and current at maximum power. This indicates reliable efficiency and power measurement results, within the uncertainty budgets of the employed measurement techniques. This work reports the first efficiency measurement of a fully $Mg_2(Si,Sn)$-based TEG.

Figure 6 shows the performance of other TEG lab prototypes reported in literature for the low-to-mid-temperature range, especially silicide-based TEGs. It can be seen that Sb- and Te-based modules still have better performance; however, they are composed of materials which are more toxic and have a lower temperature application range.[59,60] The power output of our TEG is higher than the power reported for the only other fully $Mg_2(Si,Sn)$-based TEG, due to a shorter and wider leg geometry (no measured efficiency reported).[44] Both its power output and efficiency are higher than the performance reported for a segmented TEG combining the high performance of silicides and BiTe.[29] Moreover, the performance of our TEG is similar to the $Mg_2(Si,Sn)$/HMS TEG reported by Skomedal et al.[41] while offering a simpler design. It is also much higher than the performance of other green materials class such as oxides. Finally, room for (large) improvement, discussed later, is identified in our TEG and the expected performance would exceed most previously reported values of silicide modules.

In order to reach the predicted optimal performance (increase by 30%), the origin of the differences between predicted and measured performance needs to be identified. The reduced power mainly originates from the electrical resistance, for which there is large disagreement between the measurement and the CPM calculations. From SEM investigations on a similar

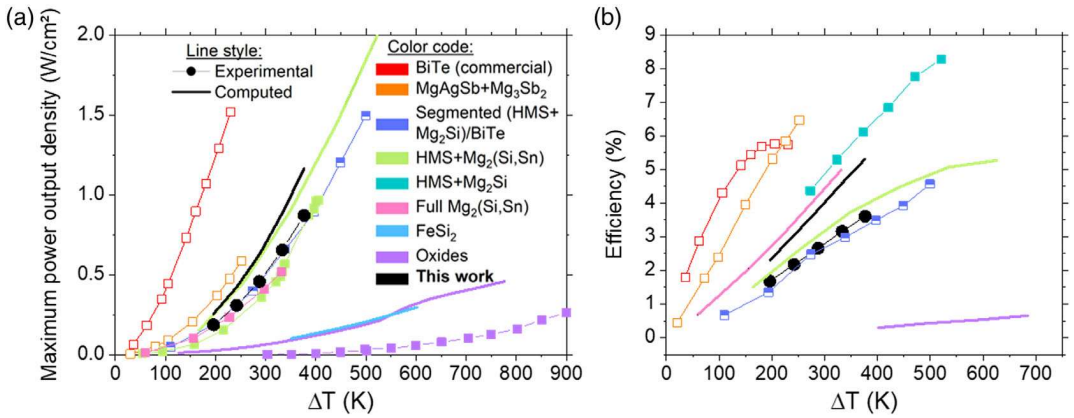

Figure 6. Performance of literature silicide-based and low-temperature TEGs: a) maximum power and b) efficiency. The legend indicated in (a) is magnified in c) for better readability and also applies to (b). Symbols + lines indicate measured data; simple lines indicate calculated data. Empty symbols indicate toxic compounds. Data were taken from other studies.[29,41,44,59–64]

unmeasured TEG, it is plausible that cracks were present close to one or several TE/Al interfaces before starting the module test measurement. This agrees with the fact that the resistance at the start of the measurement was already higher than expected. It is possible that the cracks expanded during the first heating step, which would increase the inner resistance. An increase is seen in the open-circuit voltage during the first heating step. Since the TE leg's properties are found to be relatively stable, this indicates that the temperature difference across the TE legs increased during this cycle. A corresponding increase in heat flow should be observed if this was due to better thermal transmission; however, the heat flow decreases during the first cycle, which could be explained by the widening of the cracks in the legs.

Cracks were already observed in $Mg_2(Si,Sn)$ legs composing TEGs. Mejri et al.[65] and Skomedal et al.[41] both reported crack formation on the hot side of the TEG after characterization. Kaibe et al.[42] provided finite elements methods analysis of their cascaded TEG (partially composed of $Mg_2(Si,Sn)$) and confirmed that tensile stresses are localized at the interface of the hot side electrode of the silicide module, which is probably a major origin of the reported fatigue damage.

Given that the cracks are parallel to the interface, it is unlikely that they are due to a too high axial pressure, but IT could rather be an indication of a mismatch in CTE, which has already been seen for other electrodes. The Al and Cu foils (CTE of $21–24 \times 10^{-6}$ and $17 \times 10^{-6}\,K^{-1}$ respectively) of the metallization were contacted at 475 °C, which means that if there was a CTE mismatch between the TE material (CTE of $Mg_2(Si,Sn)$ about $16–18 \times 10^{-6}\,K^{-1}$[65–67]) and those layers, the cracks should have already appeared in the metallized legs before TEG assembly (280 °C). Therefore, the thermal stress probably arises from Al_2O_3 in the DBC plate (CTE $8 \times 10^{-6}\,K^{-1}$) and not from the metallic layers.

Such stress could be partially relieved using DBC plates only at the cold side, while using a more flexible design at the hot side (i.e., cut DBC plates or loose metallic bridges[68,69]). Besides changing the TEG design toward more flexible constructions and material choice with better accordance of CTE, other parameters can be optimized to increase mechanical stability of the module. Two studies reported a reduced stress by changing the shape of the cross section of the TE legs,[70,71] and increasing leg length is also recommended,[72] although the latter will have a direct impact on the module´s thermal resistance.

Nevertheless, the increase of open-loop voltage and inner resistance compensate such as the maximum power is stable during both cycles of the measurement. The efficiency, similar to the heat flow, settles after the first heating and keeps a stable value during the second cycle of the measurement. Considering the heat flow measurement, besides its larger specified measurement uncertainty (which is not directly applicable to our TEG due to its geometry), it is also possible that it was overestimated due to a thermal bypass. It is indeed likely that some heat is transmitted as radiation between the heater and the bottom part of the TEG or the HFM, given its small size. This heat would impact the heat flow measurement in the HFM and therefore the efficiency value. Such thermal bypass can be estimated by calculating the radiative heat flow Q_{rad} emitted by the Cu heater and received by the exposed surfaces of the bottom DBC and the top of the HFM. Following the procedure described in SI, it is found $Q_{rad} \approx 0.3$ W at $T_{h,m} = 400$ °C while the difference between expected and measured values of Q_0 and Q_{opt} is ≈2 W. The real value of Q_{rad} is probably larger, considering that thermal bypass would also be absorbed by the lateral sides of the HFM, which would have an impact on the measured temperature profile, used to determine the heat flow. Such calculations are however quite complicated; therefore, a simple, quantitative estimate cannot be given. As a consequence, the measured efficiency is probably underestimated and the "real" value could actually rather be ≈4.2% at $T_{h,m} = 400$ °C (dividing measured maximum power by expected heat flow at maximum power). To get more accurate values, the measurement setup could be optimized to better accommodate small device geometries and limit parallel parasitic heat flows, using heating and cooling elements of matching cross section compared with the TEG surface.

Finally, the use of the CPM calculations is found to be reliable and beneficial for the evaluation of the performance of this TEG and as a valuable tool to identify room for improvement.

6. Conclusion

In this article, we present a fully $Mg_2(Si,Sn)$-based TEG, with the first reported conversion efficiency measurement for such a module. The reliability of the measurement is assessed by comparing it to constant property modeling calculations, which give a satisfyingly good match (<2% deviation for current at maximum power, <3% difference for maximum power output, deviation within measurement uncertainty range for heat flow and efficiency). We report a maximum power output of 0.55 W (0.9 W cm^{-2} considering TE area) and a maximum efficiency of 3.6%, which are well within the range of the reported silicide-based modules. The measured efficiency is likely underestimated due to radiative thermal bypass and the real value could actually reach 4%.

The cycling behavior of several module parameters as well as the deviation between measured and calculated inner electrical resistance suggests crack formation in the TE legs during thermal cycling related to TEG measurement. Room for improvement of module performance is identified and suggestions for next designs are given. The predicted maximum power output for reasonable inner resistance is 1.2 W cm^{-2} and the predicted maximum efficiency is 5.3%, which is significantly higher than currently reported experimental values.

Supporting Information

Supporting Information is available from the Wiley Online Library or from the author.

Acknowledgements

The authors would like to gratefully acknowledge the endorsement for the DLR executive Board Members for Space Research and Technology, as well as financial support from the Young Research Group Leader Program. The authors would also like to acknowledge Przemyslaw Blaschkewitz for his help with the thermoelectric measurements, as well as Adina Frank for her assistance with the PVD coatings. J.C. and P.P. would like to thank the DAAD fellowship programs no. 57424731 and no. 247/2017, respectively. J.D.B. acknowledges support by the Deutsche Forschungsgemeinschaft (DFG, German Research Foundation), project number 396709363. P.Z. gratefully acknowledges financial support for the project "Thermoelectric Standardization for High Temperatures" (TEST-HT, grant number 03VP04401), granted by the German Federal Ministry of Education and Research.

Open Access funding enabled and organized by Projekt DEAL.

Conflict of Interest

The authors declare no conflict of interest.

Data Availability Statement

The data that support the findings of this study are available from the corresponding author upon reasonable request.

Keywords

constant property modelling, conversion efficiency measurement, CPM, heat flow, power generation, TEG, thermoelectric generator, thermoelectrics

Received: May 30, 2022
Revised: June 23, 2022
Published online:

[1] S. Twaha, J. Zhu, Y. Yan, B. Li, *Renewable Sustainable Energy Rev.* **2016**, *65*, 698.
[2] S. Karellas, A.-D. Leontaritis, G. Panousis, E. Bellos, E. Kakaras, *Energy* **2013**, *58*, 147.
[3] N. Jaziri, A. Boughamoura, J. Müller, B. Mezghani, F. Tounsi, M. Ismail, *Energy Rep.* **2020**, *6*, 264.
[4] D. G. Ebling, A. Krumm, B. Pfeiffelmann, J. Gottschald, J. Bruchmann, A. C. Benim, M. Adam, R. Labs, R. R. Herbertz, A. Stunz, *J. Electron. Mater.* **2016**, *45* 3433.
[5] K. Li, G. Garrison, Y. Zhu, M. Moore, C. Liu, J. Hepper, L. Bandt, R. Horne, S. Petty, *J. Power Sources* **2021**, *485*, 229266.
[6] L. K. Allison, T. L. Andrew, *Adv. Mater. Technol.* **2019**, *4* 1800615.
[7] H. M. Elmoughni, A. K. Menon, R. M. W. Wolfe, S. K. Yee, *Adv. Mater. Technol.* **2019**, *4*, 1800708.
[8] M. N. Hasan, M. Nafea, N. Nayan, M. S. Mohamed, *Adv. Mater. Technol.* **2022**, *7*, 2101203.
[9] P. Gorai, V. Stevanović, E. S. Toberer, *Nat. Rev. Mater.* **2017**, *2* 17053.
[10] B. B. Iversen, *Nat. Mater.* **2021**, *20* 1309.
[11] G. J. Snyder, E. S. Toberer, *Materials for Sustainable Energy: A Collection of Peer-Reviewed Research and Review Articles from Nature Publishing Group*, World Scientific, London, UK **2011**, pp. 101–110.
[12] A. Sankhla, A. Patil, H. Kamila, M. Yasseri, N. Farahi, E. Mueller, J. de Boor, *ACS Appl. Energy Mater.* **2018**, *1* 531.
[13] H. Kamila, A. Sankhla, M. Yasseri, N.P. Hoang, N. Farahi, E. Mueller, J. de Boor, *Mater. Today:. Proc.* **2019**, *8*, 546.
[14] V. Trivedi, M. Battabyal, P. Balasubramanian, G. M. Muralikrishna, P. K. Jain, R. Gopalan, *Sustainable Energy Fuels* **2018**, *2* 2687.
[15] S. Muthiah, R. C. Singh, B. D. Pathak, P. K. Avasthi, R. Kumar, A. Kumar, A. K. Srivastava, A. Dhar, *Nanoscale* **2018**, *10* 1970.
[16] A. Ostovari Moghaddam, A. Shokuhfar, Y. Zhang, T. Zhang, D. Cadavid, J. Arbiol, A. Cabot, *Adv. Mater. Interfaces* **2019**, *6* 1900467.
[17] P. Jood, J. P. Male, S. Anand, Y. Matsushita, Y. Takagiwa, M. G. Kanatzidis, G. J. Snyder, M. Ohta, *J. Am. Chem. Soc.* **2020**, *142* 15464.
[18] K.-M. Song, D.-K. Shin, K.-W. Jang, S.-M. Choi, S. Lee, W.-S. Seo, I.-H. Kim, *J. Electron. Mater.* **2017**, *46* 2634.
[19] R. He, G. Schierning, K. Nielsch, *Adv. Mater. Technol.* **2018**, *3* 1700256.
[20] H. Hachiuma, K. Fukuda, in *Proc. of the Fifth European Conf. on Thermoelectrics*, Odessa, Ukraine, September 10–12 **2007**.
[21] G. Schierning, *Nat. Energy* **2018**, *3* 92.
[22] J. Yu, Y. Xing, C. Hu, Z. Huang, Q. Qiu, C. Wang, K. Xia, Z. Wang, S. Bai, X. Zhao, L. Chen, T. Zhu, *Adv. Mater.* **2020**, *10* 2000888.
[23] J.-M. Oh, C. C. Venters, C. Di, A. M. Pinto, L. Wan, I. Younis, Z. Cai, C. Arai, B. R. So, J. Duan, G. Dreyfuss, *Nat. Commun.* **2020**, *11* 1.
[24] P. Jood, M. Ohta, A. Yamamoto, M. G. Kanatzidis, *Joule* **2018**, *2* 1339.
[25] C. Bode, J. Friedrichs, R. Somdalen, J. Köhler, K. Büchter, C. Falter, U. Kling, P. Ziolkowski, K. Zabrocki, E. Müller, D. Kožulović, *Proceedings of the ASME 2016 International Mechanical Engineering Congress and Exposition. Volume 1: Advances in Aerospace Technology*, ASME, Phoenix, Arizona, USA, November 11–17 **2016**, V001T03A041, https://doi.org/10.1115/IMECE2016-66650.
[26] N. Farahi, C. Stiewe, D. Y. N. Truong, J. de Boor, E. Müller, *RSC Adv.* **2019**, *9* 23021.

[27] A. Bali, R. Chetty, A. Sharma, G. Rogl, P. Heinrich, S. Suwas, D. K. Misra, P. Rogl, E. Bauer, R. C. Mallik, *J. Appl. Phys.* **2016**, *120* 175101.
[28] J. de Boor, T. Dasgupta, U. Saparamadu, E. Müller, Z. F. Ren, *Mater. Today Energy* **2017**, *4*, 105.
[29] H. S. Kim, K. Kikuchi, T. Itoh, T. Iida, M. Taya, *Mater. Sci. Eng., B* **2014**, *185*, 45.
[30] P. Balasubramanian, M. Battabyal, A. Chandra Bose, R. Gopalan, *Mater. Sci. Eng., B* **2021**, *271*, 115274.
[31] J. Chu, J. Huang, R. Liu, J. Liao, X. Xia, Q. Zhang, C. Wang, M. Gu, S. Bai, X. Shi, L. Chen, *Nat. Commun.* **2020**, *11*, 2723.
[32] J. Camut, N. H. Pham, D. Y. Nhi Truong, G. Castillo-Hernandez, N. Farahi, M. Yasseri, E. Mueller, J. de Boor, *Mater. Today Energy* **2021**, *21*, 100718.
[33] J. Camut, S. Ayachi, G. Castillo-Hernández, S. Park, B. Ryu, S. Park, A. Frank, C. Stiewe, E. Müller, J. de Boor, *Materials* **2021**, *14*, 6774.
[34] G. Castillo-Hernández, E. Müller, J. de Boor, *Materials* **2022**, *15*, 779.
[35] T. Sakamoto, T. Iida, Y. Taguchi, S. Kurosaki, Y. Hayatsu, K. Nishio, Y. Kogo, Y. Takanashi, *J. Electron. Mater.* **2012**, *41* 1429.
[36] T. Nemoto, T. Iida, J. Sato, T. Sakamoto, T. Nakajima, Y. Takanashi, *J. Electron. Mater.* **2012**, *41* 1312.
[37] T. Nemoto, T. Iida, J. Sato, H. Suda, Y. Takanashi, , *J. Electron. Mater.* **2014**, *43* 1890.
[38] T. Nemoto, T. Iida, J. Sato, T. Sakamoto, N. Hirayama, T. Nakajima, Y. Takanashi, *J. Electron. Mater.* **2013**, *42* 2192.
[39] T. Tohei, S. Fujiwara, T. Jinushi, Z. Ishijima, *International Symposium on Interfacial Joining and Surface Technology (IJST2013)*. **2014**. Icho Kaikan, Osaka University, Japan, November 2013.
[40] K. R. Tarantik, J. D. König, M. Jägle, J. Heuer, J. Horzella, A. Mahlke, M. Vergez, K. Bartholomé, *Mater. Today:. Proc.* **2015**, *2* 588.
[41] G. Skomedal, L. Holmgren, H. Middleton, I. S. Eremin, G. N. Isachenko, M. Jaegle, K. Tarantik, N. Vlachos, M. Manoli, T. Kyratsi, D. Berthebaud, N. Y. Dao Truong, F. Gascoin, *Energy Convers. Manage.* **2016**, *110*, 13.
[42] H. Kaibe, I. Aoyama, M. Mukoujima, T. Kanda, S. Fujimoto, T. Kurosawa, H. Ishimabushi, K. Ishida, L. Rauscher, Y. Hata, S. Sano, *ICT 2005. 24th Inter. Conf. on Thermoelectrics, 2005*, IEEE, Piscataway, NJ **2005**.
[43] P. Gao, *Mg2(Si, Sn)-Based Thermoelectric Materials and Devices*, Michigan State University, Michigan, US **2016**, p. 128.
[44] G. K. Goyal, T. Dasgupta, *Mater. Sci. Eng., B* **2021**, *272*, 115338.
[45] P. Ponnusamy, J. de Boor, E. Müller, *Appl. Energy* **2020**, *262*, 114587.
[46] S. Ayachi, G. Castillo Hernandez, N. H. Pham, N. Farahi, E. Müller, J. de Boor, *ACS Appl. Mater. Interfaces* **2019**, *11* 40769.
[47] N. H. Pham, N. Farahi, H. Kamila, A. Sankhla, S. Ayachi, E. Müller, J. de Boor, *Mater. Today Energy* **2019**, *11*, 97.
[48] D. Platzek, G. Karpinski, C. Stiewe, P. Ziolkowski, C. Drasar, E. Müller, *ICT 2005. 24th Inter. Conf. on Thermoelectrics*, IEEE, Piscataway, NJ **2005**.
[49] P. Ziolkowski, G. Karpinski, T. Dasgupta, E. Müller, *Physica Status Solidi* **2013**, *210* 89.
[50] M. Gao, D. M. Rowe, in *CRC Handbook of Thermoelectrics* (Ed: D.M. Rowe), CRC press, Boca Raton **1995**.
[51] J. de Boor, C. Gloanec, H. Kolb, R. Sottong, P. Ziolkowski, E. Müller, *J. Alloys Compd.* **2015**, *632*, 348.
[52] P. Ziolkowski, P. Blaschkewitz, E. Müller, *Measurement* **2021**, *167*, 108273.
[53] P. Ziolkowski, P. Blaschkewitz, E. Müller, *Measurement* **2021**, *177*, 109247.
[54] P. Ziolkowski, R. Chetty, P. Blaschkewitz, M. Ohta, A. Yamamoto, E. Müller, *Energy Technol.* **2020**, *8* 2000557.
[55] P. Ziolkowski, P. Blaschkewitz, B. Ryu, S. Park, E. Müller, *Materials* **2022**, *15*, 1627.
[56] B. Ryu, J. Chung, S. Park, *iScience* **2021**, *24* 102934.
[57] D. M. Rowe, in *Thermoelectrics Handbook: Macro to Nano* (Ed: D.M. Rowe), CRC press, Boca Raton **2006**.
[58] H. J. Goldsmid, in *CRC Handbook of Thermoelectrics* (Ed: D.M. Rowe), CRC press, Boca Raton **1995**.
[59] P. Ying, R. He, J. Mao, Q. Zhang, H. Reith, J. Sui, Z. Ren, K. Nielsch, G. Schierning, *Nat. Commun.* **2021**, *12* 1121.
[60] A. Nozariasbmarz, B. Poudel, W. Li, H. B. Kang, H. Zhu, S. Priya, *iScience* **2020**, *23* 101340.
[61] S. Mahmoudinezhad, A. Rezania, P. A. Cotfas, D. T. Cotfas, L. A. Rosendahl, *Energy* **2019**, *168*, 823.
[62] R. Funahashi, S. Urata, T. Mihara, N. Nabeshima, K. Iwasaki, *Mass and Charge Transport in Inorganic Materials III*, Trans Tech Publications Ltd, October 10 **2006**, https://doi.org/10.4028/www.scientific.net/ast.46.158.
[63] R. Funahashi, S. Urata, K. Mizuno, T. Kouuchi, M. Mikami, *Appl. Phys. Lett.* **2004**, *85* 1036.
[64] P. Qiu, J. Cheng, J. Chai, X. Du, X. Xia, C. Ming, C. Zhu, J. Yang, Y.-Y. Sun, F. Xu, X. Shi, L. Chen, *Adv. Mater.* **2022**, *12* 2200247.
[65] M. Mejri, Y. Thimont, B. Malard, C. Estournès, *Scr. Mater.* **2019**, *172*, 28.
[66] Y. Gelbstein, J. Tunbridge, R. Dixon, M. J. Reece, H. Ning, R. Gilchrist, R. Summers, I. Agote, M. A. Lagos, K. Simpson, C. Rouaud, P. Feulner, S. Rivera, R. Torrecillas, M. Husband, J. Crossley, I. Robinson, *J. Electron. Mater.* **2014**, *43* 1703.
[67] P. Gao, I. Berkun, R. D. Schmidt, M. F. Luzenski, X. Lu, P. Bordon Sarac, E. D. Case, T P. Hogan, *J. Electron. Mater.* **2014**, *43* 1790.
[68] P. Qiu, T. Mao, Z. Huang, X. Xia, J. Liao, M. T. Agne, M. Gu, Q. Zhang, D. Ren, S. Bai, Xun. Shi, G. J. Snyder, L. Chen, *Joule* **2019**, *3* 1538.
[69] Z. Bu, X. Zhang, Y. Hu, Z. Chen, S. Lin, W. Li, Y. Pei, *Energy Environ. Sci.* **2021**, *14* 6506.
[70] U. Erturun, K. Erermis, K. Mossi, *Appl. Energy* **2015**, *159*, 19.
[71] N. K. Karri, C. Mo, *J. Electron. Mater.* **2018**, *47* 3127.
[72] N. K. Karri, C. Mo, *J. Electron. Mater.* **2018**, *47* 6101.

Supplementary Information

Comparison of the Seebeck coefficients of the legs before TEG assembly and after TEG measurement (4 cycles in total)

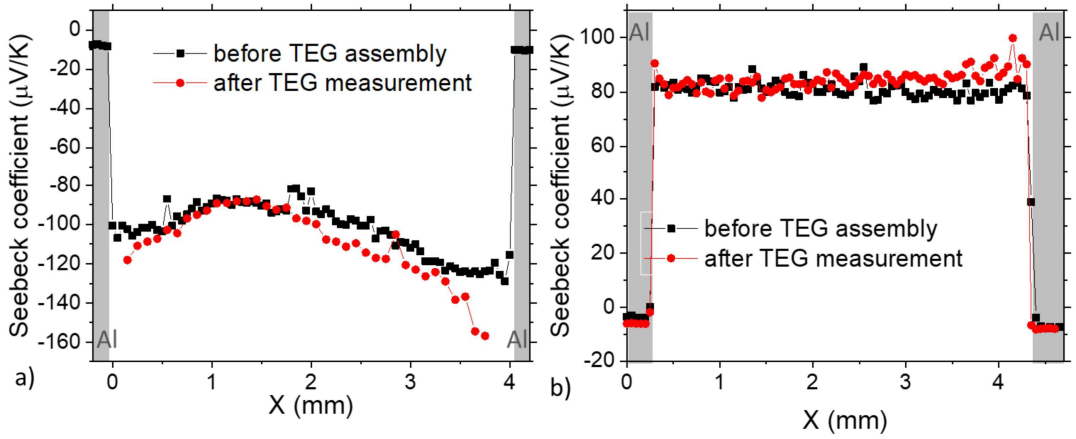

Figure S1 – Seebeck coefficient line-scans of an a) n-type, b) p-type leg prior to TEG assembly, and after four-cycles measurement of the TEG. No change was observed for the p-type legs.

Comparative line-scans of the Seebeck coefficient of the TEG legs are shown in Figure S1. An increase of about 7% of the spatially-averaged n-type Seebeck coefficient is reported (after a total of 5 measurement cycles), while the p-type material almost did not change (<4%, could be due to the wear of the tip). Such a change in carrier concentration is typically observed in n-type $Mg_2(Si,Sn)$ due to Mg evaporation, which increases the concentration in Mg vacancies (acceptor defects), partly compensating n-type conductivity [1-4]. More drastic n-type $Mg_2(Si,Sn)$ degradation in TEGs has been reported before [5, 6], which is why the search and use of a protective coating is underway [7-12]. In our case, a 7% increase of the n-type absolute average Seebeck coefficient (from -102 µV/K to -109 µV/K) would approximately result in a 3.5% increase of the open-circuit voltage, while in the measured data, a significant increase of 12% is observed between the start and end of the first cycle. Therefore, although it partly contributes to the increase in open-loop voltage, the change in the TE materials is far too small to be the main origin for this behavior.

Using a Single Parabolic Band model and assuming constant mobility, a 7% and 4% increase of the n-type and p-type (respectively) absolute average Seebeck coefficient would approximately result in a respective increase of 12% and 6% of their electrical resistivity. This would lead to an increase in total electrical resistance of approximately 9% (less, if the contact resistance is considered), while an increase of 28% was observed within the first measurement cycle. Therefore, although some change in the TE materials could be occurring, the extent of the change is far too small to explain the experimental data, which is why the paper mainly focuses on the cracks.

Determining the temperature difference applied to the TE legs with the equivalent thermal circuit

Figure S2 shows a schematic of the temperature profile along the measurement column, with the various temperatures and temperatures differences that are considered in the main text. The controlled, measured temperatures $T_{\mathrm{h,m}}$ and $T_{\mathrm{c,m}}$, are the temperatures at the heater and cooler in contact with the TEG. However, there are thermal losses along the coupling and the DBC layers, so the real, effective temperatures that are applied to the TE legs, $T_{\mathrm{h,TE}}$ and $T_{\mathrm{c,TE}}$, need to be calculated.

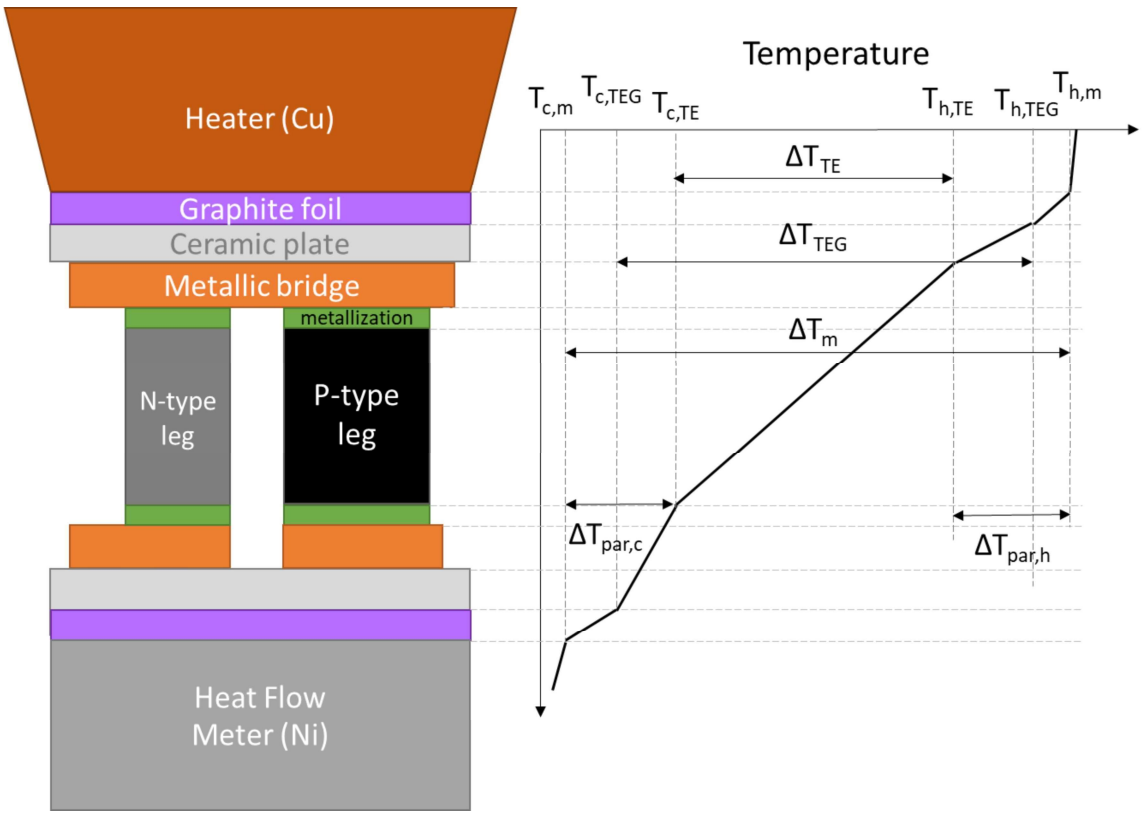

Figure S2 - Schematics of the elements and the temperature profile of the measurement column surrounding the TEG. The copper bridges on the outside of the TEG (between the ceramic plate and the graphite foil) are omitted. The dimensions of the components are arbitrary and the temperature drops are schematic and qualitative. $T_{c,m}$ and $T_{h,m}$ are the measured cold and hot side temperatures at the heat flow meter and the heater close to the TEG, respectively, $T_{h,TEG}$ and $T_{c,TEG}$ are the temperatures at the hot and cold side of the TEG, respectively, and $T_{h,TE}$ and $T_{c,TE}$ are the temperatures at the hot and cold side of the TE legs, respectively. $\Delta T_{par,h}$ and $\Delta T_{par,c}$ are the parasitic temperature drop at the coupling zones between the TE legs and the HFM/heater, respectively.

a) Additional information on the method using the measured open-circuit voltage $U_{0,\mathrm{m}}$

Figure S1 shows the gradient in n-type Seebeck coefficient in the n-type leg prior to TEG assembly. This is due to a local decrease in carrier concentration close to the Al metallizations, possibly due to Zn diffusion, as was already reported in previous work [13]. It was shown that for Mg_2X materials, the deviation from linearity of the temperature profile is slight [14], therefore the temperature-average equals the spatial average of the Seebeck coefficient. On a non-contacted (gradient-free) material, α= -90 µV/K (when measured with the PSM). The average of the leg shown in Figure S1 is -101 µV/K. A 11% increase in absolute n-type Seebeck coefficient would imply an increase of ~ 6% of the open-loop voltage, comparing gradient-free to actual legs.

b) Method using the measured open-loop heat flow $Q_{0,\mathrm{m}}$

At open-loop, there is no power generation and the heat flow is the same along the measurement column. Therefore, the following can be written:

$$Q_{0,\mathrm{m}} = K \cdot \Delta T_{\mathrm{TE}} \tag{S1}$$

As can be seen, ΔT_{TE} can be determined using the measured open-loop heat flow and the thermal conductance of the TE legs (calculated). This method could be less sensitive to changes in carrier

concentration, using κ instead of α, however the measurement uncertainty on heat flow is larger than the one of the open-loop voltage. It is also sensitive to the geometrical uncertainties of the legs.

c) Method calculating the thermal resistances of the coupling layers ("layer model")

The equivalent thermal circuit of the TEG is represented in Figure S3. All thermal contact resistances are neglected, as they are supposed to be extremely low, as well as the thermal losses across the metallic Cu bridges, located on each side of the DBC plates, and across the Cu-Al metallization of the TE legs. Since those layers are metallic, they all have very large thermal conductivity, therefore they should not lead to significant temperature losses.

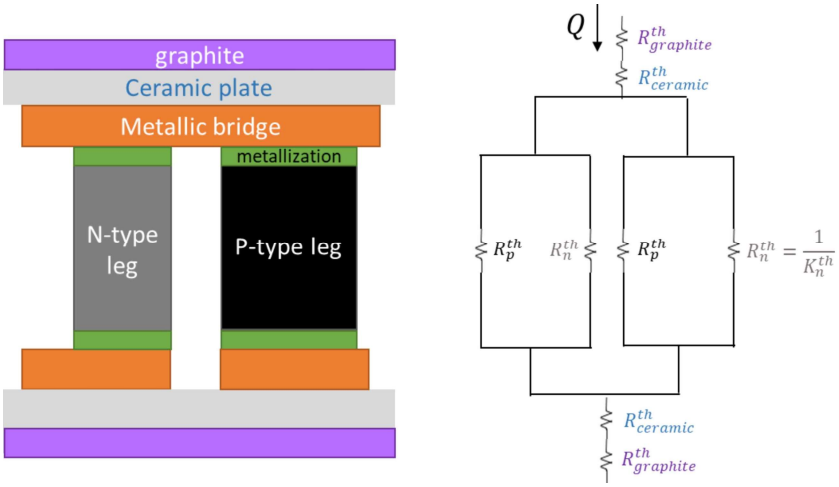

Figure S3 – Schematics of the TEG and coupling layers (left), corresponding equivalent thermal circuit (right)

The thermal losses through the Al_2O_3 plate of the DBC and through the graphite foil can be calculated such as:

$$\Delta T_{\mathrm{gr}} = Q_{0,\mathrm{m}}/K_{\mathrm{gr}} = \frac{Q_{0,\mathrm{m}}}{h_{\mathrm{gr}} \cdot A_{\mathrm{Cu}}} \tag{S2}$$

$$\Delta T_{\mathrm{cer}} = Q_{0,\mathrm{m}}/K_{\mathrm{cer}} = \frac{d_{\mathrm{cer}} \cdot Q_{0,\mathrm{m}}}{A_{\mathrm{DBC}} \cdot \kappa_{\mathrm{Al2O3}}} \tag{S3}$$

where K_{gr} and K_{cer} are the thermal conductances of the graphite and Al_2O_3 plate respectively, h_{gr} is the heat transfer coefficient of the graphite foil given in Figure S4, A_{DBC} is the area of the DBC plate and A_{Cu} is the surface occupied by Cu bridges on the outside surfaces of the TEG (against which the graphite is pressed), d_{cer} is the thickness of the ceramic (Al2O3) plate of the DBC and κ_{Al2O3} is the thermal conductivity of Al_2O_3 taken from literature [15].

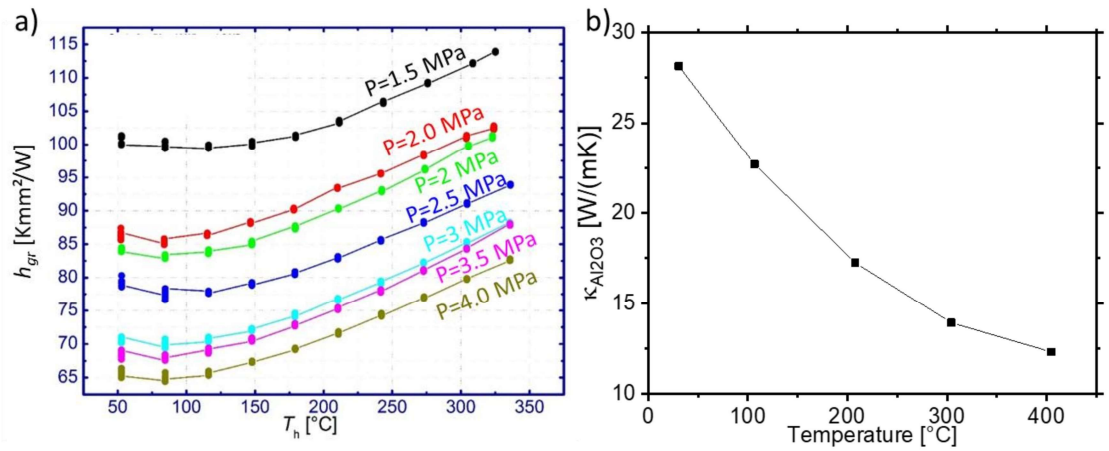

Figure S4 – a) heat transfer coefficient of the graphite foil, determined experimentally, b) thermal conductivity of Al_2O_3, data taken from [15].

Errors in underlying input data for ρ_{gr} and κ_{Al2O3}, and geometrical uncertainties can inevitably lead to flawed values for ΔT_{gr} and ΔT_{cer}, respectively, and the measurement uncertainty of the heat flow should be considered. This method assumes a 1D model, where heat is transferred homogeneously across all surfaces, which is not fully correct.

This method has the advantage of accounting for the temperature dependence of the thermal conductances of the coupling layers, and therefore does not assume symmetric loss compared to the other methods. However, due to the numerous assumptions and unknowns (contact resistances), and to the increasing error on heat flow with increasing temperature, this method is found to lead to overestimated temperature difference at the TE legs. It can however be used to determine minimum T_{c} and maximum T_{h} values at lower temperatures and therefore detect errors for other methods.

d) Comparison of the temperatures at the TE legs for the different methods

Table S1 compares the temperatures at the TE legs obtained from the discussed methods. It can be seen that the method using the open-loop heat flow like presented in b) ("Q_0 method") gives $\Delta T_{\mathrm{TE}} \geq \Delta T_{\mathrm{m}}$ for highest temperatures, which is unrealistic. This is due to the increasing uncertainty measurement of $Q_{0,\mathrm{m}}$ and this is why this method was not used. It should also be noted that the methods relying on $Q_{0,\mathrm{m}}$ result consistently in larger ΔT_{TE} than the first approach, possibly indicating an overestimation of the measured heat flow.

Table S1 – Comparison of the temperatures at the TE legs for the different methods. "U_0 method" is the method used in the main paper, "Q_0 method" is presented in b) in this section, the "layering model" is presented in c) in this section.

T_h (°C)				T_c (°C)			
$T_{h,m}$	U_0 method	Q_0 method	Layer model	$T_{c,m}$	U_0 method	Q_0 method	Layer model
400	380	402	391	24	44	22	31
351	335	350	343	24	40	25	30
300	289	297	294	27	37	29	31
250	243	247	246	25	32	28	29
201	196	197	197	24	29	28	28

Assessment of symmetric/asymmetric temperature losses

In the main text, calculations are made assuming symmetrical parasitic losses at the hot and cold sides. The reliability of this assumption is unclear, therefore we present other calculations for "worst case scenarios", where all the temperature is lost either at the hot or the cold side (using the "U_0 method"

like in the main text). The resulting deviations with measured data for optimum current and maximum power are shown in Figure S5. Obviously, the data for symmetric assumption is generally closer to the measured data, as the other calculations are made for extreme, unrealistic conditions. Looking at equations (7) and (10) in the main text, it is seen that I_{opt} depends on $\Delta T_{\mathrm{TE,opt}}$ while P_{max} depends on $\Delta T_{\mathrm{TE,opt}}{}^2$. Therefore, the deviation due to wrong $\Delta T_{\mathrm{TE,opt}}$ should be higher for P_{max} than for I_{opt}, which is observed in case of 100% losses at the hot side and for symmetric losses, but to a much lighter extend for the case of 100% losses at the cold side. It can therefore be supposed that the real distribution of heat losses leans towards >50% on the cold side but further characterization would be required to confirm and quantify this.

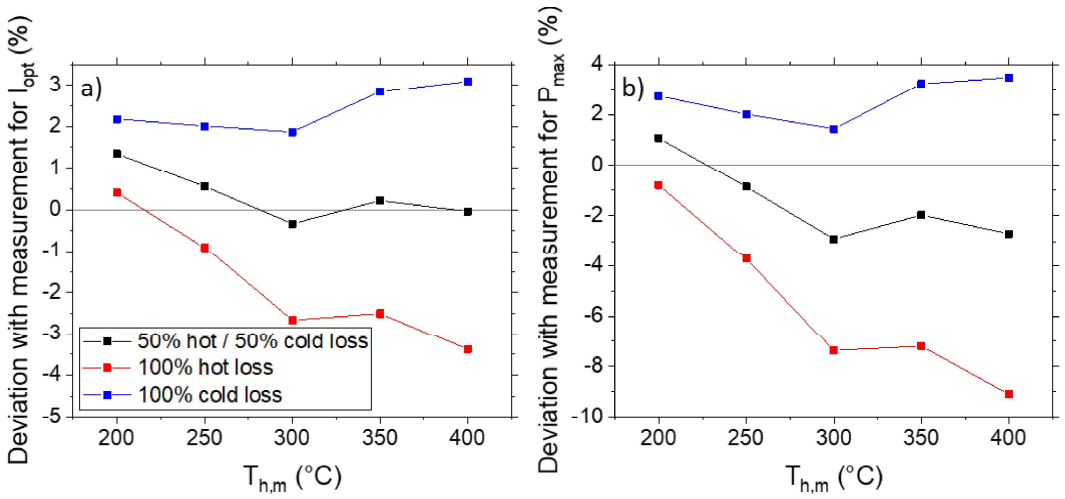

Figure S5 – Deviation between measured data and calculations of a) the current at maximum power, b) the maximum power. One calculation assumes symmetric temperature loss between hot and cold sides (as shown in the main paper) (black), a second assumes total temperature loss at the hot side (red), a third assumes total temperature loss at the cold side (blue). The legend in a) also applies to b).

TEGMA measurement close-ups

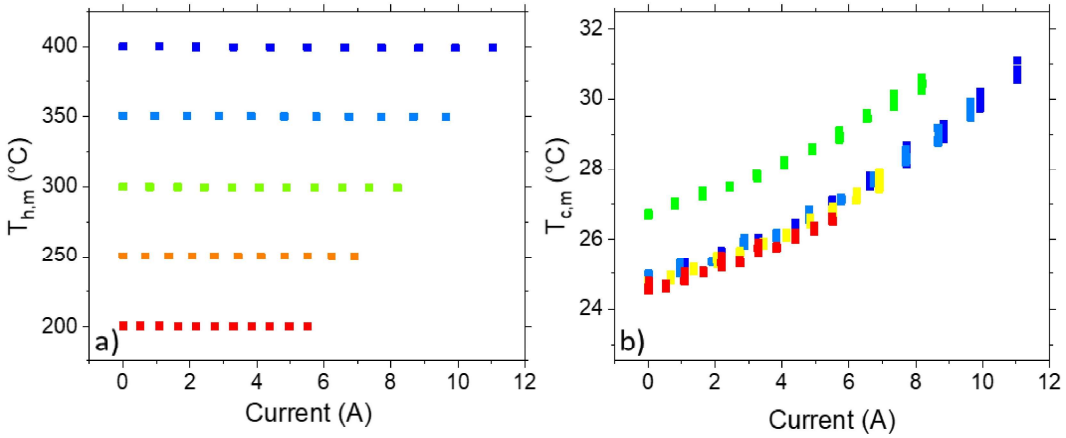

Figure S6 – Variation of measured a) hot, b) cold sides temperatures at the heater and HFM, respectively, with current. The color code in b) corresponds to the temperature steps shown in a). The data presented in this figure is from the first cooling step.

Figure S6 shows the temperature at the TEG hot and cold sides with with varying current. The hot side temperature is stable at each step (< 1 K variation), while a small change is observed at the cold side temperature (< 6 K) for increasing current due to Peltier heat. For $T_{\mathrm{h,m}} = 400°C$, $I_{\mathrm{opt,m}} = 5.4\ A$ while the current at maximum efficiency $I_{\mathrm{opt},\eta,\mathrm{m}} = 5.3\ A$ (for a current range going from 0 to 10 A). Therefore, the temperature conditions for both current values will be very similar, which is why only the conditions at maximum power are used in the main text.

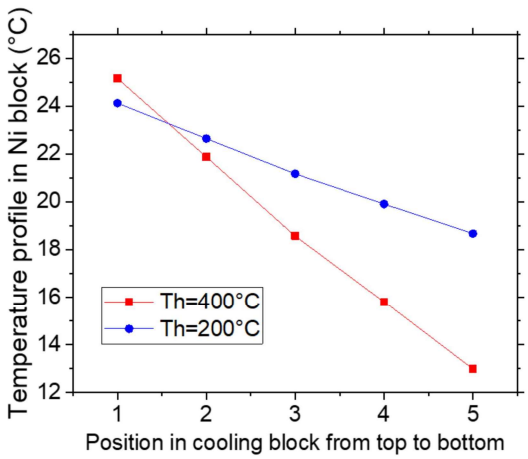

Figure S7 - Temperature profile in the Ni block on the cold side of the TEG. Position 1 is the closest to the TEG, position 5 is the closest to the cooling system.

Figure S7 shows the temperature profiles for two different hot side temperatures in the cooling block in contact with the TEG, it can be seen that they are very close to linearity. The temperature drops are large enough to provide a reliable measurement of the heat flow coming out of the TEG, and therefore a reliable efficiency measurement.

Derivation of the effective contact resistivity

The total electrical resistance due to contacts in the TEG can be written such as:

$$R_{\mathrm{c,tot}} = 2 \times N \times (R_{\mathrm{c,p}} + R_{\mathrm{c,n}}) \tag{S4}$$

With $R_{\mathrm{c,n}}$ and $R_{\mathrm{c,p}}$ the contact resistance for the one interface of one n-leg and p-leg, respectively. In our modules, as was shown in the methods of the main paper, the electrical resistivity (geometry-independent) is the same for n- and p-type legs. Therefore:

$$r_{\mathrm{c,n}} = r_{\mathrm{c,p}} = R_{\mathrm{c,n}} \times A_{\mathrm{n}} = R_{\mathrm{c,p}} \times A_{\mathrm{p}} \tag{S5}$$

$$R_{\mathrm{c,p}} = R_{\mathrm{c,n}} \times A_{\mathrm{n}}/A_{\mathrm{p}} \tag{S6}$$

$$R_{\mathrm{c,tot}} = 2N \times R_{\mathrm{c,n}}(1 + A_{\mathrm{n}}/A_{\mathrm{p}}) \tag{S7}$$

$$R_{\mathrm{c,n}} = \frac{R_{\mathrm{c,tot}}}{2N(1 + A_{\mathrm{n}}/A_{\mathrm{p}})} = \frac{r_{\mathrm{c,n}}}{A_{\mathrm{n}}} \tag{S8}$$

Assuming that all the measured electrical resistance which is not the resistance of the TE legs, is a contact resistance, the measured effective contact resistivity can be written such as:

$$r_{\mathrm{c,m}} = \frac{(R_{\mathrm{m}} - R_{\mathrm{legs}})A_{\mathrm{n}}}{2N\left(1 + \frac{A_{\mathrm{n}}}{A_{\mathrm{p}}}\right)} \tag{S9}$$

Estimation of the thermal bypass by radiation

The radiative heat flow from a surface 1, of area A_1 and at temperature T_1, to a surface 2 of area A_2 and at temperature T_2, is given by:

$$Q_{1\to2} = \frac{\sigma_b\left({T_1}^4 - {T_2}^4\right)}{\frac{1-\varepsilon_1}{A_1\varepsilon_1} + \frac{1}{A_1F_{1\to2}} + \frac{1-\varepsilon_2}{A_2\varepsilon_2}} \tag{S10}$$

where ε_1 and ε_2 are the emissivities of surfaces 1 and 2 respectively (0.87 was considered, for oxidized copper), σ_b is the Stefan-Boltzmann constant. $F_{1\to2}$ is the few factor from surfaces 1 to 2. In the case of two parallel rectangles, it is given by [16]:

$$F_{1-2} = \frac{1}{(x_2 - x_1)(y_2 - y_1)} \sum_{l=1}^{2}\sum_{k=1}^{2}\sum_{j=1}^{2}\sum_{i=1}^{2}(-1)^{(i+j+k+l)} G(x_i, y_j, \eta_k, \xi_l) \tag{S11}$$

$$G = \frac{1}{2\pi}\left\{\begin{array}{l}(y-\eta)\left[(x-\xi)^2 + z^2\right]^{1/2} \tan^{-1}\left\{\dfrac{y-\eta}{\left[(x-\xi)^2 + z^2\right]^{1/2}}\right\} \\ +(x-\xi)\left[(y-\eta)^2 + z^2\right]^{1/2} \tan^{-1}\left\{\dfrac{x-\xi}{\left[(y-\eta)^2 + z^2\right]^{1/2}}\right\} \\ -\dfrac{z^2}{2}\ln\left[(x-\xi)^2 + (y-\eta)^2 + z^2\right]\end{array}\right\} \tag{S12}$$

Where x, y, z, η and ξ are the spatial coordinates of the rectangles such as represented in Figure 8a below.

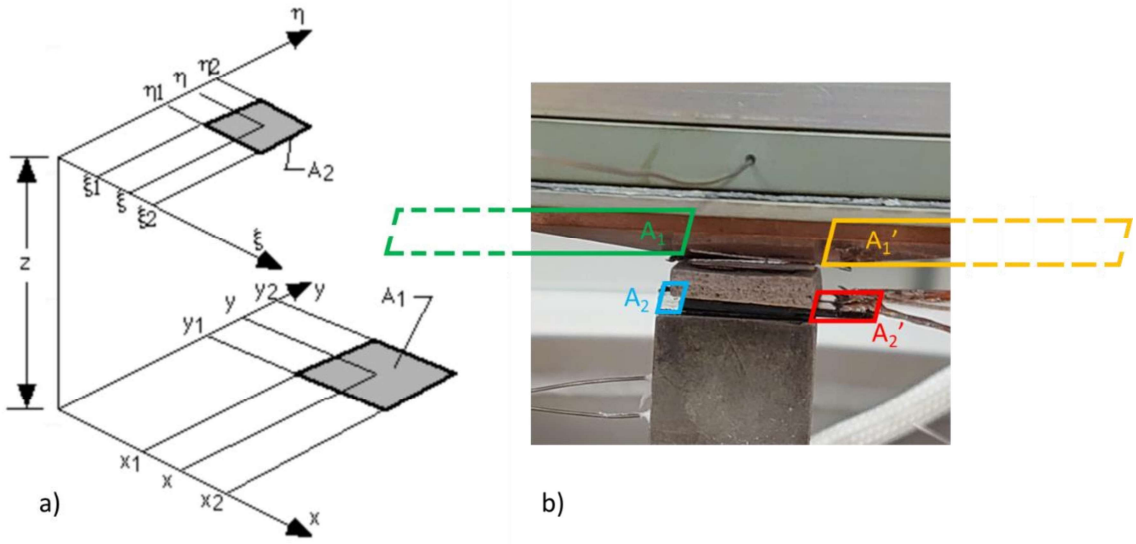

Figure 8 - a) coordinates of the rectangles for the calculations of $F_{1\to2}$, taken from [16], b) schematic of the experimental cases considered for $F_{1\to2}$ calculations.

The radiative bypass heat flow, Q_{rad}, is composed of two contributions in our case: between surfaces 1 and 2 (exposed portion of the top of the HFM), and surfaces 1' and 2' (exposed portion of the bottom DBC of the TEG), as represented in Figure 8b. The coordinates represented in Figure 8a used for the calculations are given in Table S2.

Table S2 – Coordinates used for the calculations of $F_{1\to2}$ and $F_{1'\to2'}$

	x_1	x_2	y_1	y_2	ξ_1	ξ_2	η_1	η_2	z
A_1 , A_2	0	9.5	0	20	0	0.4	9	11	6
$A_{1'}$, $A_{2'}$	0	9.5	0	20	0	1.5	9.25	10.75	5

The following can therefore be written:

$$Q_{\text{rad}} = Q_{1\to2} + Q_{1'\to2'} \tag{S13}$$

This gives $Q_{\mathrm{rad}} \approx 0.3 + 1.1 \approx 1.4$ at $T_{\mathrm{h}} = 400$ °C. Since the heat flow is measured at the cold side of the TEG, such heat bypass would be added to the measured heat flow without contributing to the power generation. In the main text, it is reported that at $T_{\mathrm{h}} = 400$ °C, the measured heat flow $Q_{\mathrm{opt,m}}$~ 15 W while its predicted value is ~ 13 W. The bypassing radiative heat flow therefore partially explains the difference between the measured and predicted value. The true value of Q_{rad} could actually be much higher due to the bypass towards the lateral sides of the HFM as well, where the temperature profile used to determine the heat flow is measured. This can however not be simply estimated as it is a much more complicated case, a quantitative assessment can therefore not be given.

References:

1. Ayachi, S., et al., *On the Relevance of Point Defects for the Selection of Contacting Electrodes: Ag as an Example for Mg2(Si,Sn)-based Thermoelectric Generators.* Materials Today Physics, 2021. **16**: p. 100309.
2. Camut, J.P.H.N., et al., *Aluminum as promising electrode for Mg2(Si,Sn)-based thermoelectric devices.* Materials Today Energy, 2021. **21**.
3. Kato, D., et al., *Control of Mg content and carrier concentration via post annealing under different Mg partial pressures for Sb-doped Mg2Si thermoelectric material.* Journal of Solid State Chemistry, 2018. **258**: p. 93-98.
4. Sankhla, A., et al., *On the role of Mg content in Mg2 (Si, Sn): Assessing its impact on electronic transport and estimating the phase width by in situ characterization and modelling.* Materials Today Physics, 2021: p. 100471.
5. de Padoue Shyikira, A., G. Skomedal, and P.H. Middleton, *Performance evaluation and stability of silicide-based thermoelectric modules.* Materials Today: Proceedings, 2020.
6. Skomedal, G., et al., *Design, assembly and characterization of silicide-based thermoelectric modules.* Energy Conversion and Management, 2016. **110**: p. 13-21.
7. Battiston, S., et al., *Multilayered thin films for oxidation protection of Mg2Si thermoelectric material at middle–high temperatures.* Thin Solid Films, 2012. **526**: p. 150-154.
8. D'Isanto, F., et al., *Oxidation protective glass coating for magnesium silicide based thermoelectrics.* Ceramics International, 2020. **46**(15): p. 24312-24317.
9. Gucci, F., et al., *Oxidation protective hybrid coating for thermoelectric materials.* Materials, 2019. **12**(4): p. 573.
10. Nieroda, P., et al., *New high temperature amorphous protective coatings for Mg2Si thermoelectric material.* Ceramics International, 2019. **45**(8): p. 10230-10235.
11. Sadia, Y., D. Ben-Ayoun, and Y. Gelbstein, *PbO–SiO2-based glass doped with B2O3 and Na2O for coating of thermoelectric materials.* Journal of Materials Research, 2019. **34**(20): p. 3563-3572.
12. Tani, J.-i., M. Takahashi, and H. Kido, *Fabrication of oxidation-resistant β-FeSi2 film on Mg2Si by RF magnetron-sputtering deposition.* Journal of Alloys and Compounds, 2009. **488**(1): p. 346-349.
13. Camut, J., et al., *Overcoming Asymmetric Contact Resistances in Al-Contacted Mg2 (Si, Sn) Thermoelectric Legs.* Materials, 2021. **14**(22): p. 6774.
14. Ponnusamy, P., J. de Boor, and E. Müller, *Using the constant properties model for accurate performance estimation of thermoelectric generator elements.* Applied Energy, 2020. **262**: p. 114587.
15. Galusek, D. and D. Galusková, *Alumina matrix composites with non-oxide nanoparticle addition and enhanced functionalities.* Nanomaterials, 2015. **5**(1): p. 115-143.
16. Ehlert, J.R. and T.F. Smith, *View factors for perpendicular and parallel rectangular plates.* Journal of thermophysics and heat transfer, 1993. **7**(1): p. 173-175.

6. Chapter 6: Discussion

6.1. Combined (PSM-SPB) model for inhomogeneous material (CMIM)

In the paper shown in the previous section, CPM calculations were performed assuming a homogeneous leg with properties such as measured for an as-sintered pellet. In reality, as mentioned in the SI, n-type legs show a gradient in carrier concentration close to the metallization layers. This extension of the previous discussion will investigate the differences between results reported in the paper (assuming homogeneous legs) and data obtained using an SPB model to determine a spatial property profile for inhomogeneous legs (varying carrier concentration) under a thermal gradient.

As mentioned in section 1.3.1, the SPB model is a generally accepted model for TE properties [150] which has been successfully employed for this material system [32, 72, 116, 121, 151-157]. It assumes that the conduction in a material is governed only by a single band with a parabolic shape, which leads to a significant simplification of the general transport equations.

The SPB model relies on several basic quantities: the reduced chemical potential (η_c), the mobility parameters for acoustic phonon scattering (AP) and alloy scattering (AS) mechanisms ($\mu_{0,AP}$ and $\mu_{0,AS}$, respectively) and the density of states effective mass (m_D^*) [151, 158]. In our case, we also use the lattice thermal conductivity (κ_{lat}) as an input parameter. The microscopic parameters are linked to the measured transport quantities by the following equations, which are given here in the specific form corresponding to AP and AS as relevant scattering mechanisms. Some equations were already presented in section 1.3.1 but are repeated for completeness:

$$\eta_c = \frac{E_F}{k_B T} \tag{53}$$

$$\alpha = \frac{k_B}{e}\left(\frac{2F_1}{F_0} - \eta_c\right) \tag{54}$$

$$n = 4\pi\left(\frac{2m_D^* k_B T}{h^2}\right)^{1.5} F_{\frac{1}{2}}(\eta_c) \tag{55}$$

$$\mu_{AP} = \mu_{0,AP}\cdot\psi(\eta_c) = \frac{\sqrt{8\pi}e\hbar^4\rho_d {v_l}^2}{3{E_{Def}}^2 m_s^{*2.5}(k_B T)^{1.5}}\psi(\eta_c) \tag{56}$$

$$\psi(\eta_c) = \frac{3\sqrt{\pi}}{16}\frac{F_{-0.5}(\eta_c)}{F_0(\eta_c)} \tag{57}$$

$$\mu_{AS} = \mu_{0,AS}\cdot\psi(\eta_c) = \frac{64e\hbar^4 N_0}{9(2\pi)^{1.5}y(1-y)E_{AS}^2 m_s^{*2.5}(k_B T)^{0.5}}\psi(\eta_c) \tag{58}$$

$$\frac{1}{\mu} = \frac{1}{\mu_{\mathrm{AP}}} + \frac{1}{\mu_{\mathrm{AS}}} \tag{59}$$

$$\sigma = \mu e n \tag{60}$$

$$\kappa = \kappa_{\mathrm{lat}} + \kappa_{\mathrm{e}} = \kappa_{\mathrm{lat}} + L\sigma T \tag{61}$$

$$L = \left(\frac{k_{\mathrm{B}}}{e}\right)^2 \frac{3F_0(\eta_{\mathrm{c}})F_2(\eta_{\mathrm{c}}) - 4{F_1}^2}{F_0(\eta_{\mathrm{c}})^2} \tag{62}$$

where k_{B} is Boltzmann's constant, $\hbar$ is the reduced Planck constant, $F_i(\eta)$ the Fermi integral of order i, and E_F is the Fermi energy, y is the alloy atomic composition in Sn such as $Mg_2Si_{1-y}Sn_y$ (y = 0.7 in our case).

A scattering parameter of $\lambda = 0$ is assumed, corresponding to the energy dependence of scattering with AP and AS. λ governs the power law dependence of the relaxation time on reduced carrier energy such as $\tau_s = \tau_{0,s}\varepsilon^{\lambda-1/2}$ (where $\tau_{0,s}$ is a relaxation time constant, ε is the reduced energy).The other parameters are described in Table 8. These parameters were obtained from literature, for samples whose properties match ours [81], and are therefore applicable. In [81], m_D^* is obtained from fitting measured data and this value is used to calculate m_s^*.

Table 8 – Parameters used for the Single Parabolic Band model calculations of $Mg_2Si_{0.3}Sn_{0.7}$

Parameter (units)	Symbol	Value (SI units)	Reference
Average density of states effective mass	m_D^*	$2.1 \cdot m_0$	[151]
Band degeneracy	N_{v}	6	[116]
Single band mass	m_s^*	$m_D^*/N_v^{2/3}$	-
Theoretical mass density (g/cm^3)	ρ_{D}	3.117	[151]
Longitudinal speed of sound (m/s)	v_{l}	5290	linear with y, [151]
AP deformation potential constant	E_{Def}	$9.8 \cdot e$	[121]
Alloy scattering potential	E_{AS}	$0.5 \cdot e$	[116, 121]
Number of atoms per unit volume (m^{-3})	N_0	$4.105 \cdot 10^{28}$	linear with y, [116]

m_0 is the electron rest mass, κ_{lat} is obtained with measured experimental data (κ_{exp}, σ_{exp}, α_{exp}) of our as-sintered (unaltered) n-type material: $\kappa_{\mathrm{lat}} = \kappa_{\mathrm{exp}} - L'\sigma_{\mathrm{exp}}T = \kappa_{\mathrm{exp}} - \left[1.5 + \exp\left(-\frac{|\alpha_{\mathrm{exp}}|}{116}\right)\right]\sigma_{\mathrm{exp}}T$ [15]. The equation used for L' is a numeric approximation obtained via fitting [159]. The obtained data is fitted with a third order polynomial to be used in the SPB

equations. In this case, we obtain $\kappa_{\mathrm{lat}} = 1.63[\frac{\mathrm{W}}{\mathrm{mK}}] - 2.21 \cdot 10^{-3}[\frac{\mathrm{W}}{\mathrm{mK^2}}] \cdot (T - 273) + 1.21 \cdot 10^{-6}[\frac{\mathrm{W}}{\mathrm{mK^3}}] \cdot (T - 273)^2 + 3.09 \cdot 10^{-9}[\frac{\mathrm{W}}{\mathrm{mK^4}}] \cdot (T - 273)^3$ with T in K. The comparison between SPB-modelled data (for $n = 2.28 \cdot 10^{26}$ m^{-3}, obtained by graphically solving equations (54) and (55) with the Pisarenko plot and the experimental Seebeck coefficient) and measured data is shown in Figure 36.

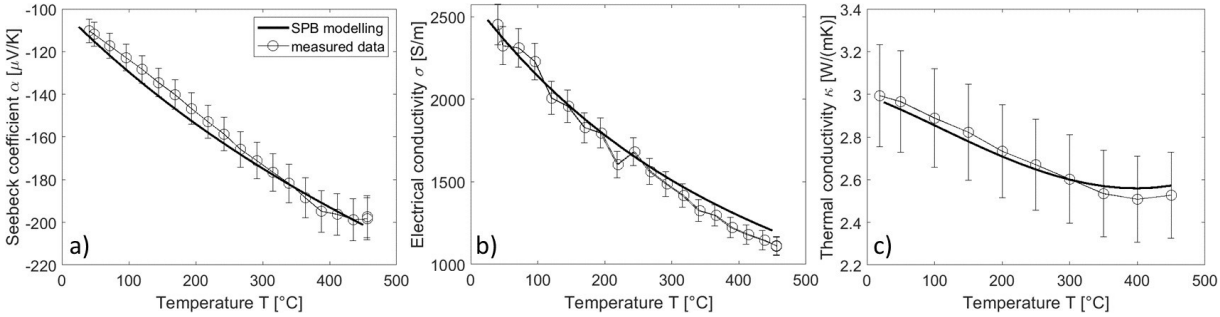

*Figure 36 - comparison between SPB modelled data (for $n = 2.28 \cdot 10^{26}$ m^{-3}and parameters from **Error! Reference source not found.**) and measured data: a) Seebeck coefficient, b) electrical conductivity, c) thermal conductivity. Uncertainties of the Seebeck coefficient and electrical conductivity measurement are 5%, of the thermal conductivity 8%.*

A spatial Seebeck profile at room temperature is obtained scanning an n-type leg with the PSM and this PSM $\alpha_{\mathrm{PSM}}(x)$ profile is converted into a reference $\alpha_{\mathrm{ref}}(x)$ profile using previously measured data, assuming a constant relative difference between α_{PSM} and α_{ref}, such as $\alpha_{\mathrm{ref}}(x_1) = \alpha_{\mathrm{PSM}}(x_1)\alpha_{\mathrm{ref}}(x_0)/\alpha_{\mathrm{PSM}}(x_0)$. i.e. for this case sample a value of $\alpha_{\mathrm{PSM}}(x_0)$=-90 µV/K in the PSM corresponds to a room-temperature value of $\alpha_{\mathrm{ref}}(x_0)$=-109 µV/K in the HT-*S*-σ ($_{\mathrm{ref}}$). The Seebeck coefficient values obtained with the PSM are less accurate than (and underestimated compared to) those obtained with the HT-*S*-σ, due to the temperature difference between the effective position of the thermocouple junction and the point where the potential is measured [143]. This leads to an empirically determined deviation of the measured Seebeck values in the PSM between 10% and 15%, while the measurement uncertainty of the HT-*S*-σ is 5%. The deviation between PSM and HT-*S*-σ values previously cited (-90 µV/K and -109 µV/K respectively) is 17%, which lies within the combined uncertainty for both devices (15-20%).

As described in section 1.3.1 and equations (54) and (55) above, the room-temperature Seebeck coefficient can be linked to the carrier concentration in the SPB model. A carrier concentration profile can therefore be obtained from the PSM line-scan.

The SPB model allows to predict the TE properties depending on the carrier concentration and the temperature. $n(x)$ is obtained from the PSM measurements as previously described, while $T(x)$ during the TEGMA measurement is obtained assuming a linear profile between $T_{\mathrm{h,TE}}$ and $T_{\mathrm{c,TE}}$. As explained in 1.2.1, the linearity of the temperature profile can be assumed for Mg_2X

materials in spite of the interplay between Thomson heat, $\kappa(T)$ and Joule heat, as shown by Ponnusamy *et al*. [28, 160].

From $n(x)$ and $T(x)$, the Seebeck coefficient, electrical resistivity and thermal conductivity profiles are obtained. This procedure is represented in Figure 37.

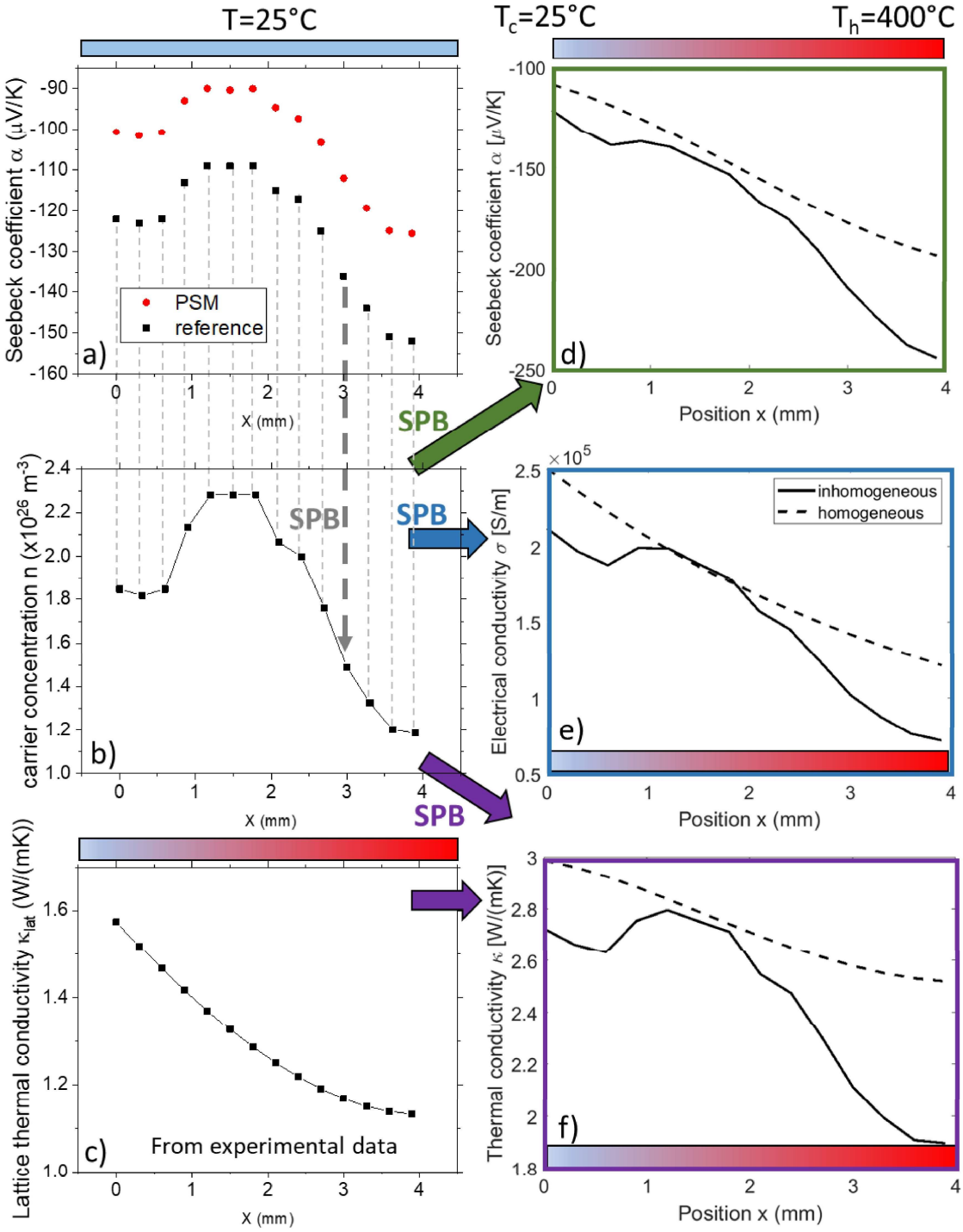

Figure 37 - Schematics of the calculation of the properties profile for an inhomogeneous leg (CMIM): a) exemplary line scan of the Seebeck coefficient at room temperature, measured with PSM and proportionally "converted" into HT-S-σ values, b) carrier concentration (spatial) profile obtained from a) using the SPB model, c) lattice thermal conductivity obtained from Seebeck coefficient and electrical resistivity of the sample directly after sintering. d) corresponding Seebeck coefficient profile

calculated using SPB, e) corresponding electrical resistivity profile calculated using SPB, f) corresponding thermal conductivity profile calculated using SPB. The legend in e) also applies to d) and f): a comparative profile for a homogeneous material (using fitted measured as-sintered properties) is added in dashed lines. In c), d), e) and f), a linear temperature profile is assumed between T_c = 25 °C and T_h = 400 °C.

Once the properties profiles have been established, the property averaging followed by the CPM calculations can be done using the same equations as presented in the section 5, assuming unchanged p-type properties. Comparative results for the case with homogeneous and inhomogeneous n-type properties are presented in Figure 38.

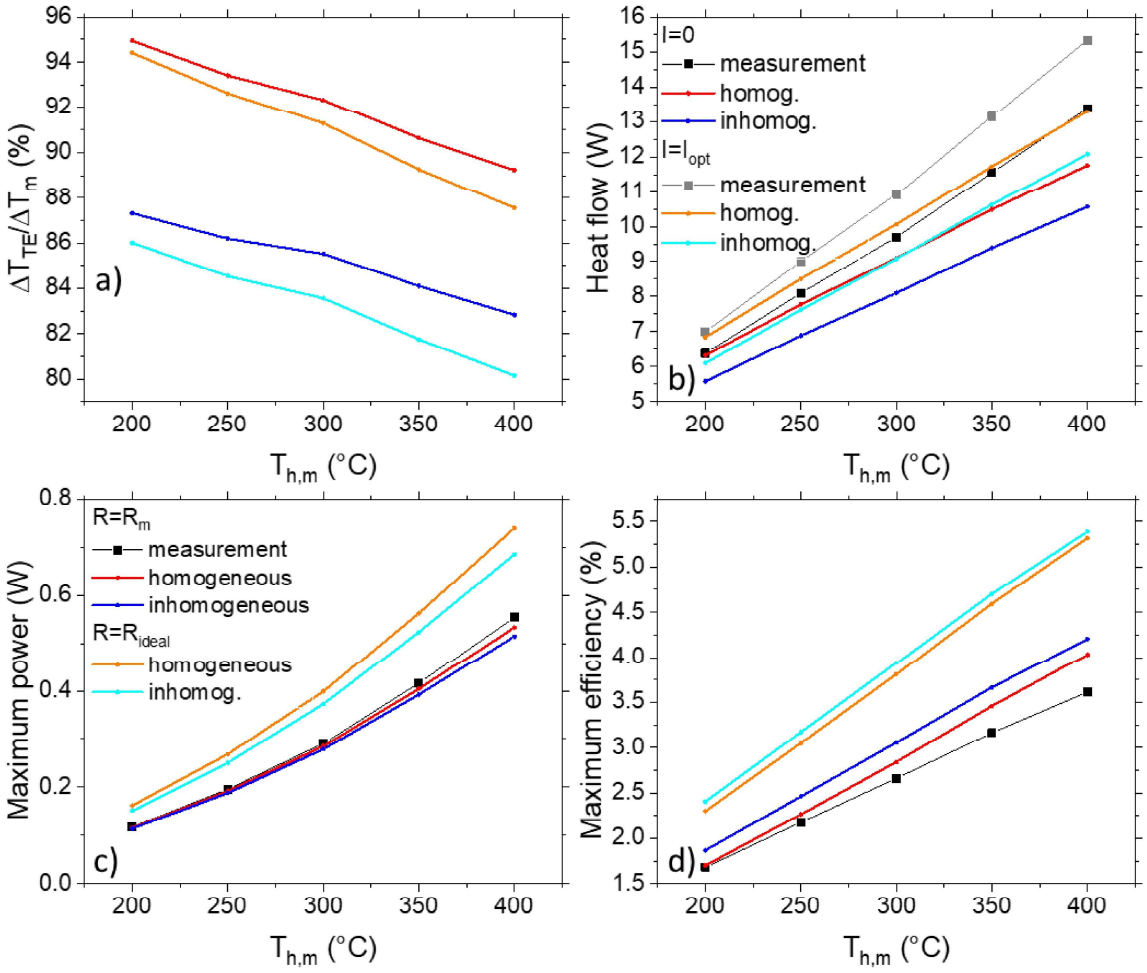

Figure 38 – Comparison of experimental data (measured during cooling in stabilized steps) to CPM calculated data for a TEG with homogeneous and inhomogeneous n-type legs: a) Ratio of the temperature difference at the TE legs and the measured temperature difference at I=0 and I_{opt}, b) heat flows at I = 0 and I_{opt}, c) maximum power for measured inner resistance and ideal inner resistance (low contact resistances), d) maximum conversion efficiency for measured inner resistance and ideal inner resistance. Legend in b) also applies in a); legend in c) also applies in d).

Going from the homogeneous material to the inhomogeneous material, it is intuitively understood that the average absolute Seebeck coefficient and electrical resistivity of the leg increase while its thermal conductivity decreases (carrier loss at the metallization interfaces). This trend is observed in the CPM results shown in Figure 38, as the temperature difference at the TE legs (based on measured open-loop voltage and the input Seebeck coefficient) and the

heat flows decrease for the legs with a gradient. It is also estimated that the portion of the measured resistance that is due to the TE materials increases from 70% for a TEG with homogeneous legs to 74% for a TEG with a gradient on their n-type legs. This difference is the reason why the relative difference in maximum power between inhomogeneous and homogeneous material (Figure 38c) is smaller for $R = R_{\mathrm{m}}$ than for $R = R_{\mathrm{ideal}}$, since in the first case the measured resistance value is used for both materials, while for the second case the resistance value is based on the calculated resistance of the TE materials, which differs between homogeneous and inhomogeneous leg.

The portion of parasitic resistance is large in both cases; therefore, the main finding of the paper remains: cracks form, propagate and are responsible for the suboptimal performance of the TEG. By solving this problem, the maximum power output could be increased by 26%, with a corresponding power density of 1.08 W/cm². The fact that higher efficiency is predicted considering the gradient rather than the homogeneous material is explained in Figure 39b. Indeed, it can be seen that in the considered carrier concentration range (which is the range covered by the inhomogeneous leg profile), the predicted figure of merit decreases with increasing carrier concentration, at all temperature between 25 °C and 450 °C. The inhomogeneous material has a lower average carrier concentration ($1.3 \cdot 10^{26}$ m^{-3}, while for homogeneous material $n = 2.3 \cdot 10^{26}$ m^{-3}), which is why it has a higher overall figure of merit and a higher efficiency. For the power, it can be seen that the optimized carrier concentration increases with temperature (i.e. a lower carrier concentration is favorable at lower temperature). Therefore, in a graded leg, some power would be gained due to the gradient on the cold side, but some power would be lost on the hot side compared to a homogeneous leg. Since the hot side temperature varies from 200 °C to 400 °C, this explains why the difference between both cases increases (in favor of the homogeneous material) with increasing hot side temperature.

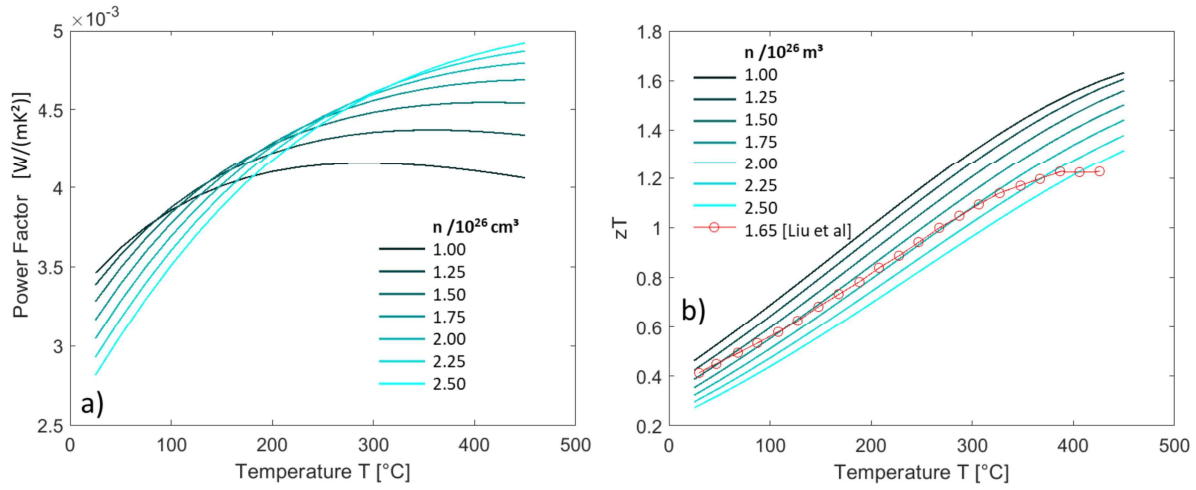

Figure 39 – a) power factor and b) zT with respect with temperature for different carrier concentrations (in m^{-3}), obtained with the SPB model. The red marked line in b) is experimental data taken from [129] for $Mg_{2.12}Si_{0.28}Sn_{0.71}Bi_{0.01}$ with a Hall carrier concentration $n_H = 1.63 \cdot 10^{26}$ cm^{-3}. It was added for visualization although no perfect match is expected as SPB parameters were obtained by different synthesis route and for different sample composition. The bending above ~ 400°C shows the contribution of non-negligible bipolar effect which is not accounted for in the SPB model.

The reason why the as-sintered material was not practically synthesized with a lower carrier concentration is that the SPB model tends to overestimate the figure of merit for low n (see e.g. [151, 152]), in practice a lower-doped material would therefore be expected to have a lower performance.

The deviation of the heat flow increases from 2–15% to 15–27% when going from a model considering a homogeneous to an inhomogeneous leg, it therefore grew beyond the estimated measurement uncertainty (13.5%). This is due to the decrease of thermal conductivity with decreasing average carrier concentration of the material. Although the exact extent of the change is uncertain due to SPB limitations at lower carrier concentrations, the trend when going from a homogeneous material to the inhomogeneous leg remains. As explained in section 5, this measurement uncertainty was obtained testing commercial TEG which have a larger number of legs, a higher filling factor and a wider geometry [145], therefore it does not necessarily strictly apply to our TEG. As discussed in the SI of section 5 ([6]), the main challenge facing this kind of small TEG prototype is the radiative thermal bypass, which could happen between the hot side and the cold side of the TEG itself, but also between the heater and the soldered cables and the HFM, where the output heat flow is measured. It is therefore assumed that at least part of this deviation is due to uncontrolled systematic measurement uncertainty due to uncontrolled thermal bypass. Generally, conductive contributions may cause a weak temperature dependence of heat flow measurement deviation whereas convective ones will increase it towards higher temperature. A separate investigation should be led to find a suitable measurement protocol for such small TEGs.

Regarding the material, a stronger deviation has to be expected for the thermal conductivity than for the electrical conductivity due to bipolar processes. This might explain the increase of the discrepancy at high temperatures.

It can be seen that for the maximum power in Figure 38c the deviation is also lower for the homogeneous than for the inhomogeneous leg (2-4% and 3-8%, respectively, with increasing temperature), while the inhomogeneous leg should be the most realistic case. It is observed that the deviations increase for higher temperatures, where in reality, the SPB model is not as reliable, as the minority carriers start contributing to the conduction [32]. This is more pronounced for lower carrier concentrations, where the conduction regime transition happens at a lower temperature. The hot-side portion of the leg is therefore where the SPB limitations and uncertainty are the most relevant due to amplified bipolar effects, since this portion has combined higher temperature and lower carrier concentration.

It can also be seen that the performance is generally predicted higher for the inhomogeneous material. This is confirmed by Figure 40 which shows the profiles of the n-type material power factor and figure of merit with a gradient between 25 °C and 400 °C. As said above, the hot side portion of the SPB data is likely not reliable (and in tendency overestimating performance), however it can be seen that on the rest of the legs, the inhomogeneous leg is predicted to have a higher performance. This shows that the gradients initially present on the n-type legs after contacting are not detrimental to the TEG performance.

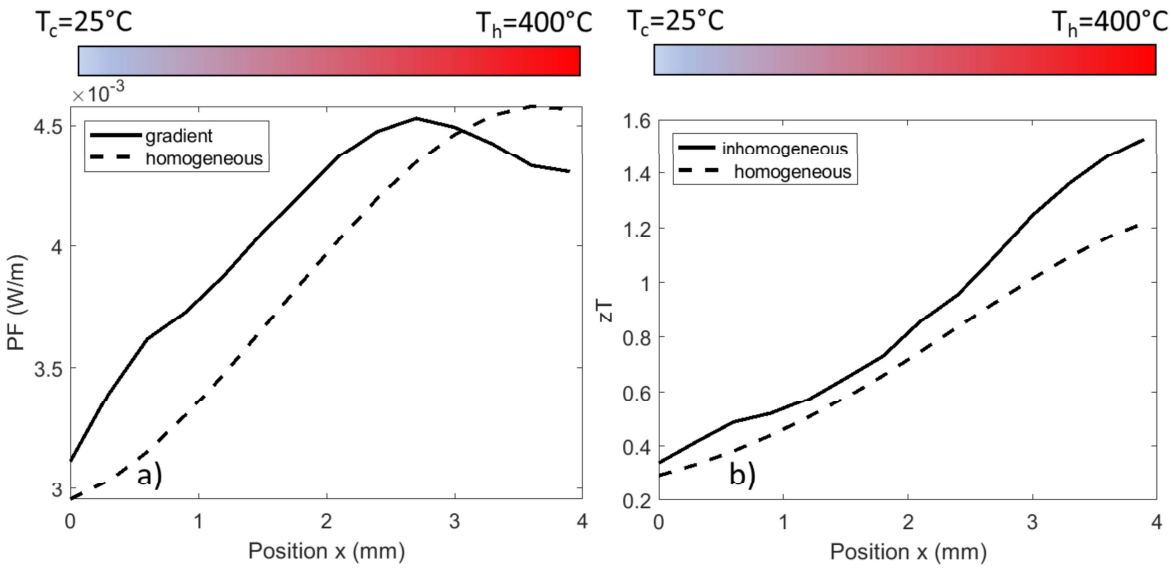

Figure 40 - Calculation of the a) PF=α²σ (power factor) , b) zT profiles for an inhomogeneous (SPB data) and a homogeneous leg (experimental data) with an assumed linear temperature profile between T_c = 25 °C and T_h = 400 °C.

It is wise to discuss whether the local change in the n-type leg could prevent the correct application of the employed model. The gradient indicates a local change in composition (likely due to Zn incorporation into or Mg removal from the TE material). This should however not have much effect on the band structure of the material [161]. Mg loss inside the TE material could have an effect on the carrier mobility, as was previously observed in [116, 121]. This can be estimated by comparing the relative change in the slope of the electrical potential along a leg on a gradient portion and a middle portion of a leg, as shown in Figure 41, to the relative difference of carrier concentration in those portions ($8.5 \cdot 10^{25}$ m^{-3} and $1.7 \cdot 10^{26}$ m^{-3}, respectively). In our case, both relative differences are about a factor of ≈ 2, which means that the electrical resistivity and the carrier concentration changed proportionally, and that mobility stayed mainly constant. This validates the use of equation (59) with a constant E_{Def} for the inhomogeneous material and is of significant importance, as a change in mobility would be one of the largest uncertainties of the SPB model.

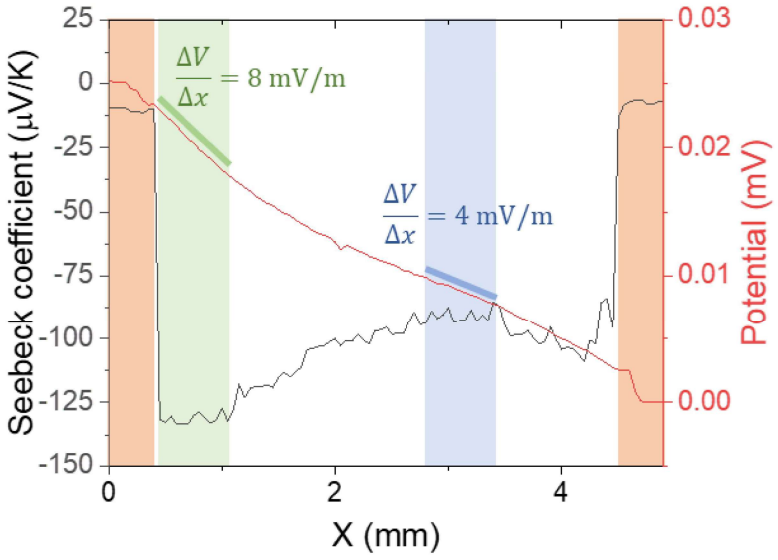

Figure 41 – Potential and Seebeck coefficient line-scan of a n-type leg with a gradient. The slopes in the electrical potential are calculated on 2 different portions of the leg to estimate the local change in resistivity.

Besides the limitations of the SPB model, part of the calculation error in the CMIM could also originate from the used methodology. The carrier concentration profile is obtained by scanning the PSM α-profile, converting it to an HT-*S*-σ α-profile and using the SPB model to correlate, for each point, α to n. To obtain the PSM-to- HT-*S*-σ conversion factor, the highest point of the PSM α-profile (lowest absolute value) is considered as the unchanged as-sintered material value. This could be a flaw in the methodology, as the whole leg could have changed during contacting by at least a small extent, even the middle section. However, this assumption has to

be made because no as-sintered pellet from the same batch was measured in the PSM at the same time as the legs were made. Indeed, the PSM-α values can be affected by the wear of the tip and by the change of device (there are several PSM machines at DLR): two PSM scans made on the same sample a few months apart are not always strictly comparable. Therefore, a reliable as-sintered PSM value cannot be obtained for those legs, as a year separates the making of the legs and the writing of this thesis. This can therefore flaw the conversion factor and lead to a slightly shifted carrier concentration profile (i.e. the overall change in the leg could be underestimated).

Nevertheless, the CPM is by definition not sensitive to fine-tuning of the TE properties, as it is based on temperature averaging, which balances out the uncertainty on the carrier concentration profile.

In this extended discussion, we present a new coupled material-device modelling approach: we developed a methodology to capture and adapt our calculations to inhomogeneous legs. This concept can be transferred to cases where the inhomogeneity is by design, for example for graded materials [25]. Applied to our work, it allows for a more trustworthy analysis of the module data: we obtain a smaller temperature difference at the TE legs and a larger deviation in heat flow and hence efficiency. As discussed above, the trend is beyond the assumptions and doubts of the SPB model. Although not completely accurate, this method is performant enough to offer deeper analysis of our experimental data: here, we identify the heat flow measurement as main future challenge for accurate measurement of small a $Mg_2(Si,Sn)$-TEG prototypes.

6.2. Open modules

In section 5, it was found that one of the main factors hindering the $Mg_2(Si,Sn)$ TEG performance was crack formation and propagation. This phenomenon is likely due to the difference between TE material and the ceramic plate which contributes notably to the thermally induced mechanical stress. In this chapter, an open design, in which the TE legs are connected solely with metallic bridges, unbonded to a ceramic plate, is tested to attempt to reduce the thermal stress. Such a design was reported recently by Goyal et al. for a similar material combination [128], without mention of mechanical failure. We build and investigate such a module, its differences in behavior compared to its DBC-based counterpart, and the new challenges that this design brings. The understanding of the TEG behavior with regard to cracking is extended by adding voltage probes between each leg in the circuit, which allows to measure the resistance of each leg individually. This is a novel method that, to the best of our

knowledge, has not been reported before for TEG investigations and can considerably deepen the TEG performance analysis.

6.2.1. Methods

a) TE material properties and functionalized legs

The same powder synthesis, pellet sintering and pellet contacting processes as described in the section 5 were used. The TE properties of as sintered pellets are reported in Figure 42. Two modules are studied in this section, mod1 and mod2, they were made with legs coming from the same pellets, therefore their properties are similar. The average *zT* between 200 and 400 °C for those p- and n-type materials are respectively 0.35 and 1.03, while for those used in section 5, they were 0.33 and 0.96 respectively. This difference falls within the measurement uncertainty and shows the reproducibility of the materials.

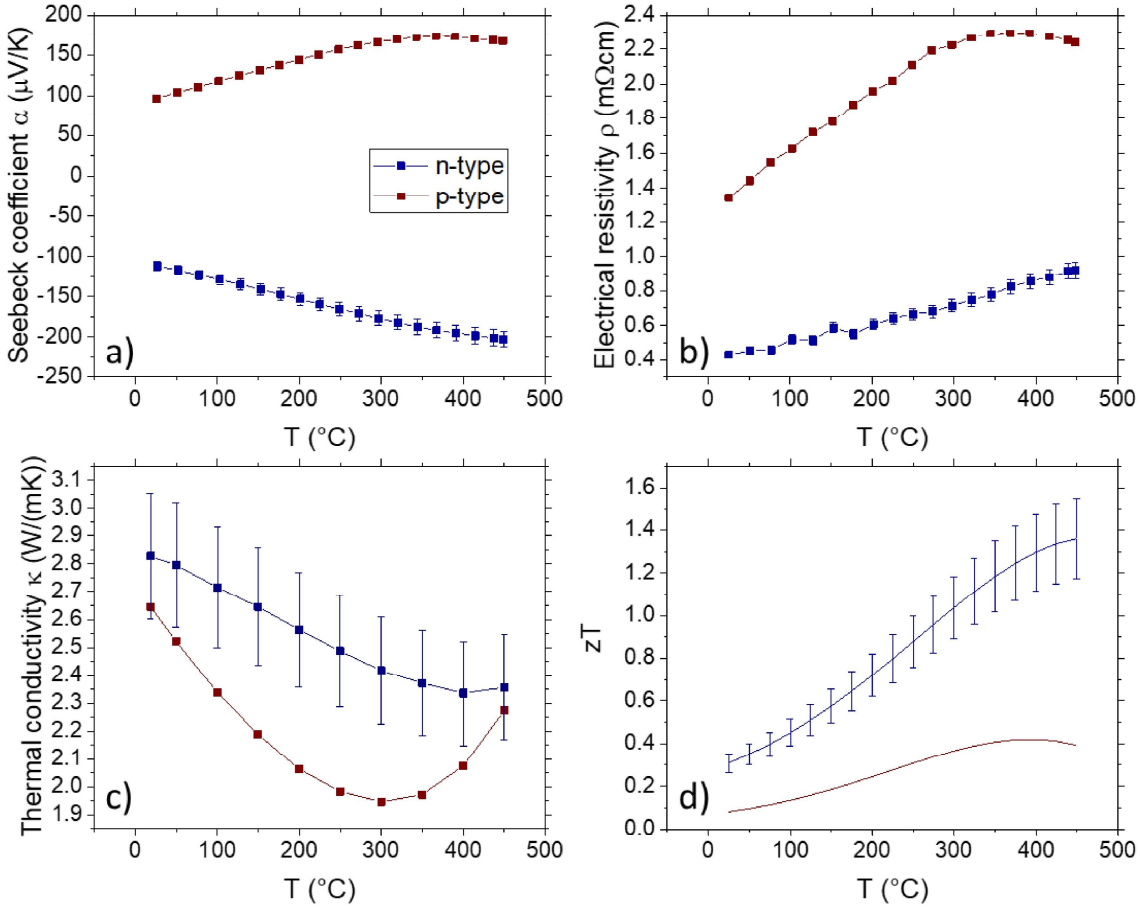

Figure 42 - Measured properties of $Mg_2Si_{0.3}Sn_{0.665}Bi_{0.035}$ (n-type) and $Mg_{1.97}Li_{0.03}Si_{0.3}Sn_{0.7}$ (p-type) materials used as input for the CPM calculations of the test modules mod1 and mod2: a) Seebeck coefficient, b) electrical resistivity, c) thermal conductivity, d) figure of merit. Uncertainties of the Seebeck coefficient and electrical conductivity measurement are 5%, of the thermal conductivity 8%. The resulting uncertainty of zT is 14%. The legend in a) also applies for b), c) and d).

Similarly to what was described in section 5, the specific contact resistance r_c is measured using a PSM [143, 144], comparing two r_c values (one using the TE material´s electrical conductivity to calculate the current density ($r_{c,j(TE)}$), one using the current passing through the sample as measured on a shunt resistor by the PSM ($r_{c,j(PSM)}$)), as reported in previously published papers [4, 35].

Evaluation of contact resistivities was conducted for the electrodes on each side of every leg. The r_c values between the TE material and the Al metallizations on each side of each leg are reported in Table 9 and Table 10. These values reflect mean values and standard deviations of statistical distributions, which have been obtained from data evaluation of 5 scanning lines widely spread (~ 2 mm) across the interface.

Table 9 - specific contact resistances (mean value ± standard deviation) of the legs used to build the module mod1. Both contacts of each leg are reported in order to check for symmetry. The potential line-scans showed no sign of cracking in any of the legs.

Leg	**n-type 1**		**n-type 2**		**p-type 1**		**p-type 2**	
Interface	Side 1	Side 2	Side 1	Side 2	Side 1	Side 2	Side 1	Side 2
$r_{c,j(TE)}$ **(μΩcm²)**	6 ± 1	2 ± 3	3 ± 2	2 ± 1	7 ± 3	2 ± 1	5 ± 2	4 ± 3
$r_{c,j(PSM)}$ **(μΩcm²)**	11 ± 1	3 ± 4	3 ± 2	3 ± 1	6 ± 3	2 ± 1	7 ± 4	4 ± 3

Table 10 - specific contact resistances (mean value ± standard deviation) of the legs used to build the module mod2. Both contacts of each leg are reported in order to check for symmetry. The potential line-scans showed no sign of cracking in any of the legs.

Leg	**n-type 1**		**n-type 2**		**p-type 1**		**p-type 2**	
Interface	Side 1	Side 2	Side 1	Side 2	Side 1	Side 2	Side 1	Side 2
$r_{c,j(TE)}$ **(μΩcm²)**	4 ± 2	7 ± 2	3 ± 3	7 ± 3	4 ± 3	4 ± 2	5 ± 3	3 ± 2
$r_{c,j(PSM)}$ **(μΩcm²)**	5 ± 3	9 ± 2	6 ± 6	12 ± 5	4 ± 3	4 ± 3	5 ± 4	3 ± 2

It can be seen that the electrical contact resistivities from both evaluation methods lie close to each other and within the limits of individual statistical distributions. Furthermore, contact resistivities are symmetric and low (≤10 μΩcm²), meaning that the contact between the TE material and the metallization should not impede the performance of the module. For the following calculations, an average value of 5 μΩcm² was considered for each TE/Al interface.

b) Module building

The details of the legs used for the fabrication of both modules is reported in Table 11. The optimum area ratio for efficiency for those materials properties is such as $A_p/A_n = 1.9$. The ratio corresponding to the real legs' cross-section reported in Table 11 is 1.8, which corresponds to a negligible relative loss in maximum efficiency of 0.2% compared to the optimum ratio.

Table 11 - Details of the legs used for the fabrication of mod1 and mod2.

	n-type	**p-type**
Effective composition	$Mg_2Si_{0.3}Sn_{0.665}Bi_{0.035}$	$Mg_{1.97}Li_{0.03}Si_{0.3}Sn_{0.7}$
Cross-section (mm x mm)	3 x 3	4 x 4
TE length before contacting (mm)	3.99	4.11
Total leg length (incl. electrodes) (mm)	4.5	

The legs are linked in an electrical circuit using copper bridges cut from a 250 µm foil (ChemPUR, 99.995% purity). The bonding of the legs to the bridges is done following the same process and components as described in section 5. A picture of such an open module is shown in Figure 43.

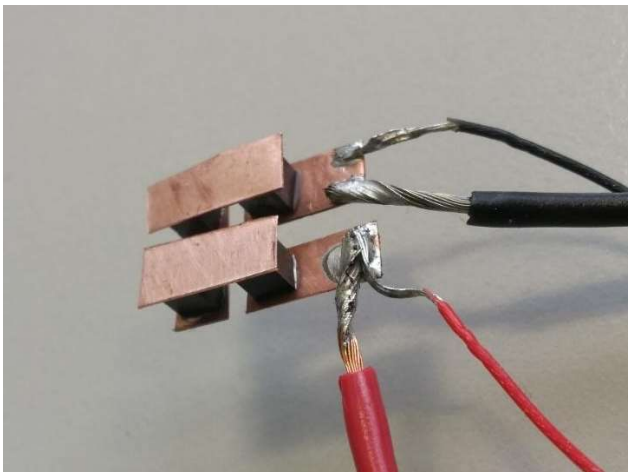

Figure 43 - Picture of an open module built with 250 µm thick Cu bridges.

c) TEG measurement

After assembly, the module performance was measured using the TEGMA, reported in [52-54], as described in section 2.2.4.

Mod1 was first measured in the same conditions as the module reported in section 5. However, to identify the origins of the observed degradation, which will be discussed below, a new

measurement method was designed. Additional voltage probes were soldered on each bridge between the legs, in order to monitor their respective electrical resistance and identify the origin of failure. This measurement design is presented in Figure 44, and will be referred to as APM for "Additional Probes Measurement", as opposed to RM for "regular measurement", which will refer to simple TEG measurements such as conducted in section 5.

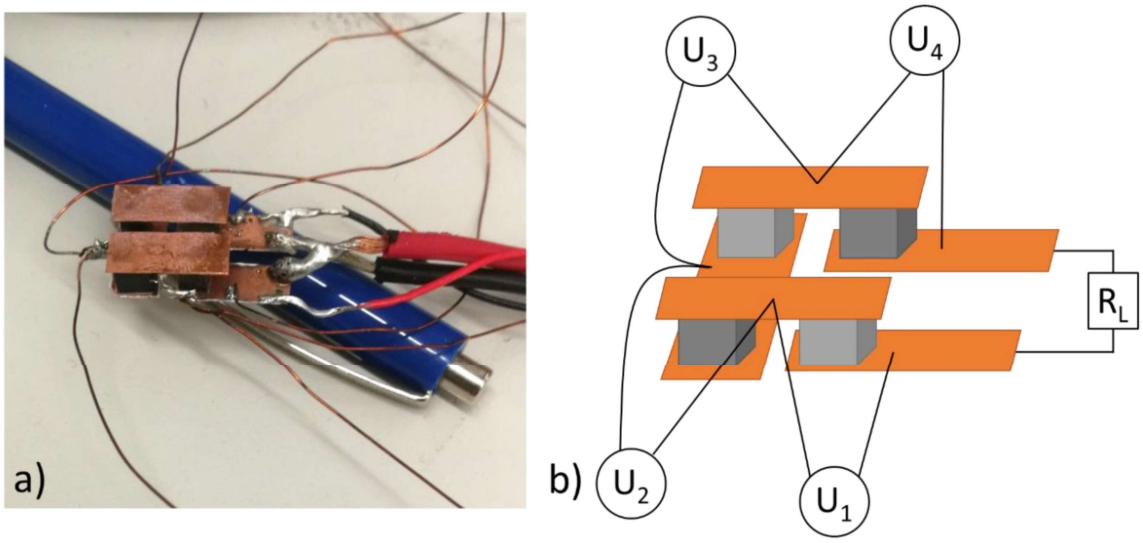

Figure 44 – a) Picture of a TEG with additional voltage probes, b) schematics of the APM.

The voltage probes are soldered on the inner side of the Cu bridges, at a distance of a few millimeters from the legs. Therefore, the resistances obtained with the measured voltages U_1, U_2, U_3, and U_4 include the resistance of the leg 1, 2, 3 and 4, respectively, as well as the resistance of the metallizations, the resistance of the fractions of metallic bridge between the leg and the probe, and the contact resistances between each of those components. The respective resistances R_1, R_2, R_3 and R_4 are obtained calculating the slope of U_1, U_2, U_3, and U_4 with respect to current. There is no compensation for the Peltier shift during the measurement as this would have required separate probes to measure the Seebeck voltage of each leg $U_{0,\mathrm{m}}(I)$ (see equation (42) in section 2.2.4), which leads to a resistance overestimation up to 5-6%. As an example, for mod2, the total resistance neglecting the Peltier shift (see equation (42) in section 2.2.4) is 16.1 mΩ, while the true resistance (considering $U_{0,\mathrm{m}}(I)$) is 15.1 mΩ for $T_{\mathrm{h,m}}$= 90 °C.

One other difference in the measurement method is the coupling layers used to transfer the heat along the measurement column and insulate the TEG electrically from the reference blocks: those layers can change measurement to measurement depending on equipment availability. The coupling details of each measurement are given in Table 12. From now on, the TEG reported in paper3 will be referred to as "modDBC". Mod3 (in Table 12) will be introduced below in this section.

*Table 12 – Coupling layers used for each TEG measurement, the measurement column is described in the order from heating block to cooling block. Elements changing from one measurement to the other are indicated in **bold**. Graphite foil is from Dr. Fritsch Gerätebau GmbH, 200 µm thickness. The hot side 250-µm Al_2O_3 plate broke after mod1-RM, which is why it was replaced by a 625-µm plate.*

Module	**Measurement column (from heating block to cooling block)**
modDBC (RM)	- Cu geometry adaptor (heater) - graphite foil - TEG (DBC on each side) - graphite foil - Ni cooling block (HFM)
mod1 – first measurement (RM)	- Cu geometry adaptor (heater) - graphite foil - **Al_2O_3 plate (250 µm)** - mod1 - thermal grease - **Al_2O_3 plate (250 µm)** - graphite foil - Ni cold side block (HFM)
mod1 – second measurement (APM)	- Cu geometry adaptor (heater) - graphite foil - **Al_2O_3 plate (625 µm)** - mod1 - thermal grease - **Al_2O_3 plate (625 µm)** - graphite foil - Ni cold side block (HFM)
mod2 (APM)	- Cu geometry adaptor (heater) - graphite foil - **Al_2O_3-coated Al foil (100 µm Al + 5 µm coating on each side)** - mod2 - thermal grease - **SiO_2 plate (660 µm)** - graphite foil - **Inconel cold side block (HFM)**

mod3 (APM1, RM and APM2)	- Cu geometry adaptor (heater) - graphite foil - **Al_2O_3-coated Al foil (100 µm Al + 5 µm coatings)** - mod3 - thermal grease **- Al_2O_3 plate (250 µm)** - graphite foil **- Ni cold side block (HFM)**

d) Numerical analysis

To compare measured data to a model calculation, the CPM is applied using the same equations as presented in section 5. For the heating data (data measured during heating up the sample), legs with a Zn-induced gradient like shown in section 6.1 are considered. For cooling data, since material change was observed (see below) and the change likely happened at the highest temperature steps, inhomogeneous legs are considered using the profile obtained after module disassembly reported below. The spatial profiles and corresponding temperature averages are obtained using the CMIM method described in section 6.1 (carrier concentration profile and SPB model).

6.2.2. Results

a) TEG performance and CPM calculations

One cycle of TEG performance measurement for mod1 is shown in Figure 45b. The maximum efficiency is around 3.6% while the maximum power output is about 0.6 W, which corresponds to a power density of 1.2 W/cm² with respect to the TE area. It can be seen that both the maximum power output and the maximum efficiency are decreasing within this first cycle. The relative changes of the main TEG parameters of mod1 and modDBC are reported in Table 13. It is seen that the trends are similar, but that the changes are detrimental for mod1 as the relative increase in inner resistance is much larger. In section 5, these trends were explained by crack

formation and propagation close to the metallization layer, which simultaneously increase the voltage and decrease the heat flow.

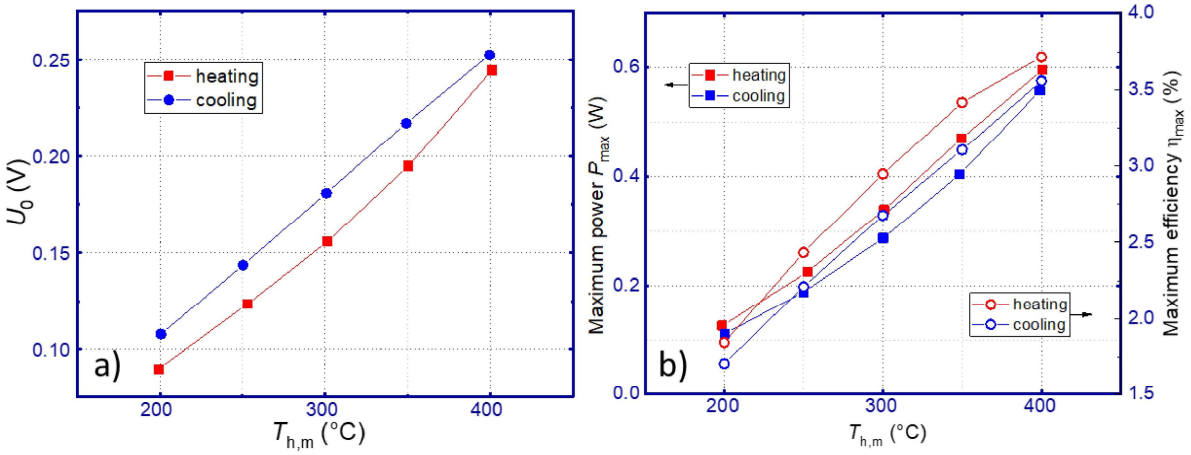

Figure 45 – First measurement cycle of mod1 at a cold side temperature of $T_{c,m} = 25\ °C$: a) open-loop voltage, b) maximum power output and maximum efficiency.

Table 13 – Comparison of the relative change between start and end of the first temperature cycle for several parameters, for the DBC module shown in section 5 and mod1

	Relative change between start and end of first cycle (%)				
Parameter	U_0	Q_0	R	P_{max}	η_{max}
modDBC	+12	-7	+19	+4	+9
mod1	+10	-3	+63	-12	-7

After all measurements (including the APM reported further below), mod1 was disassembled, the hot and cold sides of the legs were kept track of and the legs were scanned in the PSM. The corresponding PSM line-scans are shown in Figure 46. They show that the Seebeck values of the n-type legs have significantly changed at the hot side during the measurement, while the p-type legs behavior are thermoelectrically stable over time considering that the change in their spatial average is below 7%, which could be due to inter-measurement variation (tip wear, etc.). The change of the n-type legs will be discussed in a subsection below.

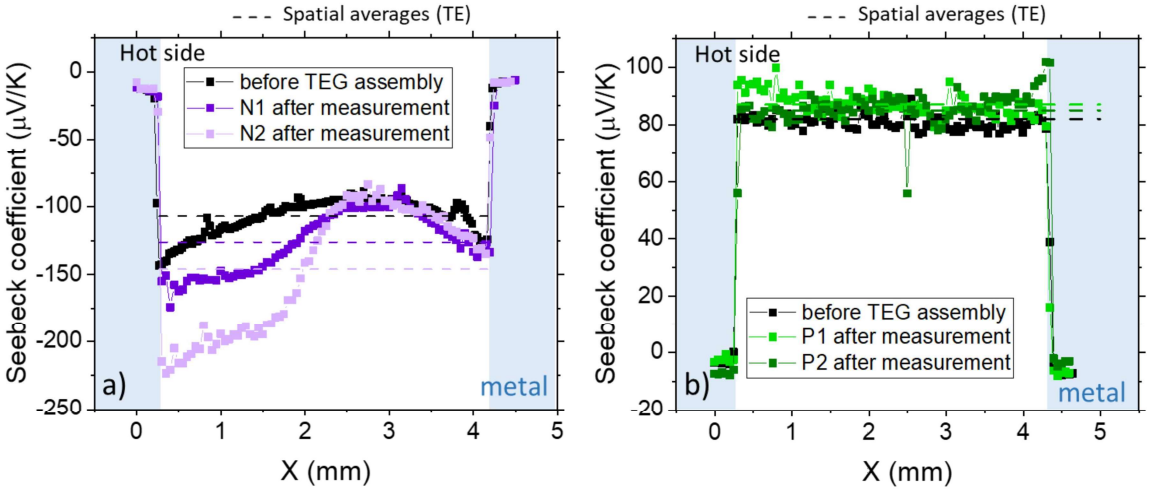

Figure 46 – Line-scans of the room-temperature Seebeck coefficient of the legs of mod1 before assembly and after one temperature cycle of TEG measurement, with corresponding spatial averages: a) n-type legs, b) p-type legs, where the spatial average lines are extended beyond the leg area for clarity.

Following the method described in sections 2.3.1 and 5, the temperatures at the TE legs were determined and are plotted in Figure 47a, using the measured open-loop voltage shown in Figure 45a. It can be seen that the ratio of ΔT across the module (along the legs) approaches and exceeds 100% during the heating step (referring to pre-TEG assembly properties assumed as remaining constant during the temperature treatment of the measurement cycle), which is not realistic. The ratio of the cooling data (assuming a property profile based on the changed material properties) is more coherent.

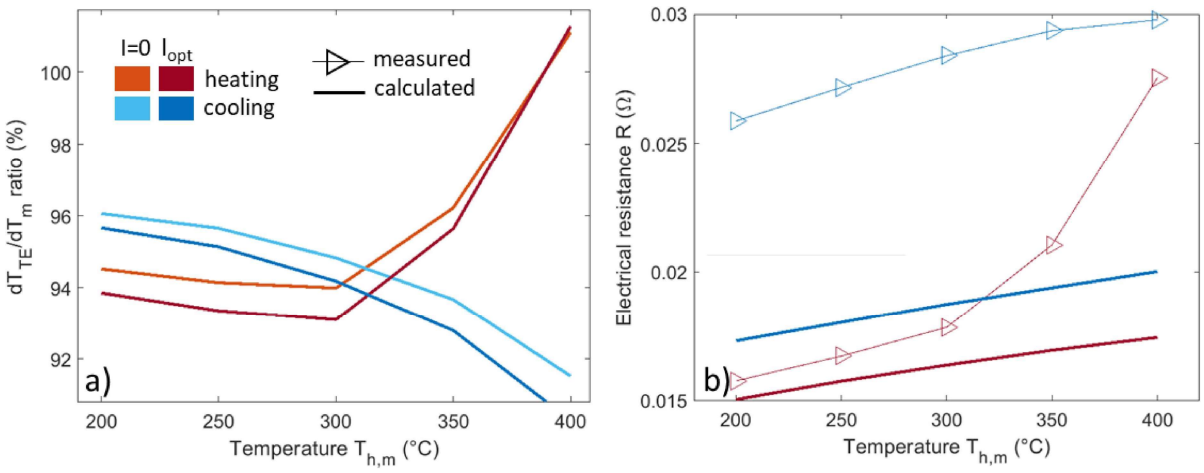

Figure 47 – Comparison of measured and calculated values for mod1 at $T_{c,m} = 25\ °C$: a) ratio of the temperature difference at the TE legs (calculated) and the temperature difference applied by the heater and the cold block (measured); b) electrical resistance. The legend in a) also applies in b). Heating data were calculated assuming TE properties of the leg prior to the TEG assembly (black in Figure 46a) while the cooling values were calculated considering the profiles obtained after the TEG measurement in Figure 46a (colored), which means that all average TE properties (α, ρ, κ) change between the calculated heating and cooling data, explaining the sudden jump at $T_{h,m}$=400 °C in a). The temperature averages are obtained using the CMIM method described in section 6.1 (carrier concentration profile and SPB model).

The trend of the heating curves observed in Figure 47a starts changing for $T_{h,m}$ > 300 °C. This change could be explained by Mg evaporation or TE-metal interdiffusion, which are both known mechanisms leading to carrier loss in n-type $Mg_2(Si,Sn)$ and are accelerated at higher temperatures [1, 2, 116, 121]. This explains the trend of the heating curves as it is likely at those stages that the n-type material started to significantly change compared to input properties, although Mg evaporation is usually observed only at higher temperatures (> 450 °C) as will be discussed below. Therefore, the input n-type Seebeck coefficient is gradually underestimated in the calculation, which leads to an overestimated ΔT_{TE}. It is therefore expected that the calculated data above 300°C for the heating branch is not representative of the physical situation and can lead to the obtained unphysical behavior in Figure 47a and increased deviation in related results below.

For the CPM calculations of the cooling data, post-measurements profiles (obtained from the Seebeck coefficient profile in Figure 46a) were used. The change of input properties between the heating data and the cooling data understandably leads to a jump between both calculations at T_h = 400 °C, while in reality measured points are much closer as the change happened gradually and continuously. Exemplary profiles of the Seebeck coefficient along the leg assuming T_h = 400 °C are shown for each leg in Figure 48, compared to experimental temperature dependence of the Seebeck coefficient obtained from the literature [129] in order to spot the temperature range where our SPB model can be applied. It is noticed that the literature data does not have exactly the same slope as our SPB model unlike what could be expected: this could be due to a slight difference in the experimental material effective mass compared to the model, which also has an impact on the carrier concentrations obtained experimentally differing from our SPB data.

It can be seen that from a certain temperature on the experimental data starts to bend much stronger compared to the results from the SPB model. This bending indicates the maximum temperature at which the SPB is reliable, as above this temperature the minority carrier contribution starts to become relevant (onset of bipolar effect) and depends on the carrier concentration due to doping. In Figure 48, this temperature is at about 350 °C for $n=0.66\cdot10^{26}$ m^{-3} (orange line), and above 400 °C for $n=1.65\cdot10^{26}$ m^{-3} (red line), and by rough linear extrapolation it would be between 250-280 °C for the lowest carrier concentration in b). A two-band (or more complex) structure model would be required to determine this point more precisely. An example for Mg_2Sn was developed in [152], but a suitable description for the solid solution employed here is not known yet.

This indicates that for N1, only about 5-10% of the leg profile length would deviate from SPB (weakly bent) while for N2 it could represent more than 30% of the leg length. This means that for the overall TEG CPM analysis of the cooling branch of the measurement, a stronger deviation between measurement and calculations is expected for $T_h > 300$ °C (on average), due to an overestimation of the Seebeck coefficient by SPB in an actually bipolar situation.

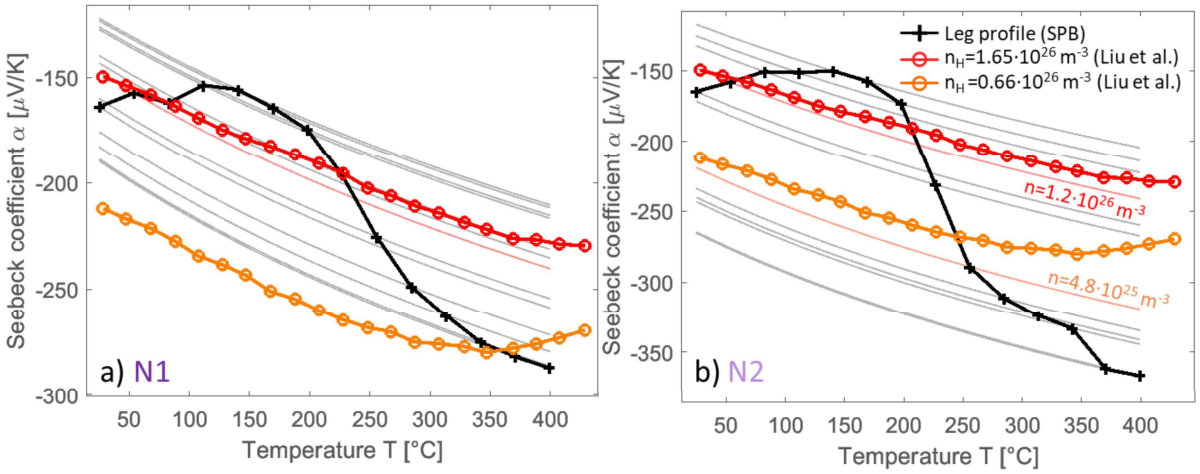

Figure 48 - Profiles of the Seebeck coefficient of the legs plotted vs local temperature a) N2, b) N1(see Figure 46), between T_c=25°C and T_h=400°C. Experimental data from literature [129] is added for comparison with red and orange symbols. Thin lines are temperature dependent SPB calculations for each carrier concentration obtained in the profile of the leg using the CMIM, following the methodology in Figure 37a-b, the lines in orange and red are the SPB data calculated for $n=1.2\cdot10^{26}$ m^{-3} and $4.8\cdot10^{26}$ m^{-3} which are graphically closest to the literature data. The legend in b) also applies in a). The values of the profiles in black are difference from what can be seen in Figure 46a, as the former are reference Seebeck coefficient values (CMIM) while the latter shows non-converted PSM experimental values.

The CMIM, based on the SPB model, assumes a carrier mobility independent from carrier concentration. This assumption can be verified using the PSM line-scans, comparing the ratio of the $U(x)$ slopes and the ratio of the carrier concentrations given by the SPB model on changed and unchanged portions of the leg, similarly to what was done in Figure 41 (section 6.1). A changed mobility has an impact on the electrical conductivity, and therefore on the predictions of I_{opt}, P and η. For the legs of mod1, those ratios differ by a factor of 2, which shows that mobility is likely changing in the degraded portion of the legs and that our model requires further improvement in the future. It can however be noted that the change in mobility was studied in the case of Mg loss in n-type $Mg_2(Si,Sn)$ [116, 162] and it was found that, although the influence was significant at room temperature, it declines with increasing temperature (as the influence of acoustic phonon scattering increases). In fact, for Mg_2Si it was found that the reduction in mobility due to Mg loss reduces from a factor of three at room to less than 20% above 300 °C. This indicates that the mobility reduction in the degraded fraction of the leg at the operation temperature is much less than inferred from the PSM measurement and the validity of the analysis is not strongly affected.

The comparison between measured and calculated data for the electrical resistance is shown in Figure 47. The deviations for relevant parameters are summarized in Table 14.

Table 14 – deviations between predicted and measured data for mod1 shown in Figure 47. The order of the value is with increasing $T_{h,m}$ (between 200°C and 400°C)

Deviation (%)	R	I_{opt} (using R_m)	Q_0	Q_{opt} (using R_m)	P_{max} (using R_m)
Heating	6 to 37	0.05 to 3.6	23 to 27	21 to 25	1 to 10
Cooling	33 to 34	2.5 to 0.15	37 to 23	34 to 21	8 to 2

The measured maximum power output is 0.6 W, which corresponds to a power density of 1.2 W/cm² (related to the TE leg area). This value however decreases over the measurement cycle. Like observed and discussed in section 6.1, the deviation for the heat flows exceeds the measurement uncertainty (13.5%), specified for larger, "standard" modules, again emphasizing dedicated measurement technique and protocol development for small modules. The reason for the observed differences between model and measurement remains unclear at this stage.

It can be seen in Figure 47b and Table 14 that the deviation between predicted and measured inner resistance was initially only 6%, and that it increased during the heating step, especially above T_h = 300 °C. Although this coincides with the suspected period of change in n-type material, it can be seen that the difference between calculated heating/cooling data is much smaller than the difference between measured heating/cooling data. This indicates that the change in n-type material is not the main origin of the deviation.

In those CPM calculations, the Cu bridges were considered in the predicted resistance of the TEG, unlike in section 5 and 6.1 (modDBC) where they were neglected (in particular in section 6.1 to keep the focus on the effect of changed material). The temperature-dependent electrical conductivity of Cu $\sigma_{\mathrm{Cu}}(T)$ was taken from [163], and the electrical resistance of each portion of bridge i was calculated such as $R_{\mathrm{Cu},i} = \frac{L_i}{\sigma_{\mathrm{Cu}}(T)A_i}$ where L_i and A_i are the length and cross-section of each portion of bridge and $T = T_{h,\mathrm{TE}}$ for the hot side and $T = T_{c,\mathrm{TE}}$ for the cold side (the temperature drop between the Cu bridges and the TE legs are therefore neglected). The length L_i is taken from the middle of the bridge between two neighboring legs (or 3 mm away for the external legs) to the center of the leg. Since the bridges are connected electrically in series, $R_{\mathrm{Cu},i}$ for all bridges are added to obtain the total resistance of the TEG.

Taking the bridges into account for modDBC here, the deviation between measured and predicted TEG resistance was at 4% at the start of the measurement and increase to 19% at the end of the first cycle. The bridges represent 6-7% of the total resistance, roughly equally shared between the hot side bridges, more resistive, and the cold side bridges which have a much larger total length. The rest of the difference in deviation from what was reported in section 5 is quantitatively explained by the transition from (assumed) homogeneous material to gradient material as discussed in section 6.1. This lower initial deviation raises doubts about the hypothesis formulated in section 5 about cracks already forming before the measurement (during TEG assembly) and it emphasizes the importance of the use of a more detailed analysis to truly understand a TEG behavior. It however does not change the conclusions that cracks do form during the TEG measurement, since the deviations still significantly increases during the measurement cycle.

Table 14 also shows that deviations at low T_h are similar for cooling and heating data at the same temperature (i.e. 2% vs 1% for P_{max}, 0.15% vs 0.05% for I_{opt}). The slight increase for the cooling data could be attributed to the uncertainty of the input n-type properties (changed profiles), which rely on the PSM measurement for the establishment of the carrier concentration profile which generates a general uncertainty on the whole profile. However, this very slight difference mostly shows that the CMIM model is consistent for significantly different profiles when compared to measured values.

The deviations also generally increase for increasing T_h, which is explained by the lower reliability of the SPB model at higher temperatures for the cooling data (see Figure 48), and by the unaccounted-for material change for heating data.

The open design of mod1, with only Cu bridges, was chosen as it was believed to avoid cracking by reducing thermal stress. However, the same large increase of inner resistance upon heating is observed, which likely indicates crack formation again. Therefore, a new measurement method was developed to locate and understand the origins of the cracking.

b) Additional voltage probes measurements (APM)

Mod2 was built and directly measured with the APM method under 200 °C, in order to avoid such change in material properties like occurred for mod1. The APM measurements are done with a device called Absolute TEGMA, on which additional voltage probes can easily be plugged. However, on this device a significantly wider block was used at the hot side, which leads to a higher uncertainty for heat flow on such small TEGs [145]; therefore the efficiency

of mod2 is not reported. The resistance of each individual leg of mod1 and mod2 was experimentally obtained using the method shown in Figure 44. The theoretical values of those resistances are obtained adding the theoretical resistance of the TE material, the contact as determined by PSM and (approximated) parts of the Cu bridges between the probes. For example, the calculated values for N2 at ΔT_{TE} = 42 °C are as follows: $R_{\mathrm{TE}} + R_{\mathrm{c}} + R_{\mathrm{Cu}} = 2.41 + 0.11 + 0.13$ mΩ. The experimental results are presented in Figure 49, along with expected resistance values. The total resistance of the legs was compared to the measured inner resistance of the module neglecting the Peltier shift, which match at 99% for both modules. The small discrepancy of 1% can possibly be explained by parts of Cu bridges which are included in the total TEG resistance measurement but not in the circuit considering individual legs. It should be noted that the total inner resistance of mod1 remains similar between RM and APM, which means that no additional damage was caused by dismounting-remounting steps.

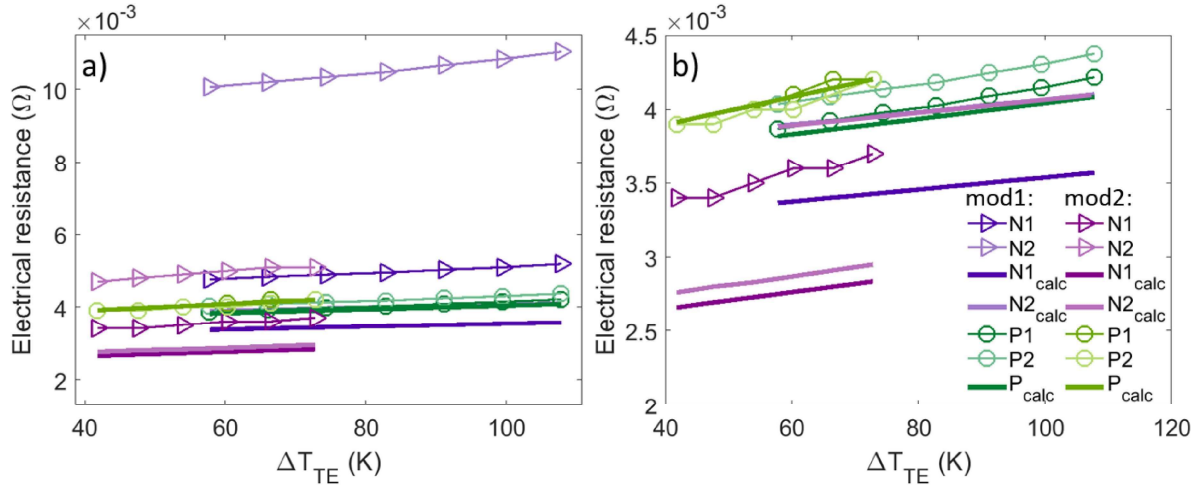

Figure 49 – a) single leg resistance obtained with APM of mod1(higher ΔT_{TE} range) and mod2 (lower ΔT_{TE} range). Symbols represent measured data; thick lines represent calculated data. Since mod1 was measured with a Ni HFM and mod2 with an Inconel HFM, cold sides temperatures were significantly different (≈23 °C for mod1 and ≈50 °C for mod2) and therefore the data is compared using ΔT_m on the x-axis. The calculations were done considering each respective temperature for the measurements. b) is a zoom-in of a) where many lines entangle, for better readability. Legend in b) also applies to a). It is worth reminding that the APM of mod1 was done after its high-temperature RM, while the mod2 was unmeasured before its APM.

It can be seen that for both modules, the resistances of the p-type legs are close to the predicted value. Some experimental values are actually below predictions for p-type legs of mod2 (1-2% relative difference), while the opposite should be observed. This could be explained by an overestimated contribution of the Cu bridge between the probes (approximated geometry, represents 4-5% of the predicted resistances) and slightly flawed temperatures at the TE legs (neglected Peltier shift) used to calculate the temperature average of the resistivity. Nevertheless, experimental and predicted values are very close, which indicates that p-type legs did not significantly degrade during TEG assembly nor measurement (on this point it is worth

noting that mod1 was already measured at high temperature in RM, dismounted then remounted for the APM, its legs therefore undertook more mechanical stress variations due to manipulation).

The n-type legs resistances are more scattered. For mod1, since the APM took place after the high-temperature RM, the predicted values of the n-type legs were calculated considering the changed carrier concentration profiles reported in Figure 46 (which is why the prediction for both legs slightly differ), therefore some uncertainty inherent to the method applies as previously described. For mod2, as the measurement was done at temperatures below 200 °C, no change in the TE material was assumed, therefore carrier concentration profiles from the two legs used for mod2 before TEG assembly were considered; they are shown in Figure 50.

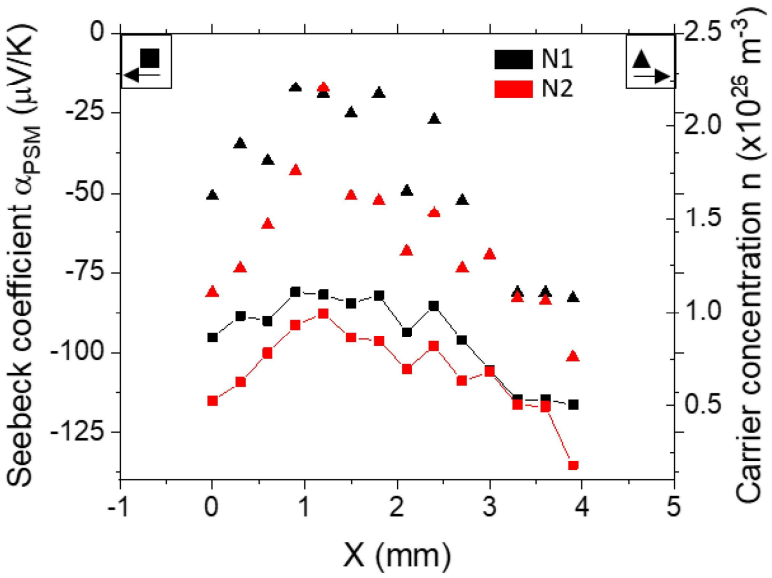

Figure 50 - PSM Seebeck coefficient and corresponding carrier concentration profiles of the legs of mod1 before TEG joining

All n-type legs are significantly more resistive than predicted (deviation higher than the possible uncertainty originating from the modelling method and SPB overestimation). Material degradation was accounted for in the predictions, therefore this increase is likely due to crack formation and propagation, or to contact degradation. It can be seen that legs from mod2 are generally less resistive than those of mod1, which could be due to the lower measurement temperature applied to the former.

Like for modDBC, an open uni-couple (one legs pair) was built in parallel to the studied TEG to be embedded and analyzed. The SEM images are shown in Figure 51 and it can be seen that, after TEG assembly, no crack has appeared close to the metallization layer contrarily to the uni-couple version of modDBC. This uni-couple is a different individual from mod1 and mod2,

however all were built with the same components and the same process, therefore it can be assumed that the observations made on the uni-couple also are representative for mod1 and mod2 after their assembly and prior to their measurement.

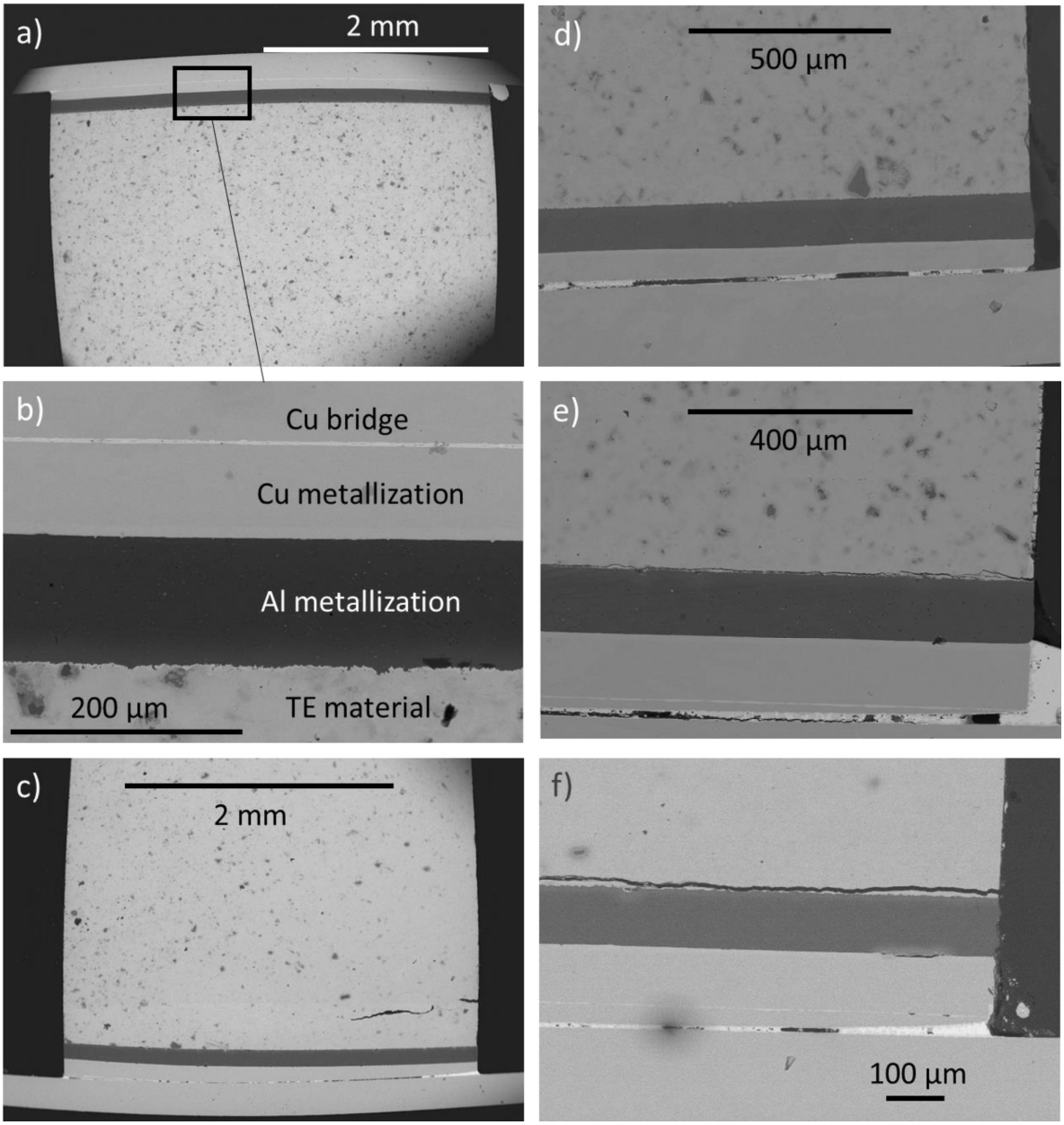

Figure 51 – a)- c): SEM pictures of the embedded uni-couple built identically to mod1 and mod2 (not measured): a) p-type leg, b) zoom-in of the interfaces between the TE material, the Al-Cu metallization, the Sn solder and the Cu bridge, c) n-type leg. d)-f): Exemplary SEM pictures of the TEG legs after measurements and disassembling: d) cold side of p-type leg (mod1-P2), e) cold side of n-type leg (mod1-N1), f) cold side of n-type leg (mod2-N2). All cracks were observed on the cold side of the n-type legs; the p-type legs are crack-free.

It is observed that the non-cycled uni-couple's interfaces are crack-free (Figure 51 a to c), while its DBC-made counterpart already showed cracking at this stage of the TEG life. However, like suspected from the APM, some cracks are visible after the TEG measurement on the n-type legs. The cracks are all located at the cold side for both mod1 and mod2 (Figure 51 d to f),

while the hot side and the complete p-type legs look crack-free. Some cracks propagated on the whole width of the leg while some are only seen on one side of the interface; their position within the complete TEG (over the full area of the contacting interface and also in the neighboring region of the TE material) could however not be tracked. It is also seen in Figure 51d and e that the soldering between the Cu metallization and the Cu bridge is of variable quality, as several voids appear in the Sn solder layer. This variability is observed on all legs, p-type included, therefore it is probably of lesser influence on the respective resistance of each leg.

6.2.3. Discussion

a) Crack formation

In Figure 49, it can be observed that the resistance of the n-type legs of mod2 does not increase unexpectantly during the measurement but is already higher than predicted from the start. This indicates that the cracking happens either during TEG assembly or during mounting (pressure) and/or initial heating in the TEGMA (before stabilization at the first temperature step at 90 °C). It would be unlikely that it happens during TEG assembly, as the corresponding embedded uni-couple was crack-free under similar assembly conditions.

For mod1, since the APM was done after a high-temperature measurement cycle, it is easily understood why the resistance of the legs was already high: as seen in Figure 47c, significant degradation was observed above 300°C during the RM. At the start of the RM, the measured resistance was only slightly higher than the predicted value, which does not indicate significant cracking from the start like for mod2.

After dismantling mod1, the contact resistances could be remeasured in the PSM. The values can be compared to an "effective contact resistance" from the APM, considering that all the electrical resistance which is not due to the TE material nor the Cu bridges is due to contacts, such as $r_{\mathrm{c,eff}} = (R_{\mathrm{leg,m}} - R_{\mathrm{TE}} - R_{\mathrm{Cu}})\mathrm{A}$. The results are shown in Table 15. The same could not be done for mod2 as legs broke (further away from the interfaces) during manipulation.

Table 15 - PSM measurements of the electrical contact resistivity between the TE material and the Al metallization $r_{c,m}$, between the TE material and the Cu (metallization or bridge) $r_{c,tot,m}$ before TEG joining and after TEG measurement for mod 1, and calculation of the effective electrical contact resistivity for each leg of mod1 and mod2. The values shown are obtained considering j_{TE} (see section 2.2.3, equation (39)), whereas values obtained using j_{PSM} are not displayed for better readability, as both values are in the same order of magnitude for all cases. The standard deviations are also not displayed for better readability, because they are in all cases lower than the average value by a factor of 2. Values in μΩcm².

		N1 (hot/cold side)	N2 (hot/cold side)	P1 (hot/cold side)	P2 (hot/cold side)
$r_{\mathrm{c,m}}$ (Al-TE)	post-APM (mod1)	4 / 25	35 / 2	7 / 9	6 / 9
$r_{\mathrm{c,tot,m}}$ (bridge-TE)		4 / 27	37 / 4	6 / 10	14 / 14
$r_{\mathrm{c,eff}}$ (between T_{h}=90°C and T_{h}=150°C)	APM (mod1)	136 to 156	568 to 631	18 to 31	44 to 56
	APM (mod2)	77 to 88	188 to 204	5 to 17	0 to 11

To give a more precise idea of the impact of the cracks, the average effective contact resistivity of mod1, at the start of the very first measurement (RM), can also be estimated using the formula $r_{\mathrm{c,av,eff}} = \frac{(R_{\mathrm{m}} - R_{\mathrm{legs}} - R_{\mathrm{Cu}})A_{\mathrm{n}}}{2N\left(1+\frac{A_{\mathrm{n}}}{A_{\mathrm{p}}}\right)}$ with the total measured resistance, the predicted resistance of all TE materials and complete Cu bridges: the obtained value is 18 μΩcm² (for a hot side temperature of 200°C), which is lower than all effective specific resistivities of mod1 after the APM.

In theory, it should be observed that $r_{\mathrm{c,tot,m}}$ (post-APM) ≈ $r_{\mathrm{c,tot,eff}}$. Although there is a coherent pattern, the discrepancy between both values is large for n-types but still visible for the p-type legs. This could be due to a difference in applied pressure during the TEGMA and PSM measurements, as a higher pressure would help to close the cracks, or bring together the surfaces of a defective contact, and lower the resistance. In the PSM, the sample is fastened between the copper blocks of the sample holder using a screw, but the manually applied pressure cannot be quantified. Furthermore, the scattering of the potential inside the bulk metallic layers adds some uncertainty to the $r_{\mathrm{c,tot,m}}$ value, as using one or the other of two neighboring points in the Cu layer would give a different drop in potential and therefore a different $r_{\mathrm{c,tot,m}}$ value. The geometry of the Cu bridges is also approximated, although the value of R_{Cu} is quite negligible (3-5%) compared to the contribution of a crack therefore the impact of this approximation is small. Finally, some deviation also certainly comes from the uncertainty of the calculated R_{legs}, which was discussed above. The deviation is lower for p-type legs.

It can be seen that, considering PSM measurements, the p-type contact resistivities did not significantly change after the TEGMA measurement compared to before the TEG assembly (Table 9), while for the n-type they clearly degraded on one side. For N1, this is the side where cracks are visible close to the metallization. Since the resolution of the PSM is 50 µm for our samples, the potential drop due to the crack is therefore measured at the same site as those due to the TE/Al interface, which gives a "combined" contact resistivity. However, for N2 the increase in contact resistivity happened at the hot side and not at the cold side, while cracks were clearly observed on the cold side and not on the hot side in the SEM (sides of the n-type legs are easily tracked with the PSM scans as the hot side shows the change in α, see Figure 46). The increased PSM-measured contact resistivity on the hot side could partially be an artifact, as the drop of potential between the last point in the TE material and the first point in the electrode is just as large as the drop between each consecutive point in the altered portion of this leg (see Figure 52). Therefore, it is possible that the calculated high contact resistivity value essentially comes from the drop of potential inside the TE material included in the interval, and that the interface resistivity itself is actually quite low. For usual material properties, the resolution of the PSM is precise enough to ensure reliable estimation of the contact resistivity; it is however seen here that the resolution is not precise enough in case of a dramatically altered material.

Another possibility could be that the SEM observations are not representative: it is possible that there is also a crack deeper at the hot side interface. However, the leg was studied on several occasions in the SEM, being re-grinded each time, and no crack was seen at the different depths that were observed.

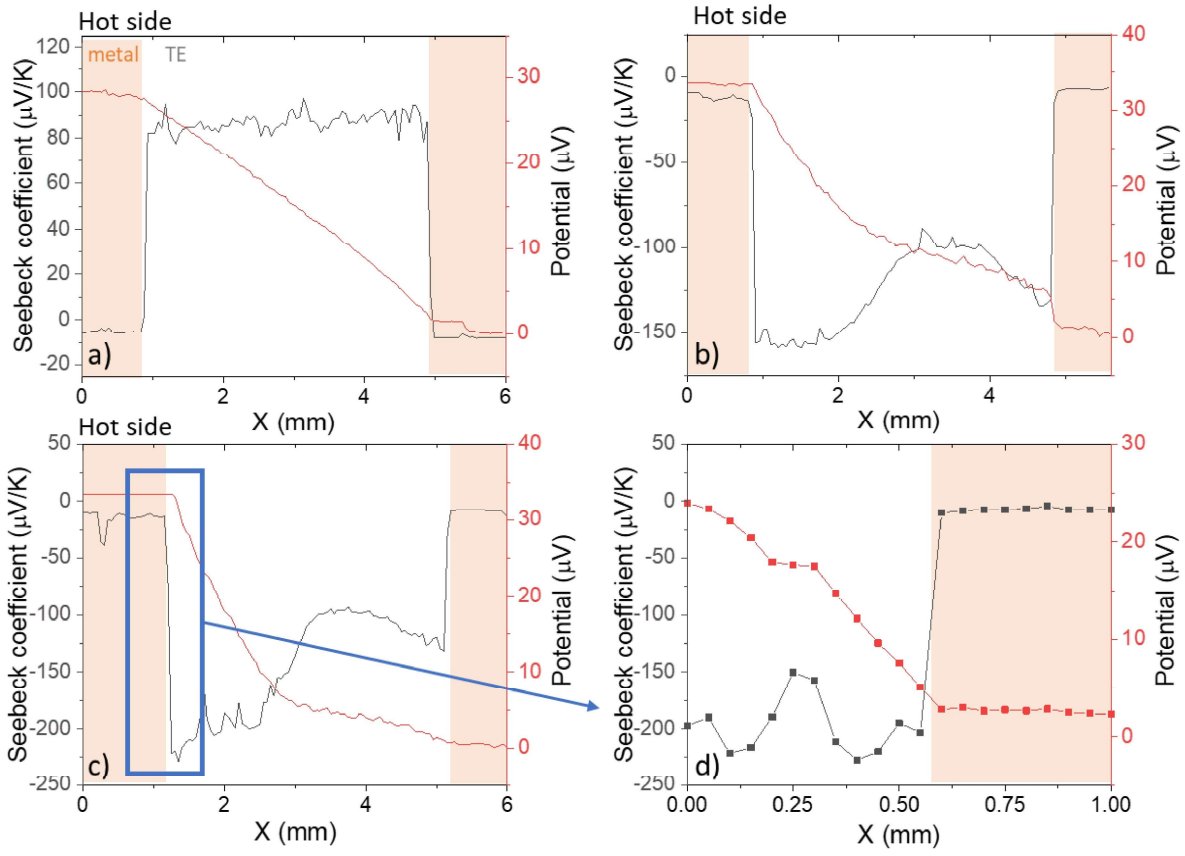

Figure 52 – PSM measurements (potential and Seebeck line-scans) of the legs after mod1 disassembly: a) P1 (P2 is similar), b) N1, c), N2, d) the left side of the scan in c) was remeasured separately to obtain the contact resistivity value, to avoid potential overflow as visible in c. The leg was inserted in the opposite orientation.

The low contact resistivity at the cold side of N2, despite the crack observed in the SEM, could indicate that the crack is rather localized and does not spread on the whole cross-section, or the effect of a higher pressure applied in the PSM (which could close the cracks during the measurement). No sudden drop in potential within the TE material is seen in the potential line-scans showed in Figure 52, which means that there should be no crack within the bulk of the legs. The very high resistivity of N2 remains therefore unexplained.

The cracks in the n-type legs are observed on the side that was kept cold during measurement. This again dismisses the possibility of cracking due to mismatching CTE between TE material, Al or Cu, as the components in the cold region did not significantly expand during the measurement.

Such cracks have not been reported for similar modules: Goyal *et al*. [128], who used the same open design as us, did not report any mechanical failure and Skomedal *et al*. [84], who used an open-design on the hot side only, reported degradation of the material and cracks close to the

metallization rather on the hot side, for a TEG with $Mg_2(Si,Sn,Ge)$ as n-type material, but none for the $Mg_2(Si,Sn)$-containing TEGs.

It was desired that our open design would avoid such cracking, as it would allow the cold side to slide to accommodate the hot side expansion, but it is not what we observe. One explanation could be the pressure applied on our TEG during the TEGMA measurement, which would "pin" the bridges by adhesive friction and prevent them from sliding horizontally. Substantiating this hypothesis would however require mechanical modelling as, to the best of our knowledge, no such work has been reported so far.

No crack is observed close to the hot sides, unlike in the DBC-based uni-couple. This shows that removing the ceramic plate from the assembly did relieve significant thermal stress on the hot-side interface. For this aspect, the open design was therefore beneficial.

A last conclusion that can be drawn from Figure 49 is that the difference in resistance between altered and unaltered leg is smaller than the increase in resistance due to the presence of cracks. Therefore, cracking is the major challenge to overcome in order to improve the TEG performance. N-type and p-type $Mg_2(Si,Sn)$ have fairly similar mechanical properties, so their difference in cracking behavior is unlikely to originate from one material being stronger or weaker [103]. Furthermore, they are contacted using the same components and the same process, therefore the difference probably does not originate from those factors either. Finally, the main difference between n- and p-type legs is their geometry, as the p-type legs have a wider cross-section. Although longer legs can accommodate thermal expansion of the hot side by bending [48], the thermal expansion of the bridge is proportionally less significant for a wider leg, which could explain the different behavior observed.

Therefore, a last module was built (mod3) with wider legs to test this theory. The length of the TE legs is ≈ 3 mm and the cross-section of the p-type and n-type legs is 4.5 x 4.5 mm² and 3.1 x 3.1 mm², respectively. The legs are shorter than for the previous modules due to a shortage of available powder, so the cross-sections were adapted so that the ratio of length/side of the n-type legs is >1. The properties of the as-sintered materials used for the legs of mod3 and the pre-TEG assembly contact resistivity measurement are given in Figure 53 and Table 16 respectively. The average zT between 200 °C and 400 °C for those p- and n-type materials are respectively 0.35 and 0.88. The n-type properties are lower than usual batches due to a punctual change of operator.

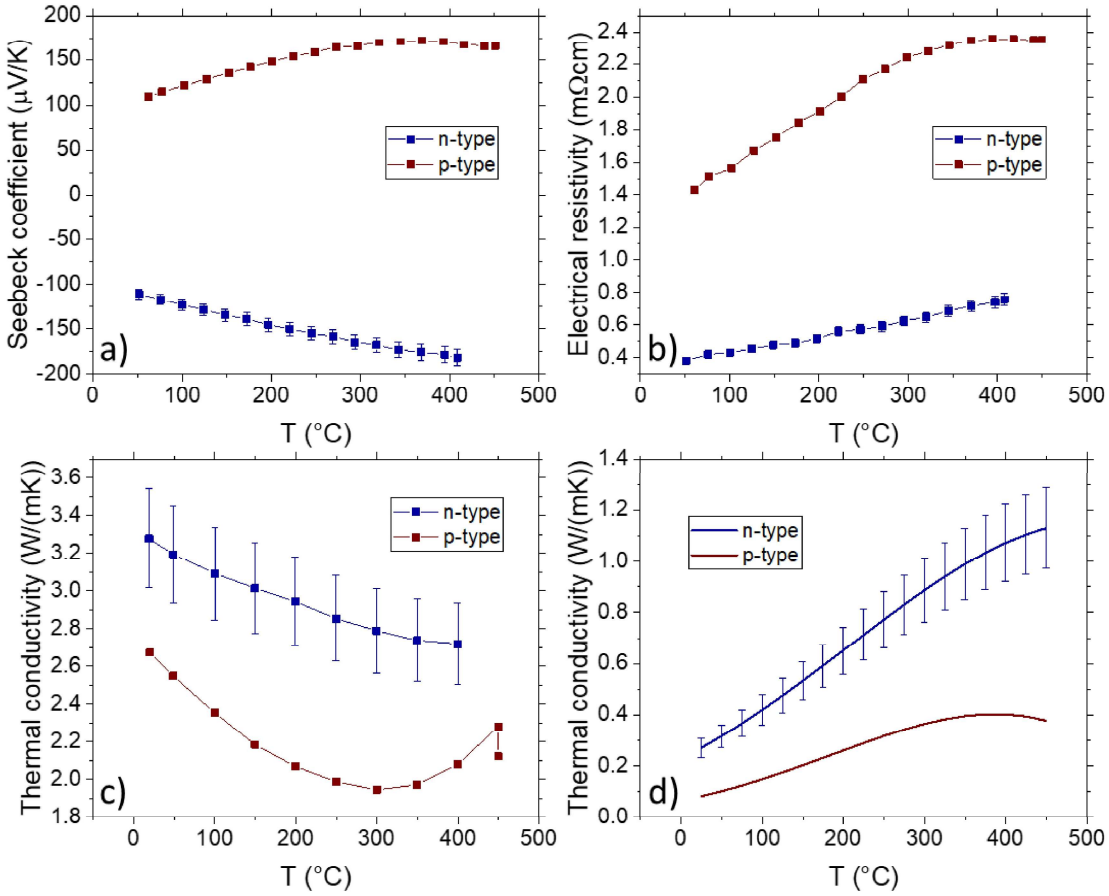

Figure 53 - Measured properties of $Mg_2Si_{0.3}Sn_{0.665}Bi_{0.035}$ (n-type) and $Mg_{1.97}Li_{0.03}Si_{0.3}Sn_{0.7}$ (p-type) materials used for the legs of mod3: a) Seebeck coefficient, b) electrical resistivity, c) thermal conductivity, d) figure of merit. Uncertainties of the Seebeck coefficient and electrical conductivity measurement are 5%, of the thermal conductivity 8%. The resulting uncertainty of zT is 14%.

Table 16 - specific contact resistances (mean value ± standard deviation) of the legs used to build the module mod3, by PSM measurement. Both contacts of each leg are reported in order to check for symmetry. The potential line-scans showed no sign of cracking in any of the legs.

Leg	**n-type 1**		**n-type 2**		**p-type 1**		**p-type 2**	
Interface	**Side 1**	**Side 2**	**Side 1**	**Side 2**	**Side 1**	**Side 2**	**Side 1**	**Side 2**
$r_{c,j(TE)}$ (µΩcm²)	4 ± 2	4 ± 3	5 ± 5	4 ± 2	6 ± 5	7 ± 5	11 ± 10	5 ± 4
$r_{c,j(PSM)}$ (µΩcm²)	4 ± 3	5 ± 3	6 ± 5	5 ± 3	6 ± 5	7 ± 5	12 ± 11	5 ± 5

After assembly, mod3 was directly measured with the APM method (below 210 °C to limit the change of the n-type legs). Therefore, carrier concentration profiles of each leg before TEG joining were used for the calculation of the theoretical resistances of the n-type legs (see Seebeck coefficient profiles in Figure 60 below). The results of the APM, predicted resistance and effective contact resistances are shown in Figure 54 and Table 17. The resistance of the complete TEG matches the added resistances of each leg at 98%.

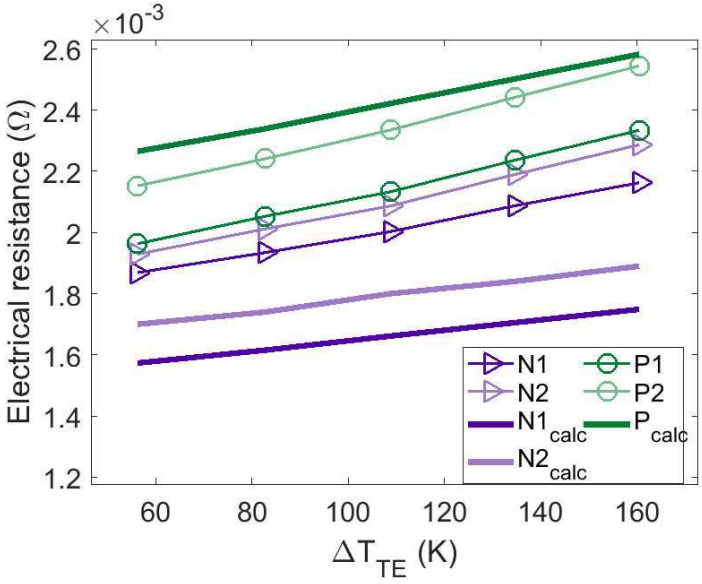

Figure 54 - single legs resistance obtained with APM of mod3.Contact resistivity values of 5 and 7 μΩcm² were considered for n-type and p-type legs respectively. Symbols represent measured data, thick lines represent calculated data. The measured cold side temperature was kept at $T_{c,m}$= 25°C.

Table 17 – effective contact resistivity for each leg in the APM1 of mod3 such as $r_{c,eff} = (R_{leg,m} - R_{TE} - R_{Cu})A$.

	$r_{c,eff}$ (μΩcm²)			
$T_{h,m}$ (°C)	N1	P1	N2	P2
90	38	-47	32	-9
120	41	-44	36	-6
150	43	-44	38	-4
180	47	-40	43	2
210	50	-36	48	6

It can be seen that the effective contact resistivity is of the same order of magnitude for both n-type legs, which indicates that if the legs cracked, they both did very similarly, while a large variability was observed for previous modules. For both p-type legs, the measured resistance is lower than the predicted resistance, although for P2 the difference is very small, which could be explained by a wrong estimation of the resistance of the Cu bridges.

These errors would however not fully explain the large deviation observed for P1. When looking mod3 in the optical microscope, a fine silvery line linking both metallizations can be observed on P1, as shown in Figure 55b, and the presence of at least one Zn-filled crack was confirmed in SEM, in Figure 55d. This can happen if the TE material cracks during contacting (475°C): the molten Zn coating can fill those cracks that link the electrodes on each side. It is unclear whether in this case the molten Zn links both electrodes, as in the SEM the crack

appeared empty over a third of the leg length, on the cold side. It is however possible that deeper in the leg, the crack gets wider and is filled along the complete length. Nevertheless, even a partially filled crack could partly electrically bypass the TE material. The legs are visually checked before use however the crack is thin enough to have gone unnoticed.

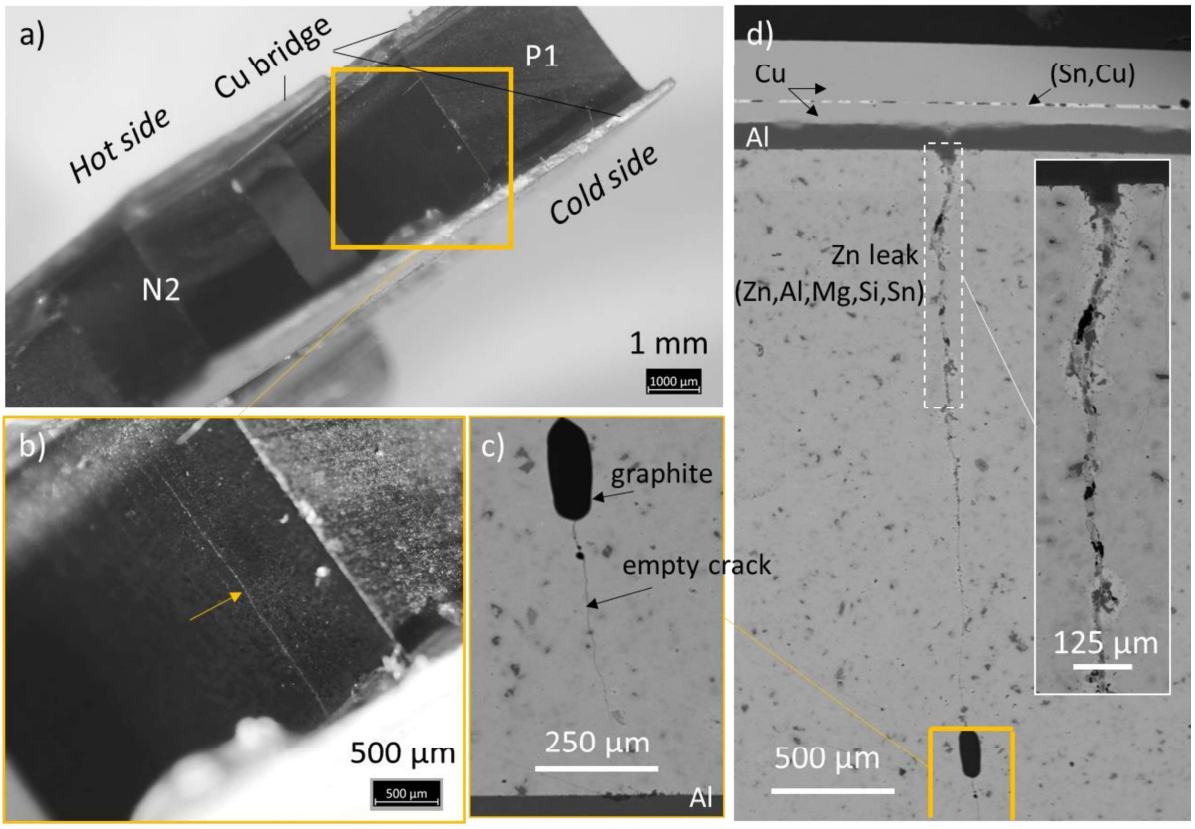

Figure 55 – a) optical microscope picture of the module after APM (the probes were removed), b) zoom-in of a) on the inner side of P1 leg where a crack is visible (highlighted by the arrow), c) SEM view of the crack on the cold side after all measurements (APM1, RM, APM2, see Figure 59), d) SEM view of the crack on the hot side after all measurements (APM1, OM, APM2, see Figure 59). Molten Zn has flown inside the crack, showing features similar to what was observed at the Al/Zn/Mg_2(Si,Sn) interface in [5]: (Zn,Al,Mg) phase in the crack with Al precipitates, Sn-rich phase in the TE material at the interface. Below the graphite particle, the crack is empty (at this depth in the leg). No similar crack was observed on the other legs.

This Zn-filled crack very likely acts as a partial shortcut along the leg. Such a shortcut with a non-continuous conductive channel (local change of width, conductivity) would have an impact on the current density in the sample, as the current in the TE material would not flow in 1D (between both ends of the leg) but, in the vicinity of the crack, rather in 3D with a bending towards the crack (meaning that the electrical potential does not show a gradient only in the length direction, but also along its width and depth). 2D mappings of the electrical potential and Seebeck coefficient on the side of the leg where the filled crack was observed are shown in Figure 56, where the shortcut would be expected to be near Y ~ 3.5 mm. A small decrease can be seen in the electrical potential on the upper three lines, but no local decrease in the Seebeck

coefficient, as could be suspected, is observed. As the scanned lines are separated by intervals of 0.2 mm, it is possible that the crack is too thin and located between two line-scans (resolution 0.05 mm), which would explain why it is not visible in the Seebeck coefficient mapping. To better understand the electrical behavior of this leg, 2D or even 3D modelling would be required.

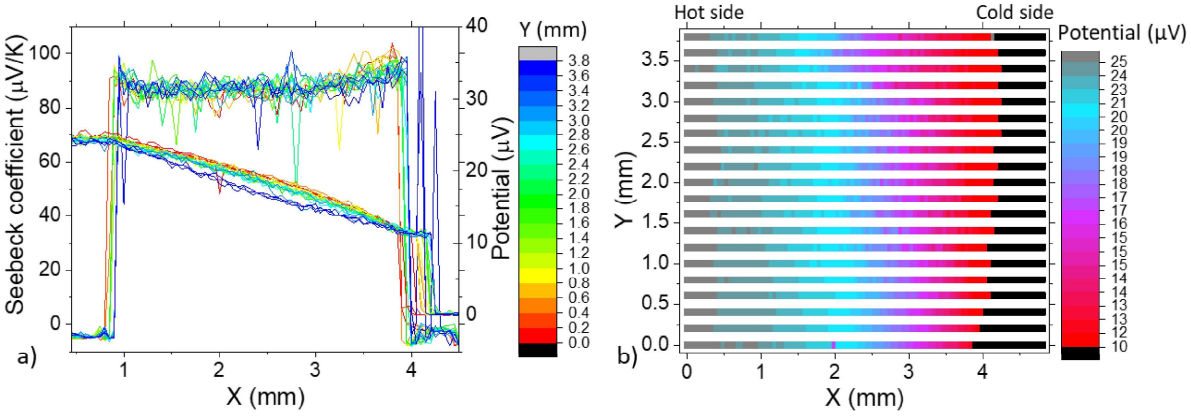

Figure 56 - PSM a) gathered line-scans of electrical potential and Seebeck coefficient, b) 2D mapping of electrical potential, for P1 of mod3 (after APM2). The slight gradient in the Seebeck coefficient (of the order of 5 µV/K in average between the middle and the sides of the leg) was already observed before TEG joining.

Figure 56 shows that the filled crack is disturbing only locally the 1D flow of current and does not affect the Seebeck coefficient in the scanned range. Therefore, it can be assumed that the contact resistivity values of the legs before TEG joining, measured in the PSM, are reliable, and that the uncertainty on CPM calculations is relatively small.

The initial average effective contact resistivity $r_{\mathrm{c,av,eff}} = \frac{(R_{\mathrm{m}} - R_{\mathrm{legs}} - R_{\mathrm{Cu}})A_{\mathrm{n}}}{2N\left(1+\frac{A_{\mathrm{n}}}{A_{\mathrm{p}}}\right)}$ of each module is summed up in Table 18. Neglecting the impact of the shortcut in mod3, there is an improvement from mod1/mod2 to mod3. This is explained by the fact that for mod2 the n-type legs were already cracked at the start of the APM, while for mod3 the resistances of the n-type legs are reasonably low.

Table 18 - average effective contact resistance of each module at the start of their first measurement. The value for mod3 should be considered carefully due to the shortcut in one p-type leg (overestimated predicted resistance) and the property change beyond the SPB model in one n-type leg (underestimated predicted resistance).

TEG	**modDBC**	**mod1**	**mod2**	**mod3**
initial $\boldsymbol{r_{\mathrm{c,av,eff}}}$ (µΩcm²)	13	18	41	2*

For mod1, the drastic increase of inner resistance was observed for $T_{h,m} \geq 300$ °C. Therefore, the next step for mod3 analysis is to put it through a high temperature measurement to see if legs mechanically resist above those temperatures. The measurement (heating step) and CPM calculations are presented in Figure 57. By mistake, the RM was run for $T_{h,m}$ between 250 °C and 450 °C instead of the usual 200 °C and 400 °C, and only the heating data is available. As for mod1, measured at higher temperatures, some change is observed in the n-type legs. The Seebeck coefficient profiles are shown in Figure 58. The CPM calculations in Figure 57 were therefore made considering both profiles after TEG joining and after the measurements, to establish boundaries of where the predicted performance of the module lies, as it is unknown how the materials have changed with temperature during the RM.

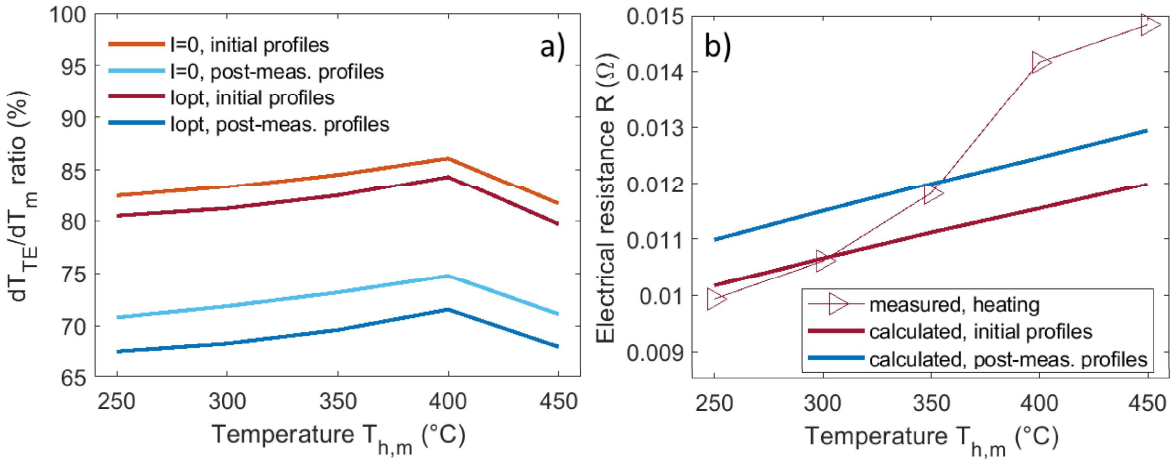

Figure 57 – RM (heating data) of mod3 for $T_{c,m}$=25°C: a) ratio of the temperature difference at the TE legs (calculated) and the temperature difference applied by the heater and the cooling block (measured); b) electrical resistance. For both a) and b) red-hued data is calculated considering carrier concentration profiles of the legs before TEG joining and blue-hued curves is calculated considering carrier concentration profiles after all measurements, shown in Figure 58.

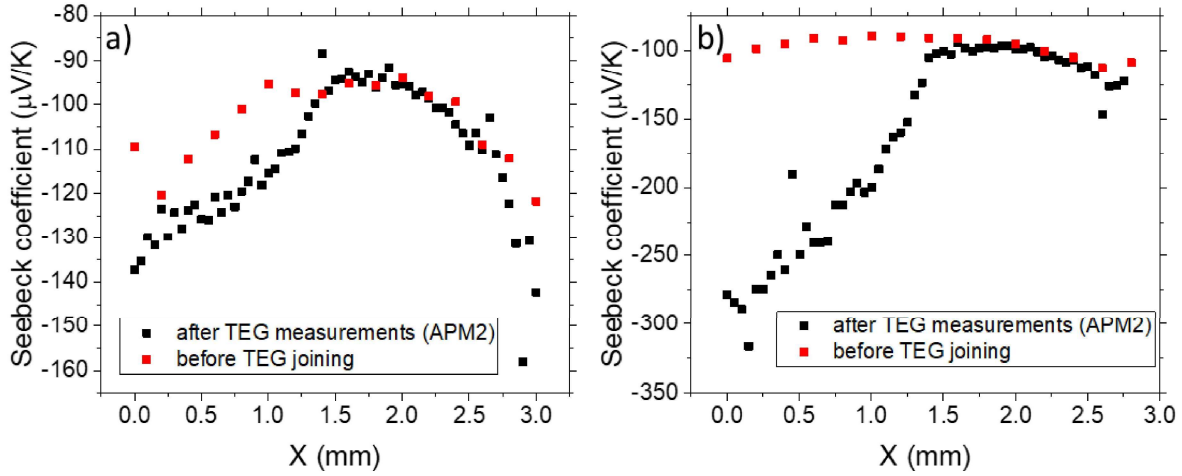

Figure 58 – Seebeck coefficient line-scans before TEG joining and after all TEG measurements (after APM2, see below) of: a) N1 of mod3, b) N2 of mod3.

It can be seen in a) that the trend of the curves changes from $T_{h,m}$=400 °C, but oppositely to what would be expected from n-type degradation. The trend does not coincide with the trend observed in b), which could indicate that they are not explained by the same factors. The value of the ratio between external temperature difference and temperature difference at the TE legs is also lower than for previous measurements: this is attributed to the fact that here, heating data is analyzed, while for previous modules cooling data was considered. During the first heating of the measurement, the coupling is usually not yet optimal, which could explain the larger parasitic losses in Figure 57a.

In Figure 57b, we again see an increase of the inner resistance from $T_{h,m}$=300 °C for mod3. The relative increase between $T_{h,m}$=300 °C and $T_{h,m}$=400 °C is comparable between mod1 and mod3: 7% and 8% respectively. It can be seen that the point at 350 °C remains below the predicted line considering changed material (see Figure 58), therefore that magnitude of increase could be due to material degradation only, but it is unlikely. Is should also be reminded that in this case, the CPM has a larger error due to its negligence of 2D effects, while for shorter and wider legs constriction resistance may play a larger role (higher current density at the side of the legs facing inwards), and locally the shortcut in P1 makes the current density even less homogeneous in this leg.

Mod3 was dismounted and voltage probes were re-wired to make a second APM, in order to determine where the TEG failed. Figure 59a shows the comparison of the total inner resistance of the whole TEG between all three measurements.

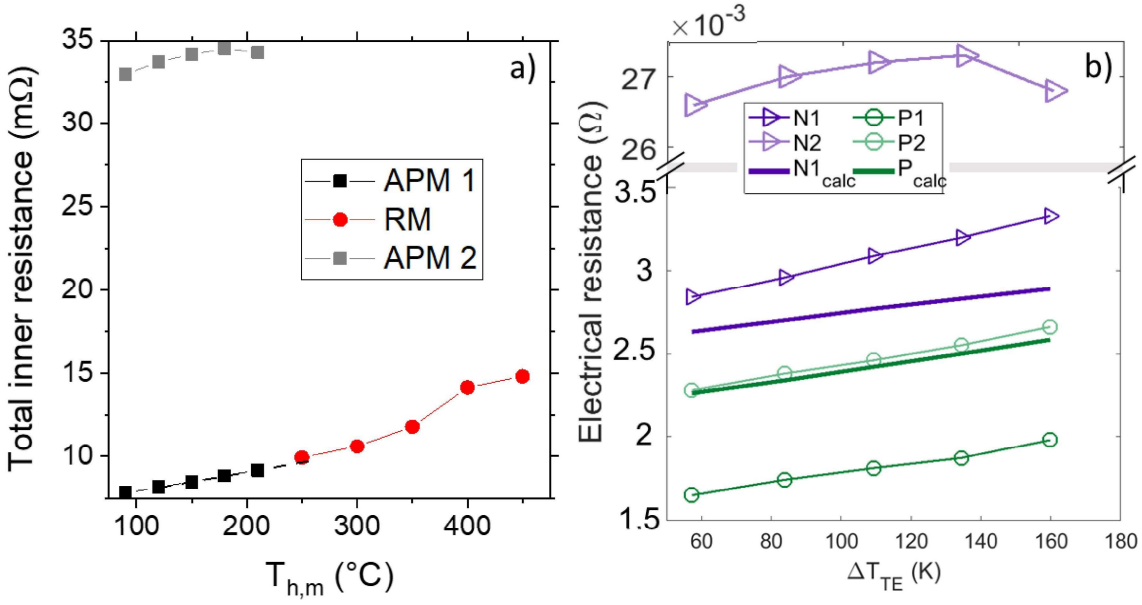

Figure 59 – a) total inner resistance of mod3 between each measurement, in chronological order: APM1, RM and APM2; b) APM2 results of mod3. The predicted N1 value considers the carrier concentration profiles after all measurements, shown in Figure 58; N2 prediction is not included due to the changed properties beyond the SPB model (discussed below). Black dashed line in a) is an extrapolation of measured data.

It can be seen that the total inner resistance remains about the same between APM1 and RM, and drastically increases between RM and APM2. This can be due to the fact that cooling data was not measured in the RM, which means that the TEG was cooled down at a faster rate (continuously from 450 °C to room temperature instead of holding consecutive steps). This faster cooling rate, under load, could lead to thermal stress accumulation and further cracking. It is also plausible that dis- and remounting is partially responsible, as cracks could have been opened and without later getting closed again under pressure.

Figure 59b shows the results of APM2. After APM2, mod3 was dismantled and each leg was measured in the PSM: 2D mappings of N2 are shown in Figure 60, the results of the contact resistivities are presented in Table 19. Then the legs were embedded and analyzed in the SEM, as presented in Figure 61.

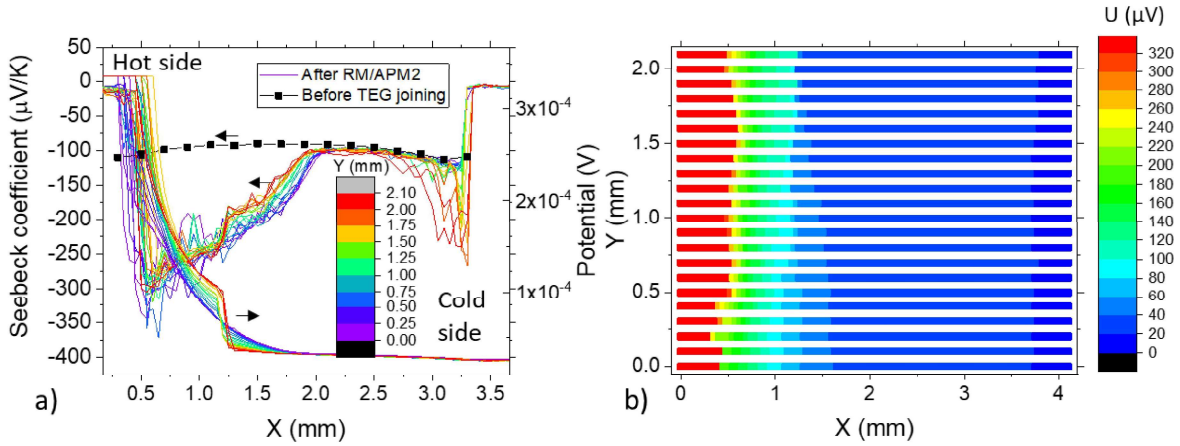

Figure 60 - 2D mappings of a) Seebeck coefficient, b) electrical potential of N2 of mod3 after APM2 measurement. It should be mentioned that the change in Seebeck coefficient observed in a) on the cold side is only significant on the five upper lines of the line-scan. On the other lines, it is similar to the leg pre-TEG joining. It should be noted that the change in potential on the cold side is comparable to leg N1; the seemingly flatness is only a matter of scale.

It should be noted that for N2, in Figure 60, the ratio of the slopes between X = [0.45;0.8] and X = [2.05;2.65] (~ 0.02) differs by a factor > 2 from the ratio of the carrier concentrations (~0.09) obtained with SPB considering the Seebeck coefficient of those portions (respectively $n = 1.8 \cdot 10^{25}$ m^{-3} for α_{ref} = -335 µV/K and $n = 2 \cdot 10^{26}$ m^{-3} for α_{ref} = -116 µV/K). This means that the mobility is not constant on the changed portion of the leg, contrarily to the case seen in section 6.1, and that the SPB model cannot be trustfully applied to this leg. The reasons for this difference will be discussed below. The electrical resistivity of the hot side portion of N2 is in reality higher than predicted, therefore the blue line in Figure 57b should be considered with caution.

The APM2 shows dramatically high resistance for N2 (while for APM1 both n-type legs had similar resistances), which is explained combinedly by the crack observed in the TE bulk in the potential lines (Figure 58), the general increase of bulk resistivity beyond SPB and the contact resistivity measured at the hot side in the PSM (Table 19). In the SEM, a dramatic reaction at the hot side interface can be seen. It was likely triggered by the melting (slightly above 200 °C) of the solder that was used to attach the additional probes for APM1 and could not be removed completely before RM. The reacted area is ~ 0.3 mm large and contains large voids. Although no crack can be seen, it can be suspected that the phases formed are electrically resistive, given the high absolute Seebeck value on the hot side portion, or that more voids were created at the interface deeper in the bulk, which would explain the high contact resistivity measured at this interface. This also explains the very large change in Seebeck coefficient observed on the hot portion of the leg (-250 to -350 µV/K), which goes beyond what was observed in complete Mg evaporation studies ([116] and corresponding Supplementary Information). Many counter-

doping defects could have formed due to the solder elements diffusion in the TE material, which degraded the material even more than what was previously observed. The crack detected in the potential line in Figure 58 was however not seen in the SEM; it could lie deeper in the material.

Table 19 - PSM measurements of the electrical contact resistivity between the TE material and the Al metallization $r_{c,m}$, between the TE material and the Cu bridge $r_{c,tot,m}$ after TEG measurement for mod3, and calculation of the effective electrical resistivity $r_{c,eff} = (R_{leg,m} - R_{TE} - R_{Cu})A$ from APM2 for each leg. The values shown are obtained considering j_{TE}(see section 2.2.3, equation (39)), values obtained using j_{PSM} are not displayed for better readability, as both values are in the same order of magnitude for all cases. The standard deviations are also not displayed in cases where they are lower than the average value by a factor of 2, for better readability. N2 is not included due to its non-constant mobility.

	N1 (hot/cold side)	**P1 (hot/cold side)**	**P2 (hot/cold side)**
$r_{c,m}$ (Al-TE)	5 / 2	12±11 / 38±87	8 / 5
$r_{c,tot,m}$ (bridge-TE)	6 / 3	8±7 / 154±141	10 / 5
effective $r_{c,eff}$ (for T_h=90°C to T_h=150°C)	109 to 135	-113 to -108 (non-monotonous)	18 to 30

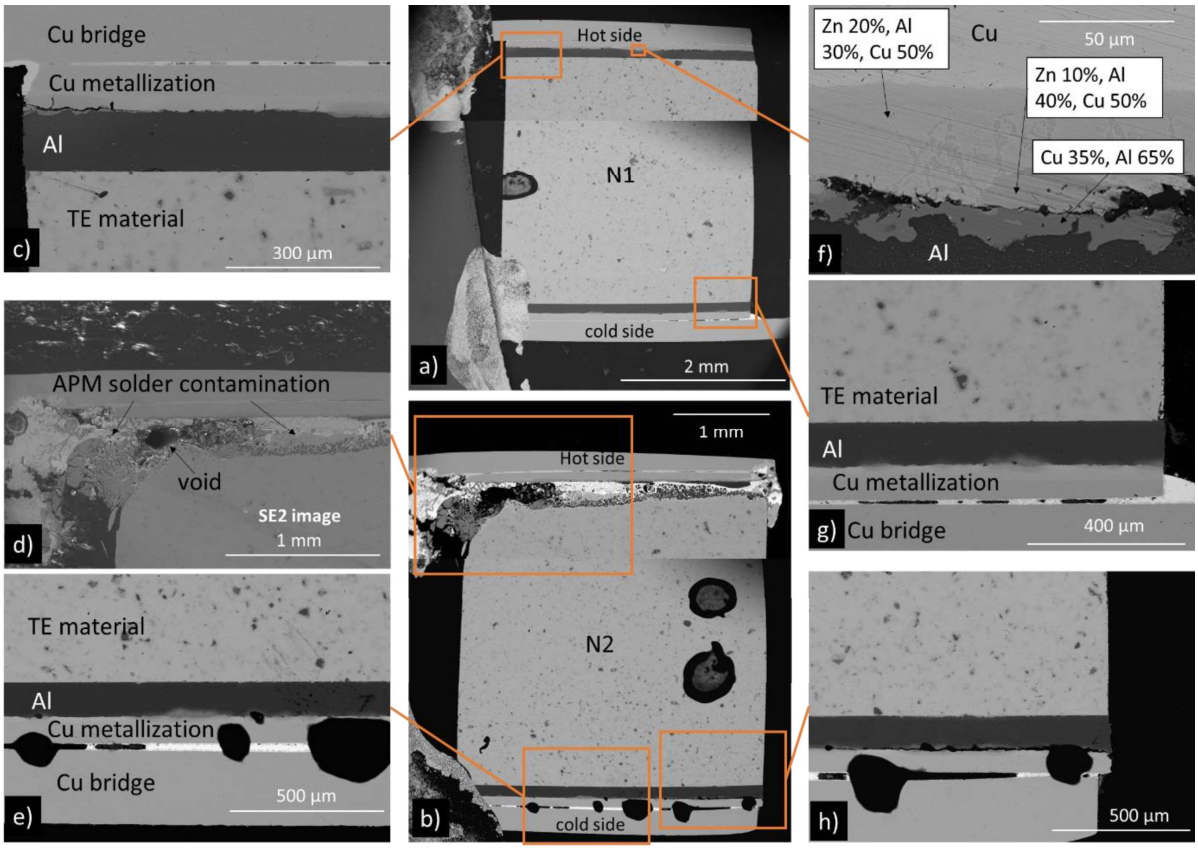

Figure 61 – SEM images of mod3 after all APM/RM measurements were completed: a) N1, b) N2, c) zoom-in of hot side interface of N1, d) zoom-in of hot side interface of N2 (secondary electrons image), e) zoom-in of center cold side interface of N2, f) zoom-in of hot side Al-Cu metallizations interface of N1 (the compositions are in at.%), g) zoom-in of cold side interface of N1, h) zoom-in of edge of cold side interface of N2. All images are obtained with backscattered electrons except d). For this module, Zn foil (20 µm) was inserted between Al and Cu during contacting. The large reacted area on the hot side of N2 is due to solder contamination (from the APM probes).

It can be additionally noted, from Figure 61a,c,g, that the Al-TE interfaces of N1 show no sign of degradation, either mechanical or chemical.

The effective contact resistance of N1 deduced from the APM2 increased compared to APM1, while in the PSM the effective contact resistance from TE material to Cu bridge remains very low (< 10 μΩcm²) and no crack is observed at the interface. This could again be explained by a crack, deeper in the material, closing in the PSM due to the applied pressure (reduced $r_{c,tot,m}$ in the PSM). It can be concluded that the properties of the electrical contacts depend on pressure and the specific mounting situation and are therefore not really reliable.

A crack can be seen at the edge of the Al-Cu interface in Figure 61c, which seems too localized to have a significant impact on electrical conduction. For this module, an additional Zn coating (20 μm thick) was inserted between Al and Cu during leg metallization because it was suspected that the coatings on the outside of the Al foils were slightly damaged, hence the larger reaction layer than for other modules. This could be the reason for cracking at this location, as more (Al,Zn,Cu) compounds, potentially brittle phases, are formed. A similar case is observed for the cold side of N2: a crack can be seen on the edge of the leg between Al and Cu (in Figure 61e-h, stops at a third of the width) but the contact resistivity measured on this side with the PSM remains low. It can also be noted that, contrarily to previous open TEGs, on N1, the crack is located on the hot side in Figure 61c and not the cold side.

The resistance of P2 remained similar between both APMs, and the contact resistivity values obtained with the PSM and with the APMs are quite consistent. However, for P1 the resistance decreased between APM1 and APM2. This could be a sign of a worsened shortcut brought by the Zn-filled crack, likely due to the high temperature RM. The PSM values show slight asymmetry, with a higher contact resistance on the cold side of the leg, and also an increase of the contact resistance between TE and bridges compared to between TE and Al. Visual explanations for this result (crack, partial delamination) were not found in the SEM investigations. This repeating pattern of inconsistent observations (different contact resistivities from PSM and TEGMA and/or missing cracks in the SEM) raises a clear need for improvement in the current methodology.

From the mod3 experiment, it can be deduced that increasing the legs cross-section was effective in preventing initial cracking of the legs (below 300 °C). It also seems to increase the TE-Al interface strength, as cracking did not occur at this location for mod3 but rather at the Al-Cu interface, although this could also be due to the addition of the Zn foil. A similar TEG

should be built (without Zn foils, with cleaning the solder left after APM) and measured (at $T_{h,m} \leq 400$ °C and with slower, measured cooling steps) to draw more reliable conclusions on the mechanical strength of wider legs above 300 °C.

b) N-type material change

After the various TEG measurements, the mod1, mod2 and modDBC were dismantled and a mapping of the Seebeck coefficient of the n-type legs was performed. The results are shown in Figure 62 and the embedded legs in Figure 63. Several PSM devices are available at DLR and thus there can be some device-to-device variation for the measurement of the same sample. Therefore, a reference sample for each module was respectively scanned with the same PSM, for better comparability. Both legs of each module were scanned with the same device. The legs of mod3 were not included in this figure as they were accidentally measured at $T_{h,m} = 450$ °C and there was solder contamination.

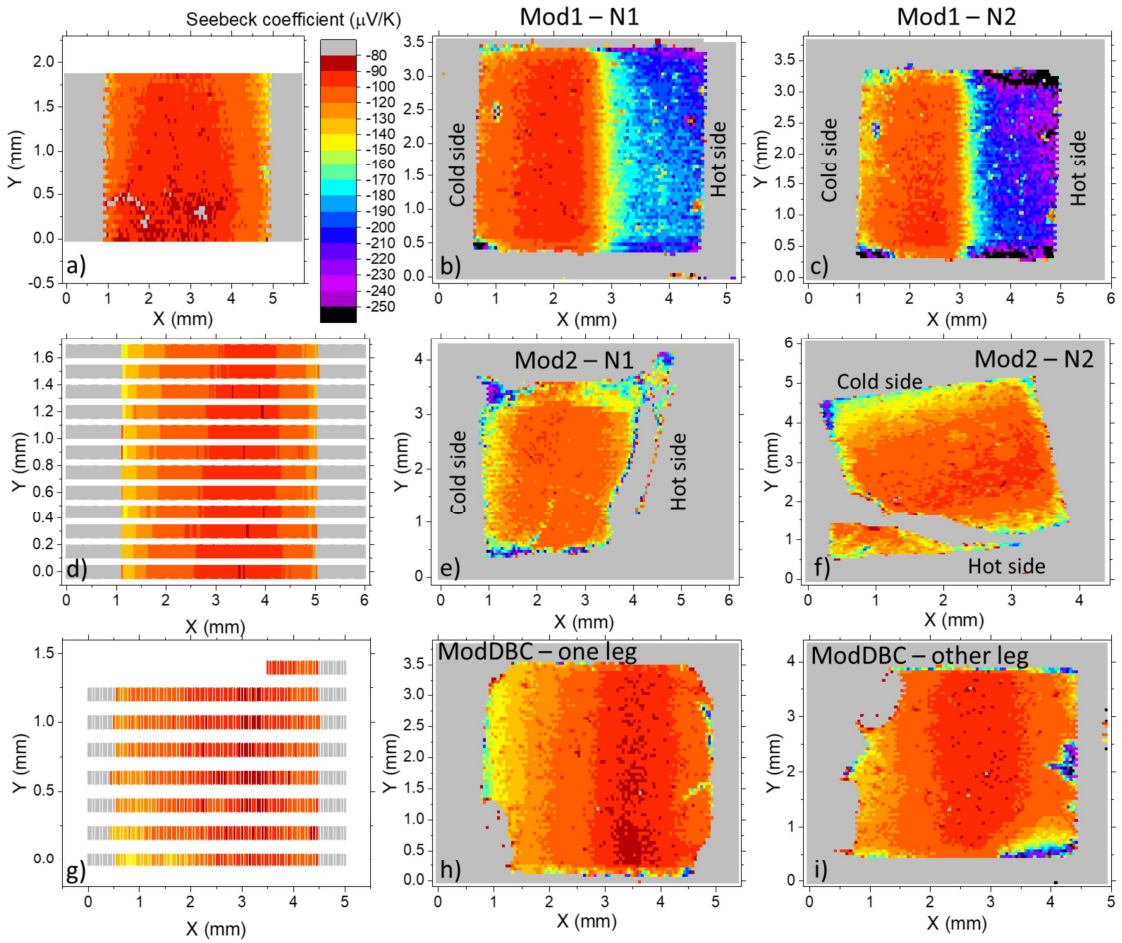

Figure 62 - PSM mapping/linescan of the Seebeck coefficient of: a) functionalized leg similar to the ones used to build mod1 and mod2 before TEG joining (PSM reference for b) and c)); b) mod1- N1 after RM+APM; c), mod1 – N2 after RM+APM; d) functionalized leg similar to the ones used to build mod1 and mod2 before TEG joining (PSM reference for e) and f)); e) mod2 – N1 after APM; f) mod2 – N2 after APM; g) as sintered pellet of the powder batch used for the legs of modDBC (PSM reference

for h) and i)); h) and i) mixed n-type legs of modDBC after several RMs. The legs in e) and f) are broken and embedded (see Figure 63), which is why gaps are seen. a), b), c) and d),e),f) were measured with a different PSM. d) and g) were scanned with a coarser mesh, which is why the other figures are more detailed.

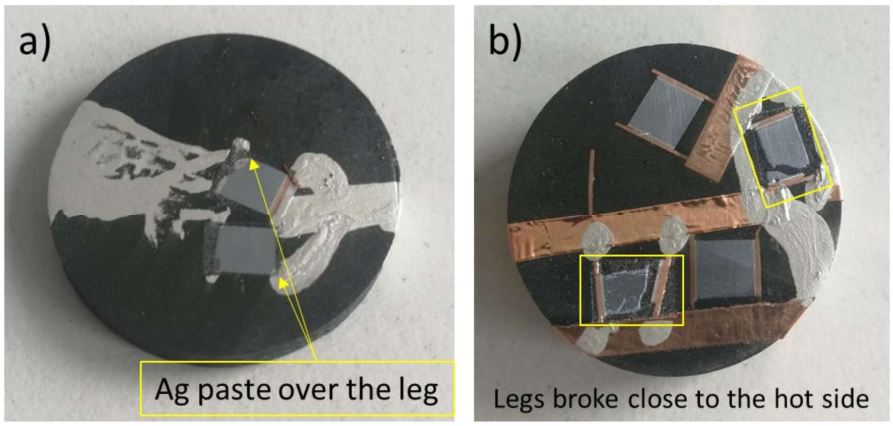

Figure 63 - a) modDBC embedded n-type legs, b) mod2 embedded legs

As previously seen in Figure 46, the legs of mod1 have significantly changed, N2 even more than N1, while the legs of mod2 and the DBC-based TEG are quite unchanged. In n-type $Mg_2(Si,Sn)$ legs, there are two known mechanisms which can lead to a loss of carriers: Mg loss (increasing the number of Mg vacancies) or counter-doping foreign atom diffusion [1, 2, 116, 121]. Mg loss can occur due to evaporation, which is usually studied in annealing experiments, but it could also occur due to Mg diffusion in the metallization, out of the TE material. Although both mechanisms are thermally induced, it was shown that Mg evaporation did not significantly occur for durations of 40h at 380 °C under vacuum (< 5% change of the electrical conductivity), while a significant, almost linear change was observed at 430 °C [116]. Mg evaporation would be suspected in Figure 62 if the Seebeck coefficient was more altered on the hot side edges of the legs, since Mg would evaporate from the part of the hot material which is in contact with the outside atmosphere. Such features are seen in the legs of mod1 and in leg N1 of mod2, which indicates Mg evaporation, however given the large-scale change within the bulk of the leg, it is unlikely that it is the main driver of the leg alteration mechanism. Moreover, the calculations of $\Delta T_{TE}/\Delta T_m$ presented in Figure 47a showed that the n-type legs seemed to start changing significantly right above 300 °C, as the trend of the curve inverts, while Mg loss should mostly occur at higher temperatures. Mod1 was measured for one cycle with $T_{h,m}$ going from 200 °C to 400 °C (RM), and then for one cycle with $T_{h,m}$ going from 90 °C to 150 °C (APM), while mod2 was only measured for one cycle with $T_{h,m}$ going from 90 °C to 140 °C (APM). This would explain the difference between the legs of mod1 and mod2, which was kept below 300 °C. This case is an example where the PSM is a very valuable tool, as it allows quite fine 2D mappings of the Seebeck coefficient.

A local change is also seen at the edges on the cold side for some legs. Given the punctual shape of those areas, they could rather be explained by local solder contamination which could have happened during the TEG assembly: as the solder (Sn) melts while pressure is applied, it is possible that small drops are squeezed out on the sides of the legs and that the drop gets in contact with the TE material.

When modDBC was dismantled, it had been measured for a total of 5 cycles with T_h going from 200 °C to 400 °C (only two were shown in section 5 since the following cycles were made for further internal tests), therefore, a similar or larger change than mod1 legs would be expected. In the Supportive Information, it is also shown that the change in n-type legs was minimal after the two cycles reported in the paper, like in Figure 62h and i.

The main difference between those two TEG is the presence or absence of cracks at the hot metallization. Cracks in modDBC would have impeded diffusion between the TE material and the metallization, while diffusion could have happened in mod1. This would explain the difference in material change despite the similar temperature exposure. This is also highlighted in mod3 in Figure 60a (red lines), where the drop of potential at x = 1.2 mm, likely a crack, coincides with a sudden change in the Seebeck coefficient.

This analysis is however questioned by the leg N1 of mod3, which was exposed to temperatures between 400-450°C, does not present cracks at the Al-TE interface but does, anyway, not show such a significant change in its Seebeck coefficient profile. One possibility is that there is a crack deeper in the leg, that was not visible in the SEM investigation, while being closed by the pressure in the PSM and therefore not detected electrically. It is also possible that there are other parameters beyond our current knowledge and further investigation (on single legs) is needed to understand the mechanism behind the material change. Oppositely, the observations made on this leg confirm that it is unlikely that material degradation is only due to Mg evaporation.

In the search for long-term stability of the TEG, implementing a diffusion barrier could therefore be necessary. In order to select diffusion barriers candidates, the diffusing species must be identified.

EDX linescans were performed along the legs N1 and N2 of mod1, but no composition gradient was detected, similarly to other works where changes in properties were observed [2, 5]. This is explained by the small number of foreign atoms necessary to induce a visible change in the Seebeck coefficient, far below the amount detectable by EDX (~1 at%).

It was shown in section 4 that some change in carrier concentration may occur due to Zn diffusion, which is why the functionalized legs show a gradient even before TEG-making. The diffusion coefficient of Zn in $Mg_2(Si,Sn)$ is unknown, however it can be seen on the Al-Zn phase diagram that Zn has a very large solubility in Al between 200°C and 400°C [164], which would indicate that over time, Zn could preferentially diffuse into the Al layer than inside the TE material. Furthermore, the contacting of Zn-coated foils is made at higher temperature (475°C for 10 min, Zn is liquid), with a resulting gradient in Seebeck coefficient showing values of ~ -120 µV/K close to the metallizations. After the TEGMA measurements (~ 30 hours with T_h between 300 °C and 400 °C), the Seebeck coefficient on the changed portion of the leg is between -160 µV/K and -200 µV/K. If Zn diffusion was the main driving factor for the TE material's alteration, a stronger change could be expected directly after contacting, as diffusion of liquid Zn would be faster. For Ag in Mg_2Si [1], a diffusion length of 0.1 mm would be reached for 10 min at 475 °C (contacting step), 0.07 mm for 11h at 300 °C (intermediate TEGMA measurement) and 0.3 mm for 11h at 380 °C (highest temperature step of the TEGMA, considering the temperature applied at the TE material). 0.1 mm and 0.3 mm diffusion lengths would be noticeable with the measurement tools available. Moreover, in comparison to Ag, Zn has a smaller ionic radius and should therefore be a faster diffuser. Furthermore, those temperature conditions are very different from Ag melting point (962 °C), while they are very close to Zn melting point (420 °C), which could enhance Zn diffusion even more. It cannot be guessed how much the difference in the time scales of the thermal steps weighs in the diffusion behavior in our case but it is clear that Zn diffusion cannot be dismissed as origin of the material change.

Cu is known to be a fast diffuser, however considering $D_0 = 5 \cdot 10^{-5}$ m²/s and $Q = 130$kJ/mol as the parameters for the diffusion coefficient of Cu into Al (taken from [165]), the diffusions lengths for the contacting step (10 min at 475 °C) and for the TEGMA measurement (considering 10h at 380 °C) would be 7 µm and 12 µm, respectively. The Al layer which is between Cu and TE is ~100 µm thick, so it is unlikely that Cu has reached the TE material at the end of mod1 building and analysis.

The possible influence of Al diffusion into $Mg_2(Si,Sn)$ was discussed in section 3. It was found unlikely that Al was altering the carrier concentration in the TE material, as no gradient was observed after the contacting experiments.

Mg, however, is a small and very mobile atom. The Al-Mg phase diagram shows a solubility of ~ 10 at.% of Mg in Al [166] and it is known that only a small fraction of Mg leaving the material can make a large difference in the Seebeck coefficient of $Mg_2(Si,Sn)$.

To determine which species are involved in the detrimental diffusion mechanisms in functionalized legs, comparative annealing experiments involving different material layering could be done (only TE, TE with only Zn, TE with only Al, TE with only Cu). Some of those configurations were already studied in previous work [4, 35], however, the analysis of the experiments was limited by the coincidence with Mg evaporation occurring due to the lack of an efficient protective coating. The search for such a coating is underway and is also a major milestone in the development of stable $Mg_2(Si,Sn)$-based TEG [167-172]. Some electromigration phenomenon could also be occurring, in which case a difference between annealing experiments and TEGMA measurements would be observed for similar legs in similar time/temperature conditions.

6.2.4. Summary

Several TEGs were built with an open design and were characterized. Although no crack was observed directly after TEG joining with the open design, contrarily to the DBC-based design it appeared that the change of design was not sufficient to avoid mechanical failure due to thermal stress arising from temperature gradients along the legs during TEG measurement (hot side/cold side).

The origin of this cracking was systematically tracked using additional voltage probes in order to individually obtain the resistance of each leg composing the TEG. This new measurement technique allowed to identify that cracking in the n-type legs, specifically, was the origin of the increase in inner resistance.

The main diverging parameter between the n-type and p-type leg, in terms of the influence on mechanical behavior, was geometry. Indeed, n-type and p-type $Mg_2(Si,Sn)$ have fairly similar mechanical properties, and the legs are metallized with the same material layers, following the same process, but the p-type cross-section is significantly larger. Therefore, a last open TEG was built with wider legs to test whether this strategy would be effective to increase the mechanical strength of the n-typed legs. This strategy showed improvement in the mechanical behavior of the TEG, since no increase of the electrical resistance was observed with a hot side temperature remaining below 300 °C, while for previous modules it was observed from the very start of the measurement. These encouraging results suggest that tuning the leg geometry could be a solution for mechanically stronger TEGs.

The analysis of the results of this work showed some differences between the contact resistivities deduced from the TEGMA and measured in the PSM, which indicate a strong dependence of this parameters on pressure and/or leg positioning. Furthermore, in case of a large measured contact resistivities, cracks were not necessarily observed on the corresponding areas in the SEM, while chemical contact degradation is unlikely. An important point highlighted by this work is therefore the need for a more precise methodology to precisely investigate leg degradation.

7. Chapter 7: Conclusion and Outlook

7.1. Conclusion

When the work presented in this thesis was started, $Mg_2(Si,Sn)$ was a well-investigated TE material class in terms of properties optimization and understanding [63, 72, 81, 116, 121-123, 129]. However, research on the next steps in the development of a TEG made of these materials was scarce. Moderately satisfying electrodes were tested, the best option being Ag which showed low contact resistances but altered the properties of the n-type material [1, 2], while other tested electrodes generally led to cracking or delamination [2, 3]. Additionally, no fully $Mg_2(Si,Sn)$-based TEG was reported in literature, meaning that no research on their manufacturing, mechanical behavior, performance characterization nor performance modelling was available.

In this thesis, we paved the road to such a $Mg_2(Si,Sn)$-based TEG, by addressing various issues such as electrode selection and development, as well as TEG manufacturing, characterization and modelling.

In section 3, it was first found that Al was a promising electrode for $Mg_2(Si,Sn)$, as published in [4]. Al was identified as interesting candidate for its CTE and melting point which were compatible with $Mg_2(Si,Sn)$, and for its ductility which can help accommodate mechanical stress at the interface with the TE material. Upon experimental testing, no cracking nor delamination occurred contrarily to previously reported electrodes, which indicates favorable thermomechanical compatibility and contact resistivities below the set threshold of 10 $\mu\Omega cm^2$ were measured, while no change in the TE materials were observed. The interface directly after contacting is free of visible reacted areas, which start to grow with annealing without increasing the contact resistivity. Al was therefore the first and so far only electrode which combined mechanical and chemical stability for $Mg_2(Si,Sn)$, which is a very important and necessary discovery to build long-lasting and performant TEG with this material.

The main drawback of using Al as electrode for $Mg_2(Si,Sn)$ was found to be the lack of reproducibility of the samples with respect to the observed electrical contact resistances. While some samples had satisfyingly low contact resistivities, significant asymmetry in contact resistivity values between both interfaces of the samples was frequently occurring. In section 4, published in [5], this asymmetry was found to originate from the dicing step. As the dicing step is unavoidable in the current leg fabrication process (direct bonding of metallic foil), finding a way to avoid the increase of the contact resistivity on one of the sides was necessary.

As Al is known to be very prone to oxidation, ion etching the Al foils and sputtering a layer of oxidation barrier was tested before contacting. It was found to be an effective strategy to maintain symmetrically low contact resistivities after the dicing step. Zn was chosen and used as a "sacrificial" oxidation barrier material due to its low melting point and high solubility in Al. It was meant to act as a solder by melting during the contacting step, after which protecting the Al from oxidation was no longer needed. The diffusion of Zn led to the appearance of a gradient in the Seebeck coefficient from the interfaces towards the middle of the n-type leg (similarly to Ag) while no effect was observed on the p-type material. Potential interaction of Zn with $Mg_2(Si,Sn)$ was investigated using DFT point defect calculations, which allowed to identify a plausible interaction mechanism (Zn diffusion and substitution) which explains the experimental results. The use of Zn was kept in the following work as a temporary technological solution to move forward in the steps of TEG development.

In the study reported in section 5, the third ever full $Mg_2(Si,Sn)$-based TEG was build and characterized [6] (a single one was reported at the start of the thesis work [127]). We reported the first efficiency measurement of such a module and measured a high power density, significantly higher compared to the first similar module reported before the start of this work [127]. Our TEG performance scales with other silicide-based TEG (not Mg_2X-only) already reported in literature [84, 128] despite its mechanical degradation. Two measurement cycles were performed and, besides some changes in the first heating discussed below, the TEG performance stayed relatively stable. The measurements were compared to and validated with theoretical predictions using CPM, showing measurement-calculations deviations below 5% for current at maximum power and maximum power. It was found that both efficiency and power output could be realistically increased by 30% by improving the mechanical stability of the module. Indeed, an increase of the inner resistance was observed upon the first heating, very likely due to thermally induced stress which led to cracking. This thermal stress was imputed to the Al_2O_3 plate of the DBC substrates used in the TEG design.

This CPM analysis presented in section 5 was done assuming a homogeneous n-type material, neglecting the inhomogeneity induced by Zn diffusion observed in section 4. An innovative analysis method combining experimental carrier concentration profiling and the SPB model to improve the CPM/continuum theory was implemented in section 6.1, which modified the conclusions previously drawn. With this upgraded material transport model, the deviation between calculations and measurement of the heat flow increases above the measurement uncertainty. The reason for the observed differences between model and measurement remains

unclear at this stage. The conclusions on crack formation remain however relevant, and became the focus of the following work.

It was hypothesized in [6] (section 5) that the cause of cracking was the thermomechanical stress brought by the Al_2O_3 plate of the DBC substrates. Therefore, an open module design with only Cu bridges was tested in section 6.2. Comparison between measured and calculated properties of mod1 and modDBC indicated crack formation as one source of discrepancy but were not sufficient to identify the origin of these cracks. For this reason, a novel measurement approach was developed using additional voltage probes, soldered in order to monitor the resistance of each leg during the measurement and locate more precisely the place of degradation. It was observed that the n-type legs were always the elements where resistance increased compared to predictions, even if keeping the hot side temperature below 200 °C, while the p-type legs matched their predicted values. As mechanical properties, metallization layers and contacting processes are similar for both materials, it was hypothesized that the main factor which determined the cracking behavior was the leg geometry. Another open module was built with wider legs and similarly measured. It was newly found that increasing the cross-section of the legs partially solved the problem, as no degradation was observed if the hot side temperature remained below 300 °C. This last experiment indicates that the TEG making process which was developed in this thesis works, at least initially, and that monitoring the resistance of each leg is a very valuable technique in the development of a TEG.

Lastly, our work on contacting and TEG building and characterization pointed out very good chemical and mechanical stability of the p-type legs in the first few measurement cycles, as no cracking, contact degradation nor change in TE properties was ever observed with the p-type material.

Overall, in this work, we combined many different experimental characterization techniques (SEM, EDX, TE properties measurement, PSM for contact resistivities and 2D-mapping of Seebeck coefficient) and modelling techniques (DFT defect calculations, SPB model, CPM) to gain understanding on how to successfully select and contact an electrode to obtain functionalized legs, to build, characterize and improve a working TEG.

7.2. Future work

This worked further paved the way towards fully $Mg_2(Si,Sn)$-based TEG. However, some work remains to be done to fully optimize those TEG and ensure high, long-term performance.

a) Material stability

A key improvement lies in the n-type material stability investigation and/or in the search of a proper coating, first to ensure long-term TEG performance and secondly to investigate diffusion mechanisms between metallization and TE material with more clarity. The search for a compatible coating is underway, see e.g. [167-172], while the idea of optimizing a Mg-poor n-type material, less prone to properties deterioration due to Mg loss, is being considered. One question which remained in section 3 ([4]) was whether material degradation upon annealing was due to Mg evaporation (very likely) or stable, counter-doping Al-related defects formation (less likely). Solving the Mg evaporation issue by the use of a coating or a better suited stoichiometry would help to clear out this uncertainty. Similarly, the question as to which element is responsible for the observed n-type material degradation after TEG measurements could be answered in such conditions. Moreover, it is possible that a Mg-poor n-type $Mg_2(Si,Sn)$ material would be less easily "polluted" by foreign elements, which would increase its stability considering the multi-components design of a TEG.

b) Contacting

A second key improvement lies in the further optimization of the contacting step:

- Zn was found to be an efficient oxidation barrier for Al foils, but showed the disadvantage of altering the n-type TE properties. It would therefore be beneficial to find a replacement for the Zn layer. DFT calculations could be used to evaluate potential candidates, by predicting stable counter-doping defects [1].
- Instead of using the direct bonding between a metallic foil and a TE pellet to obtain functionalized legs, Al and external Cu metallizations could be directly sputtered on the TE material. This would have several advantages such as not needing an oxidation layer, as the Al would be sputtered on etched TE material under inert atmosphere, and likely not requiring pressure, which could avoid vertical cracking in the legs as observed for mod3 in section 6.2. It would also allow to obtain a large number of functionalized legs in one process. This option was not studied in this work because the dicing of the legs would have had to be very precise while necessarily made in ethanol. The facilities available in our laboratory did not allow to fulfill both criteria. The evaluation of the contact resistivity between Al and the TE material could be challenging due to the resolution of the PSM (50 µm), however the sputtered Al-Cu layers could be soldered to a thicker Cu foil (as they would be in a full TEG) and the overall resistance between the TE material and this external Cu foil could then be monitored and optimized.

Depending on the element responsible for the further degradation of the n-type legs during the TEG measurements, which remains to be identified, a diffusion barrier layer should also be implemented to protect the TE material. Its nature and location would depend on the element that it is intended to block.

c) Cracking

The third key of improvement is the understanding of the cracking behavior in modules, in particular open modules. First, a replicate of mod3 should be remade, using optimal n-type powder and ensuring that no shortcut is present in any leg, to validate the preliminary conclusions drawn in section 6.2. If resistance still increases above 300 °C for this TEG, further optimization and understanding will be required. If it remains that the p-type legs are unaltered while the n-type mechanically degrade even with increasing their respective cross-sections, various hypothesis can be made:

- Zn (or another element) diffusion locally changes the mechanical properties of the n-type material, making it more prone to cracking than the p-type leg. Mechanical testing of Zn-doped material could be made to check this hypothesis, or a replicate of mod3 with homogeneous n-type legs.
- The origin of the different behavior between both types originates from the difference in cross-section itself: the p-type has a larger cross-section, which makes its legs sturdier and dominating the mechanical behavior of the TEG (pulling/pushing the n-type legs).

These hypotheses could be tested by making a replicate of mod3 with only p-type legs (two wider, two thinner, same geometries as mod3). The performance testing of this TEG would be useless, but electrical resistances of each leg could still be measured. If the thinner p-type legs crack, it would mean the cross-section difference is the origin of the problem; if no leg cracks, it would mean that the n-type material is more brittle. A further way of relieving thermal stress could be to use thinner, more flexible Cu bridges, but this raises the issue of mechanical integrity of the TEG (ease to manipulate) and would increase the inner resistance of the TEG.

Besides increasing cross-sectional area, significantly increasing leg length can allow for more bending of the material which could relieve some of the thermal stress, it may therefore be an alternative strategy. It was successfully followed by Goyal *et al*. [128], who did not report any cracking for a similar module design and materials, with much longer leg length compared to their cross-section.

Further mechanical experimental characterization of materials and further TEG mechanical FEM simulation are nevertheless required for deeper understanding of those matters.

An open question left from section 6.2 is the step at which cracking happens. A lacking measurement in the chain of events is the inner resistance of the TEG before applying the pressure and the temperature difference in the TEGMA, in order to understand if the cracking in mod1 and mod2 originated from the joining step or from the mechanical/thermal loadings. Lastly, the influence on cracking of heating, cooling rates and holding times in the TEGMA should be investigated, to understand if mod3 likely cracked during the cooldown of the RM or in the mechanical/thermal loadings of the next measurement (APM2).

d) TEG manufacturing

The soldering process could be investigated and optimized. In this work, Sn foils were chosen due to their known chemical affinity with Cu. Sn has a melting point at ~220 °C while the TEG were measured with a hot side temperature between 100 and 400 °C. The fact some legs cracked at the hot side shows that solid compounds were indeed formed, because if the Sn solder liquefied during the measurement, this would have allowed the legs to slide and prevented cracking. Nevertheless, Sn could be mechanically or chemically suboptimal, and a solder with a melting point between 400 and 500 °C could be more beneficial at the hot side due to its higher chemical stability. This field remains to be more thoroughly investigated.

Semi-open modules, with DBC at the cold side, could also be tested as they would have a better mechanical integrity as fully open modules. Cracking post-TEG joining would however need to be monitored, or cold-side joining would need to be conducted at lower temperatures.

e) TEG characterization and modelling

It was seen in section 6.1 that the heat flow measurements for our small TEGs did not agree with the predictions and are possibly prone to significant measurement uncertainties. An important step for further progress would be to build measurement tools (heating block, HFMs) adapted to such small geometries.

The APM technique could be optimized by using soldering techniques on the hot side which can withstand temperatures above 200 °C. This would allow to combine high temperature performance measurement and APM and avoid the mounting/dismounting operations.

In DLR, a measurement system allows the simultaneous determination of all of TE properties and figure of merit [173]. It allows to measure samples that correspond to our legs' geometries,

unlike the HTSσ, and it could be used on single n-type legs to measure their average properties which could then be compared to the average obtained with the carrier concentration profiling and the SPB model.

After mechanical and chemical stability of the TEG is achieved, the reliability of the CPM should be re-assessed. Indeed, in section 5 ([6]) the calculations of the current at maximum power, heat flow at maximum power and maximum power were done using the measured inner resistance value instead of the predicted one, due to the crack preventing a precise, quantifiable prediction. Replicating those calculations with a quantifiable prediction of the electrical resistance for a non-cracked TEG would give a better idea of the precision of the CPM for our TEG.

Overall thermal resistance of the coupling layers between the TEGMA and the TEG (graphite, thermal paste, ceramic plates, etc.) could be evaluated by replacing the TEG by an Inconel block and measuring the temperatures along it with thermocouples. This data can then be used to verify the temperatures at the TE legs obtained with the measured open-loop voltage and the input effective Seebeck coefficient. Finally, this data would also allow to better evaluate the assumption of symmetrical losses of temperature between hot and cold side couplings, although this would be more reliable once the stability and/or homogeneity of the n-type material is ensured.

In the Table 20 below are summarized the coupling layers used for each TEG measurement presented in this thesis and the corresponding ratio between the temperature difference at the TE legs and the external temperature difference (at the heater/HFM). By comparing the two measurement of mod1, it can be seen that, obviously, a thicker ceramic plate leads to a larger temperature loss. Comparing the APM1 ($T_{\mathrm{h,m}}$ below 200 °C) and RM ($T_{\mathrm{h,m}}$ between 250 °C and 450 °C) of mod3, for which at the start the inner resistance was similar and that have the same coupling layers, shows the increase of temperature loss proportionally with the applied temperature difference. This can be counter-intuitive, as the thermal contact resistances could rather be decreasing with increasing temperature due to radiation. The comparison of APM1 and APM2 illustrates the influence of (likely) cracks at the TE/metallization interfaces, which increase the temperature difference at the TE legs. Comparing the three RM measurements which were done at the same temperature differences, it can be seen that, contrarily to what could be expected, the much thinner Al_2O_3-coated Al foil does not significantly contribute to decrease the temperature loss. The effects of the coupling layers on $\Delta T_{\mathrm{TE}}/\Delta T_{\mathrm{m}}$ are however

difficult to reliably analyze, given the variously cracked (or non-cracked) states of most TEGs at the start of their measurement.

Table 20 - Coupling layers of TEG measurements and ratio between the temperature difference at the TE legs and the external temperature difference (at the heater/HFM)

TEG	Measurement	Coupling (layers that differ)	$\Delta T_{TE}/\Delta T_{m}(I=0)$ (%)
modDBC	RM	No thermal grease (DBC)	87 (end of first cycle)
mod1	RM	Al_2O_3 plate (250 µm) (hot+cold) thermal grease (cold)	94 (start) 96 (end)
	APM	Al_2O_3 plate (625 µm) (hot+cold) thermal grease (cold)	89 (start)
mod2	APM	Al_2O_3-coated Al foil (hot) SiO_2 plate (660 µm) (cold) thermal grease (cold) Inconel HFM (cold)	91 (start)
mod3	APM1	Al_2O_3-coated Al foil (hot) Al_2O_3 plate (250 µm) (cold) thermal grease (cold)	87 (start)
	RM		83 (start)
	APM2		89 (start)

Finally, our results also strongly suggested that the measurement of contact resistivity (and the corresponding ability to detect the presence of cracks) was very dependent on the pressure applied during characterization. This pressure could not be monitored for PSM measurements in this work, it would however be very beneficial to find a way to quantify it for further characterization and understanding. To optimize the analysis of the electrical potential in the PSM, fittings could also be applied on the several sections of the leg (metallizations, TE material) to attenuate the noise which could hide low contact resistivities.

f) Further optimizations

On the long term, further optimization could be made, such as the implementation of graded legs [25] to increase the performance of the TE legs, as well as increasing the size (number of pairs) of the TEG to further its mechanical stability on a larger scale and heavier, more intricated designs.

References

Below are the references used in Chapters 1 (Introduction), 2 (Methods), 6 (Discussion) and 7 (Conclusion and Outlook).

1. Ayachi, S., et al., *On the Relevance of Point Defects for the Selection of Contacting Electrodes: Ag as an Example for Mg2(Si,Sn)-based Thermoelectric Generators.* Materials Today Physics, 2021. **16**: p. 100309.
2. Pham, N.H., et al., *Ni and Ag electrodes for magnesium silicide based thermoelectric generators.* Materials Today Energy, 2019. **11**: p. 97-105.
3. Ayachi, S., *Developing contacting solutions for Mg2 (Si, Sn)-based thermoelectric generators: evaluating Cu and Ni45Cu55 as candidates for contacting electrodes, and establishing the importance of charged point defects in the contacting process*, in *Institute of Technology for Nanostructures (NST)*. 2021, University of Duisburg-Essen: Duisburg, Germany.
4. Camut, J., et al., *Aluminum as promising electrode for Mg2(Si,Sn)-based thermoelectric devices.* Materials Today Energy, 2021. **21**.
5. Camut, J., et al., *Overcoming Asymmetric Contact Resistances in Al-Contacted Mg2 (Si, Sn) Thermoelectric Legs.* Materials, 2021. **14**(22): p. 6774.
6. Camut, J., et al., *Efficiency measurement and modelling of a high performance Mg2 (Si, Sn)-based thermoelectric generator.* Advanced Engineering Materials, 2022.
7. Smil, V., *Energy transitions: global and national perspectives*. 2016: ABC-CLIO.
8. He, J. and T.M. Tritt, *Advances in thermoelectric materials research: Looking back and moving forward.* Science, 2017. **357**(6358): p. eaak9997.
9. Jaziri, N., et al., *A comprehensive review of Thermoelectric Generators: Technologies and common applications.* Energy Reports, 2020. **6**: p. 264-287.
10. Ebling, D.G., et al., *Development of a System for Thermoelectric Heat Recovery from Stationary Industrial Processes.* Journal of Electronic Materials, 2016. **45**(7): p. 3433-3439.
11. Li, K., et al., *Thermoelectric power generator: Field test at Bottle Rock geothermal power plant.* Journal of Power Sources, 2021. **485**: p. 229266.
12. Goupil, C., *Continuum theory and modeling of thermoelectric elements*. 2015: John Wiley & Sons.
13. Gurevich, Y.G. and J.E. Velazquez-Perez, *Peltier Effect in Semiconductors*, in *Wiley Encyclopedia of Electrical and Electronics Engineering*. 2014. p. 1-21.
14. Rowe, D.M., *General Principles and Basic Considerations*, in *Thermoelectrics Handbook: Macro to Nano*, D.M. Rowe, Editor. 2006, CRC press: Boca Raton.
15. Snyder, G.J. and E.S. Toberer, *Complex thermoelectric materials*, in *Materials for sustainable energy: a collection of peer-reviewed research and review articles from Nature Publishing Group*. 2011, World Scientific. p. 101-110.
16. Gao, M., *Thermoelectric Module Design Theories*, in *Thermoelectrics Handbook: Macro to Nano*, D.M. Rowe, Editor. 2006, CRC press: Boca Raton.
17. Thiébaut, E., et al., *Maximization of the thermoelectric cooling of a graded Peltier device by analytical heat-equation resolution.* Physical review applied, 2017. **8**(6): p. 064003.
18. Rowe, D.M., *Thermoelectrics handbook: macro to nano*. 2005, CRC press.
19. Antonova, E.E. and D.C. Looman. *Finite elements for thermoelectric device analysis in ANSYS*. in *Thermoelectrics, 2005. ICT 2005. 24th International Conference on*. 2005. IEEE.

20. Kim, C.N., *Development of a numerical method for the performance analysis of thermoelectric generators with thermal and electric contact resistance.* Applied Thermal Engineering, 2018. **130**: p. 408-417.
21. Hogan, T. and T. Shih, *Modeling and characterization of power generation modules based on bulk materials.* Thermoelectrics Handbook: Macro to Nano, 2006: p. 12.1-12.23.
22. Oliveira, K.S., R.P. Cardoso, and C.J. Hermes, *Two-Dimensional Modeling of Thermoelectric Cells.* 2014.
23. Sherman, B., R. Heikes, and R. Ure Jr, *Calculation of efficiency of thermoelectric devices.* Journal of Applied Physics, 1960. **31**(1): p. 1-16.
24. Brandt, J.A., *Solutions to the differential equations describing the temperature distribution, thermal efficiency, and power output of a thermoelectric element with variable properties and cross sectional area.* Advanced Energy Conversion, 1962. **2**: p. 219-230.
25. Ponnusamy, P., et al., *Grading studies for efficient thermoelectric devices using combined 1D material and device modeling.* Journal of Applied Physics, 2022. **132**(11): p. 115702.
26. Ponnusamy, P., J. de Boor, and E. Müller, *Discrepancy between constant properties model and temperature-dependent material properties for performance estimation of thermoelectric generators.* Entropy, 2020. **22**(10): p. 1128.
27. Zeier, W.G., et al., *Engineering half-Heusler thermoelectric materials using Zintl chemistry.* Nature Reviews Materials, 2016. **1**(6): p. 1-10.
28. Ponnusamy, P., J. de Boor, and E. Müller, *Using the constant properties model for accurate performance estimation of thermoelectric generator elements.* Applied Energy, 2020. **262**: p. 114587.
29. Han, C., Z. Li, and S. Dou, *Recent progress in thermoelectric materials.* Chinese Science Bulletin, 2014. **59**(18): p. 2073-2091.
30. Goldsmid, H.J., *Conversion Efficiency and Figure-of-Merit*, in *CRC Handbook of Thermoelectrics*, D.M. Rowe, Editor. 1995, CRC press: Boca Raton.
31. Neamen, D.A., *Semiconductor physics and devices: basic principles*. 2003: McGraw-hill.
32. de Boor, J., *On the applicability of the single parabolic band model to advanced thermoelectric materials with complex band structures.* Journal of Materiomics, 2021. **7**(3): p. 603-611.
33. Kim, H.-S., et al., *Understanding bipolar thermal conductivity in terms of concentration ratio of minority to majority carriers.* Journal of Materials Research Technology, 2021. **14**: p. 639-646.
34. Aswal, D.K., R. Basu, and A. Singh, *Key issues in development of thermoelectric power generators: High figure-of-merit materials and their highly conducting interfaces with metallic interconnects.* Energy conversion management, 2016. **114**: p. 50-67.
35. Ayachi, S., et al., *Developing Contacting Solutions for Mg2Si1–x Sn x-Based Thermoelectric Generators: Cu and Ni45Cu55 as Potential Contacting Electrodes.* ACS Applied Materials Interfaces, 2019. **11**(43): p. 40769-40780.
36. He, R., G. Schierning, and K. Nielsch, *Thermoelectric Devices: A Review of Devices, Architectures, and Contact Optimization.* Advanced Materials Technologies, 2018. **3**(4): p. 1700256.
37. D'Angelo, J.J., et al., *Electrical Contact Fabrication and Measurements of Metals and Alloys to Thermoelectric Materials.* Materials Research Society Symposium Proceedings, 2008. **1044**: p. 449-455.

38. de Boor, J., et al., *Fabrication and characterization of nickel contacts for magnesium silicide based thermoelectric generators.* Journal of Alloys and Compounds, 2015. **632**: p. 348-353.
39. Bjørk, R., *The universal influence of contact resistance on the efficiency of a thermoelectric generator.* Journal of electronic materials, 2015. **44**(8): p. 2869-2876.
40. S. M. Sze and K.K. Ng, *Metal-Semiconductor Contacts*, in *Physics of Semiconductor Devices*. 2006, John Wiley & Sons, Inc. p. 134-196.
41. Zhang, Z. and J.T. Yates Jr, *Band bending in semiconductors: chemical and physical consequences at surfaces and interfaces.* Chemical reviews, 2012. **112**(10): p. 5520-5551.
42. R. F. Pierret, *MS Contacts and Schottky Diodes*, in *Semiconductor Device Fundamentals*, I. Addison-Weasley Publishing Company, Editor. 1996, John Wiley & Sons, Inc: USA. p. 134-196.
43. Tung, R.T., *The physics and chemistry of the Schottky barrier height.* Applied Physics Reviews, 2014. **1**(1): p. 011304.
44. Qin, Y.-F. and S.-Q. Wang, *Ab-initio study of the role of Mg2Si and Al2CuMg phases in electrochemical corrosion of Al alloys.* Journal of The Electrochemical Society, 2015. **162**(9): p. C503.
45. Timsit, S. *Electrical contact resistance: properties of stationary interfaces*. in *Electrical Contacts-1998. Proceedings of the Forty-Fourth IEEE Holm Conference on Electrical Contacts (Cat. No. 98CB36238)*. 1998. Arlington, VA, USA: IEEE.
46. Erturun, U., K. Erermis, and K. Mossi, *Influence of leg sizing and spacing on power generation and thermal stresses of thermoelectric devices.* Applied Energy, 2015. **159**: p. 19-27.
47. Jia, X. and Y. Gao, *Estimation of thermoelectric and mechanical performances of segmented thermoelectric generators under optimal operating conditions.* Applied Thermal Engineering, 2014. **73**(1): p. 335-342.
48. Karri, N.K. and C. Mo, *Structural Reliability Evaluation of Thermoelectric Generator Modules: Influence of End Conditions, Leg Geometry, Metallization, and Processing Temperatures.* Journal of Electronic Materials, 2018. **47**(10): p. 6101-6120.
49. He, J. and T.M. Tritt, *Advances in thermoelectric materials research: Looking back and moving forward.* Science, 2017. **357**(6358).
50. Fanciulli, C., *Thermoelectric Harvesting: Basics on Design Optimization and Applications*, in *Advances in Thermoelectricity: Foundational Issues, Materials and Nanotechnology*, D. Narducci, G. J. Snyder, and C. Fanciulli, Editors. 2021, IOS Press: Amsterdam.
51. Von Lukowicz, M., et al., *Thermoelectric generators on satellites—An approach for waste heat recovery in space.* Energies, 2016. **9**(7): p. 541.
52. Huang, K., et al., *A novel design of thermoelectric generator for automotive waste heat recovery.* Automotive Innovation, 2018. **1**(1): p. 54-61.
53. Orr, B., et al., *A review of car waste heat recovery systems utilising thermoelectric generators and heat pipes.* Applied thermal engineering, 2016. **101**: p. 490-495.
54. Zhou, M., et al., *A review on heat and mechanical energy harvesting from human–Principles, prototypes and perspectives.* Renewable Sustainable Energy Reviews, 2018. **82**: p. 3582-3609.
55. Liu, X., et al., *Significant Roles of Intrinsic Point Defects in Mg2X (X = Si, Ge, Sn) Thermoelectric Materials.* Advanced Electronic Materials, 2016. **2**(2): p. 1500284.
56. Rull-Bravo, M., et al., *Skutterudites as thermoelectric materials: revisited.* RSC Advances, 2015. **5**(52): p. 41653-41667.

57. Puyet, M., et al., *Beneficial effect of Ni substitution on the thermoelectric properties in partially filled Ca y Co 4− x Ni x Sb 12 skutterudites.* Journal of applied physics, 2005. **97**(8): p. 083712.
58. Chen, S. and Z. Ren, *Recent progress of half-Heusler for moderate temperature thermoelectric applications.* Materials Today, 2013. **16**(10): p. 387-395.
59. Sakurada, S. and N. Shutoh, *Effect of Ti substitution on the thermoelectric properties of (Zr, Hf) NiSn half-Heusler compounds.* Applied Physics Letters, 2005. **86**(8): p. 082105.
60. Kutorasinski, K., et al., *Importance of relativistic effects in electronic structure and thermopower calculations for Mg2Si, Mg2Ge and Mg2Sn.* Physical Review B, 2014. **89**(11): p. 115205.
61. Stella, A., et al., *Pressure coefficient of the band gap in Mg2Si, Mg2Ge, and Mg2Sn.* physica status solidi (b), 1967. **23**(2): p. 697-702.
62. Morris, R.G., R.D. Redin, and G.C. Danielson, *Semiconducting Properties of Mg2Si Single Crystals.* Physical Review, 1958. **109**(6): p. 1909-1915.
63. Liu, W., et al., *Convergence of Conduction Bands as a Means of Enhancing Thermoelectric Performance of n-type Mg2Si1-xSnx Solid Solutions.* Physical Review Letters, 2012. **108**(16): p. 166601.
64. Trivedi, V., et al., *Microstructure and doping effect on the enhancement of the thermoelectric properties of Ni doped Dy filled CoSb 3 skutterudites.* Sustainable Energy Fuels, 2018. **2**(12): p. 2687-2697.
65. Ostovari Moghaddam, A., et al., *Ge-Doped ZnSb/β-Zn4Sb3 Nanocomposites with High Thermoelectric Performance.* Advanced Materials Interfaces, 2019. **6**(18): p. 1900467.
66. Jood, P., et al., *Na Doping in PbTe: Solubility, Band Convergence, Phase Boundary Mapping, and Thermoelectric Properties.* Journal of the American Chemical Society, 2020. **142**(36): p. 15464-15475.
67. Yang, S., et al., *Thermal stability study of melt spun TAGS-80 thermoelectric bulks.* Journal of Materials Science: Materials in Electronics, 2017. **28**(20): p. 15279-15283.
68. Wu, F., et al., *Effects of Ce, Y, and Sm doping on the thermoelectric properties of Bi2Te3 alloy.* Progress in Natural Science: Materials International, 2013. **23**(4): p. 408-412.
69. Poudel, B., et al., *High-Thermoelectric Performance of Nanostructured Bismuth Antimony Telluride Bulk Alloys.* Science, 2008. **320**(5876): p. 634-638.
70. Fedorov, M.I., V.K. Zaitsev, and G.N. Isachenko. *High effective thermoelectrics based on the Mg2Si-Mg2Sn solid solution*. in *Solid State Phenomena*. 2011. Trans Tech Publ.
71. Zaitsev, V., et al., *Highly effective Mg2Si1−xSnx thermoelectrics.* Physical Review B, 2006. **74**(4): p. 045207.
72. de Boor, J., et al., *Recent progress in p-type thermoelectric magnesium silicide based solid solutions.* Materials Today Energy, 2017. **4**: p. 105-121.
73. Bashir, M.B.A., et al., *Recent advances on Mg2Si1− xSnx materials for thermoelectric generation.* Renewable Sustainable Energy Reviews, 2014. **37**: p. 569-584.
74. de Boor, J., et al., *Thermoelectric performance of Li doped, p-type Mg2(Ge,Sn) and comparison with Mg2(Si,Sn).* Acta Materialia, 2016. **120**: p. 273-280.
75. Kamila, H., et al., *Synthesis of p-type Mg2Si1-xSnx with x= 0-1 and optimization of the synthesis parameters.* Materials Today: Proceedings, 2019. **8**: p. 546-555.
76. Farahi, N., et al., *High efficiency Mg 2 (Si, Sn)-based thermoelectric materials: scale-up synthesis, functional homogeneity, and thermal stability.* RSC Advances, 2019. **9**(40): p. 23021-23028.
77. Hasbuna, K., *Influence of the Composition of p-type Mg2X (X: Si, Ge, Sn) on the Thermoelectric Properties and Electronic Band Structure.* 2021.
78. Bellanger, P., et al., *Effect of microstructure on the thermal conductivity of nanostructured Mg2(Si,Sn) thermoelectric alloys: An experimental and modeling approach.* Acta Materialia, 2015. **95**: p. 102-110.

79. Gao, P., et al., *The p-type Mg2LixSi0.4Sn0.6 thermoelectric materials synthesized by a B2O3 encapsulation method using Li2CO3 as the doping agent.* Journal of Materials Chemistry C, 2016. **4**(5): p. 929-934.
80. Zhang, Q., et al., *Low effective mass and carrier concentration optimization for high performance p-type Mg2(1-x)Li2xSi0.3Sn0.7 solid solutions.* Physical Chemistry Chemical Physics, 2014. **16**(43): p. 23576-23583.
81. Sankhla, A., et al., *Mechanical alloying of optimized Mg2 (Si, Sn) solid solutions: understanding phase evolution and tuning synthesis parameters for thermoelectric applications.* ACS Applied Energy Materials, 2018. **1**(2): p. 531-542.
82. Tang, X., et al., *Ultra rapid fabrication of p-type Li-doped Mg2Si0.4Sn0.6 synthesized by unique melt spinning method.* Scripta Materialia, 2016. **115**: p. 52-56.
83. Kaibe, H., et al. *Development of thermoelectric generating stacked modules aiming for 15% of conversion efficiency*. in *ICT 2005. 24th International Conference on Thermoelectrics, 2005.* 2005. IEEE.
84. Skomedal, G., et al., *Design, assembly and characterization of silicide-based thermoelectric modules*. Energy Conversion and Management, 2016. **110**: p. 13-21.
85. Mejri, M., et al., *Thermal stability of Mg2Si0.55Sn0.45 for thermoelectric applications.* Journal of Alloys Compounds, 2020. **846**: p. 156413.
86. Gao, P., et al., *Transport and mechanical properties of high-ZT Mg 2.08 Si 0.4− x Sn 0.6 Sb x thermoelectric materials.* Journal of Electronic Materials, 2014. **43**(6): p. 1790-1803.
87. Gelbstein, Y., et al., *Physical, mechanical, and structural properties of highly efficient nanostructured n-and p-silicides for practical thermoelectric applications.* Journal of Electronic Materials, 2014. **43**(6): p. 1703-1711.
88. Mejri, M., et al., *Characterization of the thermo-mechanical properties of p-type (MnSi1. 77) and n-type (Mg2Si0. 6Sn0. 4) thermoelectric materials.* Scripta Materialia, 2019. **172**: p. 28-32.
89. Schmidt, R.D., et al., *Room-temperature mechanical properties and slow crack growth behavior of Mg 2 Si thermoelectric materials.* Journal of electronic materials, 2012. **41**(6): p. 1210-1216.
90. Huang, Z., et al., *Electronic structural, elastic properties and thermodynamics of Mg17Al12, Mg2Si and Al2Y phases from first-principles calculations.* Physica B: Condensed Matter, 2012. **407**(7): p. 1075-1081.
91. Wang, L., et al., *Fabrication and mechanical properties of bulk nanocrystalline intermetallic Mg2Si.* Materials Science Engineering: A, 2007. **459**(1-2): p. 216-222.
92. Milekhine, V., et al., *Mechanical properties of FeSi (ε), FeSi2 (ζα) and Mg2Si.* Intermetallics, 2002. **10**(8): p. 743-750.
93. Schmidt, R.D., et al., *Mechanical properties of Mg2Si thermoelectric materials with the addition of 0–4 vol% silicon carbide nanoparticles (SiC NP).* Journal of Materials Science, 2015. **50**(11): p. 4034-4046.
94. Whitten, W., P. Chung, and G. Danielson, *Elastic constants and lattice vibration frequencies of Mg2Si.* Journal of Physics and Chemistry of Solids, 1965. **26**(1): p. 49-56.
95. Muthiah, S., et al., *Mechanical properties of thermoelectric n-type magnesium silicide synthesized employing in situ spark plasma reaction sintering.* Materials Research Express, 2017. **4**(7): p. 075507.
96. Davis, L., W. Whitten, and G. Danielson, *Elastic constants and calculated lattice vibration frequencies of Mg2Sn.* Journal of Physics and Chemistry of Solids, 1967. **28**(3): p. 439-447.

97. Li, X., et al., *Elastic and Thermodynamic Properties Prediction of Mg 2 Sn and MgTe by First-Principle Calculation and Quasi-Harmonic Debye Model.* Journal of Electronic Materials, 2020. **49**(1): p. 464-471.
98. Gelbstein, Y., et al., *Mechanical properties of PbTe-based thermoelectric semiconductors.* Scripta Materialia, 2008. **58**(4): p. 251-254.
99. Schmitz, A., et al., *Current assisted sintering of PbTe—Effects on thermoelectric and mechanical properties.* Materials Research Bulletin, 2017. **86**: p. 159-166.
100. He, R., et al., *Studies on mechanical properties of thermoelectric materials by nanoindentation.* physica status solidi, 2015. **212**(10): p. 2191-2195.
101. Morelli, D., et al., *Low-temperature transport properties of p-type CoSb3.* Physical Review B, 1995. **51**(15): p. 9622.
102. Klobes, B., et al., *Lattice dynamics and elasticity in thermoelectric Mg2Si1−xSnx.* Physical review materials, 2019. **3**(2): p. 025404.
103. Castillo-Hernández, G., E. Müller, and J. de Boor, *Impact of the Dopant Species on the Thermomechanical Material Properties of Thermoelectric Mg2Si0.3Sn0.7.* Materials, 2022. **15**(3).
104. Schmidt, R.D., et al., *The temperature dependence of thermal expansion for p-type Ce0. 9Fe3. 5Co0. 5Sb12 and n-type Co0. 95Pd0. 05Te0. 05Sb3 skutterudite thermoelectric materials.* Philosophical Magazine, 2012. **92**(10): p. 1261-1286.
105. Flanders, L.A., et al. *Improvements in Materials and Processes for Segmented BiTe/PbTe-BiTe/TAGS/PbSnTe based Thermoelectric Generators*. in *AIP Conference Proceedings*. 2005. American Institute of Physics.
106. Ngan, P.H., L. Han, and D.V. Christensen, *Joining of half-heusler and bismuth tellurides for segmented thermoelectric generators.* Journal of Electronic Materials, 2018. **47**(1): p. 701-710.
107. Dunn, B.D., *Materials and processes: for spacecraft and high reliability applications*. 2016: Springer.
108. Sundman, B., H.L. Lukas, and S.G. Fries, *Computational thermodynamics: the Calphad method*. 2007: Cambridge university press Cambridge.
109. Tumminello, S., et al., *Applications of thermodynamic calculations to practical TEG design: Mg 2 (Si 0.3 Sn 0.7)/Cu interconnections.* Journal of Materials Chemistry A, 2021. **9**(36): p. 20436-20452.
110. Goyal, G.K. and T. Dasgupta, *Generic Approach for Contacting Thermoelectric Solid Solutions: Case Study in n-and p-Type Mg2Si0. 3Sn0. 7.* ACS Applied Materials Interfaces, 2021. **13**(17): p. 20754-20762.
111. Tarantik, K.R., et al., *Thermoelectric Modules Based on Silicides–Development and Characterization.* Materials Today: Proceedings, 2015. **2**(2): p. 588-595.
112. de Padoue Shyikira, A., G. Skomedal, and P.H. Middleton, *Performance evaluation and stability of silicide-based thermoelectric modules.* Materials Today: Proceedings, 2020.
113. Kim, H.S., et al., *Design of segmented thermoelectric generator based on cost-effective and light-weight thermoelectric alloys.* Materials Science Engineering: B, 2014. **185**: p. 45-52.
114. de Boor, J., et al., *Thermal stability of magnesium silicide/nickel contacts.* Journal of Electronic Materials, 2016. **45**(10): p. 5313-5320.
115. Mitra, K., S. Mahapatra, and T. Dasgupta, *Fabrication of Nickel Contacts for Mg 2 Si Based Thermoelectric Generators via an Induction Assisted Rapid Monoblock Sintering Technique.* Journal of Electronic Materials, 2019. **48**(3): p. 1754-1757.
116. Sankhla, A., et al., *On the role of Mg content in Mg2 (Si, Sn): Assessing its impact on electronic transport and estimating the phase width by in situ characterization and modelling.* Materials Today Physics, 2021: p. 100471.

117. Zhang, Y., et al., *High-temperature and high-power-density nanostructured thermoelectric generator for automotive waste heat recovery.* Energy Conversion and Management, 2015. **105**: p. 946-950.
118. El Oualid, S., et al., *High Power Density Thermoelectric Generators with Skutterudites.* Advanced Energy Materials, 2021. **11**(19): p. 2100580.
119. Hatzikraniotis, E., et al., *Efficiency Study of a Commercial Thermoelectric Power Generator (TEG) Under Thermal Cycling.* Journal of Electronic Materials, 2010. **39**(9): p. 2112-2116.
120. Barako, M.T., et al., *Thermal Cycling, Mechanical Degradation, and the Effective Figure of Merit of a Thermoelectric Module.* Journal of Electronic Materials, 2013. **42**(3): p. 372-381.
121. Sankhla, A., et al., *Analyzing thermoelectric transport in n-type Mg2Si0.4Sn0.6 and correlation with microstructural effects: An insight on the role of Mg.* Acta Materialia, 2020. **199**: p. 85-95.
122. Kato, D., et al., *Control of Mg content and carrier concentration via post annealing under different Mg partial pressures for Sb-doped Mg2Si thermoelectric material.* Journal of Solid State Chemistry, 2018. **258**: p. 93-98.
123. Kato, A., T. Yagi, and N. Fukusako, *First-principles studies of intrinsic point defects in magnesium silicide.* Journal of Physics: Condensed Matter, 2009. **21**(20): p. 205801.
124. Yasseri, M., et al., *Influence of Mg loss on the phase stability in Mg2X (X=Si, Sn) and its correlation with coherency strain.* Acta Materialia, 2021. **208**: p. 116737.
125. Nemoto, T., et al., *Improvement in the durability and heat conduction of uni-leg thermoelectric modules using n-type Mg 2 Si legs.* Journal of electronic materials, 2014. **43**(6): p. 1890-1895.
126. Tohei, T., et al. *Bondability of Mg2Si element to Ni electrode using Al for thermoelectric modules*. in *International Symposium on Interfacial Joining and Surface Technology (IJST2013)*. 2014. Icho Kaikan, Osaka University, Japan, 27-29 November, 2013.
127. Gao, P., *Mg2(Si, Sn)-based thermoelectric materials and devices*. 2016, Michigan State University: Michigan State University. p. 128.
128. Goyal, G.K. and T. Dasgupta, *Fabrication and testing of Mg2Si1-xSnx based thermoelectric generator module.* Materials Science and Engineering: B, 2021. **272**: p. 115338.
129. Liu, W., et al., *Advanced thermoelectrics governed by a single parabolic band: Mg 2 Si 0.3 Sn 0.7, a canonical example.* Physical Chemistry Chemical Physics, 2014. **16**(15): p. 6893-6897.
130. Orenstein, R., et al., *Using phase boundary mapping to resolve discrepancies in the Mg2Si–Mg2Sn miscibility gap.* Journal of Materials Chemistry A, 2021. **9**(11): p. 7208-7215.
131. Castillo Hernandez, G., *Thermal and mechanical properties of Mg2Si1-xSnx (x= 0–1) for thermoelectric generators*, in *FB 08 - Biologie und Chemie*. 2022, JLU Gießen, Germany.
132. Kamila, H., et al., *Analyzing transport properties of p-type Mg 2 Si–Mg 2 Sn solid solutions: optimization of thermoelectric performance and insight into the electronic band structure.* Journal of Materials Chemistry A, 2019. **7**(3): p. 1045-1054.
133. Mileiko, S.T., *Metal and ceramic based composites*. 1997: Elsevier.
134. Grasso, S., Y. Sakka, and G. Maizza, *Electric current activated/assisted sintering (ECAS): a review of patents 1906–2008.* Science and Technology of Advanced Materials, 2009. **10**(5): p. 053001.
135. Upadhyaya, G.S., *Powder metallurgy technology*. 1997: Cambridge Int Science Publishing.

136. Vernon-Parry, K.D., *Scanning electron microscopy: an introduction.* III-Vs Review, 2000. **13**(4): p. 40-44.
137. Zhou, W., et al., *Fundamentals of scanning electron microscopy (SEM)*, in *Scanning microscopy for nanotechnology*. 2006, Springer. p. 1-40.
138. Yasseri, M., et al., *Rapid determination of local composition in quasi-binary, inhomogeneous material systems from backscattered electron image contrast.* Materialia, 2018. **2**: p. 98-103.
139. de Boor, J. and E. Müller, *Data analysis for Seebeck coefficient measurements.* Review of Scientific Instruments, 2013. **84**(6): p. 065102.
140. de Boor, J., et al., *High-temperature measurement of Seebeck coefficient and electrical conductivity.* Journal of electronic materials, 2013. **42**(7): p. 1711-1718.
141. Sankhla, A., et al., *Mechanical Alloying of Optimized Mg2(Si,Sn) Solid Solutions: Understanding Phase Evolution and Tuning Synthesis Parameters for Thermoelectric Applications.* ACS Applied Energy Materials, 2018. **1**(2): p. 531-542.
142. Borup, K.A., et al., *Measuring thermoelectric transport properties of materials.* Energy & Environmental Science, 2015. **8**(2): p. 423-435.
143. Ziolkowski, P., et al., *Probing thermopower on the microscale.* physica status solidi, 2013. **210**(1): p. 89-105.
144. Platzek, D., et al. *Potential-Seebeck-microprobe (PSM): measuring the spatial resolution of the Seebeck coefficient and the electric potential*. in *ICT 2005. 24th International Conference on Thermoelectrics, 2005.* 2005. IEEE.
145. Ziolkowski, P., P. Blaschkewitz, and E. Müller, *Heat flow measurement as a key to standardization of thermoelectric generator module metrology: A comparison of reference and absolute techniques.* Measurement, 2021. **167**: p. 108273.
146. Ziolkowski, P., P. Blaschkewitz, and E. Müller, *Validation of commercial Bi2Te3-based thermoelectric generator modules for application as metrological reference samples.* Measurement, 2021. **177**: p. 109247.
147. Ziolkowski, P., et al., *Interlaboratory Testing for High-Temperature Power Generation Characteristics of a Ni-Based Alloy Thermoelectric Module.* Energy Technology, 2020. **8**(11): p. 2000557.
148. Ziolkowski, P., et al., *International Round Robin Test of Thermoelectric Generator Modules.* Materials, 2022. **15**(5).
149. Armstrong, H., et al., *Estimating energy conversion efficiency of thermoelectric materials: constant property versus average property models.* Journal of Electronic Materials, 2017. **46**(1): p. 6-13.
150. Bhandari, C.M. and D.M. Rowe, *Optimization of Carrier Concentration*, in *CRC Handbook of Thermoelectrics*, D.M. Rowe, Editor. 1995, CRC press: Boca Raton.
151. Kamila, H., et al., *Analyzing transport properties of p-type Mg2Si–Mg2Sn solid solutions: optimization of thermoelectric performance and insight into the electronic band structure.* Journal of Materials Chemistry A, 2019. **7**(3): p. 1045-1054.
152. Naithani, H. and T. Dasgupta, *Critical Analysis of Single Band Modeling of Thermoelectric Materials.* ACS Applied Energy Materials, 2020. **3**(3): p. 2200-2213.
153. Jiang, G., et al., *High performance Mg2 (Si, Sn) solid solutions: a point defect chemistry approach to enhancing thermoelectric properties.* Advanced Functional Materials, 2014. **24**(24): p. 3776-3781.
154. Nieroda, P., et al., *Structural and Thermoelectric Properties of Polycrystalline p-Type Mg2− x Li x Si.* Journal of Electronic Materials, 2016. **45**(7): p. 3418-3426.
155. Macario, L.R., et al., *Thermoelectric properties of Bi-doped magnesium silicide stannides.* ACS applied materials & interfaces, 2018. **10**(47): p. 40585-40591.

156. Liu, W., et al., *Enhanced hole concentration through Ga doping and excess of Mg and thermoelectric properties of p-type Mg2 (1+ z)(Si0. 3Sn0. 7) 1− yGay.* Intermetallics, 2013. **32**: p. 352-361.
157. Kim, G., et al., *Co-doping of Al and Bi to control the transport properties for improving thermoelectric performance of Mg2Si.* Scripta Materialia, 2016. **116**: p. 11-15.
158. May, A.F. and G.J. Snyder, *Introduction to modeling thermoelectric transport at high temperatures*, in *Materials, preparation, and characterization in thermoelectrics*. 2017, CRC press. p. 207-224.
159. Kim, H.-S., et al., *Characterization of Lorenz number with Seebeck coefficient measurement.* APL Materials, 2015. **3**(4): p. 041506.
160. Ponnusamy, P., et al., *Efficiency as a performance metric for material optimization in thermoelectric generators.* Journal of Physics: Energy, 2021.
161. Zwolenski, P., J. Tobola, and S. Kaprzyk, *A theoretical search for efficient dopants in Mg 2 X (X= Si, Ge, Sn) thermoelectric materials.* Journal of Electronic Materials, 2011. **40**(5): p. 889-897.
162. De Boor, J., et al., *Microstructural effects on thermoelectric efficiency: A case study on magnesium silicide.* Acta materialia, 2014. **77**: p. 68-75.
163. Yang, P., et al., *Analysis of Peak Electromagnetic Torque Characteristics for Superconducting DC Induction Heaters.* IEEE Access, 2020. **8**: p. 1-1.
164. Salinas, D., S. Garcia, and J.J.J.o.A.E. Bessone, *Influence of alloying elements and microstructure on aluminium sacrificial anode performance: case of Al–Zn.* 1999. **29**(9): p. 1063-1071.
165. Du, Y., et al., *Diffusion coefficients of some solutes in fcc and liquid Al: critical evaluation and correlation.* Materials Science and Engineering: A, 2003. **363**(1-2): p. 140-151.
166. Chartrand, P. and A.D. Pelton, *Critical evaluation and optimization of the thermodynamic properties and phase diagrams of the Al-Mg, Al-Sr, Mg-Sr, and Al-Mg-Sr systems.* Journal of phase equilibria, 1994. **15**(6): p. 591-605.
167. Battiston, S., et al., *Multilayered thin films for oxidation protection of Mg2Si thermoelectric material at middle–high temperatures.* Thin Solid Films, 2012. **526**: p. 150-154.
168. D'Isanto, F., et al., *Oxidation protective glass coating for magnesium silicide based thermoelectrics.* Ceramics International, 2020. **46**(15): p. 24312-24317.
169. Gucci, F., et al., *Oxidation protective hybrid coating for thermoelectric materials.* Materials, 2019. **12**(4): p. 573.
170. Nieroda, P., et al., *New high temperature amorphous protective coatings for Mg2Si thermoelectric material.* Ceramics International, 2019. **45**(8): p. 10230-10235.
171. Sadia, Y., D. Ben-Ayoun, and Y. Gelbstein, *PbO–SiO2-based glass doped with B2O3 and Na2O for coating of thermoelectric materials.* Journal of Materials Research, 2019. **34**(20): p. 3563-3572.
172. Tani, J.-i., M. Takahashi, and H. Kido, *Fabrication of oxidation-resistant β-FeSi2 film on Mg2Si by RF magnetron-sputtering deposition.* Journal of Alloys and Compounds, 2009. **488**(1): p. 346-349.
173. Kolb, H., et al., *Simultaneous measurement of all thermoelectric properties of bulk materials in the temperature range 300–600 K.* Review of Scientific Instruments, 2015. **86**(7): p. 073901.

Co-Authorship Statement

The co-author contribution for the three publications presented in this thesis are as follows. These were published in peer-reviewed journals with accordance to the corresponding journals regulations.

Paper 1 (Chapter 3): J. Camut, N.H. Pham, D.Y. Nhi Truong, G. Castillo-Hernandez, N. Farahi, M. Yasseri, E. Mueller, J. de Boor, *Aluminum as promising electrode for Mg2(Si,Sn)-based thermoelectric devices*, Materials Today Energy, 2021, Volume 21, p. 100718, https://doi.org/10.1016/j.mtener.2021.100718.

Contributor	Affiliation and Contact details	Contribution
Julia Camut, M.Sc. (first and corresponding author)	German Aerospace Center, Institute of Materials Research, Dept. of Thermoelectric Materials &Systems, Cologne, 51147, Germany julia.camut@dlr.de	Writing - original draft, Writing - review & editing, Visualization, Investigation
Ngan Hoang Pham, Dr.rer.nat (shared first authorship)	Ångström Laboratory, Uppsala University, Sweden nngan.pham@angstrom.uu.se	Writing - original draft, Writing - review & editing, Investigation
Dao Y Nhi Truong, Dr.rer.nat	German Aerospace Center, Institute of Materials Research, Dept. of Thermoelectric Materials &Systems, Cologne, 51147, Germany daoynhi.truong@gmail.com	Writing - review & editing, Investigation
Gustavo Castillo-Hernandez, Dr.rer.nat	German Aerospace Center, Institute of Materials Research, Dept. of Thermoelectric Materials &Systems, Cologne, 51147, Germany Justus Liebig University Giesen, Institute of Inorganic and Analytical Chemistry, D–35392 Giesen, Germany. gustavo.castillo-hernandez@dlr.de	Writing - review
Nader Farahi, Dr.rer.nat	German Aerospace Center, Institute of Materials Research, Dept. of Thermoelectric Materials &Systems, Cologne, 51147, Germany nader.farahi@dlr.de	Writing - review
Mohammad Yasseri, Dr.rer.nat	German Aerospace Center, Institute of Materials Research, Dept. of Thermoelectric Materials &Systems,	Investigation

	Cologne, 51147, Germany Justus Liebig University Giesen, Institute of Inorganic and Analytical Chemistry, D–35392 Giesen, Germany. mohammad.yasseri@dlr.de	
Eckhard Müller, Dr.rer.nat	German Aerospace Center, Institute of Materials Research, Dept. of Thermoelectric Materials &Systems, Cologne, 51147, Germany Justus Liebig University Giesen, Institute of Inorganic and Analytical Chemistry, D–35392 Giesen, Germany. eckhard.mueller@dlr.de	Conceptualization, Supervision
Johannes de Boor, Dr.rer.nat Jun-Prof. (corresponding author)	German Aerospace Center, Institute of Materials Research, Dept. of Thermoelectric Materials &Systems, Cologne, 51147, Germany Institute of Technology for Nanostructures (NST), Faculty of Engineering, University of Duisburg-Essen, Germany johannes.deboor@dlr.de	Conceptualization, Supervision, Project administration, Writing - review & editing

Paper 2 (Chapter 4): J. Camut, S. Ayachi, S.; G. Castillo-Hernández, S. Park, B. Ryu, S. Park, A. Frank, C. Stiewe, E. Müller, J. de Boor, *Overcoming Asymmetric Contact Resistances in Al-Contacted Mg2(Si,Sn) Thermoelectric Legs*, Materials, 2021, 14, 6774, https://doi.org/10.3390/ma14226774

Contributor	Affiliation and Contact details	Contribution
Julia Camut, M.Sc. (first and corresponding author)	German Aerospace Center, Institute of Materials Research, Dept. of Thermoelectric Materials &Systems, Cologne, 51147, Germany julia.camut@dlr.de	Investigation, Writing—original draft, Writing—review & editing
Sahar Ayachi, Dr.rer.nat	German Aerospace Center, Institute of Materials Research, Dept. of Thermoelectric Materials &Systems, Cologne, 51147, Germany sahar.ayachi@dlr.de	Writing—review & editing
Gustavo Castillo-Hernandez,	German Aerospace Center, Institute of Materials Research, Dept. of	Investigation, Writing—review &

Dr.rer.nat	Thermoelectric Materials &Systems, Cologne, 51147, Germany Justus Liebig University Giesen, Institute of Inorganic and Analytical Chemistry, D–35392 Giesen, Germany. gustavo.castillo-hernandez@dlr.de	editing
Sungjin Park, Dr.rer.nat	Energy Conversion Research Center, Korea Electrotechnology Research Institute (KERI), 12, Jeongiui-gil, Seongsan-gu, Changwon-si 51543, Gyengsangnam-do, Korea sjinpark@keri.re.kr	Formal analysis
Byungki Ryu, Dr.rer.nat	Energy Conversion Research Center, Korea Electrotechnology Research Institute (KERI), 12, Jeongiui-gil, Seongsan-gu, Changwon-si 51543, Gyengsangnam-do, Korea byungkiryu@keri.re.kr	Formal analysis, Writing—review & editing
Sudong Park, Dr.rer.nat Prof,.	Energy Conversion Research Center, Korea Electrotechnology Research Institute (KERI), 12, Jeongiui-gil, Seongsan-gu, Changwon-si 51543, Gyengsangnam-do, Korea john@keri.re.kr	Formal analysis
Adina Frank	German Aerospace Center, Institute of Materials Research, Dept. of Thermoelectric Materials &Systems, Cologne, 51147, Germany adina.frank@dlr.de	Investigation
Christian Stiewe, Dr.rer.nat	German Aerospace Center, Institute of Materials Research, Dept. of Thermoelectric Materials &Systems, Cologne, 51147, Germany christian.stiewe@dlr.de	Writing—review & editing
Eckhard Müller, Dr.rer.nat	German Aerospace Center, Institute of Materials Research, Dept. of Thermoelectric Materials &Systems, Cologne, 51147, Germany Justus Liebig University Giesen, Institute of Inorganic and Analytical Chemistry, D–35392 Giesen, Germany. eckhard.mueller@dlr.de	Conceptualization, Supervision, Writing—review & editing

Johannes de Boor, Dr.rer.nat Jun-Prof. (corresponding author)	German Aerospace Center, Institute of Materials Research, Dept. of Thermoelectric Materials &Systems, Cologne, 51147, Germany Institute of Technology for Nanostructures (NST), Faculty of Engineering, University of Duisburg-Essen, Germany johannes.deboor@dlr.de	Conceptualization, Supervision, Writing—review & editing

Paper 3 (Chapter 5): J. Camut, P. Ziolkowski, P. Ponnusamy, C. Stiewe, E. Mueller, J. de Boor, *Efficiency Measurement and Modeling of a High-Performance Mg2(Si,Sn)-Based Thermoelectric Generator,* Adv. Eng. Mater., 2022, 2200776. https://doi.org/10.1002/adem.202200776

Contributor	**Affiliation and Contact details**	**Contribution**
Julia Camut, M.Sc. (first and corresponding author)	German Aerospace Center, Institute of Materials Research, Dept. of Thermoelectric Materials &Systems, Cologne, 51147, Germany julia.camut@dlr.de	Investigation, Methodology, Writing—original draft, Writing—review & editing
Pawel Ziolkowski	German Aerospace Center, Institute of Materials Research, Dept. of Thermoelectric Materials &Systems, Cologne, 51147, Germany pawel.ziolkowski@dlr.de	Writing—review & editing, Discussion, Measurement analysis
Prasanna Ponnusamy, Dr.rer.nat	German Aerospace Center, Institute of Materials Research, Dept. of Thermoelectric Materials &Systems, Cologne, 51147, Germany prasanna.ponnusamy@dlr.de	Writing—review & editing, Methodology
Christian Stiewe, Dr.rer.nat	German Aerospace Center, Institute of Materials Research, Dept. of Thermoelectric Materials &Systems, Cologne, 51147, Germany christian.stiewe@dlr.de	Writing—review & editing, Discussion, Measurement analysis
Eckhard Müller, Dr.rer.nat	German Aerospace Center, Institute of Materials Research, Dept. of Thermoelectric Materials &Systems, Cologne, 51147, Germany Justus Liebig University Giesen, Institute of	Conceptualization, Supervision, Project administration, Funding acquisition,

	Inorganic and Analytical Chemistry, D–35392 Giesen, Germany. eckhard.mueller@dlr.de	Writing—review & editing
Johannes de Boor, Dr.rer.nat Jun-Prof. (corresponding author)	German Aerospace Center, Institute of Materials Research, Dept. of Thermoelectric Materials &Systems, Cologne, 51147, Germany Institute of Technology for Nanostructures (NST), Faculty of Engineering, University of Duisburg-Essen, Germany johannes.deboor@dlr.de	Conceptualization, Supervision, Project administration, Funding acquisition, Validation, Writing—review & editing

DOI: 10.17185/duepublico/78190
URN: urn:nbn:de:hbz:465-20230524-115732-8